

# Development and Test of a Prototype for the PANDA Barrel DIRC Detector at FAIR

Dissertation  
zur Erlangung des Doktorgrades  
der Naturwissenschaften

vorgelegt beim Fachbereich Physik  
der Johann Wolfgang Goethe-Universität  
in Frankfurt am Main

von

Grzegorz Kalicy  
from Warsaw

Frankfurt am Main (2014)  
D(30)

vom Fachbereich Physik der  
Johann Wolfgang Goethe-Universität als Dissertation angenommen.

Dekan: Prof. Dr. Joachim Stroth

Gutachter : Prof. Dr. Klaus Peters

Prof. Dr. Michael Düren

Datum der Disputation:

# Contents

<b>1</b>	<b>Abstract</b>	<b>5</b>
<b>2</b>	<b>Introduction</b>	<b>7</b>
<b>3</b>	<b>The Development of the PANDA Barrel DIRC Prototype</b>	<b>17</b>
3.1	The PANDA Barrel DIRC . . . . .	17
3.1.1	The DIRC Concept . . . . .	17
3.1.2	The <i>BABAR</i> DIRC Counter . . . . .	23
3.1.3	The PANDA Barrel DIRC Design . . . . .	25
3.1.4	Considered Options . . . . .	31
3.2	Concept and Evolution of the PANDA Barrel DIRC Prototype . . . . .	32
3.3	Monte Carlo Simulations . . . . .	34
3.4	Reconstruction Method . . . . .	38
3.5	Components of the Prototype . . . . .	45
3.5.1	Radiators . . . . .	45
3.5.2	Focusing Optics . . . . .	51
<b>4</b>	<b>Performance of the PANDA Barrel DIRC Prototype</b>	<b>57</b>
4.1	Prototype 2011 . . . . .	57
4.1.1	Preparation and Description of the Setup . . . . .	57
4.1.2	The T9 Beam Line area in the CERN PS and the Beam Instrumentation	61
4.1.3	Data Set . . . . .	62
4.1.4	Performance of the Prototype . . . . .	63
4.2	Prototype 2012 . . . . .	70
4.2.1	Preparation and Description of the Setup . . . . .	70
4.2.2	Data Set . . . . .	77
4.2.3	Expected Performance of the Prototype . . . . .	78
4.2.4	Performance of the Baseline Configuration . . . . .	84
4.2.5	Comparison of the Bars . . . . .	97

4.2.6	Focusing Optics . . . . .	101
4.2.7	PID Study Using the TOF System . . . . .	106
<b>5</b>	<b>Conclusion and Outlook</b>	<b>109</b>
<b>6</b>	<b>Zusammenfassung</b>	<b>111</b>

# Chapter 1

## Abstract

The PANDA experiment at FAIR will perform world class physics studies using high-intensity cooled antiproton beams with momenta between 1.5 and 15 GeV/ $c$ . A rich physics program requires very good particle identification (PID). Charged hadron PID for the barrel section of the target spectrometer has to cover the angular range of 22-140° and separate pions from kaons for momenta up to 3.5 GeV/ $c$  with a separation power of at least 3 standard deviations. The system that will provide it has to be thin and operate in a strong magnetic field. A ring imaging Cherenkov detector using the DIRC principle meets those requirements. The design of the PANDA Barrel DIRC is based on the successful *BABAR* DIRC counter with several important changes to improve the performance and optimize the costs. The design options are being studied in detailed Monte Carlo simulation, and implemented in increasingly complex system prototypes and tested in particle beams. Before building the full system prototypes the radiator bars and lenses are measured on the test benches. The performance of the DIRC prototype was quantified in terms of the single photon Cherenkov angle resolution and the photon yield. Results for two full system prototypes will be presented. The prototype in 2011 aimed at investigating the full size expansion volume. It was found that the resolution for this configuration is at the level of in good agreement with ray tracing simulation results. A more complex prototype, tested in 2012, provided the first experience with a compact fused silica prism expansion volume, a wide radiator plate, and several advanced lens options for the focusing system. The performance of the baseline configuration of the prototype with a standard lens and an air gap met the requirements for the PANDA PID for most of the polar angle range but failed at polar angles around 90° due to photon loss at the air gap. Measurements with a prototype high-refractive index compound lens without an air gap at a polar angle of 128° beam angle showed a good resolution of  $\sigma_{\Theta_c} = 11.8 \pm 0.7$  mrad and a high photon yield of  $N_{ph} = 26.1 \pm 0.4$ . Even at polar angles close to 90° the photon yield with this lens exceeded 15 detected photons per particle, meeting the PANDA Barrel DIRC PID requirements for the entire phase space and demonstrating that the compact focusing DIRC is a very promising option for PANDA.



# Chapter 2

## Introduction



Figure 2.1: The FAIR accelerator facility with the highlighted path of the beam provided for the PANDA detector.

The PANDA (antiProton ANnihilation in Darmstadt) Experiment will be one of the four major experiments at the Facility for Antiproton and Ion Research (FAIR) which is currently under construction on the area of the GSI Helmholtzzentrum für Schwerionenforschung GmbH in Darmstadt, Germany. It will perform world class hadron physics using cooled antiproton beams of unprecedented intensities in the momentum range  $p = 1.5 - 15 \text{ GeV}/c$ . The layout of FAIR is presented in Fig. 2.1. It will use two synchrotrons, SIS100 and SIS300, to accelerate particles, which are later transported to the experiments. A primary beam of protons with energies up to 30 GeV interacts with a target creating secondary beams. Antiprotons are produced from protons collisions with thick Ni targets. They are accumulated, cooled, and rebunched before being transferred to the High Energy Storage Ring (HESR), where the PANDA detector is located.

A schematic of the HESR ring is shown in Fig. 2.2. Antiprotons are injected at  $3.7 \text{ GeV}/c$  and accelerated to up to  $15 \text{ GeV}/c$ . It is also possible to decelerate them down to  $1.5 \text{ GeV}/c$ .

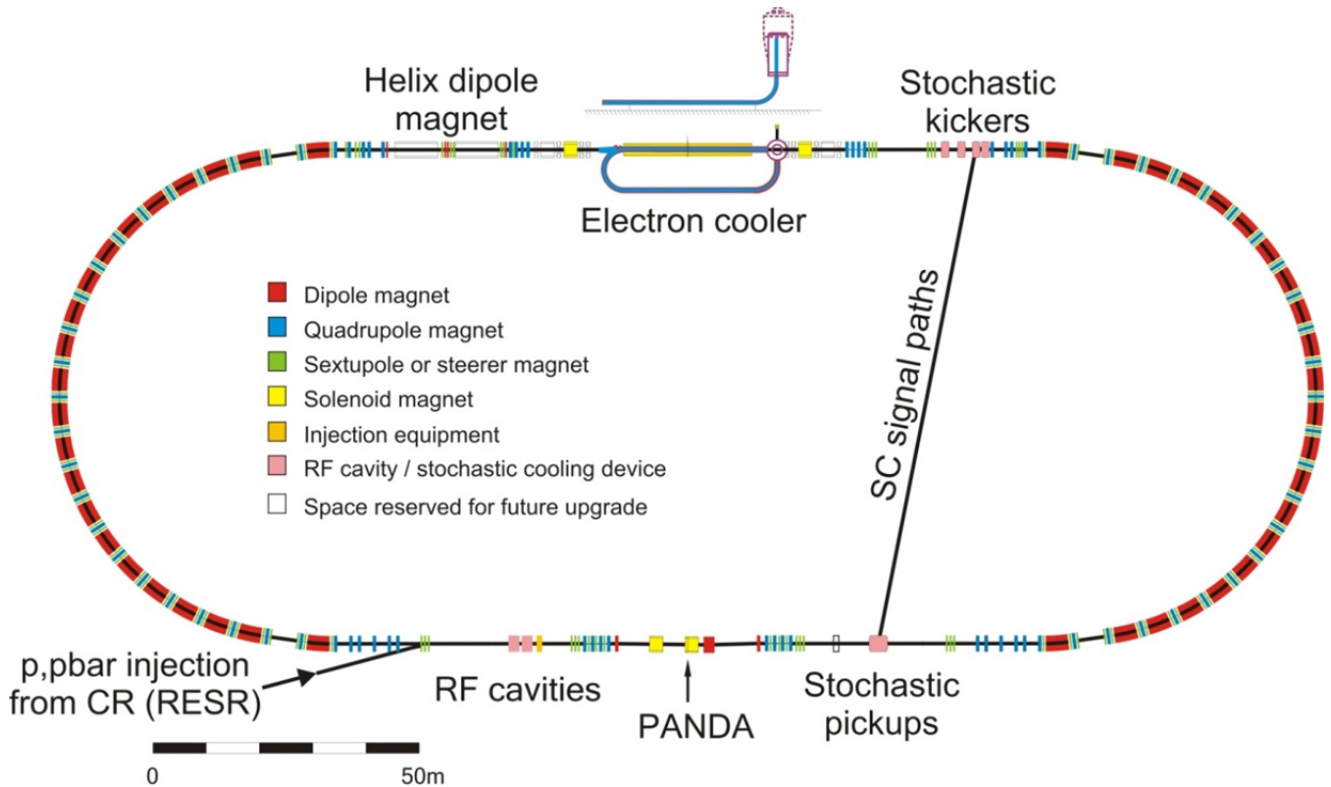


Figure 2.2: The High Energy Storage Ring providing the antiproton beam for the PANDA experiment.

There are two operating modes foreseen: the high luminosity mode and the high precision mode. Two kinds of a cooling system will be used: stochastic cooling and electron cooling. With the stochastic cooling high luminosity of  $2 \times 10^{32} \text{cm}^{-2} \text{s}^{-1}$  with  $10^{-4}$  relative momentum resolution is realized, for the full momentum range (1.5-15 GeV/c). The electron cooling will be used for experiments requiring a lower luminosity of  $2 \times 10^{31} \text{cm}^{-2} \text{s}^{-1}$ , but even better momentum resolution ( $4 \times 10^{-5}$ ). The electron cooling is limited by the energies of electrons to momenta smaller than 8 GeV/c. High luminosities will correspond to average rates of 20 MHz at the interaction point. The energy of the beam can be tuned in 50 keV steps to scan the production cross section of resonances.

A sophisticated system with a number of different cooperating complementary sub-detectors surrounds the point of collision to provide the best possible coverage of all angles and high rate capability. To achieve enough statistics PANDA will have to detect very efficiently up to  $20 \times 10^6$  interactions per second. A momentum resolution at the level of 1% and vertex information with  $700 \mu\text{m}$  resolution is required for a track information. In addition, particle identification (PID) over a wide range of momentum is of utmost importance. Only fulfilling all these requirements will make the reconstruction of the final state and the excellent identification of the reaction products possible.

The detector is shown in Fig. 2.3. In order to provide full coverage of the interaction point the detector will consist of two parts, the Forward (FS) and the Target Spectrometers (TS). The Target Spectrometer with axial symmetry surrounds the interaction point and covers polar angles above  $22^\circ$ . The Forward Spectrometer will analyze the decay products in a narrow cone of  $\pm 5^\circ$  vertically and  $\pm 10^\circ$  horizontally.

The interaction point is surrounded by the Micro Vertex Detector (MVD, Ref. [1]) which



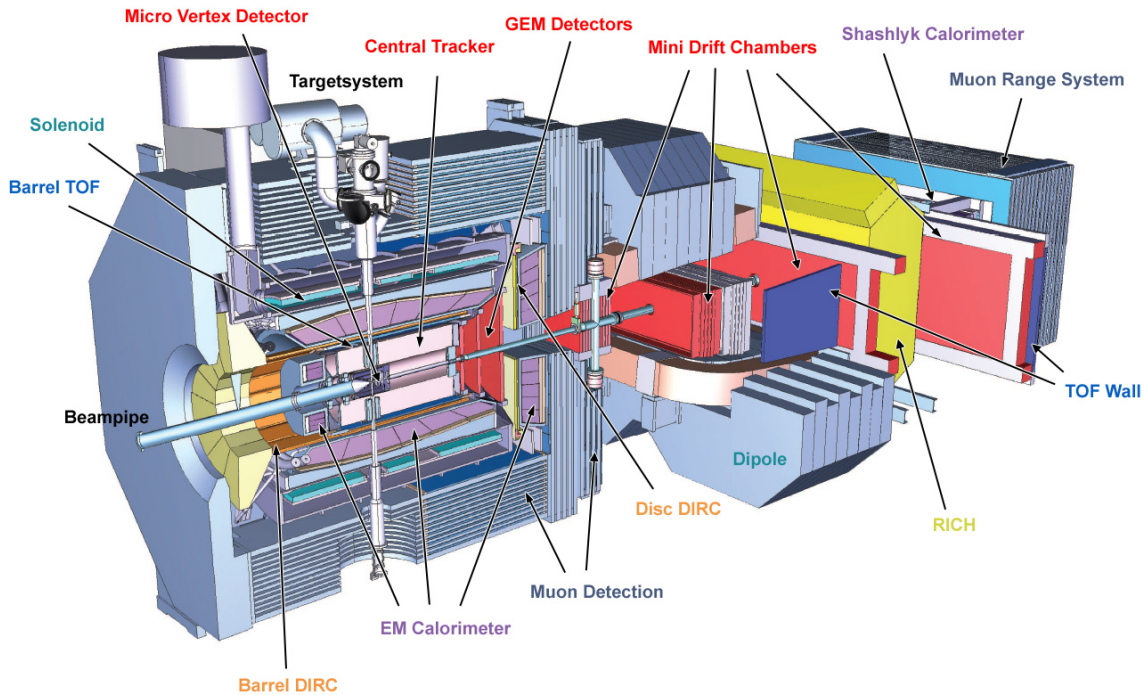


Figure 2.3: The PANDA detector with all subsystems.

consist of pixels in the inner parts, and strips in the outer part. It is enclosed by the Central Tracker based on Straw Tubes (STT, Ref. [2]) and followed by the Gas Electron Multiplier (GEM) detector in the forward direction. Next are two Cherenkov detectors, the Barrel DIRC and the Disc DIRC (Ref. [3]). Finally, there is an Electromagnetic Calorimeter (EMC, Ref. [4]) build from these parts: the barrel, and the two endcaps. These systems are inside the solenoid. The instrumented yoke hosts, in between the iron segments, detectors serving for the identification of muons (Ref. [5]). To analyze the momentum of charged particles in the forward direction a dipole magnet with a large inlet aperture will be used (Ref. [6]). Details about all the sub-systems of the PANDA detector can be found in Ref. [7].

The PANDA collaboration will study a large variety of physics topics [8]. They include precision spectroscopy of charmonium states, the search for new forms of hadronic matter, the study of hypernuclei, medium modifications of hadron properties, and nucleon structure in exclusive electromagnetic or meson final states. A very important goal for PANDA is to study the nature of many exotic states discovered in recent years, answer fundamental questions of hadron physics, and test the predictions of Quantum Chromodynamics (QCD).

QCD is well understood for high energy processes at much shorter distances than the size of a nucleon. In this case a well established calculational technique, called perturbation theory, provides results with high precision and predictive power [9]. However, at distance scales comparable to the nucleon radius (approximately  $10^{-15}$ m), marked with tilted parallel lines in Fig. 2.4, other theoretical methods are required to effectively describe the QCD. At these scales the interaction between quarks and gluons becomes too strong to investigate single quarks. Furthermore, the running coupling of the strong force, originating from the gluon self interaction, makes it impossible to perform calculations based on perturbation theory. The specialty of charmonium is, that the corresponding energy regime is exactly in the transition region between perturbation and strong QCD. Therefore, studies of this system will make it possible to improve the theoretical understanding of hadronic states in general.

Due to the abundant production of particles with gluonic degrees of freedom and particle-

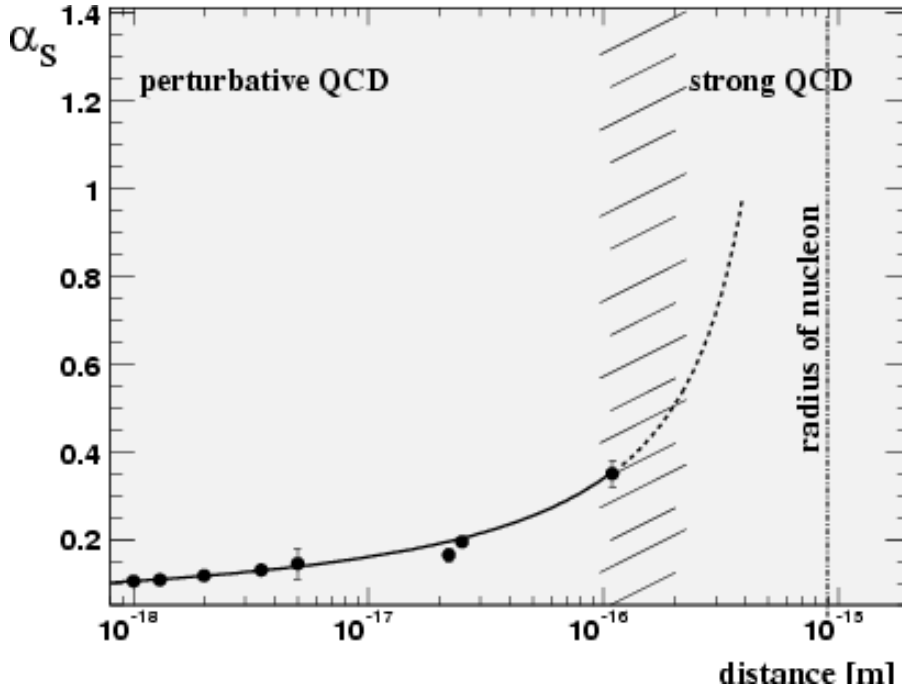


Figure 2.4: Running coupling constant  $\alpha_s$  of the strong interaction as a function of the distance. Figure from Ref. [9].

antiparticle-pairs in proton-antiproton annihilations, spectroscopy using an antiproton beam is an excellent tool to study many of the problems mentioned above. The wide range of measurements in PANDA is aimed at providing as much information as possible [10].

In order to tackle the diverse physics program of PANDA, strong demands are placed on particle reconstruction. In order to show in particular the importance of an excellent particle identification system, which is the focus of this thesis, a key experiment of PANDA will be discussed in detail: The measurement of the width of  $D_{s0}^*(2317)^\pm$ . The description of the full physics program is available for example in Ref. [10]. Prior to 2003 quark potential models provided a remarkably good description of the charmonium spectrum and the properties of any hadronic states that had been discovered in nuclear and high energy physics experiments [12]. In that year the discovery of hadrons with unexpected properties was reported by the *BABAR* collaboration in Ref. [11]. Two new  $D_s$ -like open charm states were reported: The charm-strange mesons  $D_{s0}^*(2317)^\pm$  and  $D_{s1}(2458)^\pm$ , as shown in Fig. 2.5, turned out to have quite different properties from those anticipated by theory for conventional  $c\bar{s}$  states. Their masses are approximately 150 MeV lower than expected and their widths are much narrower. Since there was no obvious interpretation of their nature, they were considered as potential exotic states. This started a run of discoveries in the following years of similarly inexplicable exotic states that continues until today. Various theoretical interpretations of the nature of those states were proposed. Many theoretical models predict different widths for the states [13], thus precise width measurement may be a key to distinguish between these models. The reference value of the  $D_{s0}^*(2317)^\pm$  width currently published by the Particle Data Group (PDG [14]) has an upper limit of  $\Gamma < 3.8$  MeV. The measurement with PANDA is expected to determine the width with a projected precision of the order of 50 keV to distinguish between the different models.

Since the  $D_{s0}$ , being a  $c\bar{s}$  state, cannot be produced directly in a formation reaction  $p\bar{p} \rightarrow X$ , the idea is to produce the  $D_{s0}^*(2317)^\pm$  mesons together with the conventional ground state  $D_s^\pm$  mesons. Therefore, the precise measurement of the production rate (cross section) of this reaction depends on the width of the  $D_s^\pm D_{s0}^*(2317)^\pm$ . The shape of the excitation function,

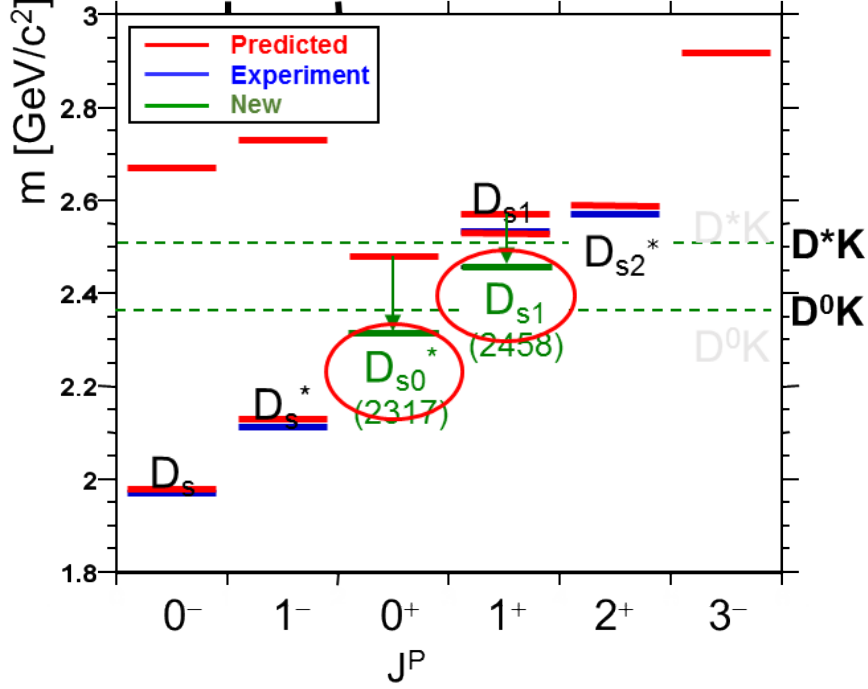


Figure 2.5: The spectrum of states predicted by the potential model (red) and measured in experiment (blue). The green bars represent the new charm-strange mesons that were discovered in 2003, with surprisingly lower energy than predicted. The dashed lines represent the threshold levels for strong decays to  $DK$  and  $D^*K$ , respectively. Figure from Ref. [11].

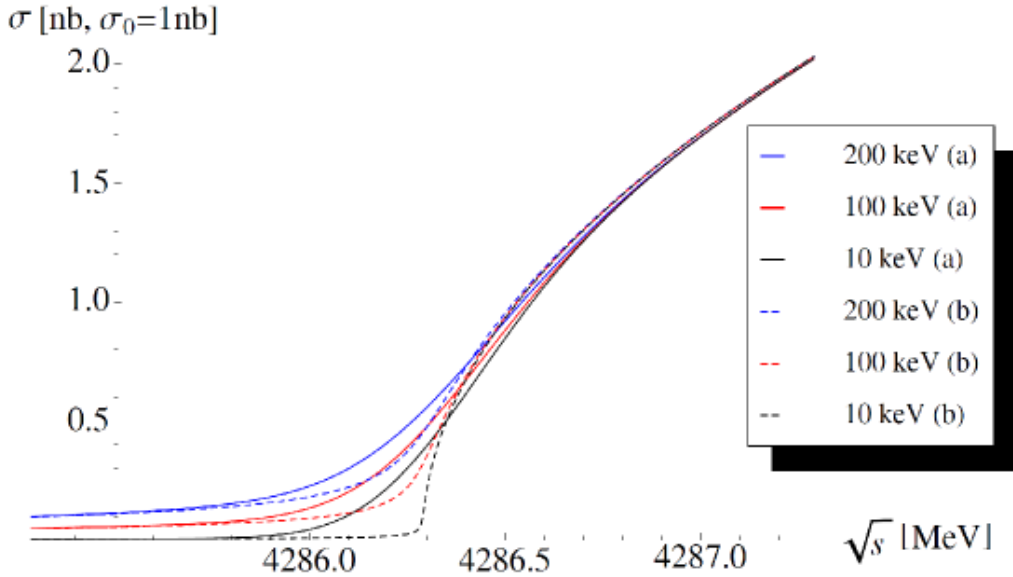


Figure 2.6: The cross section of the production of  $D_{s0}^*(2317)^\pm$  together with a recoiling conventional  $D_s^\mp$ . Different colors reflect different width assumptions and cases (solid lines) and (dashed lines) that refer to different beam momentum resolutions. Figure from Ref. [13].

which is the energy dependent cross section for both particles to appear at the same time, gives a handle to determine the width  $\Gamma$ , which is reflected in the formula for the cross section [13]:

$$f_{exc}(E) = \frac{\sigma_{\Gamma}(\sqrt{s})}{|M|^2} = \frac{\Gamma}{4\pi\sqrt{s}} \int_{-\infty}^{\sqrt{s}-m_{D_s}} \frac{\sqrt{(s - (m + m_{D_s})^2)(s - (m - m_{D_s})^2)}}{((m - m_{D_{s0}^*})^2) + (\frac{\Gamma}{2})^2} dm$$

The parameter giving access to the excitation function is the total center-of-momentum energy  $\sqrt{s}$ . It can be adjusted with very high precision by selecting the corresponding momentum of the anti-proton-beam. Examples of varying shapes of the  $f_{exc}(E)$  are shown in Fig. 2.6. Different colors reflect different width assumptions. Larger width and beam spread, where the production below nominal threshold is possible, corresponds to a smoother curve progression (e.g. blue solid line), whereas a harder kink appears for a narrow width and higher beam resolution (e.g. black dashed line).

The  $D_s^{\pm}D_{s0}(2317)^{\pm*}$  systems will be produced around the threshold of the masses. The measurement is done close to the sum of nominal masses  $\sqrt{s}/c^2 \approx m_0(D_s) + m_0(D_{s0}) = 4.286 \text{ GeV}/c^2$  of the two states involved. In order to enhance the expected number of reconstructible reactions an inclusive reconstruction approach was followed by just detecting the recoil  $D_s$ . Only the decay  $D_s^{\pm} \rightarrow \phi\pi^{\pm}$  with  $\phi \rightarrow K^+K^-$  is considered, due to its clean signature and relative high branching fraction. To identify the full reaction, a missing mass technique will be used (by considering the sum of the missing mass and the invariant mass of the  $D_s$  showing a narrow peak at the phase space limit.). Choosing the inclusive approach has its consequence. In order to reconstruct the  $D_s$  state the kaons have to be distinguished sufficiently well from pions, while the pion production cross-section is several orders of magnitude higher than that for charmed states. This means that the kaons have to be separated from a huge pionic background.

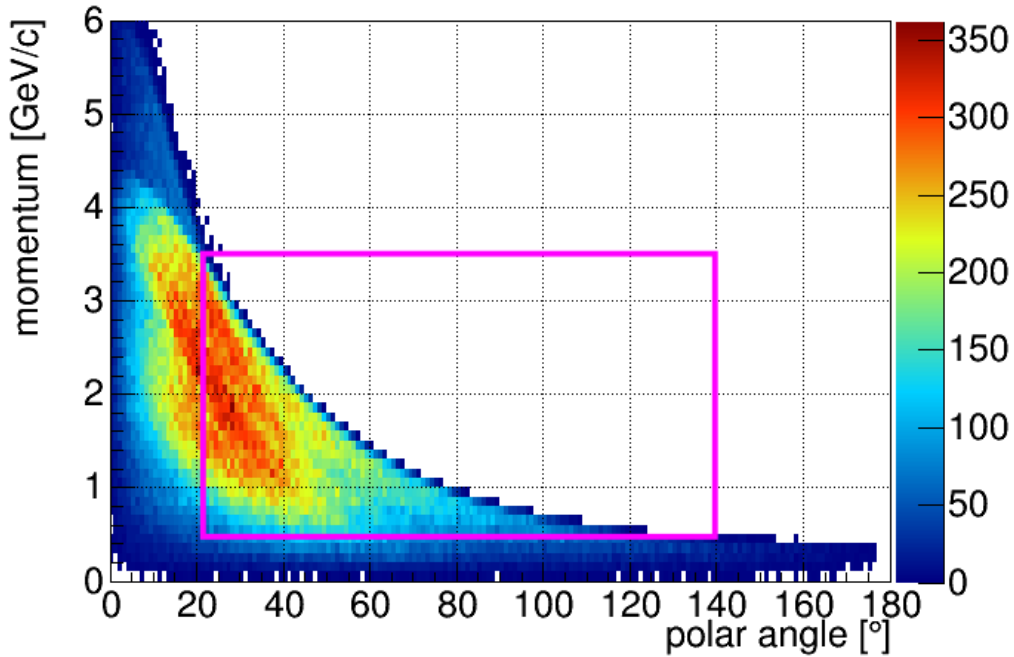


Figure 2.7: Phase space distribution of momentum vs. polar angle for kaons resulting from several PANDA benchmark channels. The box shows the phase space covered by the barrel DIRC. Figure from Ref. [15].

The situation presented in this example is not unique in PANDA since open charm, most of the time, cascades down to strangeness in the form of either  $K$  or  $\phi$  mesons, and a large pionic background has to be suppressed in many other channels. A plot showing the phase space distribution for kaons resulting from the majority of relevant reactions for the PANDA Barrel DIRC is shown in Fig. 2.7.

In the barrel region of the PANDA detector ( $22^\circ$ - $140^\circ$  polar angle) three standard deviations ( $3\sigma$ ) separation of kaons from the large pionic background will be needed for studies in the open charm sector. A dedicated subsystem has to be used to provide PID in the required momentum range of 0.5-3.5 GeV/ $c$ . It has to operate in a 2 T magnetic field of the solenoid, handle extremely high interaction rates of up to 50 MHz, and be compact to keep reasonable the cost and size of the outward following EMC.

In general, a charged particle can be identified by analysis of its interaction and determination of its mass. The mass can not be measured directly but it can be obtained from the momentum  $p$  and the velocity  $\beta = v/c$  measurements. The curvature of the track in the magnetic field is used to determine the momentum. Several different systems are capable of measuring the velocity of the particle. The choice for PANDA was limited by constraints on its construction and the momentum that it has to cover. Commonly used systems that measure the energy loss due to the ionization, for instance a tracking system which can provide PID information from the specific energy loss  $dE/dx$ , do not match the momentum range. Different particles in this kind of system are not separated well enough above 1 GeV/ $c$ . Another possible solution could be the time of flight system. Unfortunately, it would have to be extremely large to provide the sufficient  $\pi/K$  separation in the required momentum range.

The required momentum range in PANDA is a primary area for Cherenkov counters. Ring Imaging Cherenkov detectors (RICH) [16] are used in many experiments to provide charged particle identification. They utilize the dependence of the emission angle of the Cherenkov radiation, and the number of emitted photons, on the velocity of the particle. There are several kinds of Cherenkov detectors but the one that performs best in the PANDA domain is a detector using the DIRC (Detection of Internally Reflected Cherenkov light) principle [17]. Figure 2.8 shows the location of the two DIRC detectors that will be used in PANDA to provide  $\pi/K$  separation: the PANDA Barrel DIRC and the Endcap Disc DIRC. The Barrel DIRC covers polar angles from  $22^\circ$  to  $140^\circ$ , and provides 3 standard deviations of  $\pi/K$  separation up to 3.5 GeV/ $c$ . It will be described in detail in the next chapter.

The first system based on the DIRC principle was successfully used in the *BABAR* experiment and performed PID in a similar momentum range. The achieved performance matches exactly the PANDA requirements. That is why the baseline design of the PANDA Barrel DIRC was inspired by the *BABAR* DIRC. It uses thin bars made of synthetic fused silica as radiators and light guides to transport the emitted Cherenkov photons to the expansion volume where they are registered on the detector plane. The different PANDA detector layout introduces new challenges that require several key changes in the design. It has to be much more compact to simplify integration and to fit in between other systems. A focusing system and fast timing are needed to reach the resolution that will meet the physics requirements. Several design options are still being studied to optimize the performance and lower the cost of the system.

In the next chapter the development of the PANDA Barrel DIRC prototype will be presented. Prior to studies of the full prototype individual components from different manufacturers are tested in separate measurements on test benches, discussed in Sec. 3.5. The optical and mechanical quality of the DIRC radiator bars is crucial for the performance of the DIRC detector. A superior polish, parallelism, and squareness of the radiator bar surfaces are needed to efficiently transport the Cherenkov photons to the ends of the bar and to conserve the mag-

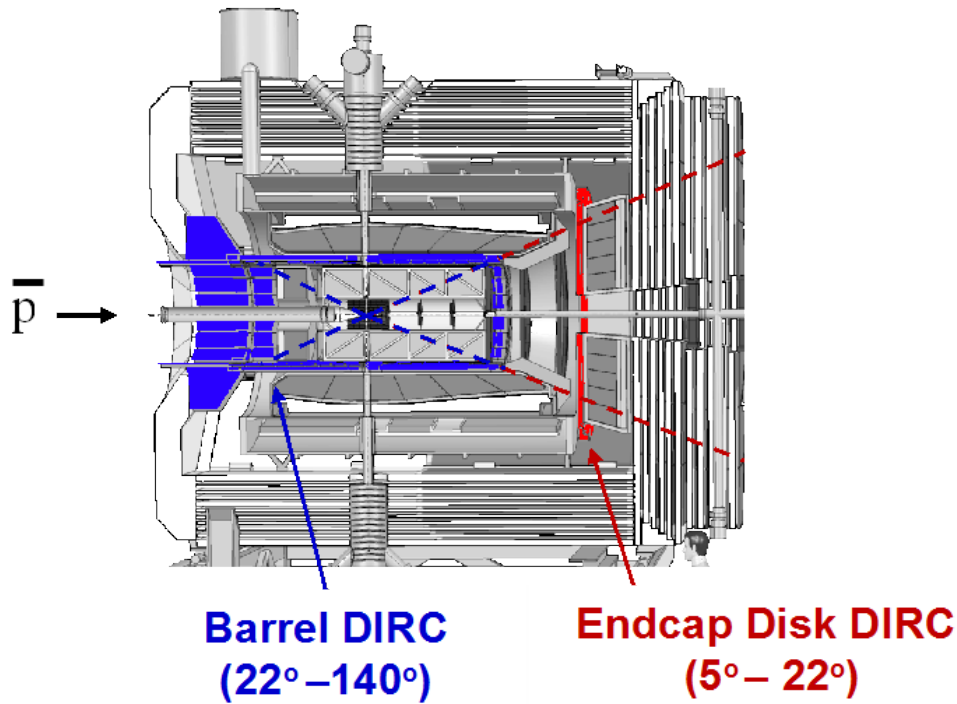


Figure 2.8: Drawing of the PANDA detector with the highlighted Barrel DIRC (blue) and the Endcap Disc DIRC.

nitude of the Cherenkov angle during the internal reflections. This rare combination of tight optical and mechanical specifications, together with relatively large size of the radiators, is a challenge to the optical industry. Seven manufacturers produced over thirty prototype radiators for the PANDA Barrel DIRC using different fabrication techniques. A special setup was built at GSI to qualify these techniques and check the agreement with the angular and surface finish specifications. It measures the photon transport efficiency using several lasers reflected multiple times in the bars. This efficiency is related to surface roughness via the scalar scattering theory [18]. The method is described, along with the production process of the bars, in Sec. 3.5.1. Focusing lenses are another component that required separate studies. The shape of the focal plane was studied to optimize the focusing required later in the prototype. The results of the lens measurement will be presented in Sec. 3.5.2.

Detailed Monte Carlo simulations are used to study potential design options. The final decision about the ultimate PANDA Barrel DIRC design will be made after validating the performance of the prototype with hadronic particle beams. Three generations of PANDA Barrel DIRC prototypes were created and tested in hadronic particle beams at GSI and CERN. The preparation phase, performance, and data analysis of the second and third prototype (tested in 2011 and 2012) are described in the chapter 4.

The PID performance of the DIRC detector is driven by the photon yield and single photon Cherenkov angle resolution. Therefore, these parameters are used to quantify the performance of each design. The approach used to determine both of these parameters is explained in Sec. 3.4. The description of the 2011 prototype is presented in Sec. 4.1. The data were collected during two campaigns in 2011, at GSI and at CERN. The single photon Cherenkov angle resolution and the photon yield of the configuration with a narrow bar, focusing lens, and an oil tank are determined for the first time. Several key design options were implemented in the third prototype and tested in the summer of 2012 at CERN. The major new feature of this

prototype was the first time use of a compact prism as the expansion volume. The description of the setup and results from selected studies can be found in Sec. 4.2. The approach and challenges of adopting the geometrical reconstruction method of the Cherenkov angle to the prism geometry, along with the general performance of the setup and error evaluation are discussed. Several methods are used to extract the single photon Cherenkov angle. Results for different synthetic fused silica bars, as well as one made of an acrylic glass, are presented. In addition to the spherical lenses with air gaps and different anti-reflective coatings a prototype of a high-refractive index compound lens was evaluated. Finally the crosscheck of the PID test was performed using the data collected from the low momentum beam to validate the reconstruction method.





# Chapter 3

## The Development of the PANDA Barrel DIRC Prototype

It was shown in the introduction that PANDA has a rich physics program, which requires for many studies an excellent particle identification. A dedicated PID system is required in the barrel part of the PANDA detector to provide clean and efficient separation between pions and kaons in the momentum range of 0.5-3.5 GeV/ $c$ . The best choice in this momentum region is a special kind of the ring imaging Cherenkov detector (RICH) called DIRC.

This chapter will start with brief explanation of the nature and properties of the Cherenkov effect, as well as a basic idea of the RICH concept. RICH detectors can perform hadronic PID for large range of momenta. The *BABAR* DIRC design aspects were the inspiration and starting point for the PANDA Barrel DIRC design. The design evolution and open questions that are currently under investigation will be discussed. In order to answer those questions the prototype program with particle beams was carried out. The main part of this chapter will deal with the preparation of the prototypes. That includes developing the concept of the full system prototype, the Monte Carlo studies of it, and selecting the components to build it. Before the construction and the studies in the beams, the prototype components are being investigated separately in the lab tests. That includes measurements of the focusing lenses but the main focus is on the radiators, since they are the heart of the DIRC system.

### 3.1 The PANDA Barrel DIRC

#### 3.1.1 The DIRC Concept

The DIRC detector is based on a concept of the Detection of Internally Reflected Cherenkov light (DIRC) produced in a solid radiator bar to identify the charged particle. It is a special type of Cherenkov counter, which uses the unique properties of the Cherenkov radiation.

The speed of light  $c$  was postulated by Einstein in the Theory of Relativity as a absolute limit on the velocity of particles. This is only true in the vacuum, while the speed at which light propagates in a material may be significantly lower than the speed of particle in this medium  $c_p = c/n$ . If a particle transverses a medium with a velocity greater than the speed of light in that medium it emits Cherenkov radiation. Major contribution in understanding and describing this effect comes from Pavel Cherenkov, Igor Tamm and Ilya Frank (Ref. [19, 20]). Already in early studies Cherenkov established several key properties of the new discovered

light. It is emitted only from the charged particles above a certain velocity threshold, with intensity proportional to the electron path length in the liquid. The emission is prompt, the light is polarized, and has a continuous wavelength spectrum. The angular distribution of the radiation, its intensity, wavelength spectrum and its dependence on the refractive index agree with the theory proposed by Frank and Tamm.

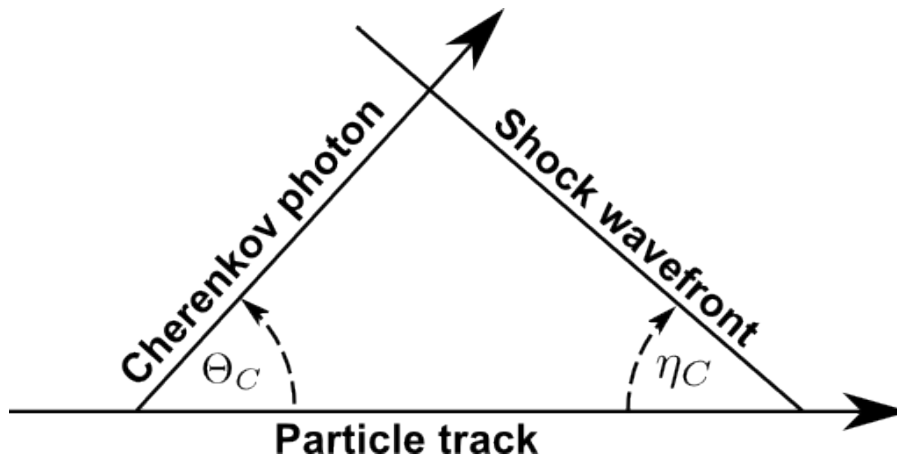


Figure 3.1: Schematic showing the Cherenkov cone. Figure from Ref. [21].

Further studies confirmed that the Cherenkov radiation is emitted uniformly in azimuth ( $\Phi_c$ ) around the particle direction with the polar opening angle  $\Theta_C$  (see Fig. 3.1) defined as:

$$\cos \Theta_c = \frac{1}{n(\lambda)\beta} \quad (3.1)$$

where  $\beta = v_p/c$ ,  $v_p$  is the particle velocity, and  $n(\lambda)$  is the index of refraction of the material, which is a function of the photon wavelength  $\lambda$ . In a dispersive medium the Cherenkov radiation cone is not exactly perpendicular to the Cherenkov propagation angle. The half angle of the cone opening marked as  $\eta_C$  in Fig. 3.1 is defined as:

$$\cot \eta_c = \left[ \frac{d}{d\omega} (\omega \tan \Theta_c) \right]_{\omega_0} = \left[ \tan \Theta_c + \beta^2 \omega n(\omega) \frac{dn}{d\omega} \cot \Theta_c \right]_{\omega_0} \quad (3.2)$$

The  $\omega_0$  is the central value of the considered frequency range. The second term in the equation implies that in the dispersive medium, where  $\frac{dn}{d\omega} \neq 0$ , the  $\eta_C$  angle is not the complement of the  $\Theta_C$  (Motz and Schiff in 1953 [22]). It can have consequence for applications with a large size or a very precise timing.

The spectrum of the photons is continuous and, in contrast to scintillation, it has no decay time. The number of Cherenkov photons  $N_{\text{photons}}$  produced by a particle with charge  $z$  is given by the Frank-Tamm equation [20]

$$N_{\text{photons}} = L \frac{\alpha^2 z^2}{r_e m_e c^2} \int \sin^2 \Theta_c(E) dE, \quad (3.3)$$

where  $L$  is the path length in cm of the particle in the medium and  $E$  is the photon energy in eV. The integral is taken over the region where  $n(E)$  is greater than 1, and  $\alpha^2/(r_e m_e c^2) = 370 \text{ cm}^{-1} \text{eV}^{-1}$ . The velocity of a particle  $\beta_t = 1/n$  is the threshold for the emission of the Cherenkov light. This radiation is rather weak, so the transversing particle loses only small fraction of its energy. That is seen in the formula above for  $\Theta_C \rightarrow 0$ .

In detectors using Cherenkov radiation the position and propagation time of the photon is measured rather than the  $\Phi_c$  and  $\Theta_c$  angles. For a particle producing Cherenkov photons, with the origin  $z_e$ , propagating in the bar with the time  $t_p$ , and detected at the point  $z_d$  (see Fig. 3.2), the equations can be written as:

$$q_x = \cos\Phi_c \sin\Theta_c, \quad (3.4)$$

$$q_y = \sin\Phi_c \sin\Theta_c, \quad (3.5)$$

$$q_z = \cos\Theta_c, \quad (3.6)$$

$$t_p = \frac{L_p}{v_p} = \frac{(z_e - z_d)}{v_p q_z}. \quad (3.7)$$

$q_x$ ,  $q_y$ , and  $q_z$  are direction cosines in the particle (q) frame of the Cherenkov photon emission (shown on the left side in Fig. 3.2), and ( $v_p$ ) is velocity. The experiment measures the position and time of the photons in the laboratory frame, defined in the right figure of Fig. 3.2, and then transformed back to the particle frame q. In order to do that additional tracking and time information is needed in most of the cases .

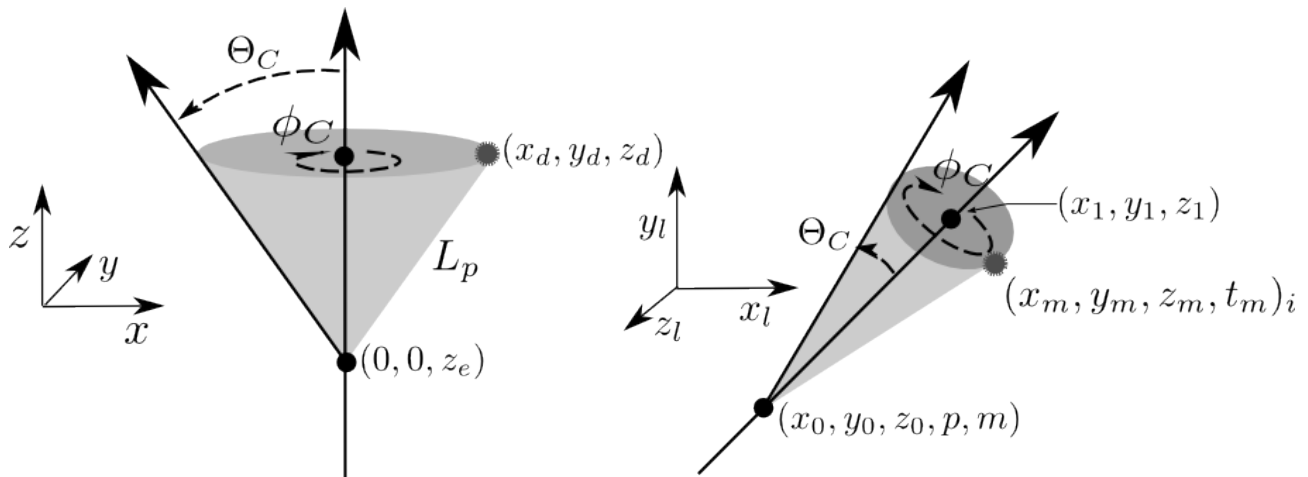


Figure 3.2: Schematic of the Cherenkov cones and reference frames with respect to the particle track (left), and in the lab coordinate system (right). Figure from Ref. [21].

In a dispersive medium, the photon propagates with the group velocity  $v_{\text{group}} = c/n_g$ . One can define the group refractive index ( $n_g$ ) as:

$$n_g(\lambda) = n(\lambda) - \lambda \frac{dn(\lambda)}{d\lambda}. \quad (3.8)$$

For photons in the visible and UV energy range  $n_g(\lambda)$  is larger than  $n(\lambda)$ . Difference between these two refractive indexes in the fused silica is shown in Fig. 3.3.

Cherenkov counters are detectors used to identify charged particles. There are many types available to perform the PID, and they can be grouped by the application of the Cherenkov radiation. The simplest type of Cherenkov counters are threshold detectors. They use the fact that only particles with velocity  $\beta > 1/n$  emit Cherenkov photons. In a basic version they provide Yes/No information on the existence of the particle type. The measured information about particle velocity is combined with the momentum information from the tracking systems

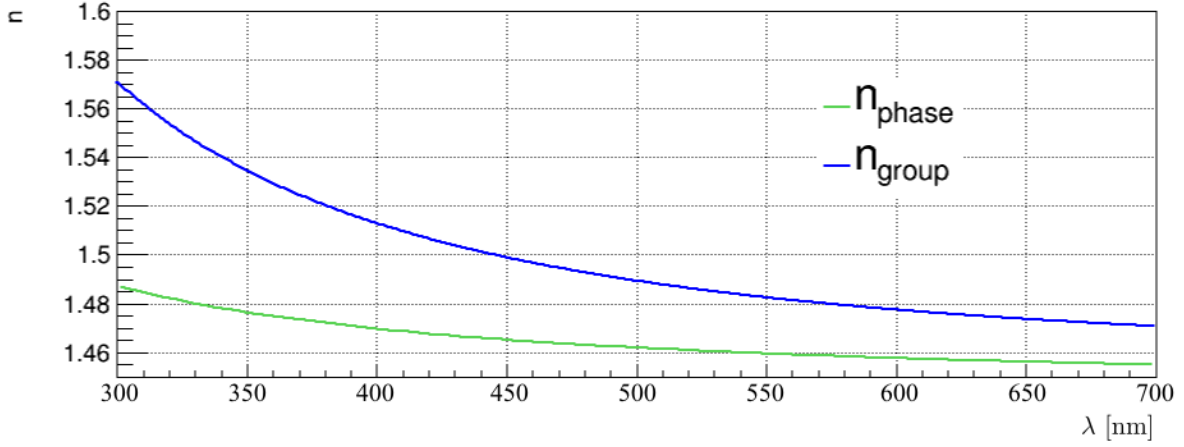


Figure 3.3: Phase (green) and group (blue) refractive indexes as a function of wavelength in the fused silica material. Figure from Ref. [15].

to determine the mass:

$$m = \frac{p}{c} \sqrt{n^2 \cos^2(\Theta_C) - 1} \quad (3.9)$$

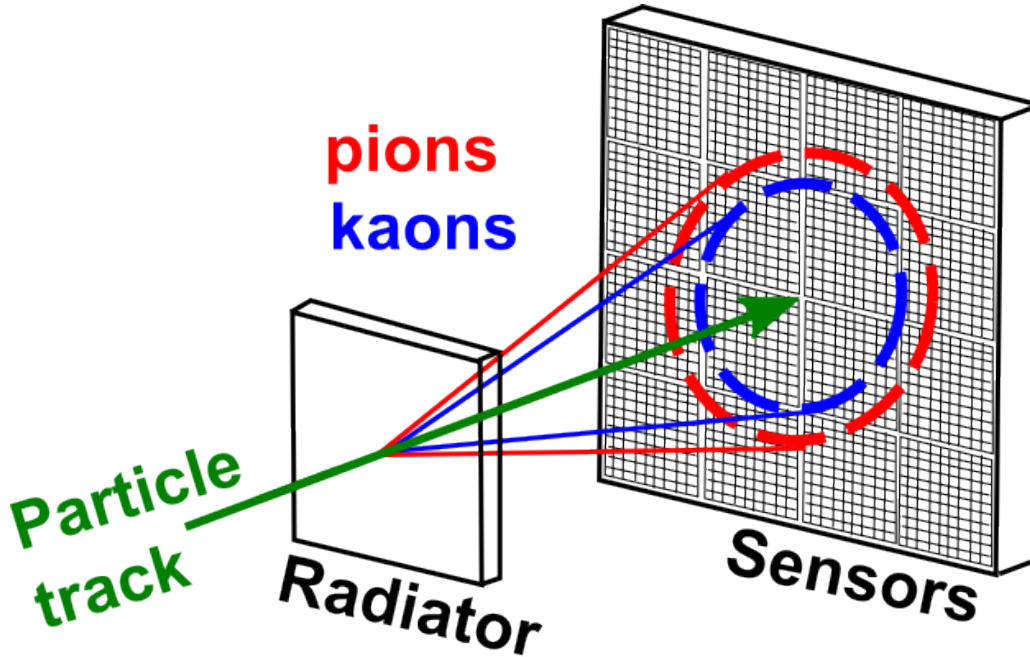


Figure 3.4: Working principle of a RICH detector. The red and blue lines correspond to Cherenkov photons emitted from pions and kaons transverse the radiator, respectively.

Ring Imaging Cherenkov Counters (RICH) [16] are more advanced type of Cherenkov detectors. They can perform hadronic PID for large range of momenta. They derive from the positions of the photons, imaged on the sensors, the emission angle and the number of detected photoelectrons. The ring-shaped image created by photons on the detector plane (See Fig. 3.4) has to be resolved in the reconstruction process. The reconstructed ring is a measure for the Cherenkov emission angle which, in combination with the momentum information, is used to determine the particle species. The relation between particle momentum and  $\Theta_C$  for the different charged particles is shown in Fig. 3.5. RICH detectors are used not only in modern high

energy physics detectors at accelerators but also at very large systems that search for or study very rare processes such as neutron decay or neutrino interactions. In the context of this thesis only the first counters are relevant.

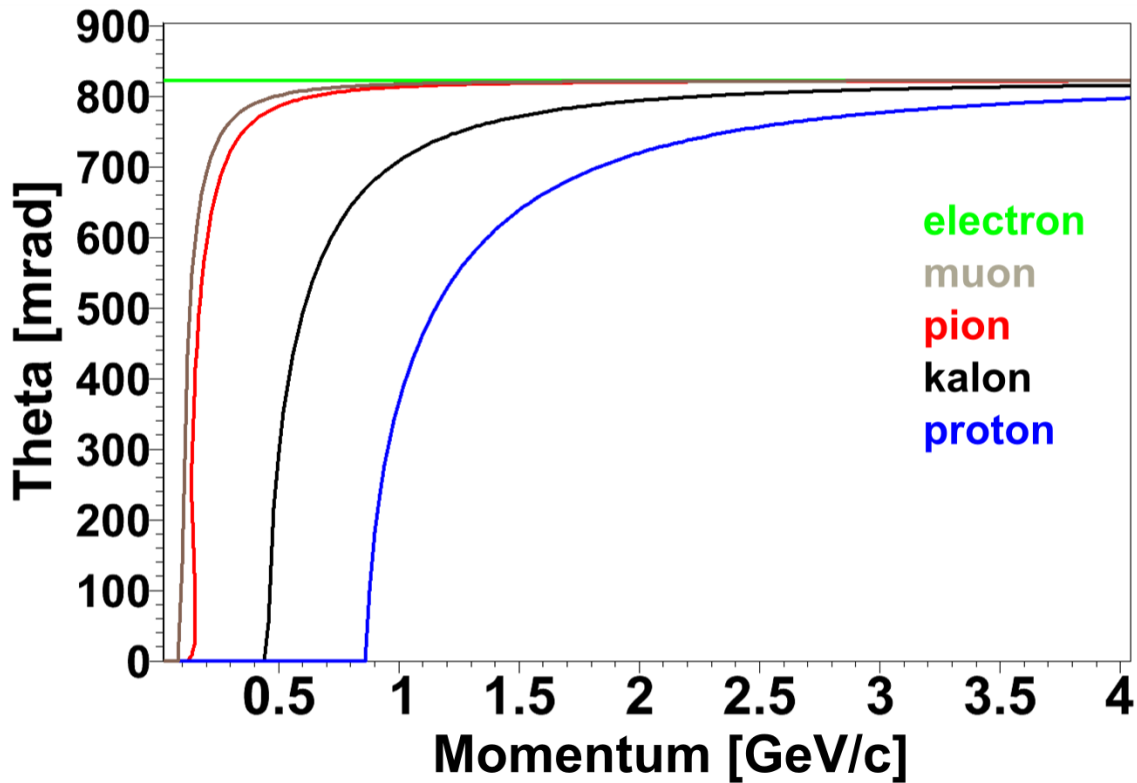


Figure 3.5: Dependence of the Cherenkov angle on the particle momentum for different particles for a fused silica radiator with  $\langle n \rangle = 1.473$ .

The main components of Cherenkov counters are: radiators, which can be in principle any medium with refractive index large enough to produce photons, mirrors/lenses for imaging, and photodetectors. In reality these systems become very complex and use sophisticated combinations of optical elements. The limited number of Cherenkov photons determines very tight constraints on the choice of the material, the size of the radiator, and the kind of photo sensor in order to detect photons as efficiently as possible. The momentum range that the detector has to work in defines the choice of the radiator and therefore the kind of the RICH detector. The particular momentum range that has to be covered in PANDA spectrometer favors the solid state radiator used in detectors based on the DIRC (Detection of Internally Reflected Cherenkov light) principle. Figure 3.6 illustrates that for the momentum range below 4 GeV/c only DIRC type detectors can reach 3 standard deviation separation, provided that the per track Cherenkov resolution is about 2 m rad.

DIRC is a special type of RICH counter, that collects and images totally internally reflected photons and utilizes the optical material of the radiator as a light guide. Photons are transported via internal reflections to a photon detector [24]. A rectangular cross section and parallel, highly polish surfaces conserve the magnitude of the Cherenkov angle during the reflections. The success of the previously build *BABAR* DIRC, in combination with a compact design, are the main reason of choosing this type of Cherenkov counter for the PANDA detector.

Figure 3.7 shows the general concept of the DIRC detectors. A charged particle traversing the radiator with velocity  $\beta$  generates a cone of Cherenkov photons. Some photons are lost but for particles with velocity  $\beta \approx 1$  some fraction always lie within the total internal reflection limit

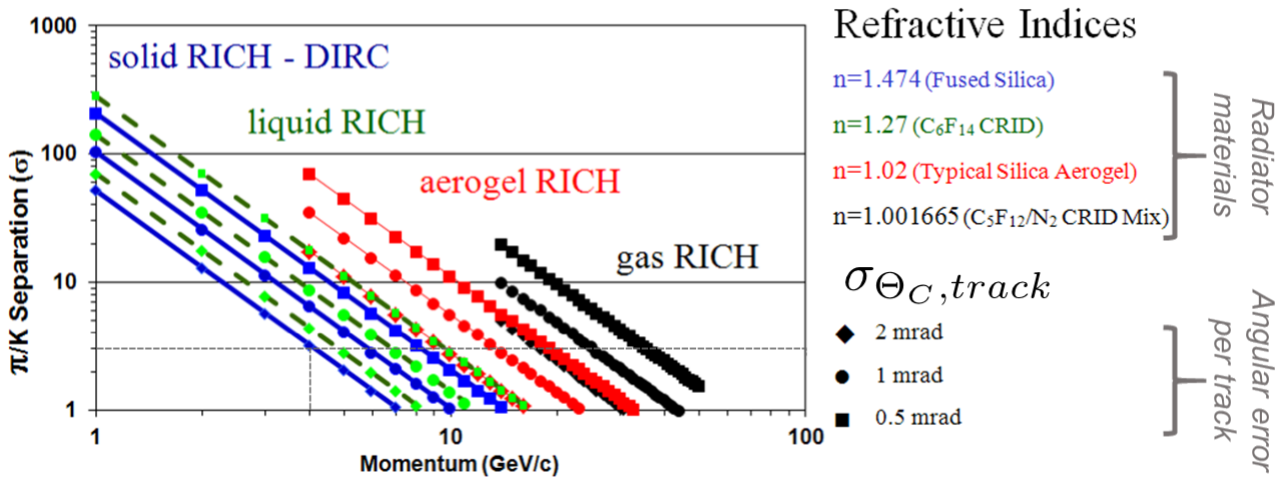


Figure 3.6:  $\pi/K$  separation for different radiator materials as a function of momentum. Colors stand for different materials and symbols indicate different assumptions for the total error of the Cherenkov angle. Figure from Ref. [23].

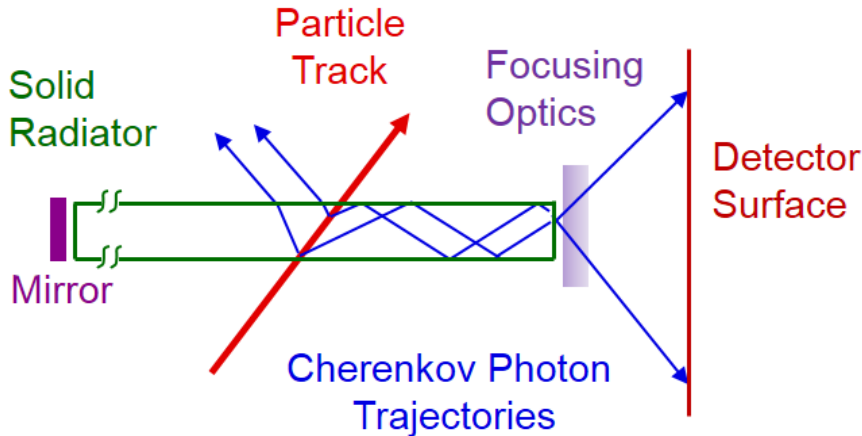


Figure 3.7: Concept of the DIRC detector.

and may be reflected several hundred times before they exit the radiator to be measured [25]. Photons which originally propagate away from the readout volume can be reflected back by a mirror attached to the end of the radiator. The radiator is typically made of fused silica with  $n \approx 1.473$  and can be a narrow bar, a wide plate or a disk. Photons that exit the radiator into the expansion region imaged in three dimensions by the array of sensors. The measured position  $(x,y)$  and time  $(t)$  define the Cherenkov angles  $\Theta_c$  and  $\Phi_c$  and the propagation time  $(t_p)$  of the photon. The observed hit patterns are not rings but rather conic sections that, for some designs, can form quite complicated patterns. In most of the cases likelihood functions are calculated for the observed hit pattern to be produced from  $e, \mu, \pi, K, p$  in the selected space (the detector itself or translated to the Cherenkov space). The DIRC detectors work primarily in the wavelength range from above 300 nm in contrary to gaseous RICH counters measuring photons below 250 nm. That defines the choice of the photon detector. A visible light sensor is required because the optical glue used to connect the optical elements limits the wavelength range to above 300 nm. There is only a limited number of sensors capable of single photon detection in the visible range such as Photomultiplier tubes (PMT), Silicon photomultipliers

(SiPM) and Micro-Channel Plate Photomultipliers (MCP-PMT). A detailed discussion on the DIRC concept can be found in [17].

### 3.1.2 The *BABAR* DIRC Counter

The first DIRC detector was proposed in 1992 for the *BABAR* experiment [17]. It was then build and successfully operated between 1999-2008 at the B Factory (PEP-II) located at the SLAC National Accelerator Laboratory [26]. It used 4.9 m long bars with a rectangular cross section 17.25 mm x 35.0 mm as radiators. Each bar was made up of four 1.225 m long pieces glued together end-to-end. These long bars were distributed over 12 hermetically sealed containers, called bar boxes, and arranged in a barrel shape, with a radius of 85 cm, around the interaction point. The photons were imaged via pin-hole focusing onto an array of 10752 densely packed PMTs. Sensors are placed at a distance of about 1.2 m from the bar end. Figure 3.8 shows a schematic of the concept used in the *BABAR* DIRC.

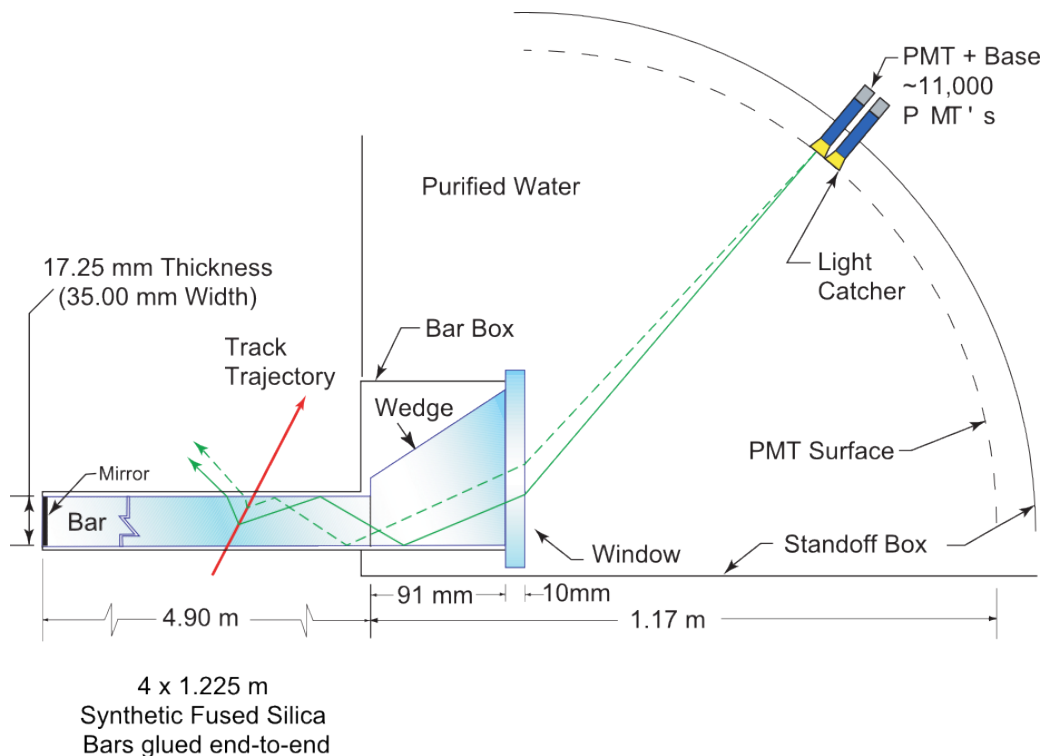


Figure 3.8: Schematic showing the concept of imaging Cherenkov photons in *BABAR* DIRC. Figure from Ref. [17].

The DIRC detector played a significant role in almost all *BABAR* physics analyses published to date. During more than 8 years of operation this robust, stable, and easy to operate system provided excellent  $\pi/K$  separation from the pion Cherenkov threshold up to 4.2 GeV/c. The observed track Cherenkov angle resolution was within 10% of the design. A lead shielding installed in 2002 and new readout electronics kept the DIRC working even at four times the design luminosity. A good timing resolution of 1 ns provided a powerful tool to reject the accelerator and event related background, a potential problem in the reconstruction. The 98% of the channels stayed fully functional until the end and there was no evidence of bar surface quality deterioration [27]. These facts made this novel concept a reference for the design of other detectors including the PANDA Barrel DIRC. In the process of optimizing the PANDA Barrel DIRC design the *BABAR* DIRC was used as the reference, so it is good to discuss what

limited its performance.

For the particle with  $\beta \approx 1$  momentum above threshold that goes through the radiator with refraction index  $n$  the number of  $\sigma$  separation  $N_\sigma$  between particles of mass  $m_1$  and  $m_2$  can be calculated as ([19]):

$$N_\sigma \approx \frac{|m_1^2 - m_2^2|}{2p^2 \sigma_{\Theta_C, track} \sqrt{n^2 - 1}} \quad (3.10)$$

$\sigma_{\Theta_C, track}^2$  is the resolution in the Cherenkov polar opening angle (3.1) of the particle track, and can be written as:

$$\sigma_{\Theta_C, track}^2 = \sigma_{\Theta_C}^2 / N_{pe} + \sigma_{\text{correlated}}^2 \quad (3.11)$$

$N_{pe}$  is the number of measured photons per track, and  $\sigma_{\Theta_C}$  is the average single photon Cherenkov angle resolution.  $\sigma_{\text{correlated}}$  consist of several correlated terms that contribute to the resolution, in particular connected to the uncertainty of the track direction. It is a sum of terms corresponding to the misalignment of the system, multiple scattering, and the resolution of the tracking system. The DIRC detector needs the track direction to perform the reconstruction, and the associated correlated error in *BABAR* was at the level of 1.5–2 mrad for high momentum particles.

$\sigma_{\Theta_C, track}$  determines the DIRC PID performance and provides information about the required single photon resolution and photon yield. The uncertainty of the single photon Cherenkov angle ( $\sigma_{\Theta_C}$ ), consist of the contribution from the sensor pixel size ( $\sigma_{\Theta_C, det}$ ), the imaging errors ( $\sigma_{\Theta_C, bar}$ ), the error due to bar imperfections ( $\sigma_{\Theta_C, transport}$ ), such as non-squareness, and the chromatic term ( $\sigma_{\Theta_C, chrom}$ ). It can be calculated as:

$$\sigma_{\Theta_C}^2 = \sigma_{\Theta_C, det}^2 + \sigma_{\Theta_C, bar}^2 + \sigma_{\Theta_C, transport}^2 + \sigma_{\Theta_C, chrom}^2 \quad (3.12)$$

The performance of the *BABAR* DIRC is summarized in Fig. 3.9, where the single photon Cherenkov angle resolution is shown in (a) as the difference between measured Cherenkov angle per photon and expected Cherenkov angle per particle ( $\Delta\Theta_{C, \gamma}$ ). It was measured to be 9.6 mrad. It includes 7 mrad contribution from PMT and bar size, 5.4 mrad from the chromatic term and, 2-3 mrad from the bar imperfections. The origin of the chromatic term ( $\sigma_{\Theta_C, chrom}$ ) is due to the wavelength of the photon and the dispersion  $n(\lambda)$  of the fused silica. The Cherenkov angle of the red photons is lower than the  $\Theta_C$  of blue photons. The 10% background under the  $\Delta\Theta_{C, \gamma}$  peak, in Fig. 3.9a, comes from combinatoric background, track overlap, accelerator background,  $\delta$  electrons in radiator bar, and reflections at fused silica/glue interface. Figure 3.9b shows that 20-60 photons were recorded per track, depending on the polar angle of the particle. A very useful feature in the *BABAR* environment were that the higher momentum was correlated with larger polar angle values, at which there was more signal photons, increasing the resolution. Finally, the track Cherenkov angle resolution is shown in Fig. 3.9. The width of the fit is 2.4 mrad, which is within 10% of the design.



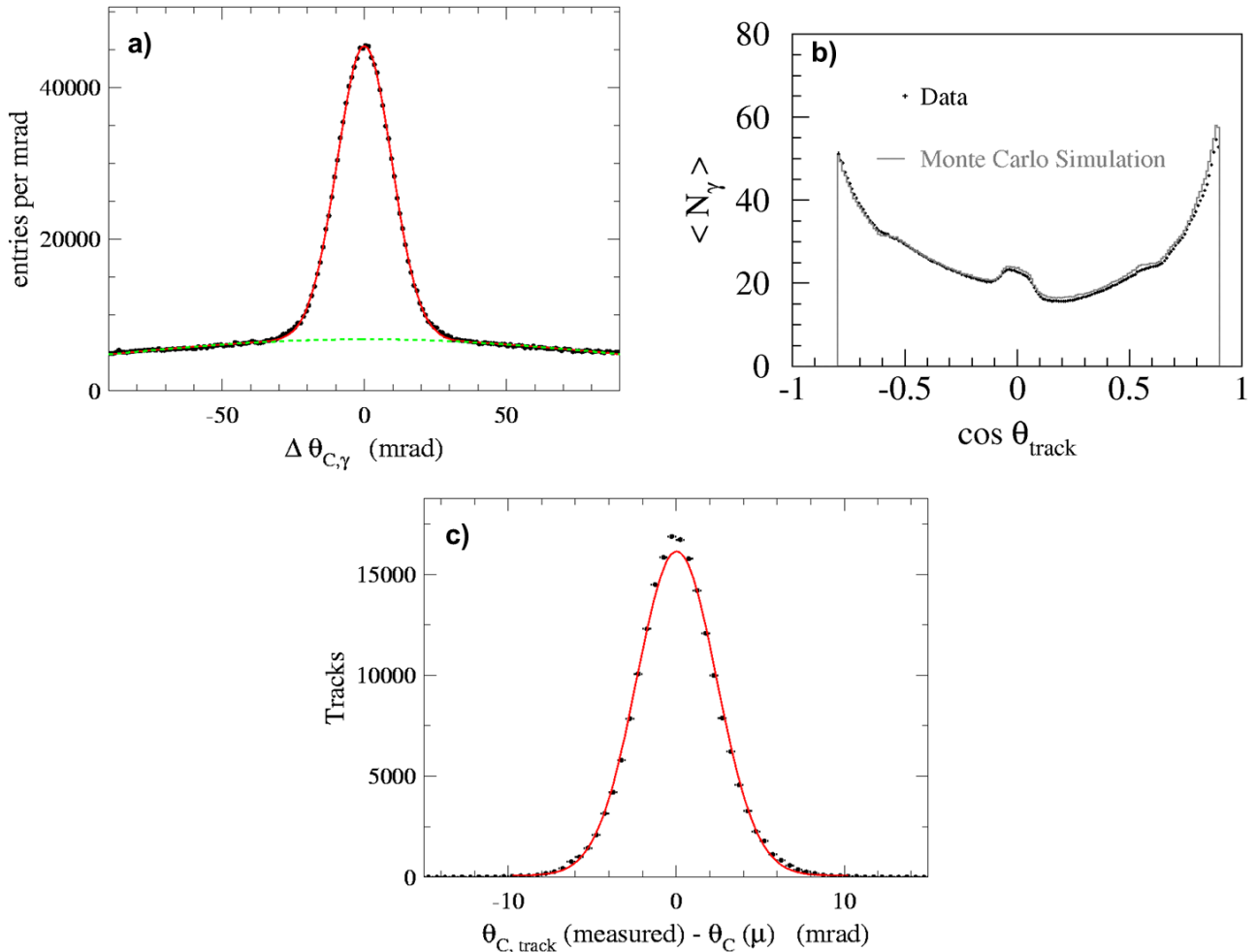


Figure 3.9: *BABAR* DIRC performance showing a) The difference between measured single photon Cherenkov angle per photon and expected Cherenkov angle per particle, b) the number of Cherenkov photons per track as a function of the polar angle, and c) the distribution of the Cherenkov angle per track.

### 3.1.3 The PANDA Barrel DIRC Design

#### The Evolution of the Design

The goal for the PANDA Barrel DIRC is to provide the separation of pions and kaons with more than 3 standard deviations ( $\sigma$ ) separation power for the particle momentum range up to  $p = 3.5 \text{ GeV}/c$ . At that momentum the Cherenkov angle separation between pions and kaons is 8.5 mrad (see Fig. 3.5). Therefore, PANDA Barrel DIRC has to achieve a track Cherenkov angle resolution of 2.8 mrad. The performance that the *BABAR* DIRC reached would meet the PANDA requirements. Because of different constraints on the construction in PANDA, the design of the DIRC detector requires important modifications to work in a new environment.

The initial design of the PANDA Barrel DIRC looked like a scaled down version of *BABAR* DIRC (Fig. 3.10a). It consisted of ninety six 2.5 m long bars, and a big single tank as an expansion volume placed outside of the magnetic yoke. Approximately 7000 Photomultiplier Tubes (PMTs) arranged on a toroidal surface measure the photon positions and time. Results from the R&D for the SuperB fDIRC [28] suggested that a more compact expansion volume, combined with focusing and smaller pixels is an attractive solution. This idea influenced the next design,

shown in Fig. 3.10b, with the “camera” expansion volume. Here, the big tank is divided into sixteen segments, each equipped with a focusing mirror. According to simulation this design would deliver around 98% Kaon identification efficiency with a pion mis-identification rate of less than 20% and, therefore, meet the PANDA PID requirements. [29].

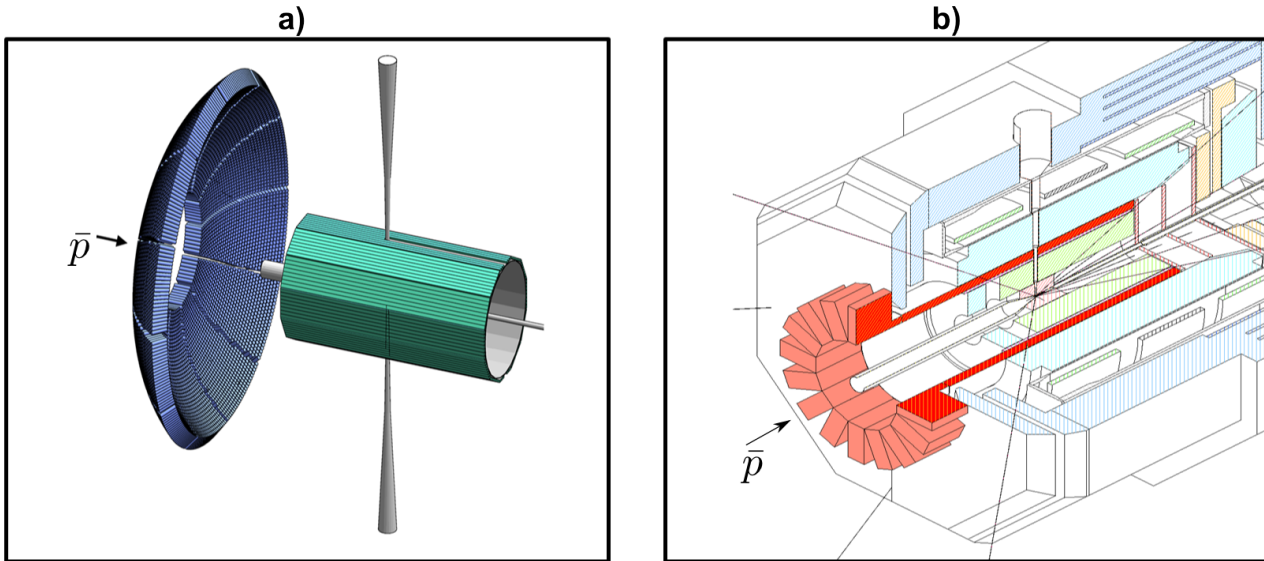


Figure 3.10: Early designs of the PANDA Barrel DIRC with the expansion volume placed outside the solenoid yoke, with a) single oil/water tank and b) segmented tank (the camera solution).

The increasingly complex design of the inner detectors and the backward endcap forced the decision to move the expansion volume inside the magnetic yoke. The advantage of moving the expansion volume inside the yoke made it possible to use shorter bars, which are biggest cost factor. Most likely it will be possible to make each long bar from two instead of three glued bars. However, the new location, within the magnetic field, eliminated PMTs as the potential sensor candidates. Study of the individual contributions to the resolution showed that the new smaller design can not perform the PID required for PANDA without focusing. In a compact design the imaging part, bar and pixel size contributions become dominant errors. In the new location there is very limited space for expansion volume and it is impossible to use focusing mirror like in fDIRC. Current studies focuses on a search of different lenses, to reduce the size of the bar image, and a type of multi-anode sensor with a smaller pixel, that can work in magnetic field.

In the PANDA Barrel DIRC, the single photon has to be detected in the magnetic field with around 5 mm spacial resolution and 100 ps timing. However, the most critical performance parameter is the rate capability. For the interaction rates observed in PANDA the resulting rates of Cherenkov photons are up to  $200 \text{ kHz/cm}^2$ . This also leads to strict requirements on the lifetime of the tubes, that have to sustain an integrated anode charge on the level of 0.5 to 5  $\text{C/cm}^2$ . In table 3.1 all the requirements are listed with the ability of fulfilling them by different types of tubes. It clearly shows that at the moment there is no alternative to MCP-PMTs for the PANDA Barrel DIRC, because PMTs do not work in magnetic field and SiPMs are not good due to the noise and dark count level.

Planacon MCP-PMTs made by PHOTONIS [30] are a candidate for the PANDA Barrel DIRC. In Fig. 3.11 the working principle of MCP-PMTs is shown, and a photo of the PHOTONIS tube. The tube has a square  $59 \times 59 \text{ mm}^2$  housing,  $53 \times 53 \text{ mm}^2$  active area, and  $8 \times 8$

Requirement	MCP-PMT	MAPMT	SiPM
Single photon sensitivity	yes	yes	yes
Low dark count rate	yes	yes	<b>no</b>
Fast timing ( $< 200$ ps)	yes	yes	yes
Good position resolution ( $< 2$ mm)	yes	yes	yes
Operation in 1 T magnetic field	yes	<b>no</b>	yes
High rate tolerance ( $> 200$ kHz/cm <sup>2</sup> )	yes	yes	yes
Long life time ( $> 1$ C/cm <sup>2</sup> /year, 10 <sup>6</sup> gain)	yes	yes	yes
Large active area ratio	yes	yes	yes
Resistant to neutron radiation	yes	yes	<b>no</b>
Availability and cost	yes	yes	yes

Table 3.1: Requirements for the Barrel DIRC sensors and the ability of fulfilling them by different types of tubes: Micro Channel Plate PhotoMultiplier Tube (MCP-PMT), Multi Anode PhotoMultiplier Tube (MAPMT), Silicon PhotoMultiplier (SiPM).

pixels. It uses a Bialkali photocathode, has single photon sensitivity, and a low dark noise of  $1$  kHz/cm<sup>2</sup>. The transit time spread is on the order of 30 ps ([31, 32]) and a spacial resolution, as defined by the pixel size of 6.5 mm, is  $\sigma = 1.9$  mm. For many years, however, MCP-PMTs suffered from a very serious lifetime limitation. Until 2011 these tubes were capable of surviving only 1 month of nominal PANDA operation at full luminosity after which the quantum efficiency dropped dramatically. The reason was photocathode aging, which is described in detail in [33]. Briefly, chemical reactions and crystal structure damages on the photocathode are caused by the ion backflow from the rest gas within the MCP-PMT. Recent improvements, including a protective layer applied between cathode and MCPs, and atomic layer deposition, improved the vacuum and significantly increase MCP-PMT lifetime. One prototype tube already reached in tests the deposited charge corresponding to 12 years of PANDA operation. These tests of MCP-PMTs from PHOTONIS and other vendors are described in [33, 34].

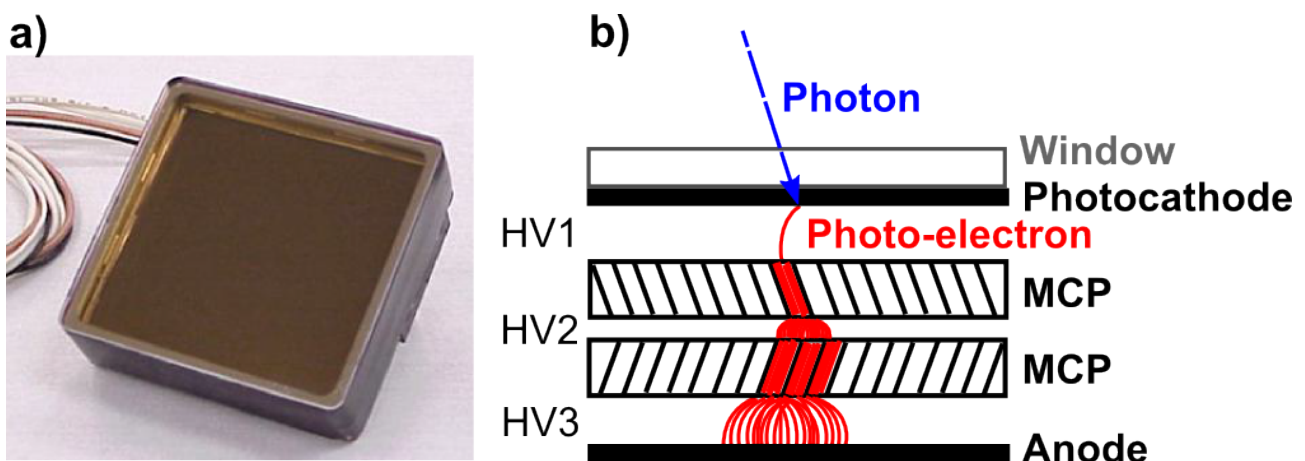


Figure 3.11: a) Photo of the PHOTONIS XP85012 Planacon MCP-PMT [30]. b) Concept of the MCP-PMT tube working principle.

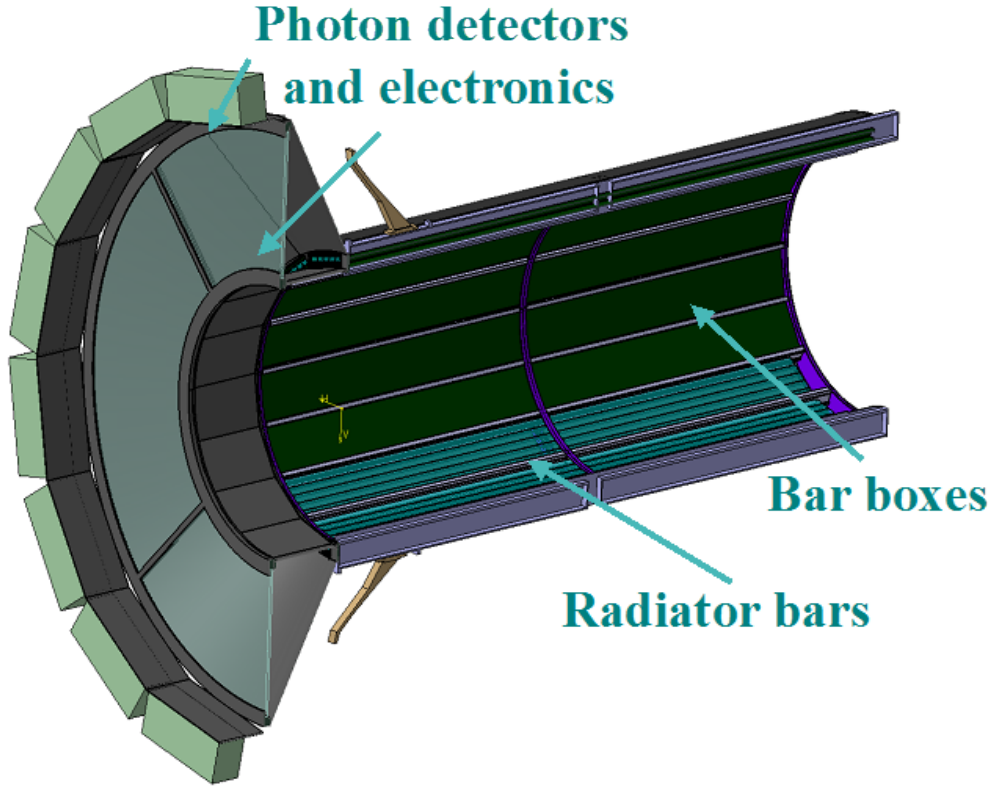


Figure 3.12: A CATIA drawing of the PANDA Barrel DIRC baseline design showing all components of the system.

### The Baseline Design

The baseline design of the PANDA Barrel DIRC is shown in Fig. 3.12. The barrel is about one meter in diameter with 80 narrow, 2.4 m long radiator bars with a cross-section of 17 mm x 32 mm each. They are distributed over 16 sections called bar boxes with 5 bars in each. A mirror attached to one side of the bar is used to reflect photons towards the readout end where they exit the bar through an attached lens. A 30 cm-deep monolithic tank filled with mineral oil is used as an expansion volume. The photon positions are recorded by an array of Planacon MCP-PMTs with 15-20k channels in total.

The mechanical design follows the general idea from the *BABAR* DIRC as well. The expansion volume can be detached for the access to the inner detectors. Bar boxes slide on wheels into slots, as shown in Fig. 3.13, what gives an access in case of a need for a maintenance and a possible staged installation. The two ring-structure, made of CFRP (Carbon-fiber-reinforced polymer), support the rails on which the bar boxes slide into the barrel. A sheet of carbon fiber outside of the ribs adds the additional stability.

The estimated single photon Cherenkov resolution for the baseline design of the PANDA Barrel DIRC is at the level of  $\sigma_{\Theta_C, \gamma} \approx 8 - 9$  mrad. It is dominated by  $\sigma_{\Theta_C, det} = 6.3$  mrad and  $\sigma_{\Theta_C, chrom} = 5.4$  mrad.

The variation of the pixel size contribution is explained in Fig. 3.14. Under an angle  $X$  the projective pixel size is smaller and should be then calculated from  $Pixel_{size} \times \cos X$ . On the other hand the imaging error becomes larger, since the pixel is out of focus and therefore the total resolution becomes worse.

The chromatic smearing is shown in Fig. 3.15. The propagation of the photons is a function

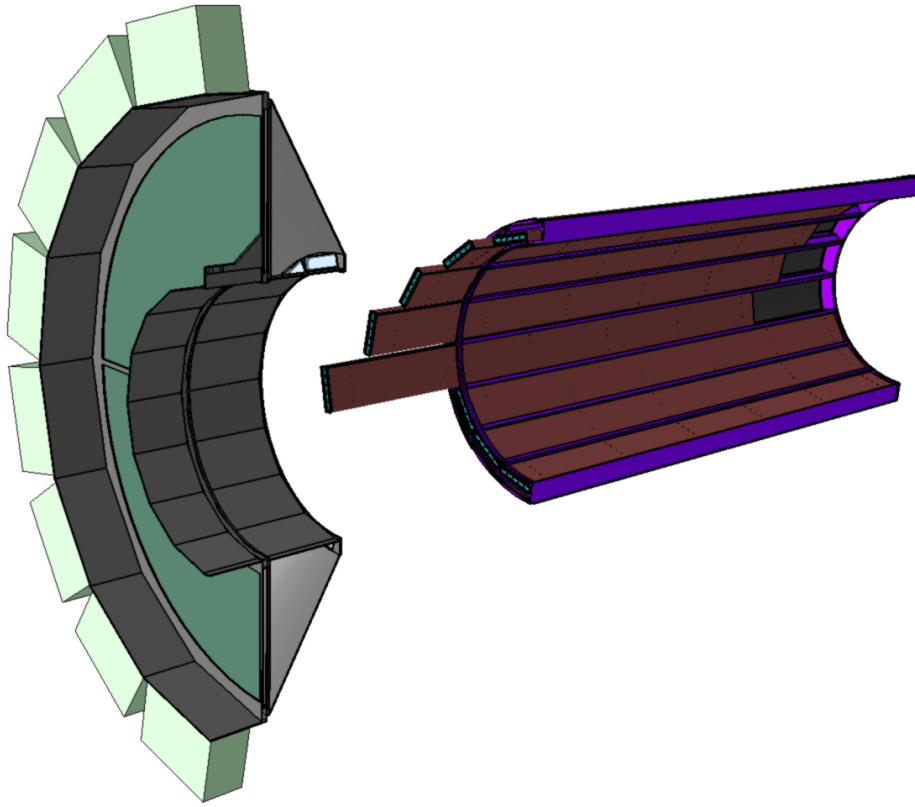


Figure 3.13: A CATIA drawing of the PANDA Barrel DIRC showing the mechanical design.

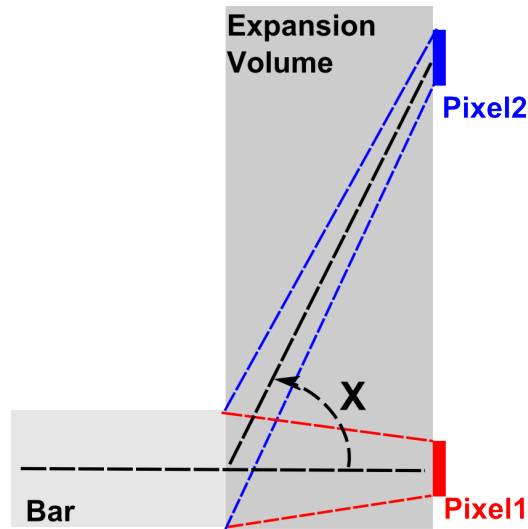


Figure 3.14: Conceptual drawing showing different pixel size seen from bar depending on its position. If the pixel size is  $pixel_{size}$  Pixel1 surface is seen directly from the bar and its size is  $pixel_{size}$  then in case of the Pixel2 it changes to  $pixel_{size} \times \cos X$ .

of the group refractive index:

$$V_{group} = \frac{c_0}{n_{group}} = \frac{c_0}{\left[ n_{phase} - \lambda \frac{dn_{phase}}{d\lambda} \right]} \quad (3.13)$$

And the red photons are faster than the blue photons causing the dispersion in time. Studies of the Focusing DIRC prototype (fDIRC [27]) shown that it is possible to correct the chromatic

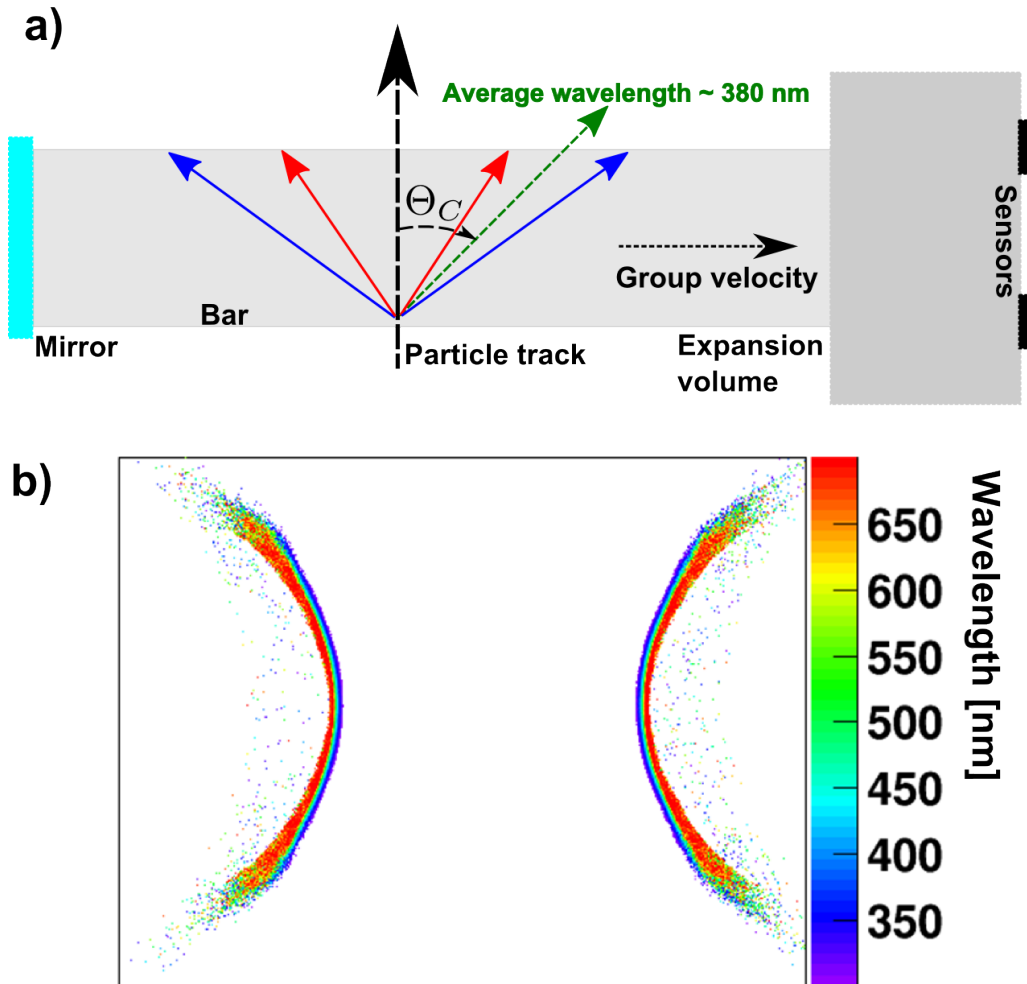


Figure 3.15: The uncertainty in the photon production angle due to the dispersion  $n(\lambda)$  of the fused silica. a) Conception of the chromatic effect shown in the drawing of the setup. b) Hit pattern from simulated data with wavelength as the color scale.

broadening with good enough time information, since the Cherenkov angle correlates with time of propagation. A resolution of the single photon arrival time on the level of 200 ps is needed [23].

$N_{pe}$  on the level of 15-50 photons is expected in the system similar to *BABAR* DIRC made of standard materials and using MCP-PMTs with baicalin photocathode. The specifications for the bar qualities, including the surface polish quality and the squareness of the sides, are defined in a way that the bar imperfections do not become a significant contribution to total resolution.

The uncertainty of the track direction is a sum of terms corresponding to the misalignment of the system, multiple scattering, and the resolution of the PANDA tracking system. The Barrel DIRC detector needs the track direction from the tracking system to perform the reconstruction, and the associated uncertainty is expected to be at the level of 1.5-2 mrad [35].

The single photon resolution and the expected number of measured photons per track result in a total resolution on the track Cherenkov angle of  $\sigma_{\Theta_C, track} \approx 2 - 2.5$  mrad [15]. The baseline design matches the PANDA PID requirements. The performance can be further improved with the ongoing studies described in the next section.

### 3.1.4 Considered Options

Although the baseline design meets the PANDA resolution requirement, but there are still additional improvements that one can consider to optimize the cost and improve the performance.

#### Expansion Volume

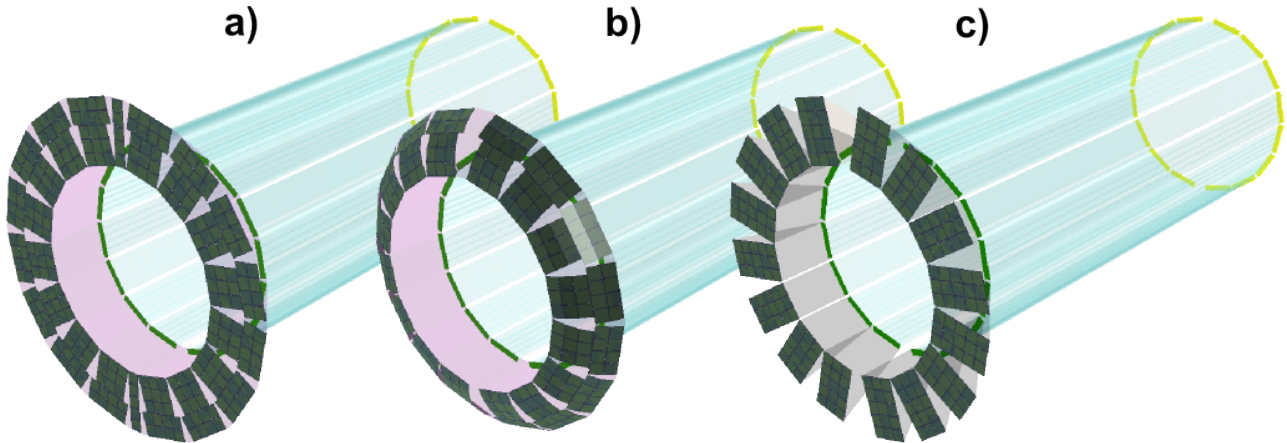


Figure 3.16: Simulated PANDA Barrel DIRC designs with different expansion volume options: a) single oil tank, b) oil tank with parabolic shaped detector surface, and c) compact fused silica prisms. Figure from Ref. [36].

One of the design elements that influences the operation and performance of the detector is the material and shape of the expansion volume. Three options which are currently under consideration are shown in Fig. 3.16. The baseline design with the large single oil tank is shown as a), the modification of that design with a curved detector plane is presented in b). The curvature is set to more closely follow the focal plane of the lens. A compact fused silica prism can be used in front of each bar box instead of the single volume filled with mineral oil. This option reduces the number of required pixels. Moreover, the prism has much better optical properties, which improves the photon yield by as much as 40%. Figure 3.16c shows the design of this solution with sixteen individual expansion prisms, each about 30 cm deep and about 30 cm high. In addition to superior optical aberration properties the fused silica expansion volume would be easier to maintain than the oil tank.

#### Radiator size

The thickness of the bars defines the number of Cherenkov photons produced per track and the amount of the material in front of the calorimeter. The width is related to the number of required bars and influences the Cherenkov angle resolution. That influences the detector cost, since its mostly driven by number of optical surfaces to polish. Studies have shown that more than 5 bars per bar box do not improve the resolution. However, three or four bars are an option, provided that spherical focusing is used to reduce the  $\sigma_{bar}$  contribution. A wide radiator plate is also under consideration, which would make it possible to use only 16 radiators. In this option a time-based reconstruction approach is used, which allows less stringent specs on the squareness and edge quality, further reducing cost. Two prototype plates were purchased, and tested in the particle beam in 2012. The detailed study of this option, addressing the issue of needed different reconstruction approach, can be found in [37].

### Focusing System

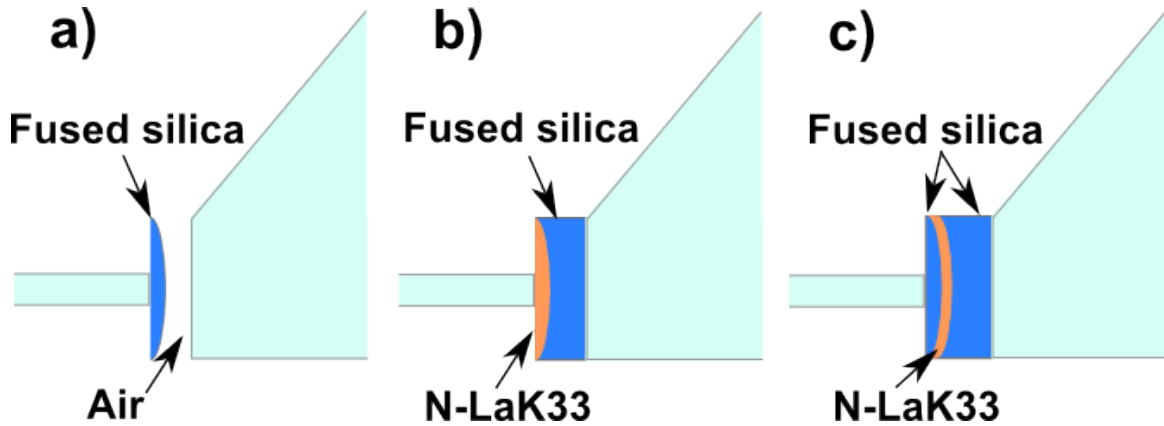


Figure 3.17: Three options for the focusing lenses: a) a standard  $SiO_2$  lens, b) two component lens with high refractive index N-LaK33 and fused silica, and c) a three component lens with combination of focusing and defocussing components.

The focusing system can be a lens attached to the read out end or a focusing mirror on the forward end of the bar. The simplest approach is a standard cylindrical or spherical lens attached to the end of the bar. The simulation done with ZEMAX [38], ray tracing, and Geant software, showed that an air gap between the lens and the expansion volume causes massive photon loss, even if anti reflective coating (AR) is used. The loss becomes most severe for particle tracks perpendicular to the bar. At that angle many photons are totally internally reflected at the curved surface of the lens. In addition a standard single lens can not match a planar detector surface. By selecting the doublet, compound lens from a material with a high refractive index, like N-LaK33, a lens system can be designed that works without any air gaps between the bar and the expansion volume. It minimize the photon loss at the transition from the lens to the EV. A combination of focusing and defocussing elements in a triplet lens can be used to achieve a flatter image as well as a higher photon yield. Schematic drawings of a standard lens, and two compound lenses without air gap are shown in Fig. 3.17.

## 3.2 Concept and Evolution of the PANDA Barrel DIRC Prototype

The main purpose of the prototype program is to validate designs and to provide the basis for the ultimate design decisions for the PANDA Barrel DIRC. The ideas and options presented in the previous section need to be validated in prototypes using the particle beams. Prototypes are built with exchangeable and modifiable components to implement and directly compare several different design aspects in one prototype. Ideally, the prototype is one slice of the full detector that can be used to evaluate the performance of the different design options. The basic components of all the PANDA DIRC prototypes are: radiator, focusing system, expansion volume, sensors, and readout electronics. The general structure of the DIRC prototype is shown in Fig. 3.18. So far, three generations of prototypes have been build and tested. In each of the them different aspects of the design were tested.

The very first prototype in 2008/2009 was built as proof-of-principle for a compact focusing DIRC. The schematic of the setup is shown in Fig. 3.19. The prototype used 800 mm-long synthetic fused silica bar with a plano-convex spherical lens coupled to the readout end. A



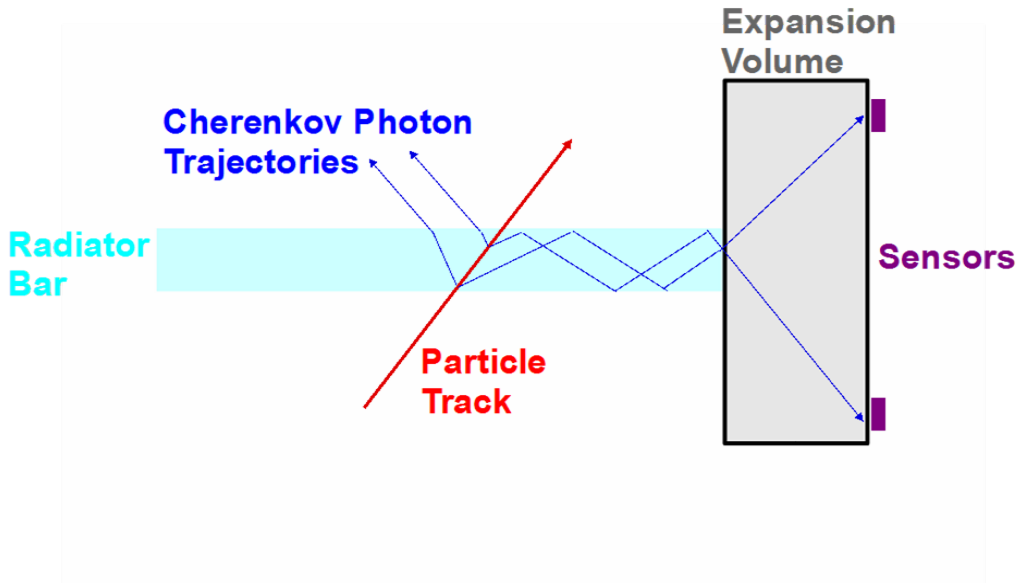


Figure 3.18: Schematic of the basic components of the DIRC prototypes.

small expansion volume with a depth of 20 cm was placed in front of the lens with 1 cm air gap. The expansion volume was filled with Marcol 82 mineral oil [39]. Four MCP-PMTs (two XP85013/A1 and two 85011 [30]) were placed at the back wall to record the photons. The setup was placed in to the beam line of a 2 GeV proton beam at GSI. Clear Cherenkov rings were observed and first tests of focusing were performed [40].

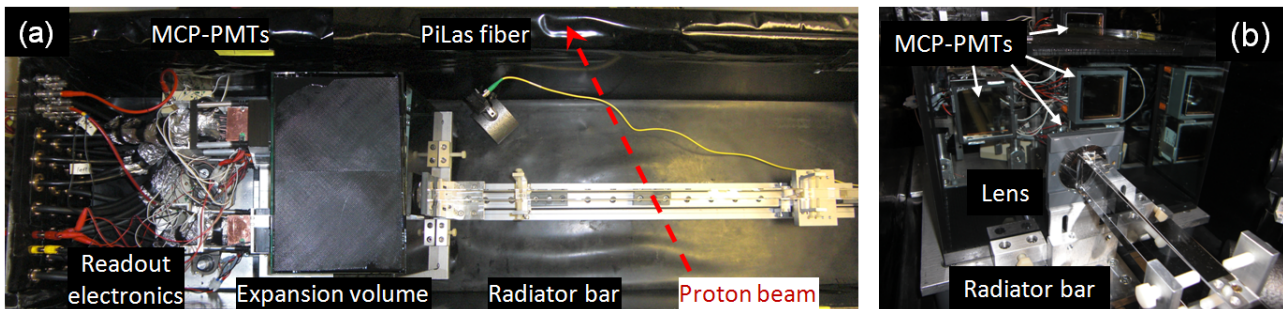


Figure 3.19: Photo of the first prototype tested in 2008/2009 at GSI.

A more complex setup was used in 2011 to study the performance of the narrow bar with the big oil tank expansion volume geometry, and to test the readout electronics. The concept of the prototype built and tested in 2011 is shown in Fig. 3.20. Focusing lenses with different Anti Reflective (AR) coatings were available and bars from different manufacturers could be tested. A variety of photodetectors, including MCP-PMTs, SiPM, and MaPMTs, could be placed on the large focal plane. The prototype was placed on a movable support structure to change its position against the beam. The data collected from two campaigns in 2011, at GSI and at CERN, were used for the first performance determination of the design using a narrow bar and a large oil tank.

The main focus of the third generation of the prototype, tested in 2012, was on the compact prism as expansion volume. It provided the first experience with the wide plate instead of a narrow bar as a radiator with a lens without an air gap. Several different bars and lenses were tested. The concept of the setup is shown in Fig. 3.20. The improved versatility and flexibility

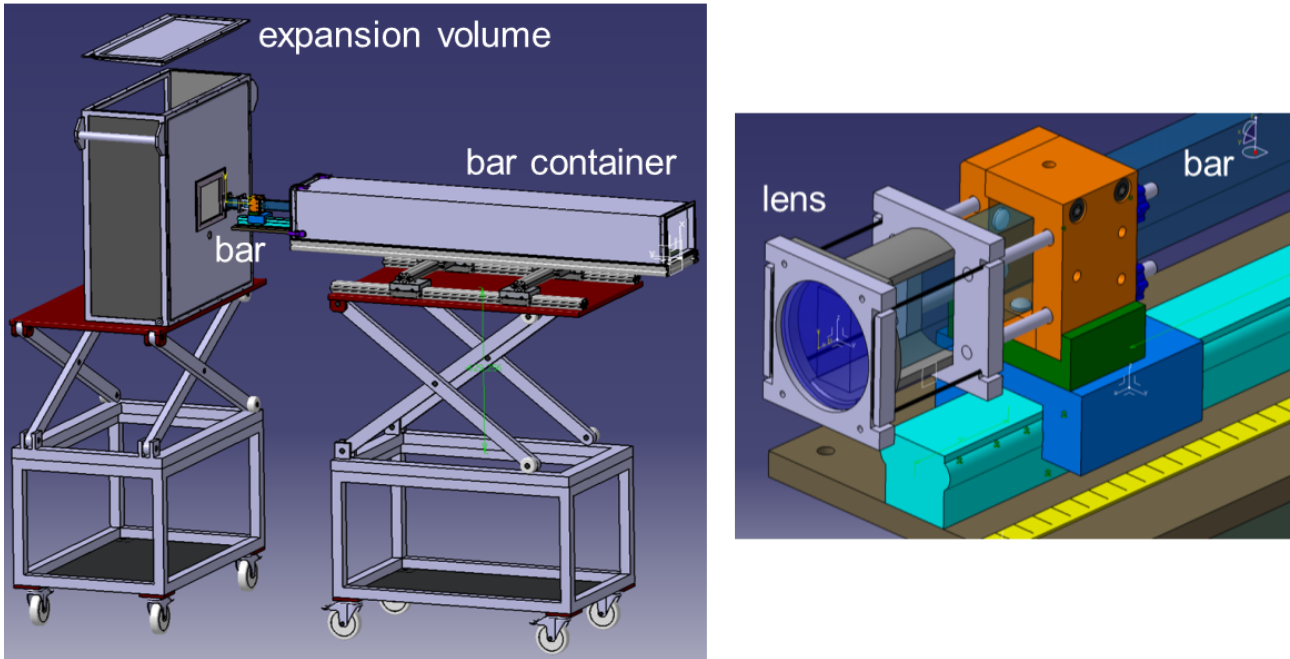


Figure 3.20: CATIA drawing of the prototype 2011.

of the setup was crucial to perform many different studies that required fast modifications, replacing components, and changing configurations.

The study of the second and third prototype is the main subject of this thesis. In the analysis, presented in the next chapter, the focus is on the narrow bar geometry, with a number of different bars and lenses and two options for the expansion volume: the large oil tank and the compact prism.

### 3.3 Monte Carlo Simulations

Studies using Monte Carlo simulation play a crucial role in every step of the PANDA Barrel DIRC development process. The output of the simulation is used to determine which of the possible design should be built in hardware and tested. The design options discussed in the previous sub-chapter are of particular interest and need to be implemented in the detailed simulation of both the prototype and the full PANDA Barrel DIRC system to determine if they are capable of delivering the required performance. Simulation is also used to select the components, optimize their placement, and prepare a plan for the test beam campaign. Finally, Monte Carlo data play an important role in the reconstruction and analysis of the experimental data.

Two software packages are available for the simulation of the PANDA Barrel DIRC: the PandaRoot framework based on Geant (Ref. [41, 42, 43, 44]) and the ray-tracing software called DrcProp (Ref. [45]). Both have their advantages and disadvantages and which one to choose depends on the nature of the study.

The PandaRoot simulation is needed to evaluate the influence of the physics processes, not included in the DrcProp, on the performance of the prototype. These processes are for example photons from secondary particles or photon transport efficiencies in the bars. Simulation studies with the PandaRoot framework were performed both for the prototype setup and for

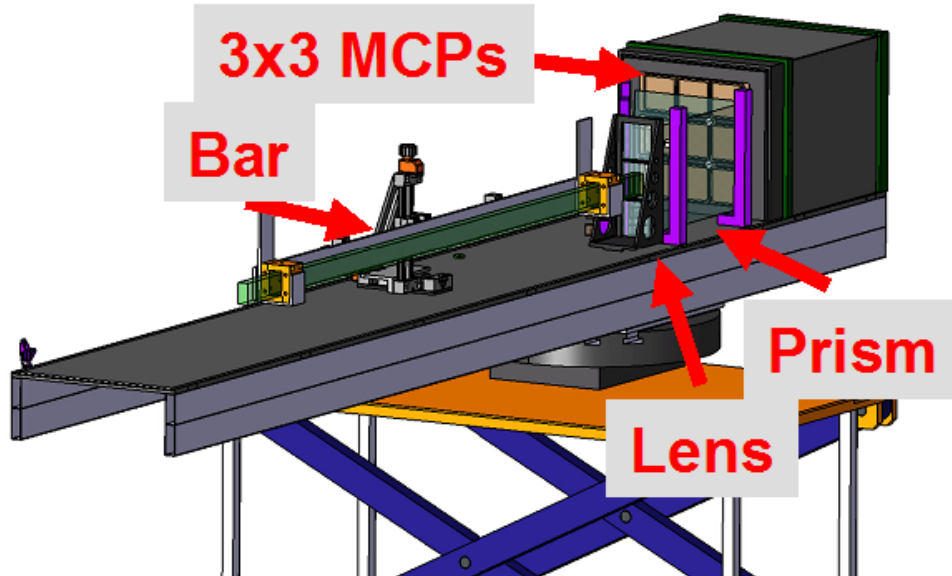


Figure 3.21: CATIA drawing of the prototype 2012.

the full PANDA Barrel DIRC system. It is part of a software framework for the future FAIR experiments called the FairRoot project. It can be used to simulate detector performances, evaluate different detector concepts, and also in future physics analysis. It is based on the packages ROOT and Virtual Monte Carlo with Geant3 and Geant4.

In the study with PandaRoot all or selected subsystems of PANDA detector can be included. Physical processes and effects can be activated to study their influence on the performance of the detector. The physics reaction is modeled with an event generator and propagated through the detector. The interactions with the materials are simulated by the chosen transport model that includes relevant interactions of particles. The format of the simulated data imitates the real signal of a particular detector.

The event display of the simulated PANDA Barrel DIRC is shown in Fig. 3.22. It is build of volumes, each defined by its shape and material. The physical properties of the materials, like density, atomic weights, etc., are used by the transport engines to simulate interactions of the particles with detector materials. Example of these interactions can be Bremsstrahlung and ionization. A material that simulates the synthetic fused silica has additional properties, that makes it possible to emit Cherenkov photons.

In this thesis, only a few selected aspects are studied with the PandaRoot simulation. It is used to evaluate the influence of the tracking systems on the Cherenkov angle resolution and the backgrounds from delta electrons and from the calorimeter back-splash. PandaRoot is powerful and contains very detailed physical simulation, but it is quite complex and frequent change of the geometry is cumbersome. It also has a limited level of access to individual interactions of photons with surfaces. Therefore, DrcProp was chosen for most studies. When a design turns out to be promising, the full PandaRoot framework is used to validate the ray-tracing results.

DrcProp is a stand-alone package that allows fast and straightforward implementation of many interesting aspects. It includes detailed material properties, such as the transmission and refractive index as a function of the photon wavelength, Rayleigh scattering in the material, and a realistic photon detection efficiency as measured in [33]. However, physics processes like

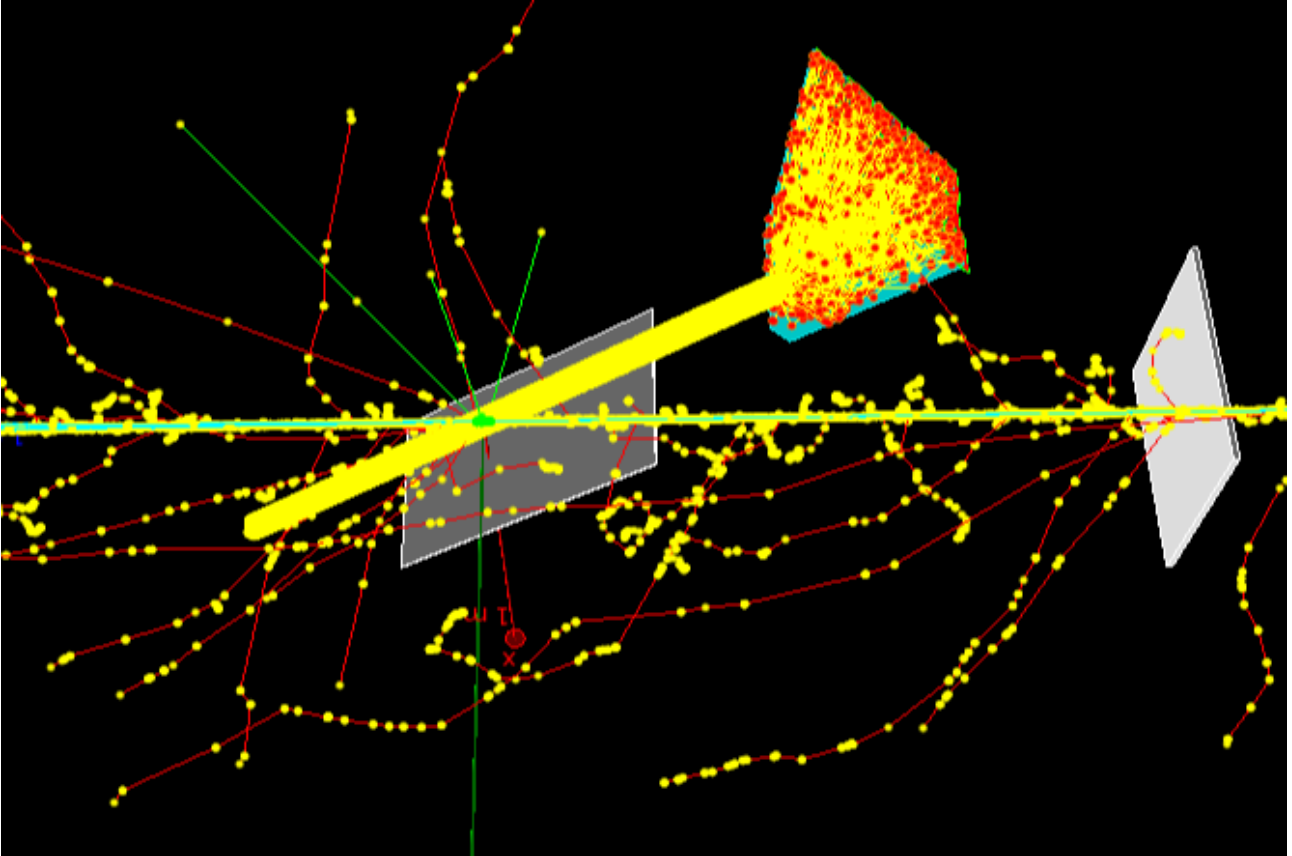


Figure 3.22: Event display from Geant simulation of the barrel DIRC detector.

multiple scattering or the creation of delta electrons and effects of the bar surface quality are not include in DrcProp. It is able to model photon yield, sensor occupancies, and is used in the reconstruction of the Cherenkov angle. It is used to simulate the response of the prototype to changes of beam parameters and different elements of the optics. The result is used to decide what configuration to test under which conditions. It is used for monitoring the prototype response during the test beam experiment.

A set of DrcProp classes is used to build a complex setup. All kind of surfaces can be used to construct separate volumes with defined optical properties. All these volumes can be arranged and coupled to generate the full setup. A so-called manager class holds one or several device systems, generates Cherenkov photons, and propagates them. It also holds the propagated photon list with informations about individual photons. The structure of the DrcProp framework allows to easily include new materials, surfaces and other elements important for the study. Photons can be generated in different ways. A photon gun generates photons with a given direction, position and wavelength. The second way to generate photons is along particle track. In this option, event by event, Cherenkov photons are emitted according to the Cherenkov equations 3.1 and 3.3. A time of propagation, the wavelength, positions at the detector plane, and many more informations of the measured photons can be saved in the output of this simulation.

DrcProp simulation of different setup geometries is performed before finalizing the exact design of the prototype to understand how the shape of the hit pattern is created and how is it sensitive to setup modifications. The DIRC hit patterns do not look like a ring observed in typical RICH detectors due to photons being transported inside the rectangular radiator bars. A prediction of the hit pattern for both prototypes is shown together with the simplified

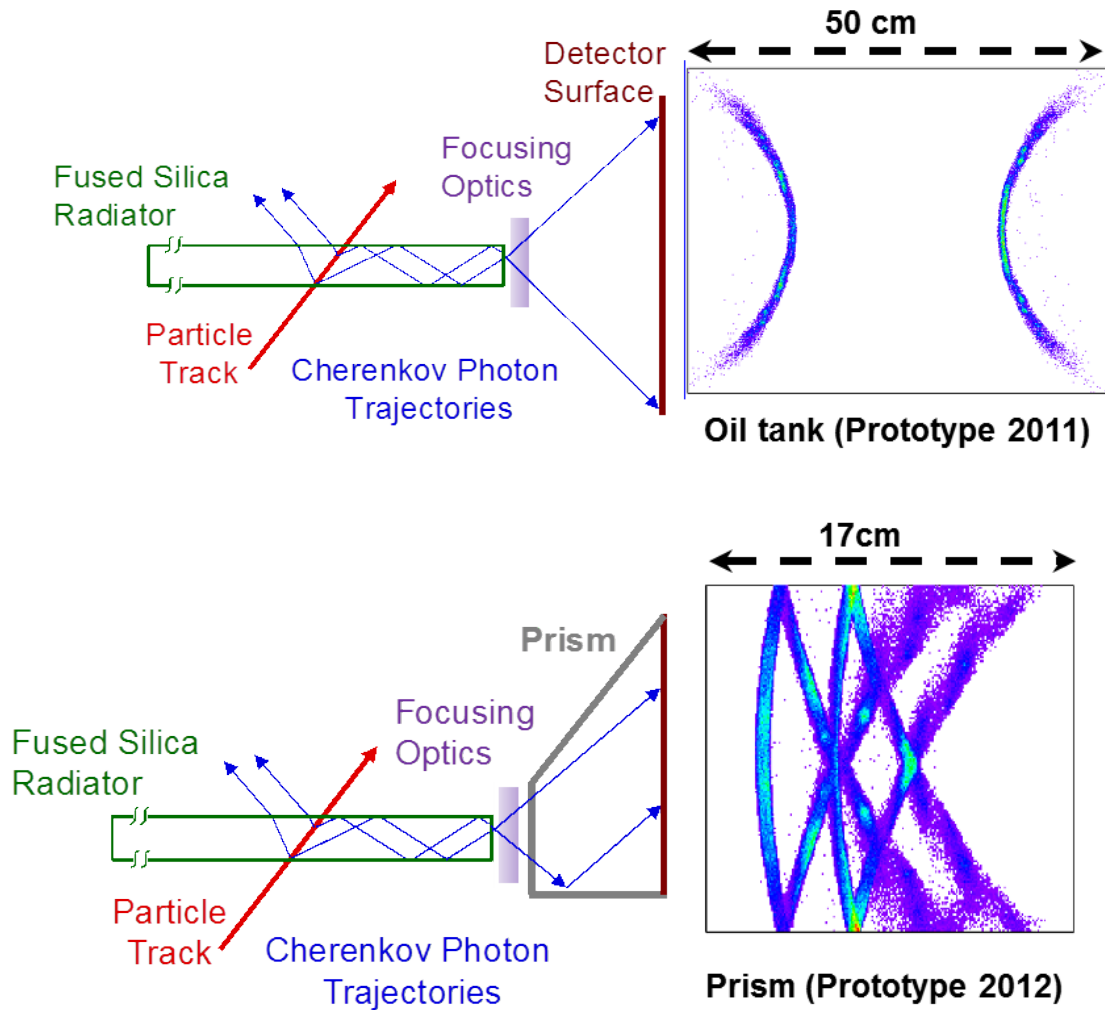


Figure 3.23: Predicted hit patterns from the DrcProp simulation. The top shows two ring segments which are the result of folding the ring in the narrow bar. No reflections happen in a large expansion volume. At the bottom a complicated “fish-like” pattern is created due to additional reflections from the sides of the prism.

schematics of the setups in Fig. 3.23. The hit pattern shown in the upper half of the figure the configuration with the big oil tank as expansion volume. A part of the ring is not internally reflected and escapes the bar immediately. The other part gets reflected many times and ends up as the two conic sections shapes shown in the top right picture. An additional folding of the image happens with the compact prism expansion volume, as visible in the bottom schematic. One entire segment is reflected from the bottom of the prism. In addition, not visible in this 2D picture, additional reflections, from the side surfaces cause the cross-like parts of the hit pattern.

In the experiment the ring images do not look so clear because of the relatively large width of the pixels with respect to the intrinsic width of the Cherenkov ring. In addition, there are the unavoidable gaps in the image coming from the frames of the sensor and the sport structure holding them in place. An example of simulated images for both expansion volume options is shown in Fig. 3.24 with the true simulated hit positions in the background to guide the eye. These kind of studies are used not only to determine the best sensor placement before the experiment but also afterwards to reproduce the conditions from the experiment.

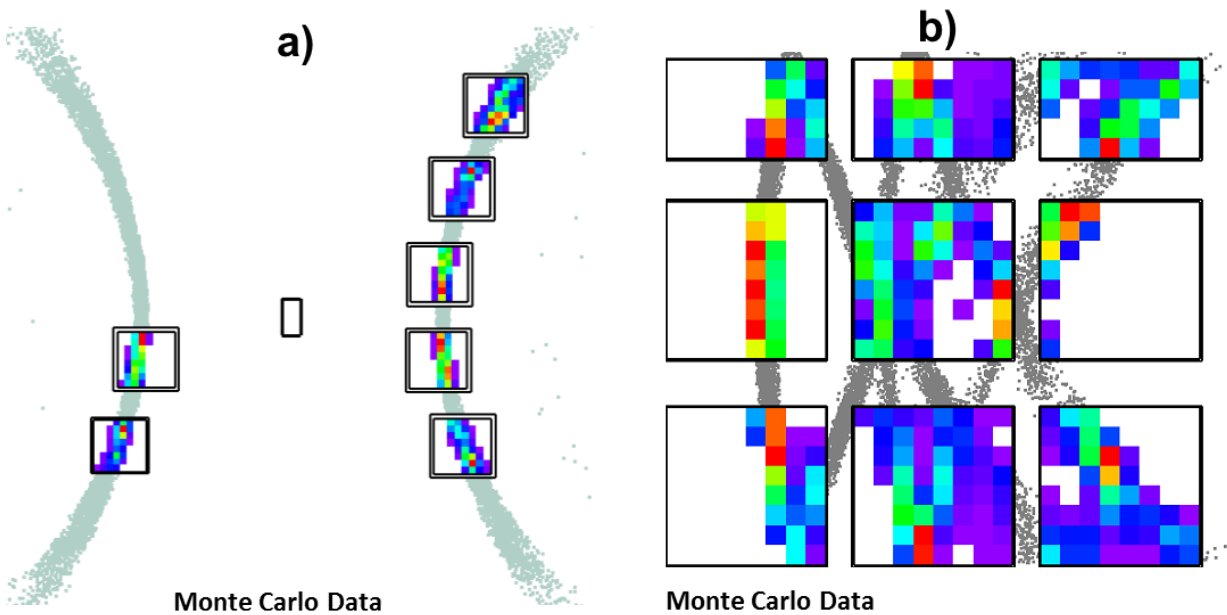


Figure 3.24: Example of the Cherenkov ring occupancy on the detector plane for simulated prototypes with the big oil tank (a) and the compact prism (b) as expansion volume.

To understand the behavior of the photons in the setup it is helpful to follow the paths of the photons. As an example, the visualization of one of the events, for the prism geometry, is shown in Fig. 3.25 for the prism geometry. The yellow arrow represents the track of the particle traversing the bar. A fraction of the Cherenkov photons, shown in red, was propagated towards the readout end, entered the expansion volume, and was recorded on the detector plane.

### 3.4 Reconstruction Method

To evaluate the performance of the prototype a special set of quantities is needed that can be measured in the beam experiment. It should be also possible to relate them to the performance reached in *BABAR*, and required for PANDA. The selected quantities are the single photon Cherenkov angle resolution (SPR) and the photon yield.

The photon yield is obtained by counting all hits within a time window in each selected event. The reconstruction method of the Cherenkov angle was based on the method developed for *BABAR* DIRC, which will be explained below in details. The time window, cuts, and all additional contributing effects are determined uniquely for each analyzed configuration and will be discussed in the result chapter.

The distribution of the true emission angles of the Cherenkov photons,  $\Theta_C$ , accumulated for 500 simulated pions, is shown in 3.26a. Particles are entering the bar with momentum of 10 GeV/c, and a polar angle of 122°. The spread of the  $\Theta_C$  values arise from chromatic smearing (see Fig. 3.3 and 3.1), since the angle depends on the wavelength, as shown in Fig. 3.26b. Most of the measured Cherenkov photons have short wavelengths. Addition cut-offs at the higher and lower wavelength are due to the acceptance of the photon detector and the transparency of optical grease.

The emission angle between the single photon and the particle track can be reconstructed

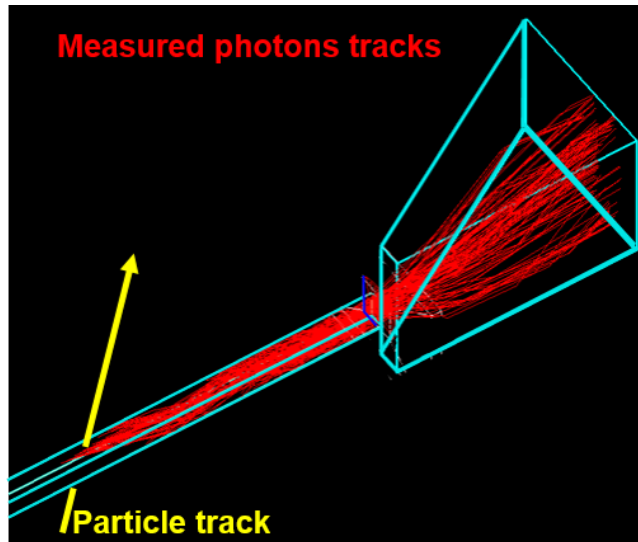


Figure 3.25: An example of the event display from DrcProp showing a simulated particle track traversing the setup with a narrow bar and the prism as the expansion volume. Photon paths that reach the detector plane are shown in red.

from the observed photon coordinates. In the following analysis a geometrical method, similar to the one of the *BABAR* DIRC, was used. The known spatial position of the bar, and the sensor pixel are used to define the 3-dimensional direction vector  $\vec{k} = (k_x, k_y, k_z)$  (see Fig. 3.27) pointing from the center of the bar end to the center of the pixel. The constants  $k_x, k_y, k_z$  are reconstructed direction cosines with respect to the main axes of the radiator bar. The vector  $\vec{k}$  is defined as the photon exit vector just inside the bar. The direction vector from the middle of the bar to the middle of the pixel uses Snell's law to determine the  $k$  vector. Together with the particle direction  $\vec{p} = (p_x, p_y, p_z)$  the Cherenkov angle for each photon can be calculated from:

$$\Theta_C = \arccos \left( \frac{|\vec{k} \times \vec{p}|}{|\vec{p}|} \right)$$

To determine the unique  $\vec{k}$  values for all the pixels, all sensors are equally illuminated using the photon gun option in the simulation.  $10^6$  uniformly distributed photons are generated at the bar end and propagated towards the readout plane. As an example, the distribution of  $k_x, k_y, k_z$  on the detector plane of a configuration with an oil tank is shown in Fig. 3.28a, b, and c, and with the arrangement of the MCP-PMTs used in 2011 in Fig. 3.28d. The transitions of the values are not smooth due to the additional reflection from the side for some of the angles. By setting the sides of the expansion volume one can avoid this complication since these photons are anyway not very valid for the reconstruction. Otherwise, mean values of the  $\vec{k}$  components are determined for every pixel and each of the individual non-ambiguous paths. These values for all types of propagation are saved in a list, the so called "Look-up" table. The look-up table is independent of the particle type, location, and momentum, uses only the known detector geometry and can be calculated prior to the experiment. The Look-up tables can be created before running the data. It is also well tested as it was used in *BABAR* experiment.

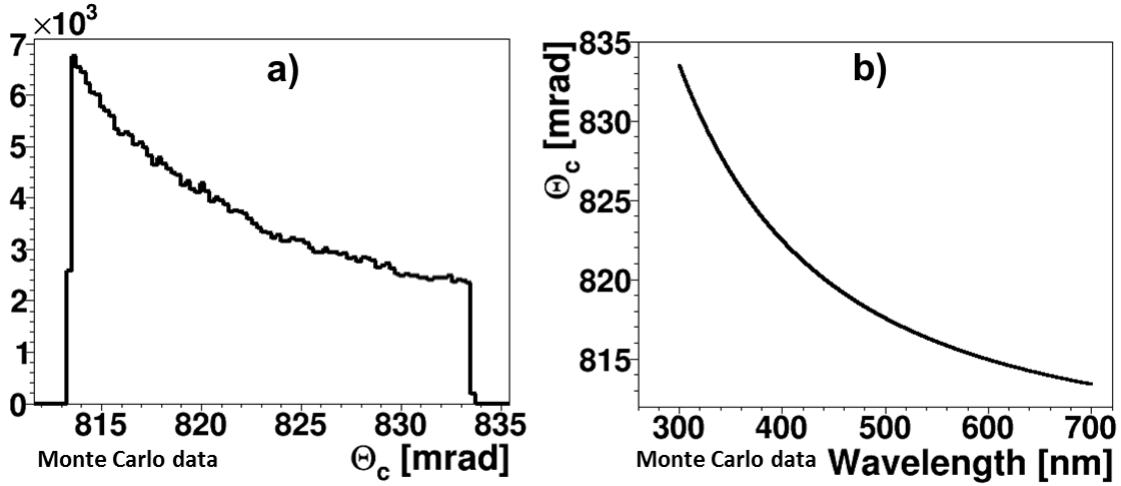


Figure 3.26: a) Distribution of single photon Cherenkov angles of the detected photons emitted by 10 GeV/c pions. b) Dependency of  $\Theta_C$  on the wavelength.

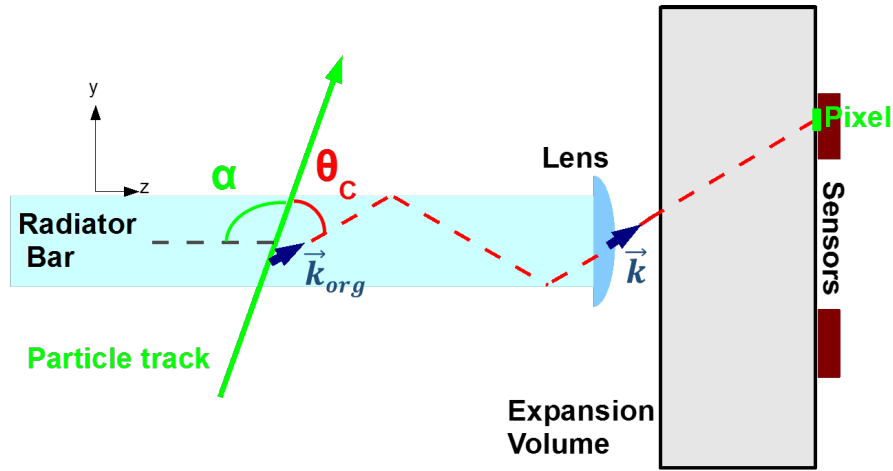


Figure 3.27: Schematic of the Prototype 2011 reconstruction concept, with one example photon track emitted from a particle. The direction vector  $\vec{k}$  is an estimator of the origin vector  $\vec{k}_{org}$ , and is used to reconstruct  $\Theta_C$ .

### Bar Ambiguities

The geometric reconstruction approach provides fundamentally only the photon exit vector at the end of the bar. The production vector is taken to have the same magnitude but the information about the sign is lost because of the unknown number of internal reflections of the photon inside the bar. Eight possible reflection types in the bar (any combination of forward/backward, up/down, left/right) have to be considered. In Fig. 3.29 a 2D simplification of this problem is shown, with 4 possible photon directions. In this case, if one of the pixels records a hit, four different directions  $\vec{k}_{org}$  have to be considered and therefore, four Cherenkov angles  $\Theta_C$  calculated. In three dimensions one has to consider 8 different possible solutions. Additional side reflections in the oil tank expansion volume increase the number of possible solutions and corresponding  $\Theta_C$  values in the spectrum to 16 possibilities. At least one of them is the correct one. The two dimensional case, with 8 values considered for a single hit, is shown in Fig. 3.30a.

The Cherenkov angle is not reconstructed from only one hit and these 8 entries but from a whole spectrum created for one track, typically at least 20 detected photons. Each hit pixel



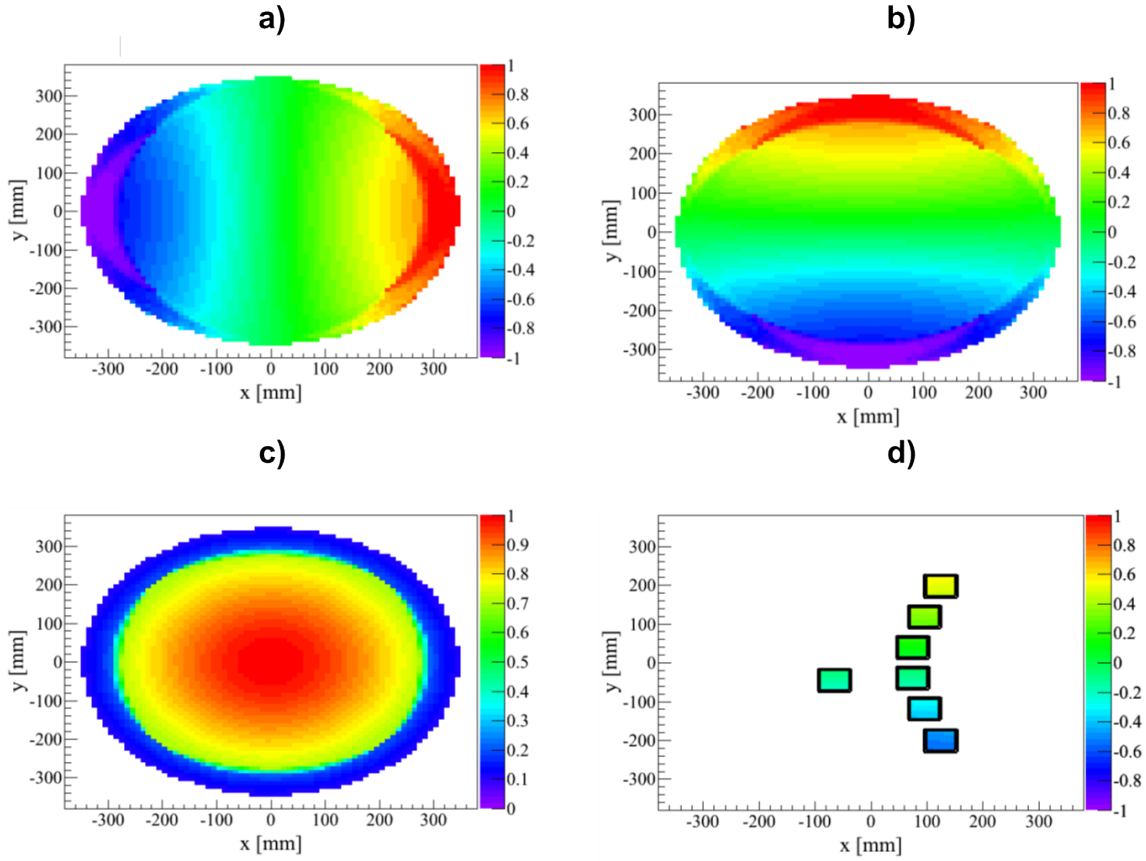


Figure 3.28: Mapping of the direction vector  $k_x, k_y, k_z$ . a), b), and c) show the distribution on the detector plane, while d) shows the  $k_y$  component mapped for the sensor arrangement from the experiment.

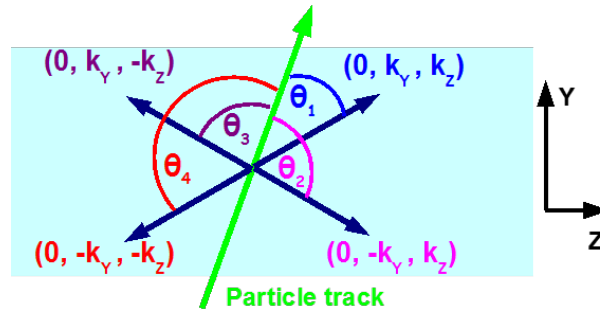


Figure 3.29: 2D simplification of the possible  $k$  solution for the original direction of the photon.

gives the right Cherenkov angle for the right combination of sign flips, and up to seven false values for the wrong assumption of the path. The spectrum from photons generated by one particle track is shown in Fig. 3.30b. After combining  $\Theta_C$  values, reconstructed for many events generating around 20 photons each, the distribution accumulates at the correct value (see Fig. 3.30c), which in this case is 822 mrad. The background comes from the ambiguities. Some of them can be eliminated with additional information. The photon arrival time can resolve backward/forward ambiguities in the bar and possible side reflections in the expansion volume. This method will be described in more detail later. In addition, by using the symmetry visible in Fig. 3.29 it is possible to eliminate left/right ambiguities with the use of the relation  $\Theta_{1,2} = 180^\circ - \Theta_{4,3}$ . Some of the possible solutions give Cherenkov value far above physical limits and can be excluded. The angle with respect to the bar surface has to be totally internally

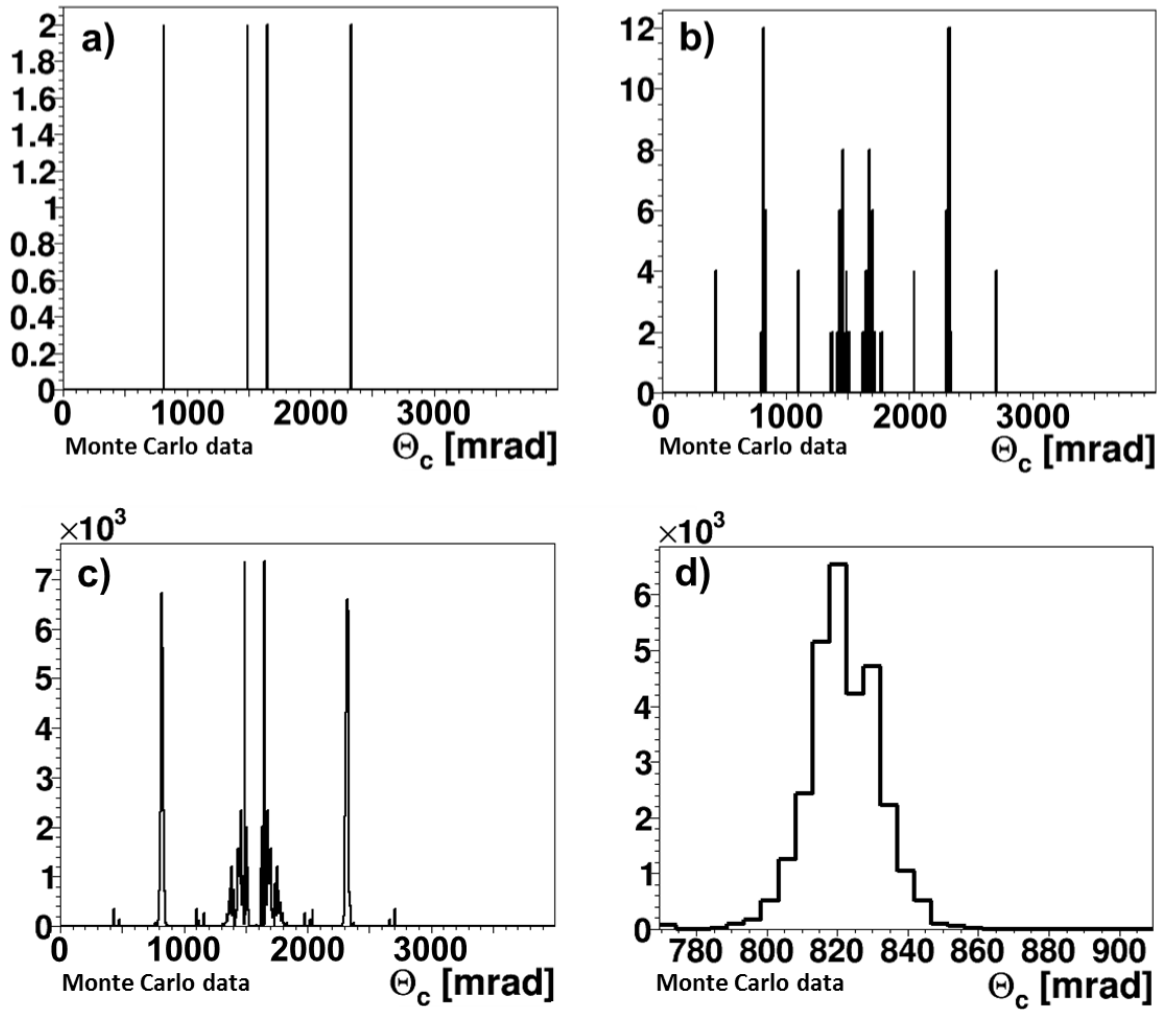


Figure 3.30: Reconstructed Cherenkov angle per photon including all possible solutions for the photon path in the bar for: a) one photon, b) photons generated by one particle, c) 210,000 events with full spectrum of  $\Theta_C$ , and d) zoomed region around the expected value.

reflecting reject ambiguities that would not be transported. The region around the expected  $\Theta_C$  is shown in Fig 3.30d.

### Prism Ambiguities

Reconstruction of the Cherenkov angle for the setup with the compact prism as an expansion volume is more complicated than with the big oil tank discussed above. Here, as shown in Fig. 3.31, there are many additional unique ways to propagate from the bar to the pixel, and it is harder to find the right solution of the photon path. The two dimensional projection shows, that the photon may be propagating on the direct path or with an additional reflection from the bottom or the top of the prism. In three dimensions there are side reflections to consider (from left/right surfaces marked in green/magenta colors in the left schematic), and a large number of possible combinations of these reflections. In total there are up to 80 possible paths for any given pixel just in the prism. Together with the bar ambiguities that gives over 600 possible  $\Theta_C$  values per hit. An example of the photon path with 4 reflections in the prism is shown in Fig 3.32. All of this adds up to additional combinatorial background.

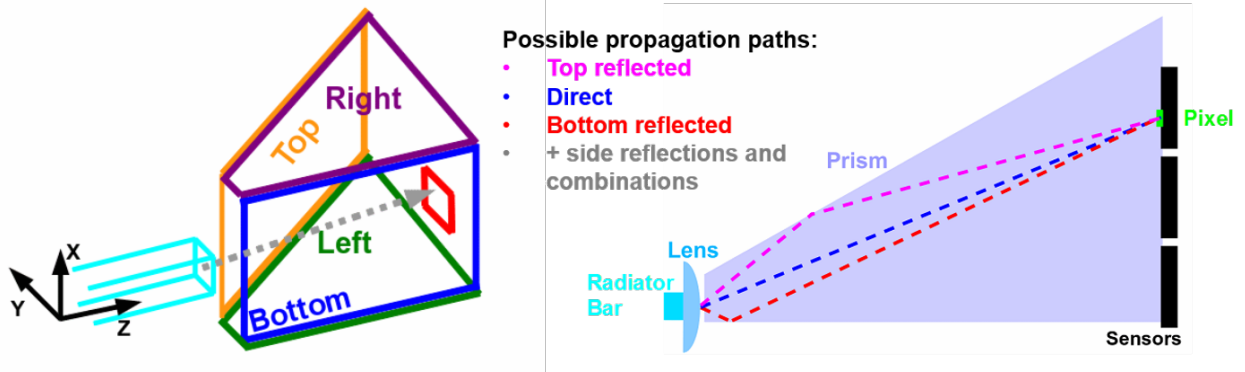


Figure 3.31: Schematics of the narrow bar and prism geometry. In the right picture, three examples for possible propagation paths of the photon from the center of the bar end to one of the pixels are shown.

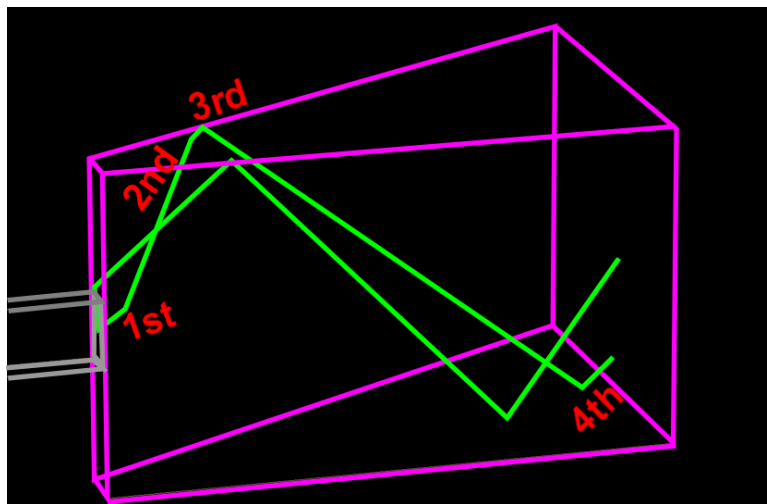


Figure 3.32: Event display from the DrcProp simulation showing two example photon tracks with three and four reflections in the prism. The numbers count the photon reflections.

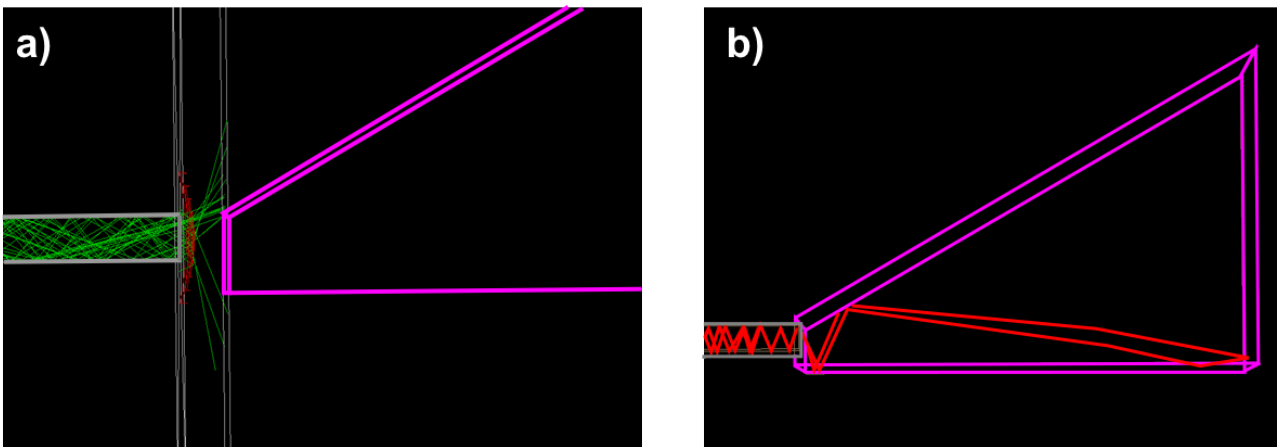


Figure 3.33: Event display from the DrcProp simulation with a few example tracks of photons with steep angles for two setups: a) with the lens and the air gap b) without focusing and the bar directly connected to the prism.

In Fig. 3.33 tracks of a photon with a steep internal reflection angle are shown for two setups. The first setup is the case with a lens and an air gap before the prism. The photons with the steepest angles are lost due to total internal reflection at the end of the bar, or because they exit at the steep angle and miss the prism. The second setup shows the bar directly coupled to the prism where even the photons with the steepest angles enter the prism. The hit patterns related to these two setups are shown in Fig. 3.34 with the photon arrival time as a color scale. It is clearly visible that for a direct coupling much larger part of the detector plane sees photons and the hit patterns are much less sharp. This is because the image is wider without focusing and the direct coupling transmits photons with steep angles. On the other hand, when the lens is used and some part of the photons are lost due to the air gap, no more than 2-3 reflections in the prism are possible and therefore much fewer ambiguities have to be resolved. In addition, the hit pattern is cleaner and easier to handle with fewer overlapping segments, which gets even more important later in the real experiment, since the image becomes less clearly defined as a result of a relatively big pixel size and the loss of some of the photons in the gaps between sensors.

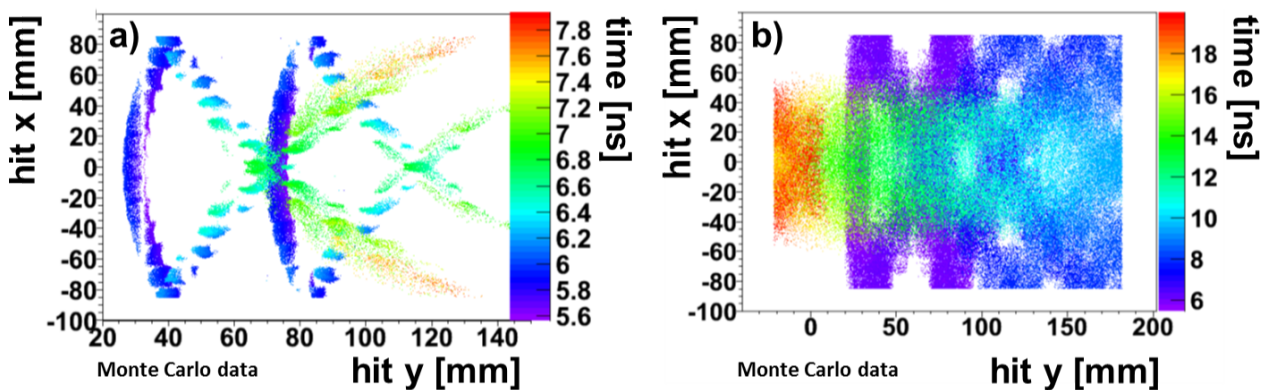


Figure 3.34: Simulated x, y position on the detector plane of measured photons, with a color scale showing the propagation time for two prototype configurations: a) with a lens and an air gap and b) without focusing and the bar directly connected to the prism.

However, even in the simpler case of the configuration, with a standard lens and an air gap, dealing with the combinatorial background in the analysis is a challenge. In Fig. 3.35b the reconstructed  $\Theta_C$  distribution is shown for configuration with the lens. In the reconstruction 32 possible paths within the expansion volume are considered but a stable fit around the expected  $\Theta_C$  value (Fig. 3.35) to extract the mean value and width of the  $\Theta_C$  peak is challenging.

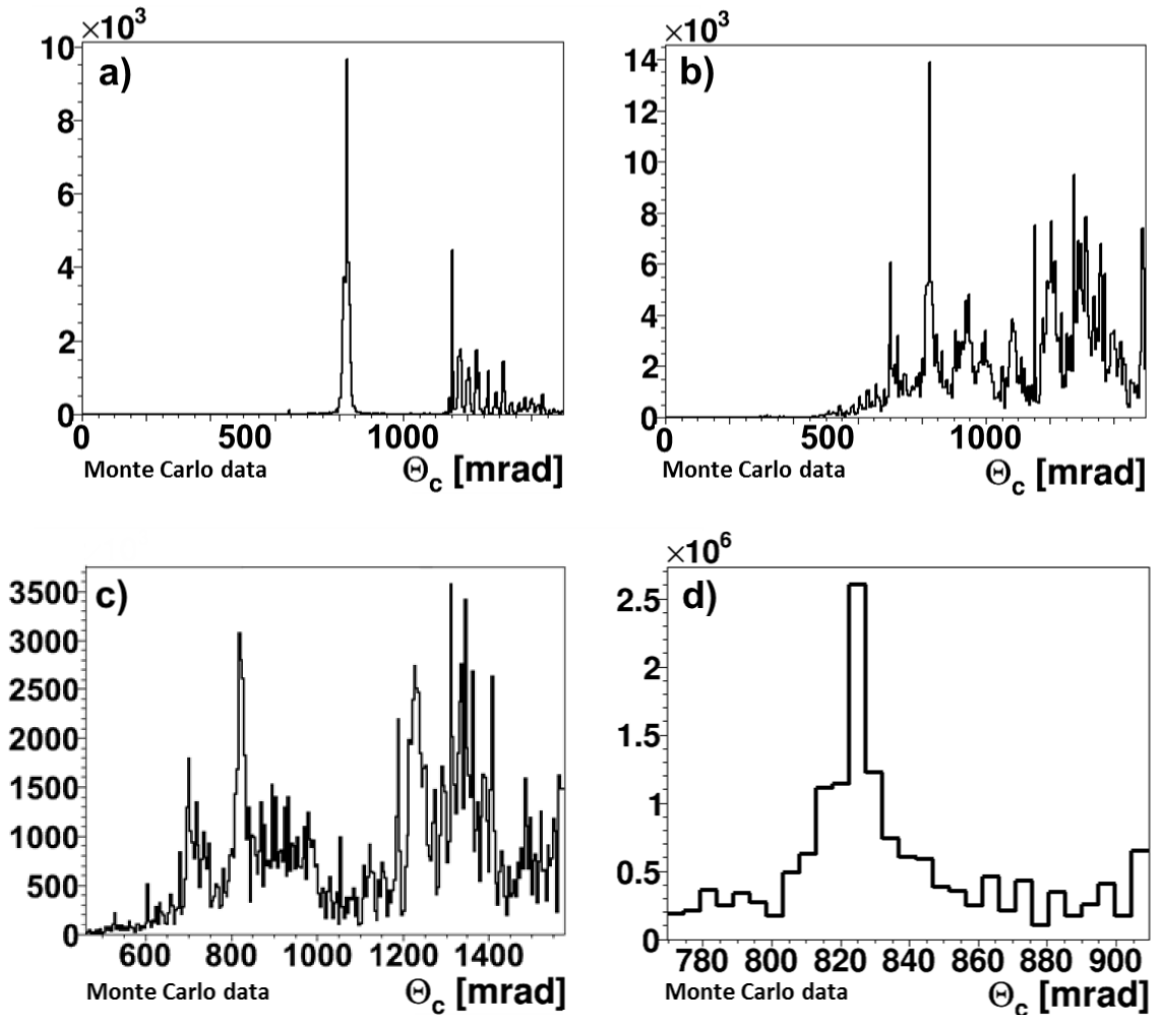


Figure 3.35: Reconstructed Cherenkov angle per photon for Monte Carlo data complicated by combinatorial background coming from: a) only bar ambiguities, and b) bar and prism ambiguities with full  $\Theta_C$  range, c) wide zoom and d) tight zoom on the reconstructed Cherenkov angle with combinatorial background from bar and prism ambiguities.

## 3.5 Components of the Prototype

### 3.5.1 Radiators

The key step in building the prototype is procuring the components. Some of them are commercially available but for some a separate prototype program is required. The most important and challenging components are the radiator bars. Only a limited number of manufacturers can produce them with the required quality. Different methods can be chosen to finish the surface of the bars. Those methods have a major influence on the quality and the cost of the prototypes and the PANDA Barrel DIRC system.

The production of the radiators is the biggest technical challenge for DIRC detectors. It was one of the main reasons of production delays for the *BABAR* DIRC and currently causes delays for the Belle II TOP counter. It is complicated to build large fused silica objects to extremely high tolerances for flatness, squareness, parallelism, optical finish, and very sharp edges. There are only few vendors worldwide capable of fulfilling this requirements. Normally, optical companies produce small, round objects like lenses or mirrors. Fifteen years ago, after a

slow startup and resolving several issues, the Rockwell/Boeing company was able to deliver more than 600 high-quality bars for the *BABAR* experiment. This company is still in operation, now known as InSync Inc. [46]. After such a long time all the companies on the market have to be re-qualified. Therefore, over 30 different prototype bars, from several vendors in Europe, USA, and Japan were bought and tested as potential bar producers for PANDA. Different fabrication processes and materials (different brands of synthetic fused silica as well as acrylic glass) were used. The production of the bars is a complex procedure that includes sawing, grinding, lapping, and polishing. The tight mechanical and optical specifications on sharp edges, surface polish, and side-to-face orthogonality pose a significant challenge to optical industry. Not all potential vendors are able to produce bars that meet all requirements simultaneously.

In the PANDA Barrel DIRC Cherenkov many photons will be internally reflected up to 200 times. The probability of photon loss during total internal reflection is determined by the optical quality of the surface, in particular the roughness. If the probability of the reflection loss for a single reflection is  $(1 - \mathcal{R})$  the total loss is  $(1 - \mathcal{R}^N)$  where  $N$  is the number of internal reflections inside the radiator. In the experiment this loss should be minimized at acceptable cost.

The quality assurance (QA) is crucial for the performance of the detector and therefore has to be performed very carefully. The bar shape is controlled via measurements of the parallelism and squareness of the radiator surfaces by the manufacturers. They are using autocollimators or precision gauges, measuring how much the shape differs from the ideal and if it is within the specifications. In addition, these measurements will be cross-checked in QA process by the PANDA collaboration using lasers and autocollimators. Similarly important is the photon transportation efficiency which is influenced by the surface roughness and the sub-surface damage. While manufacturers measure the surface roughness from outside the bar, using an interferometer, a dedicated setup has been constructed at GSI to measure the coefficient of total internal reflection directly, which is sensitive to both surface roughness and sub-surface damage.

## Material Selection

In principle any solid, optically clear material, with a refractive index in the 1.4-1.5 range, would be a possible choice for the DIRC. For the *BABAR* DIRC two kinds of quartz material were considered. Quartz crystals, which are the crystalline form of silicon dioxide ( $SiO_2$ ) are birefringent which rules them out as a potential candidate. However, the crushed and melted form of this material, called natural fused quartz, is very promising due to its polishability and long transmission length. Other option is synthetic fused silica, created by burning feedstock, for example silicon tetra-chloride ( $SiCl_4$ ), in an oxygen atmosphere. In the preparation stage of the *BABAR* DIRC different materials were studied in detail [47]. Tests of natural fused quartz and synthetic fused silica materials, obtained from different manufacturers, like Vitreosil-F [48], Suprasil [49], Spectrosil 2000 or Spectrosil B [50], are explained there. The samples of the natural fused quartz showed a rapid deterioration in the radiation damage tests due to high level of impurities. The radiation dose in PANDA is expected to be at similar level as it was in *BABAR*. Therefore, natural fused quartz is also not an option for PANDA. In addition to transmission loss, visual changes and radio-luminescence were also observed in natural fused quartz as consequences of irradiation. Similarly, the acrylic glass showed poor bulk transmission as well as insufficient surface quality and radiation hardness.

Synthetic fused silica is the best solution for the raw material of the bars in DIRC detectors, due to its long transmission length for Cherenkov photons, polishability, moderate dispersion,

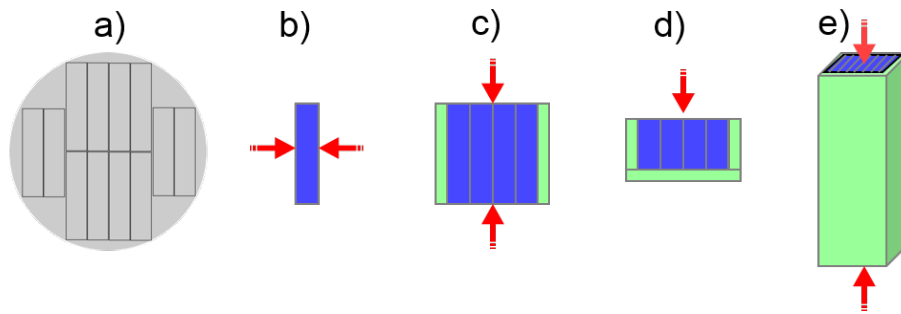


Figure 3.36: Schematic drawing of the primary stages of the radiator production process. a) shows the cross section of the fused silica ingot with marked planks that will be cut from it. Further points show steps of cutting, lapping, grinding and polishing of the bars (blue). Red arrows shows which surfaces were processed during each step. Glass planks used to protect already polished surfaces are shown in green.

and its radiation hardness [51]. It can be made very pure, making it a standard material in the fiber optics industry. For the PANDA Barrel DIRC two brands of synthetic fused silica are still under consideration. The first one, used already by *BABAR*, is Heraeus Spectrosil 2000, and the second is Corning 7980 [52].

### Bar Fabrication

The detailed sequence of the production steps can vary for every company. As an example, the procedure developed for the *BABAR* DIRC will be described based on Ref. [53]. In order to obtain radiators that match all the tight requirements, the large surfaces were ground on numerically controlled machines, lapped on a soft iron wheel, and then polished on a 4 m planetary pitch polisher. The bar edges were protected during processing by a neighboring bar or with a glass plate glued to the sides of the stack. QA measurements, performed after each step, were an essential element of the process.

Two types of synthetic fused silica, Spectrosil 2000 and Spectrosil B, were used as the raw material, supplied as cylinder-shaped ingots with a diameter of 20 cm, a length of 127 cm, and a weight of 90 kg. If the ingot passed QA tests, it was sliced into 10-12 “two-bar planks” as shown in Fig. 3.36a using a band saw for the long dimension and a chop saw for the ends. The two largest surfaces of these planks, called faces, are processed via grinding, lapping, and polishing (Fig. 3.36b). Next, four planks, each with two high-quality parallel faces with excellent surface polish, were glued together by a heat-setting wax. The outer polished faces and edges were protected by the attached glass planks and two sides of these 4 planks were subjected to the surfacing process again (Fig. 3.36c). The whole unit was cut in half on a band saw, the previously polished surfaces were covered with glass planks, while the final side surface of each of the 4-bar sub-units was processed. All of the long surfaces had been completed at this stage (Fig. 3.36d). A 32-bar unit, created by eight of the 4-bar units glued together, was ground to length, and then placed upright on an over-arm custom built lapping-and-polishing machine to finish the ends (Fig. 3.36e). After each step the units were subjected to QA measurements. The “half-moon” shaped pieces of the ingots, remaining after the first cut, were used for windows and wedges.

All methods used by industry to produce bars involve saw cuts, grinding, and lapping. After that, there is a choice of abrasive finishing, pitch polishing or the magnetorheological finishing (MRF) method. There are certain pros and cons to them. The optical finish of the *BABAR* bars

was done using Continuous Pitch Polishing (CPP). This is a non-abrasive technique that uses a material called pitch, which is a mix of mostly organic components. The exact ingredients are kept confidential by the vendors. Fluid dynamics is used to smoothen and shape the surface. With this method, surface roughness can be improved down to 1-4 Å RMS, since no material is actually being removed. Any removal of material, from grinding and lapping to abrasive polishing, causes sub-surface damage. Additionally, CPP is a high-yield operation and most of the companies capable of producing large pieces select that method. The biggest CPP machine has a diameter of 4.5 m. Few bars, each as long as 1.2-1.3 m, can be produced at the same time. The cost of the bars produced with the CPP method increased dramatically over the last 15 years and for the PANDA Barrel DIRC prototypes different methods were used trying to decrease the price. Methods using polishing abrasives bound in a solid matrix is one of them. A combination of the abrasive step using a polyurethane lap followed by acid etching and by finishing the piece on the CPP table shown promising results, and may be an option for some applications with less tight requirements. Different extrusion approaches were also studied ([40]) as a very cost efficient alternative. However, they were not able to meet the shape requirements. The CPP method is essentially guaranteed to reach 10 Å RMS or better surface roughness. The challenge therefor shifts to controlling the shape of the bar. The initial saw cut, and the grinding are important for the shape of the final piece.

Finally, it is worth mentioning the Magneto Rheological Finishing (MRF) approach that uses an accelerated magnetic liquid. A polishing head is used with a magnetic material floating on it. With a very strong magnetic field the liquid is pulled very smoothly across the surface and rotates without direct contact between the rotating head and the polishing material. The polishing head can be placed on a multi stage motion controlled setup where one can program the surface shape and, therefore, skip the fine grinding. Although this method may offer an alternative for future DIRC projects, size limitations and cost eliminate it from consideration for PANDA.

The CPP method has proven to produce high-quality bars for BABAR and Belle and is the preferred method for PANDA.

### Measurement of the Internal Reflection Coefficient of Radiator Bars

Figure 3.37 shows the setup built to perform quality assurance on the DIRC radiator bars, to monitor the production process, and to provide feedback to the manufacturers. It is capable of an indirect measurement of surface roughness to 1-2 Å precision. It is exploiting the method developed at SLAC [47] and further improved at GSI [40]. It uses the fact that the efficiency of the photon transport inside the radiator bar depends on the photon energy and the quality of the bar polish, in particular on the surface roughness. This efficiency can be determined from a measurement of the bulk attenuation and the reflection coefficient using laser beams of different wavelengths. In this measurement the intensity ( $T$ ) of the laser beam reflected multiple times inside the bar (see Fig. 3.38) is recorded and used to calculate the coefficient of total internal reflection ( $\mathcal{R}$ ) from:

$$T = \mathcal{R}^N \cdot \exp\left(-\frac{L}{\Lambda}\right), \quad (3.14)$$

where  $N$  is the number of internal reflections inside the quartz bar,  $\Lambda$  the attenuation length of fused silica and  $L$  the optical path length of the laser beam. The probability of the reflection



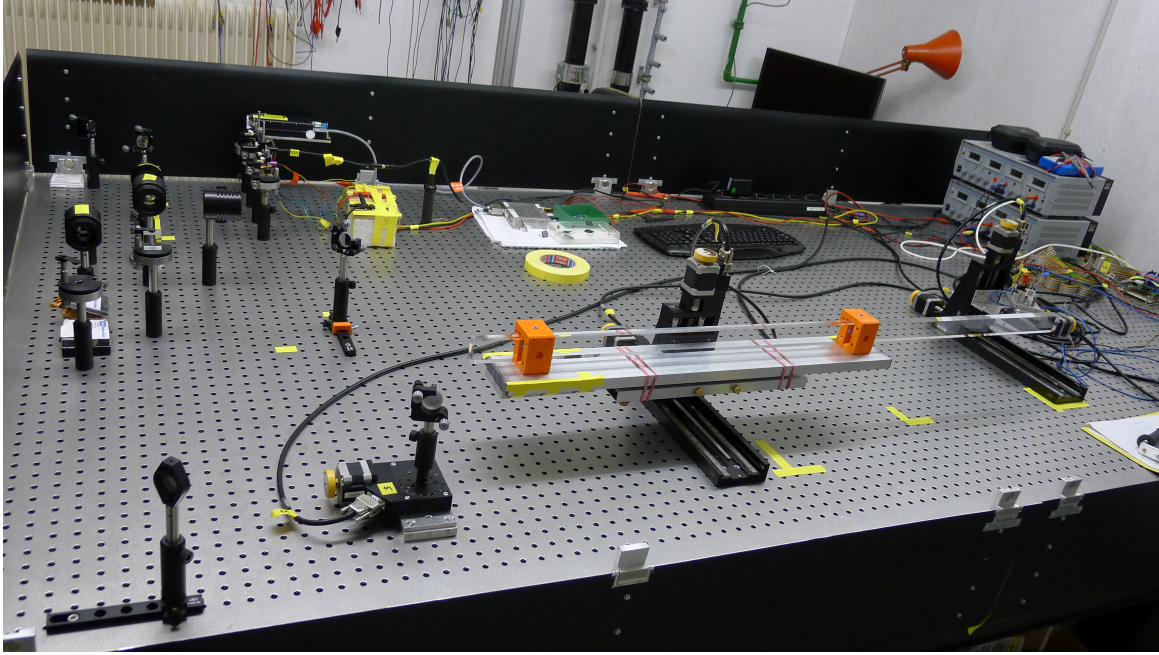


Figure 3.37: Photo of the setup for the measurements of the optical properties of the radiator bars.

loss  $(1 - \mathcal{R})$  for a single reflection is related to the surface roughness  $\sigma$  of the radiator by the scalar scattering theory [18]:

$$1 - \mathcal{R} \approx \left( \frac{4\pi \cdot \sigma \cdot n \cdot \cos(\alpha)}{\lambda} \right)^2, \quad \sigma \ll \lambda \quad (3.15)$$

where  $n$  is the refractive index,  $\lambda$  the wavelength, and  $\alpha$  is the reflection angle within the radiator bar.

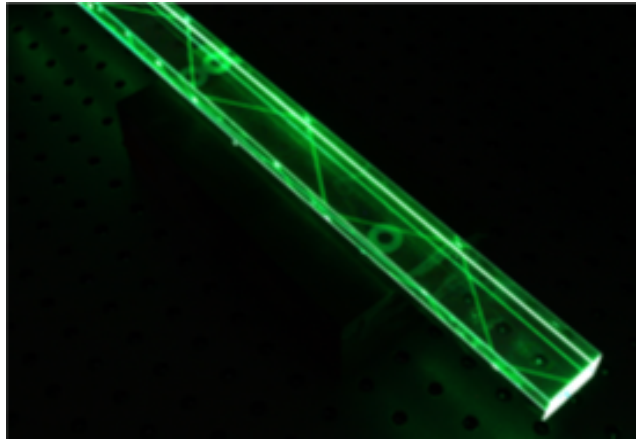


Figure 3.38: Example of a narrow prototype bar with a green laser beam internally reflected from the sides.

The schematic of the setup is shown in Fig. 3.39. The optical table was installed in a dark, temperature-stabilized cleanroom. Four lasers with different wavelengths are used. The UV laser [54] has an output power of 5 mW, a beam diameter below 1.3 mm at exit, and a beam divergence of 11 mrad. The three other laser modules have an output power of 1 mW, a beam

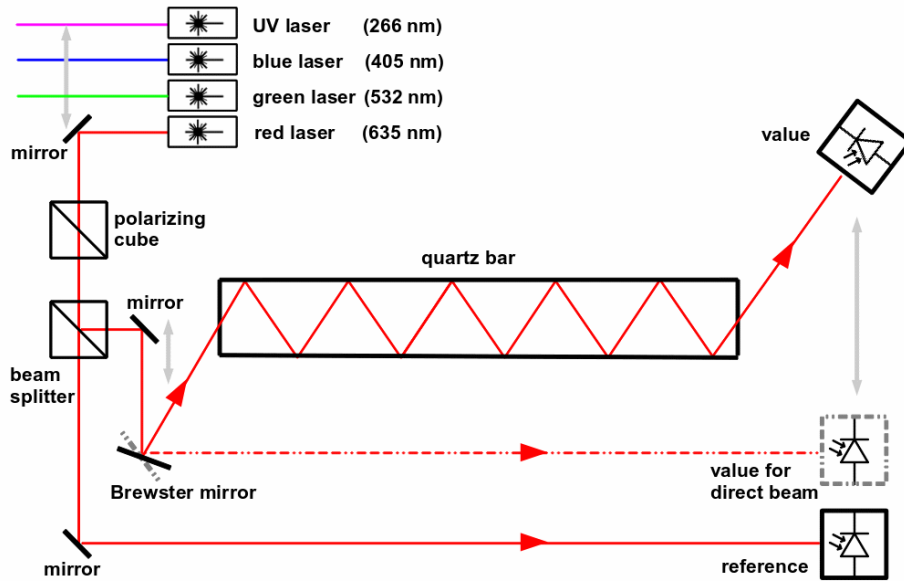


Figure 3.39: Schematic illustration of the optical setup for measuring the transmission of the beam propagating via total internal reflection. The gray arrows show the movement degrees of freedom for the motors and mirrors.

diameter at exit of 2 mm, and a beam divergence below 1 mrad. UV-enhanced aluminum mirrors, coated with  $\text{MgF}_2$ , are used to guide the laser beam. The mirrors, polarizing cube, and beam splitter are made by the Newport company [55]. The polarizing cube is made of SF 2, NSSK grade, precision annealed optical glass, providing an extinction ratio of 1000:1. The beam splitter is made of two prisms and a combination of metal and dielectric layers. In both parts antireflective coating is used to minimize surface reflection losses. The measurement is performed by recording the intensity of the laser beam with two photodiodes, S1227-1010BR or S1723-06, both with  $10 \times 10 \text{ mm}^2$  active area, made by Hamamatsu [56]. The temperature at the photodiodes is monitored. The data is collected by ADC cards [57] connected to a computer. In addition, some of the components are placed on motion control step motors, controlled from the computer, to automatize the measurement process.

All four lasers are placed on micrometer position adjusting systems. They are aligned in such a way that changing the wavelength is possible by shifting one mirror, placed in front of the lasers on a sliding stage. The selected beam is polarized and divided into two parts. One beam is guided by a mirror directly to a reference diode that is used to correct for laser intensity fluctuations. The second beam is guided to a mirror placed on the rotating motor. The bulk attenuation is measured with the beam going downstream through the bar. For the reflection coefficient measurement the beam enters the bar at the Brewster angle ( $55.5^\circ$  for 635 nm) to minimize the front surface loss and is internally reflected 15-50 times. The number of reflections inside the bar depends on the bar orientation and length. Both the bar and the photodiode are placed on linear stages. An array of points on the front surface of the bar is scanned and the mean value of the measured intensities is determined to obtain the final result. Correction factors are applied for residual reflected intensities.

A more compact version of the setup was used to evaluate the the first set of shorter prototype bars for the PANDA Barrel DIRC. The setup and measurements were described

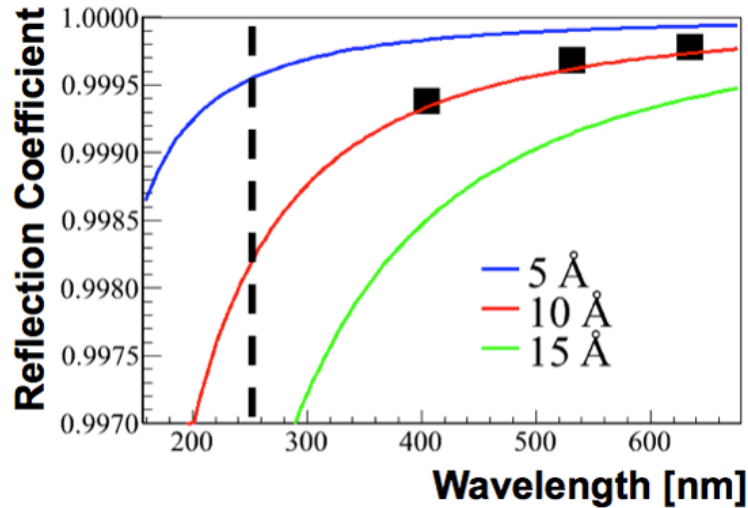


Figure 3.40: The coefficient of total internal reflection as function of the wavelength. Measured results [40] (black points) for a bar produced by Schott Lithotec are compared to predictions from scalar scattering theory for different surface roughness values (color lines). The dashed line indicates the wavelength of the new UV laser.

in detail in Ref. [40]. Figure 3.40 shows an example result for a bar produced by Schott Lithotec and the good agreement between data and scalar scattering theory. The points are the measurements while the colored lines are the predictions from the theory for different surface roughness values. The success of this compact setup motivated the development of a larger and more flexible configuration capable of measuring the bulk attenuation and reflection coefficient for bars and plates up to 2.5 m in length. This new setup will be used for the QA of the new prototype radiators and to verify the quality of the glue bonds in fully assembled radiators before installation in the bar boxes. The addition of the UV laser furthermore increases the lever arm for the surface roughness determination and makes the measurement more sensitive to possible sub-surface damage effects.

### 3.5.2 Focusing Optics

Lenses are more readily available from industry than the radiator bars, but they do have some properties that are important for a DIRC application and not immediately obvious. The pixel size and the bar size are important contributions to the Cherenkov angle resolution for small expansion volume. The influence of the bar size can be mitigated by a focusing lens. However, the focal plane of a single lens is not flat but has a parabolic shape described by the Petzval field curvature [25]. A simulation of the tank expansion volume, with and without focusing, was performed and the resulting patterns are shown in Fig. 3.41. Three effects are clearly visible: the focused (red) ring segments are almost three times thinner in the middle part than the unfocused (black) ones. Photons with steeper angles are lost in the configuration with regular lens at the bar-lens-air-expansion volume transition. It is a result of the Fresnel reflection [25] and the loss of the photons with large angles in the air gap. The middle part of the rings are better focused than the wings as a result of the curved focal “plane”.

For the prototype the parameters of the lens are selected by reconstructing the Cherenkov angle per photon and selecting the combination of air gap and focal length that provides the best average resolution. The best resolution for the prototype configuration with a standard

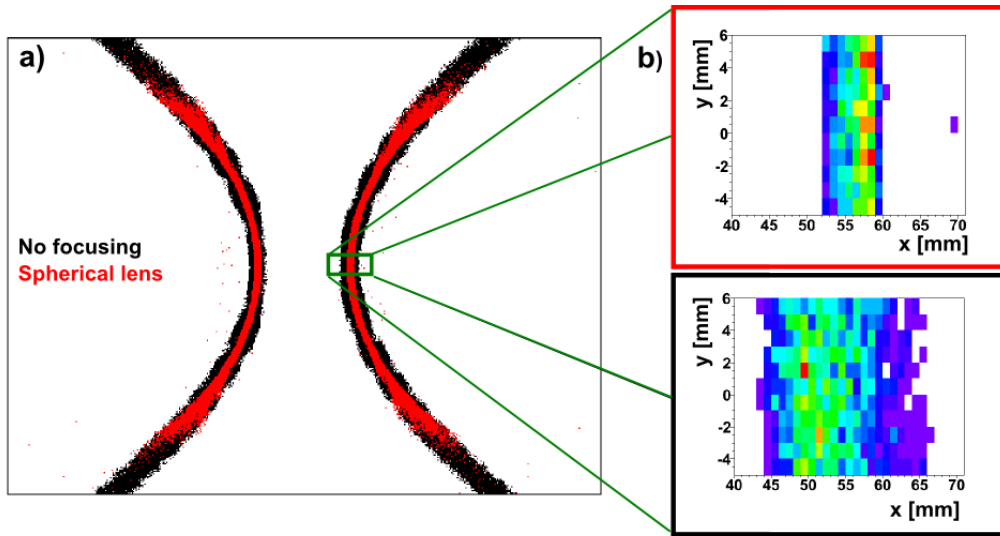


Figure 3.41: a) Hit pattern on the detector plane from Monte Carlo data. Simulation was performed for the setup with (red) and without (black) focusing. The zoom (b) to the middle part of the ring segment with the hit frequency as the color scale of the focused (top panel) and unfocused (bottom panel) ring.

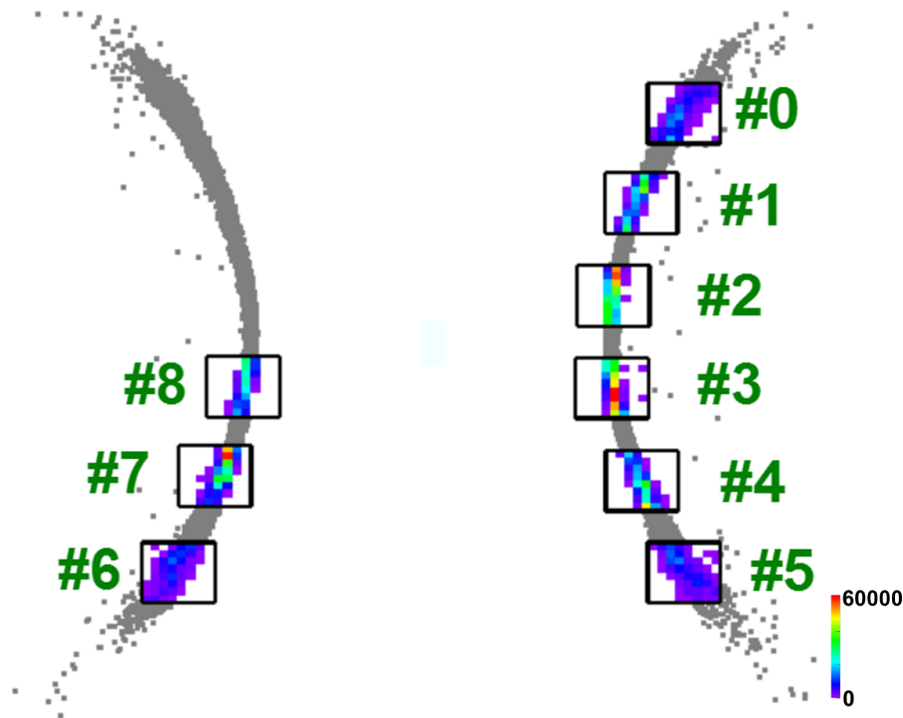


Figure 3.42: Pixelated hit positions (color) from simulated 10 GeV/ $c$  pions showing the influence of the curved focal plane of lens L1 on the ring image for the MCP-PMT layout from the 2011 prototype for 210,000 events. The gray points show the locations of the true Monte Carlo hits.

spherical lens and oil tank expansion volume was obtained from the simulation of lens with the focal length of 250 mm and an air gap of approximately 10 mm. These values were used in the simulation of the 2011 prototype. The distribution of the hits on the pixels of eight MCP-PMTs is shown in Fig. 3.42.

The Cherenkov angle resolution per photon was determined separately for sensors near the

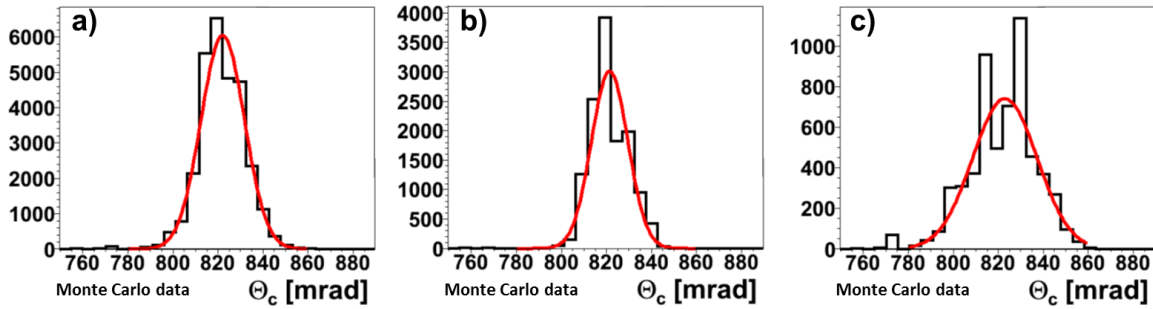


Figure 3.43: Reconstructed Cherenkov angle per photon from 2011 prototype Monte Carlo data for different parts of the rings (compare to Fig. 3.42). All MCP-PMTs (a), the central part with MCP-PMTs #2, #3, and #8 (b), and the outer part with MCP-PMTs #0, #1, #4, #5, #6, and #7 (c).

center of the ring and in the outer parts of the image. Fig. 3.43 shows that the resolution is 9.6 mrad on average for all MCP-PMTs, 8.1 mrad for the central part of the image and 14.3 mrad for the outer part. This deterioration of the image quality for steep angles is a combination of lens aberrations, the curved focal plane, and the so-called kaleidoscopic effect [58, 59].

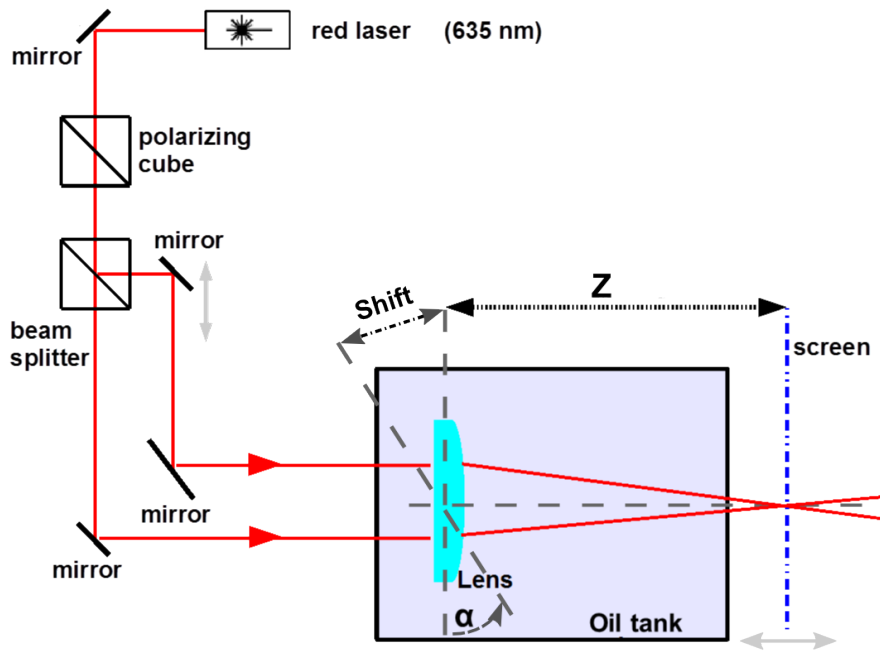


Figure 3.44: Schematic of the optical setup to measure focal length  $Z$  of the lens  $L2$  as a function of angle  $\alpha$ .  $Z$  and Shift are the measured quantities. Setup for the lens  $L1$  measurements is the same but without the oil tank.

The lenses for the experimental tests were selected from a range of commercially available models based on the best match to the parameters optimized in the DrcProp simulation. In addition a prototype high refractive lens working without additional air gap was purchased. The focal length of the selected standard lens  $L1$  and compound lens  $L2$  were also measured in the laboratory to verify the parameters and to evaluate how important the curved surface of the focal plane is for the DIRC resolution. Details of these two lenses can be found in Table 3.2.

To measure the shape of the focal plane the setup for the radiator measurements was modified as shown in Fig. 3.44. The lens was placed on the rotation stage and rotated through two parallel laser beams. Angle was calculated from the shift measurement 80 cm from the

Lens	Focal Length [mm]	Material	Coating	Type	Size (CT,H,R) [mm]	Manufacturer
L1	250	fused silica	UV AR	spherical	(9, 50, 117.4)	Newport [55]
L2	300	NLaK33B, fused silica	AR 330–460 nm	compound, cylindrical	(14.3, 175, 73.5)	Hellma Optik [60]

Table 3.2: Lenses measured in the setup. Sizes of the lenses are given in mm: central thickness (CT), height (H), and radius (R)

Shift [cm]	0	10	20	30	40	50	55	60	65	70	75
$\alpha$ [°]	0	7.2	14.4	21.6	28.9	36.4	40.2	44.0	47.9	51.9	55.9
Y [cm]	0	3.1	5.8	8.1	9.2	9.3	8.9	8.8	7.8	7.1	5.9
$Z_{L1}$ [cm]	25.5	25.3	23.5	21.9	19.1	15.7	13.8	12.6	10.5	9	7.2
$Z_{L2}$ [cm]	33.8	32.7	31.1	28.6	25.3	18.7	16.4	14	11.6	10.3	7.9

Table 3.3: Results of the focal length  $Z$  measurements as a function of laser beam angle measurements for two lenses, standard spherical lens L1 and compound high refractive index lens L2. Shift and  $Z$  are the measured quantities. Shift values are converted to the rotation angle of the lens and  $Y$  coordinate in prototype. The systematic errors on listed values are:  $\sigma_{Shift} = 3$  mm,  $\sigma_{\alpha} = 0.1^\circ$ ,  $\sigma_Y = 3$  mm, and  $\sigma_Z = 0.5$  mm.

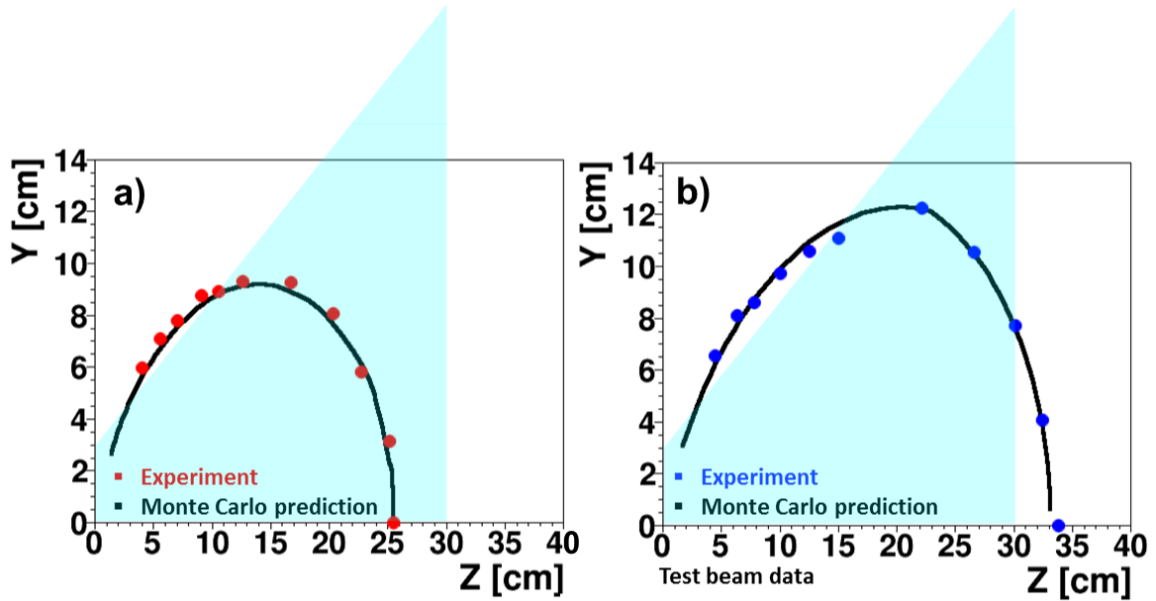


Figure 3.45: Measurements of the focal length (points) compared to Geant simulation (solid line) for lens L1 (a) and lens L2 (b) converted in to the prototype coordinate system. The cyan shape of the prism is used to show the difference between the shape of the detector plane of the prototype and the shape of the focusing plane of the lens.

rotation point. The intersection point of two laser beams determines the focal length  $Z$ . The compound lens L2 was placed inside a  $20 \times 20 \times 30$  mm<sup>3</sup> glass container filled with mineral oil to simulate the focusing behavior for the situation without the air gap. The results are shown in Fig. 3.45 and Tab. 3.3. The rotation of the lenses is converted to the coordinate system of the prototype to better compare the shape of the focal plane to the back surface of the expansion volume. The shift was measured with systematic error of 3 mm which translates to  $0.1^\circ$  error

on the rotation angle  $\alpha$  and 0.1 mm error on the Y coordinate. The systematic error of the focal length was reduced by repeating measurements to 0.5 mm. The obtained shape of the focal plane agrees with the results from the Geant simulation. In the measurements it was confirmed that the focal plane is strongly curved.





# Chapter 4

## Performance of the PANDA Barrel DIRC Prototype

The main purpose of the prototype program is to evaluate the performance of the design options and to provide the basis for the Technical Design Report for the PANDA Barrel DIRC. Some of the ideas and options, that are still under consideration for this system were presented in the previous chapter. The components and options that performed well in the simulation were selected for fabrication by industry and installed in the prototype for the tests with particle beams. This chapter discusses the two prototype generations in detail and presents the results from several test beam campaigns at GSI and CERN.

### 4.1 Prototype 2011

The concept of the prototype built and tested in 2011 was already mentioned in the previous chapter. The main goal was to establish the performance parameters of the geometry with the narrow bar and a big oil tank as expansion volume. In addition several prototype components were tested: lenses with different anti-reflective coatings, a flat mirror, several sensor types, and new readout electronics.

#### 4.1.1 Preparation and Description of the Setup

The preparation process for the test beam in 2011 was divided into two phases. The first was planning and building the prototype. The second was to place it into the 1.7 GeV/ $c$  momentum pion beam at GSI. These tests served to check all components and improve the system before the main campaign at the T9 area of the CERN PS.

A photograph of the prototype is shown in Fig. 4.1. A synthetic fused silica bar L3, with the dimensions  $17 \times 35 \times 800 \text{ mm}^3$ , made by Schott Lithotec [61], was used as radiator. A lens was attached to one bar end with optical matching liquid and held in place by a plastic holder. A mirror was mounted on the opposite end of the bar. The bar was placed at the center of the entrance window to the expansion volume and covered with a light-tight container made of aluminum.

A large tank with the size of  $800 \times 800 \times 300 \text{ mm}^3$  filled with 190 liters of mineral oil (Marcol82) was used as the expansion volume (see Fig. 4.2). The sides were made of aluminum panels and two large float glass plates served as entrance and exit windows. Aluminum covers



Figure 4.1: Photo of the prototype 2011 at CERN.

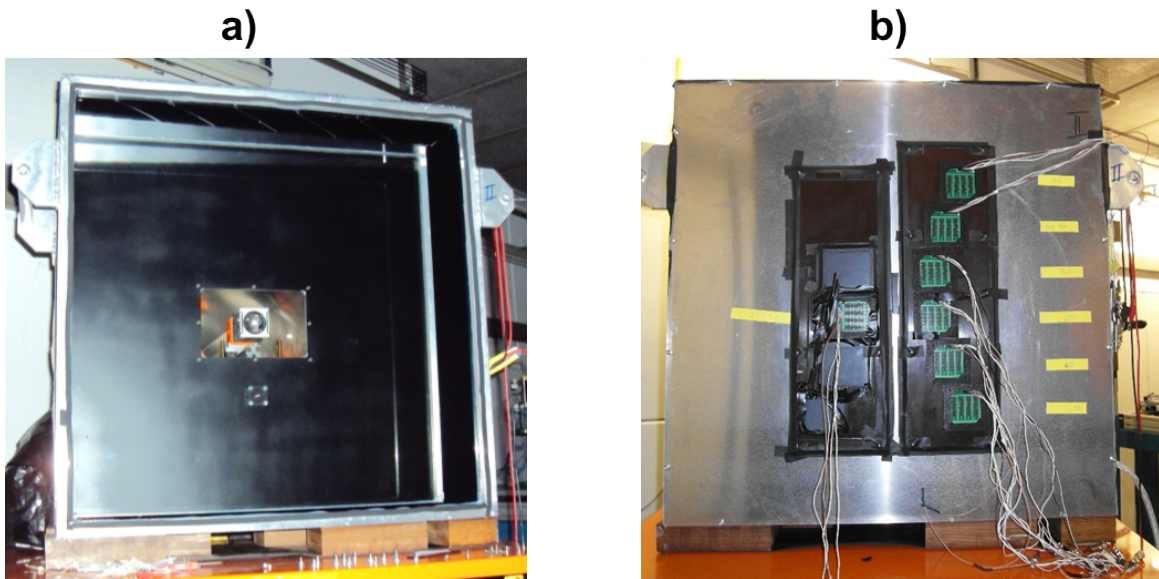


Figure 4.2: Photographs of the expansion volume seen from the back without the cover in place (a) and with the aluminum cover attached and the plastic masks holding seven sensors in place (b).

with access slots for coupling the bar and sensors to the windows made the expansion volume light tight. Baffles on the inner part of the side walls of the tank served as photon traps to avoid photon reflections. The  $800 \times 800 \text{ mm}^2$  backplane had enough space to mount and test a number of different type of sensors, which were pressed against the back window of the tank. For some runs an optical grease was applied to ensure better optical connection. The arrangement of the sensors, shown in Fig. 4.3a, was based on the expected shape and location of the rings from the DrcProp simulation Fig. 4.3b. Two plastic masks were produced with cutouts for the sensors. The horizontal location of the ring segments on the detector plane depends on the angle between the particle beam and the bar (see Fig. 4.3b). That is why the

plastic masks were produced to be movable. They were mounted on the aluminum cover in a way that allowed a fine adjustment of the horizontal position of 2 cm. In Fig. 4.4a, a photo of these masks with six sensors mounted is shown. Figure 4.4b shows the simulated ring image for this arrangement of the sensors together with a drawing of the parts of the masks. Five individual detector aluminum covers were produced for different beam angle ranges.

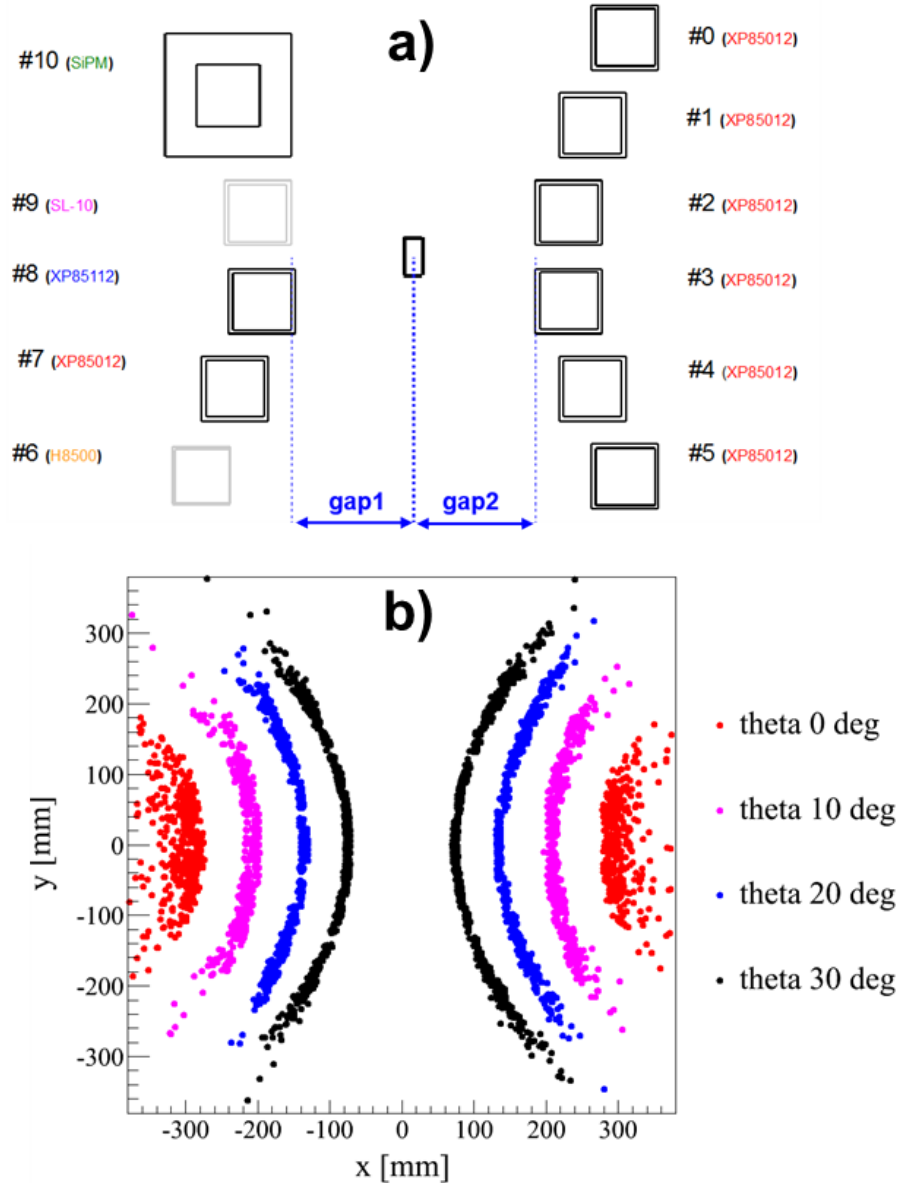


Figure 4.3: Back view of the imaging plane showing: the MCP-PMT arrangement (a) and the predicted locations of the rings for various beam angles (b).

Thirteen sensors were tested: ten MCP-PMTs (seven XP85012, and one XP85112 from PHOTONIS, as well as two SL-10 models from Hamamatsu, one R10754X-L4 and one R10754X-M16), and a SiPM array (Multi Pixel Photon Counter S10931-100P made by Hamamatsu). The list of sensors is shown in Fig. 4.1. For each tube the high voltage was set according to the vendors specifications to reach a gain of  $10^6$ . After every change of the configuration of the prototype, the timing resolution of the detectors was calibrated with a 405 nm PiLas laser diode [62]. An optical fiber, connected the PiLas pulser to a diffuser placed in a special access port below the bar at the entrance window, visible in Fig. 4.2a).

The data acquisition for the 640 channels was performed using the HADES trigger and

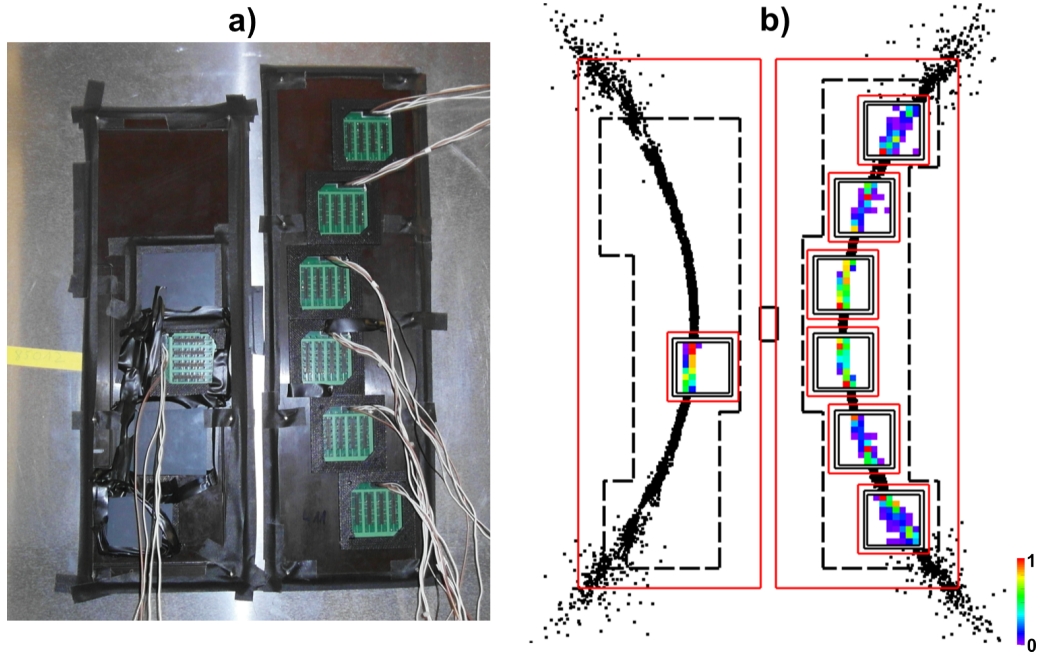


Figure 4.4: a) Photo of the support structure with seven MCP-PMTs mounted. b) Drawing of the backplane of the expansion volume with the simulated Cherenkov ring occupancy. Red squares indicate the cutouts in the aluminum cover and the dashed lines to the movable plastic masks holding the sensors.

Type	Anodes	Size (external)	Pixel Pitch
PHOTONIS 85012/85112	8x8	$59 \times 59 \text{ mm}^2$	6.5 mm
PHOTONIS 85011	8x8	$71 \times 71 \text{ mm}^2$	6.5 mm
Hamamatsu H8500	8x8	$52 \times 52 \text{ mm}^2$	6.08 mm
Hamamatsu H9500	16x16	$52 \times 52 \text{ mm}^2$	3.04 mm
Hamamatsu R10754X-M16	4x4	$27.5 \times 27.5 \text{ mm}^2$	5.275 mm
Hamamatsu R10754X-L4	1x4	$27.5 \times 27.5 \text{ mm}^2$	5.275 mm
SiPM array	8x8	$112 \times 112 \text{ mm}^2$	7 mm

Table 4.1: List of the sensors used in Prototype 2011.

readout board (TRB) with the TOF addOn. The boards were arranged in two stacks, the first holding 3 TRBs for slow control and communication and the second with 5 TRBs with TOF addOns for the readout of the prototype MCP-PMTs.

### The Readout Electronics

A very promising candidate for the readout electronics in the Barrel DIRC is the Trigger and Readout Board (TRB) system developed for the HADES experiment and adjusted to the needs of the PANDA detectors. Details about it can be found in Ref. [63], a brief description will be given here. It is a multi-purpose readout module capable of being used by many types of detectors. Three generations of this board were build so far and the second generation, TRBv2, was used for this test beam campaign.

The TRBv2 (see Fig. 4.5a) uses an ETRAX FS processor with a Linux operation system for networking and slow-control functionality. Three integrated I/O processors allow effi-

cient usage of the bandwidth. Each board includes four 32-channel Time to Digital Converter (HPTDC [64]) with 98 ps binning, 100 Mbit/s Ethernet-Connectivity, an optical link with a throughput of 2 Gbit/s, and programmable logic. A Field-programmable gate array (FPGA) is connected to all main components of the module and is responsible for the data flow on the boards.

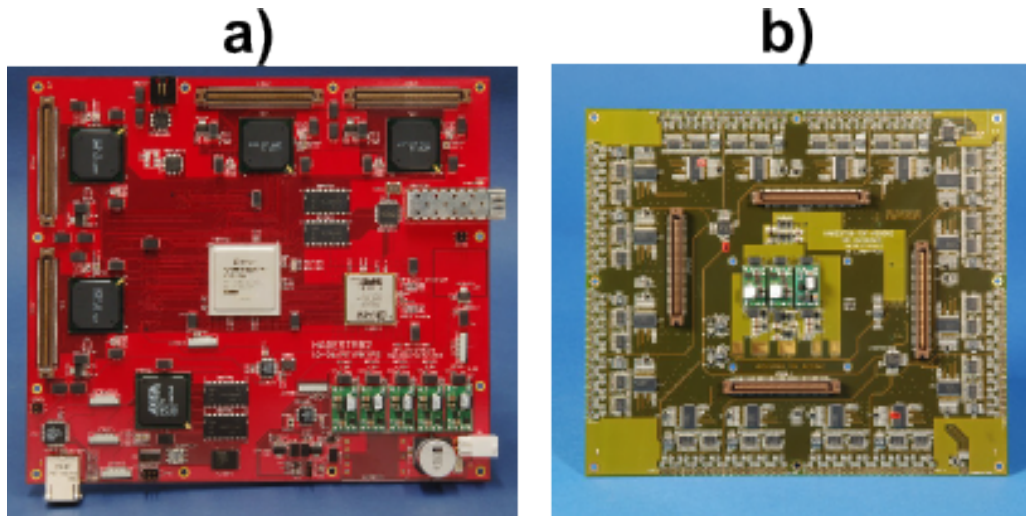


Figure 4.5: Examples of the readout boards used in the test beam campaigns: the TRBv2 board (a) and the TOF addOn (b).

The addOn board used for the prototype was a 128-channel Time of Flight (TOF) front-end discriminator module, used to convert pulse into the timing signal. The board is shown in Fig. 4.5b. It includes amplifiers and discriminators optimized for MCP-PMTs. The digitalization of the analog signal from sensors is done with the NINO-ASIC (Application Specific Integrated Circuit) [65]. The NINO is an discriminator chip that has been developed for the ALICE time-of-flight detector. The chip consists of eight channels. The pulse width is dependent on the input signal amplitude. It allows a time resolution of 50 ps, at a very high rate with a low power consumption per channel.

The BGA2712 [66] are the low noise amplifiers with gain factor of 10, developed in GSI and used to preamplify signals from the MCP-PMTs before being fed in to the read out boards. Amplified signals from pixels are transported to the TRB channels via the addOn board. The trigger is provided from an external source, distributed and controlled by the Central Trigger System (CTS). It is transferred to the Distributor board that sends it to the TRBs. The data are sent to the DAQ computer via Ethernet over a hub. The slow control board, connected to all other elements of the setup via optical links, is responsible for setting registers, threshold levels and all other parameters of the DAQ. The external trigger signal is needed in one of the channels per TRB to perform relative timing between different TRBs. The precision of the time measurement is good as long as channels within one TRB are compared. If several boards are connected, the common reference clock has to be used. The split signal from one of the triggers distributed over all used TRBs served as the common clock in the test beam.

#### 4.1.2 The T9 Beam Line area in the CERN PS and the Beam Instrumentation

The main tests of the last two prototypes, in 2011 and 2012, were performed in the T9 beam line in the CERN PS East area. Secondary beams in the momentum range from 1.5 to 10 GeV/c

can be used. Two exchangeable primary targets are available feeding the areas T9, T10, and T11, and a second one for the T7 area. Typical intensities are of the order of  $10^6$  particles with a spill length of 300 ms. The momentum, intensity, and focusing of the secondary lines can be changed by the users without entering the cave. The intensity of the beam is monitored with a scintillator and a wire chamber is used for monitoring the x/y profile at the exit of the beam pipe.

In T9 the smallest beam spot size is at the end of the beam pipe, closest to the focusing quadrupole. Most of the tests were performed with a momentum of 10 GeV/c. In this case the spot size is around 5-6 mm *rms*, and increases up to 10-12 mm *rms* at the end of the zone. For a parallel beam the spot size is 20 mm *rms*.

The exchangeable primary target selects the beam composition. The setups were tested with two kind of targets: one made of Beryllium provided an “electron-rich” beam, and one made of Aluminum that delivered the “hadron-rich” beam preferred for the DIRC system.

### 4.1.3 Data Set

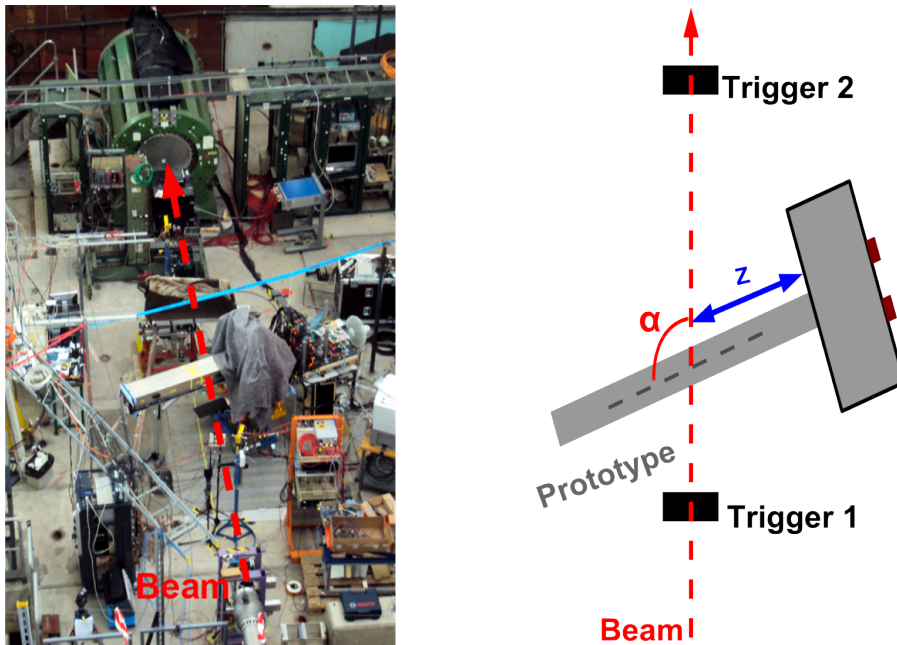


Figure 4.6: Photo showing the arrangement of the setup in the beam line at the CERN PS campaign in 2011.

The arrangement of the components that were put in the beam are shown in Fig. 4.6. The alignment of the beam instrumentation was done with a GLL2-80 Dual Plane Leveling and Alignment Laser made by Bosch [67], providing two planes (vertical and horizontal) with a self-leveling system. Two round scintillator paddles with a diameter of 40 mm were located in front and behind the prototype. The coincidences of their signals served as trigger for the DAQ to record an event.

A total of about  $130 \times 10^6$  triggers were recorded. The data were taken with different angles and sensors to study the narrow bar and oil tank type expansion volume geometry. Two runs were selected for the discussion of these configuration performance. These runs were taken with a 5.8 mm-thick standard spherical lens, made of fused silica, with a focal length of 250 mm, and air gap of 12 mm. Only MCP-PMTs sensors were used to measure the Cherenkov photons. The

performance of the other sensors due to the technical issues with the cooling and amplification was not of sufficient quality to compare to Planacon MCP-PMTs. Additional data were taken with different lens configurations and flat mirror but the prototype in 2012 provided much more comprehensive data set to answer questions about performance of these components and therefore they will be discussed in the further sections.

Most of the tests were performed with the 10 GeV/ $c$  momentum beam, focused at 7.5 m. The hadron-rich target was used and the beam polarity was positive. The results in the following section will be presented for that beam properties and two beam polar angles: 109.5° and 120°.

#### 4.1.4 Performance of the Prototype

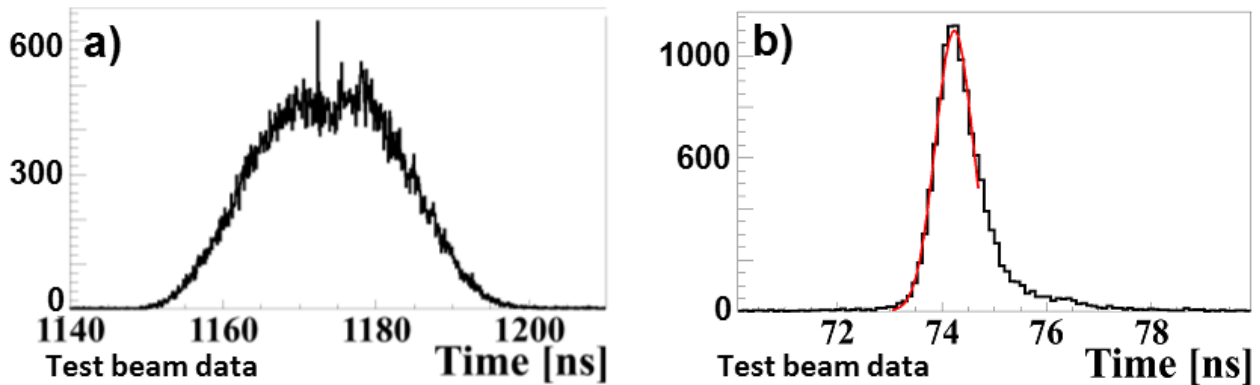


Figure 4.7: Hit time distribution for the raw signal (a) and corrected with the trigger time (b).

For more than  $2.5 \times 10^6$  events were recorded, preselected by the coincidence of the two start counters, with the polar angle of 109.5°. They generated  $79 \times 10^6$  hits, where a hit is defined as a valid time stamp in the event in any of the 640 electronics channels. 74% of them come from reference channels, the beam counters, and the electronic noise due to low discriminator threshold settings. The MCP-PMTs hits were selected based on the arrival time of the photons. The analysis procedure will be shown for 210,000 selected triggers. The raw hit time distribution is shown in Fig. 4.7a. The selection of good hits was based on distribution shown in Fig. 4.7b, which is the corrected hit time with the trigger counter used as reference.

To extract the photon yield, in each accepted event all hits within the time window of about 2 ns were counted, and plotted in the distribution shown in Fig. 4.8a. The photon yield of  $2.9 \pm 0.02$  is a mean value of the Poisson fit to the distribution. The error of 0.02 is just the statistical term while the overall error is dominated by the systematic terms and will be evaluated latter in this section. Figure. 4.8b shows the same quantity in simulation. There is a significant difference between these two numbers. To understand the value from the simulation the study of the number of photons per particle from the production to detection was performed. The propagation steps in simulation are listed in Tab. 4.2 showing what fraction of the generated photons is lost at each step. However, there are additional loss processes in the data responsible for further deterioration of the photon yield. The major loss was concluded to be due to the poor transmission of the optical grease Rhodorsil Paste 7 made by Silitech [68], used to couple the sensors to the glass window. The rather poor transparency of the grease is visible already in Fig. 4.9. An exact quantitative analysis was not possible due to the lack of a transmission data available for this particular grease. Instead, available data for Eljen EJ-550 [69] was used in simulation to study the impact of the optical grease. Although the

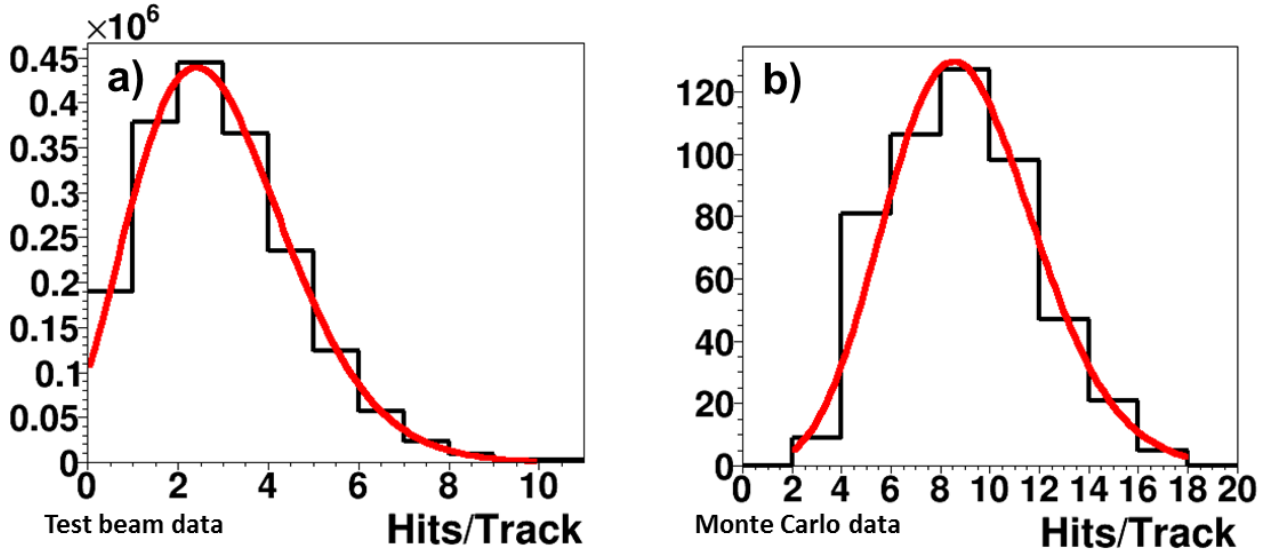


Figure 4.8: a) Number of good MCP-PMTs hits measured per trigger in 2011 CERN test beam with the beam angle to the radiator of  $109.5^\circ$ . b) Expected number of photons per particle for the Prototype 2011 without including the optical grease used to couple the sensors to the detector plane.

EJ-550 grease is optically superior the results from the simulations were reproduced with the grease layer of 3 mm. In this case the simulated photon yield decreases to below four photons per track, what is very close to the value obtained from the experiment. The experimental data is expected to contain contributions from charge sharing and delta electrons (explained in Sec. 4.2.4). However, there is not enough information to separate the individual sources and subtract their contribution in this data. More detail study of these effects was performed and is presented for the 2012 prototype.

	Generated	Internally reflected	Enter the tank	Reach detector plane	Reach sensors surface	Measured
[%]	100	59	25	20	9	0.9
Number of photons	800	472	200	160	73	7.9

Table 4.2: The expected number of photons per pion passing the 17 mm thick bar at the beam angle of  $109.6^\circ$ . A loss of the photons in the last step comes from the detector efficiency (PDE) which is the product of quantum, collection, and packing efficiencies.

In Fig. 4.10 the occupancy of the MCP-PMTs for the  $109.5^\circ$  configuration is shown. It consist of hits from 210,000 triggers. The white pixels correspond to dead electronic channels and the two white rows are missing pixels due to defective amplifiers. Non-zero counts away from the rings are the result of the noise and charge sharing effects.

The location of the observed ring segments is compared to a pixelated simulation of 210,000 pions entering the bar at an incidence angle of  $\alpha = 109.5^\circ$  shown in Fig. 4.11a. The simulation data is used in the  $\Theta_C$  reconstruction and that is why it needs to describe the data very well. The simulation using the setup parameters measured during the beam time does not match the data well enough. In order to find a better match a tuning procedure is performed. There is few possible causes of the discrepancies that needs to be investigated. In the experiment it



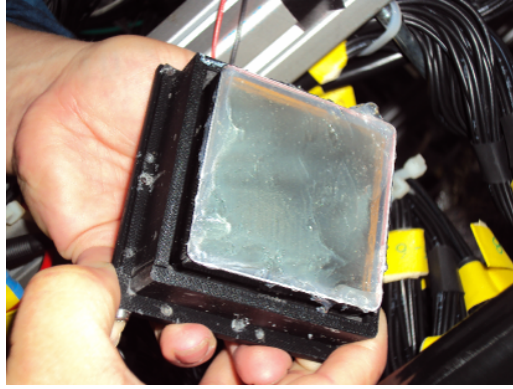


Figure 4.9: Photo of the MCP-PMT with grease applied before coupling it to backplane window of the tank.

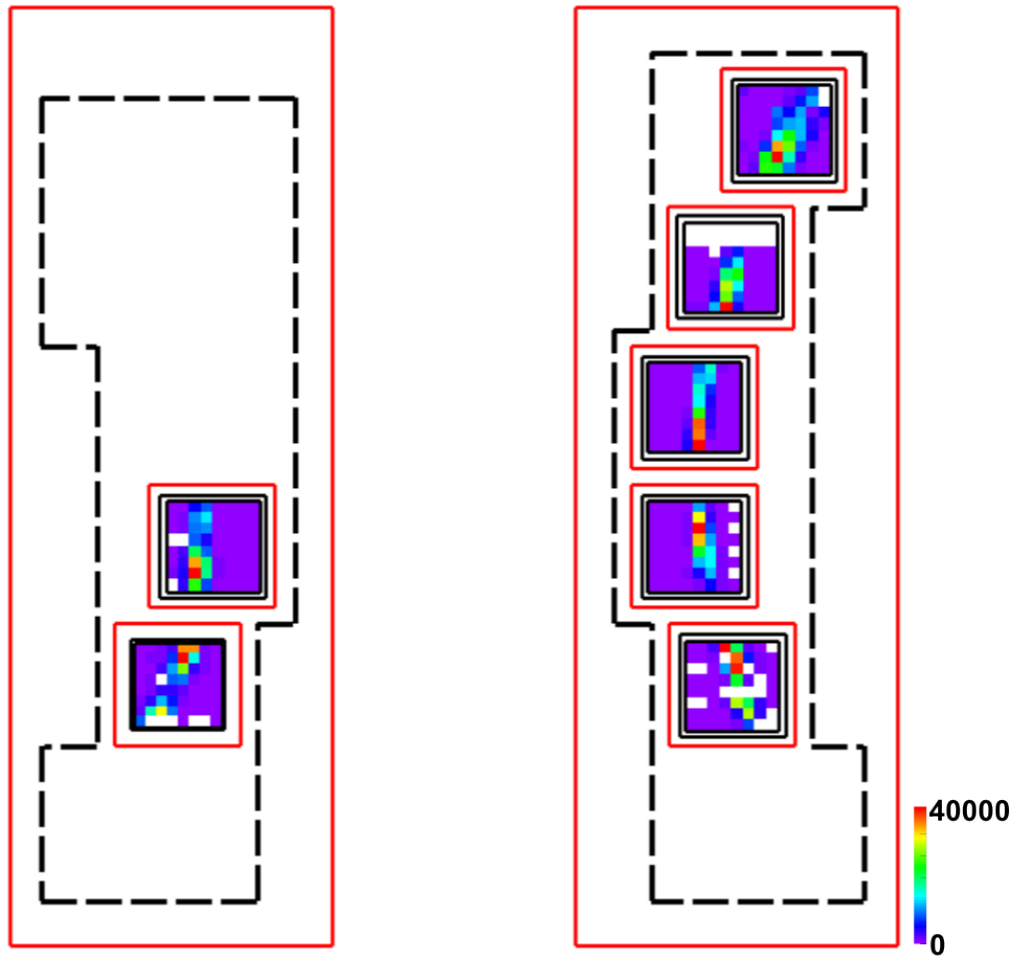


Figure 4.10: Distribution of the hits per MCP-PMT in the experimental data measured in the  $109.5^\circ$  configuration.

was very hard to measure the exact horizontal position of the MCP-PMTs and the supporting frames. The measured polar angle between the beam and the bar had rather large uncertainty of typically  $1^\circ$ . Small ranges of the suspected parameters, within the uncertainties of the measurements during the beam time, are used to find the set of parameters in simulation that best describes the experimental data. A lot of simulated runs are created with all the combinations of these parameters. Assessing of the match is performed in three ways. The first step of the evaluation is a visual comparison of the occupancies from the data and simulation.

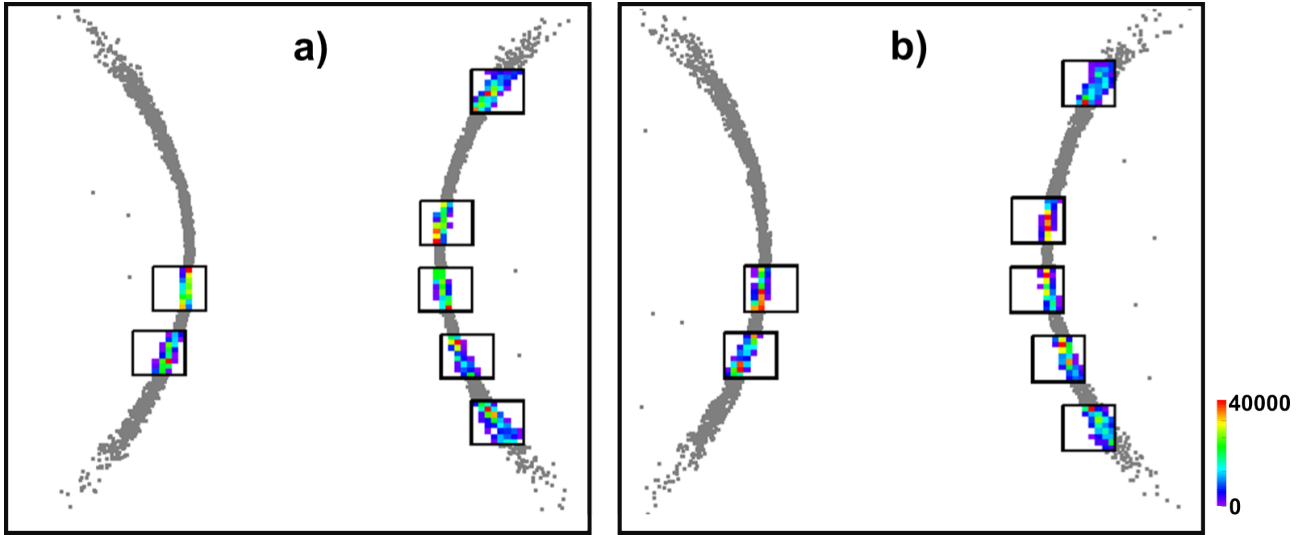


Figure 4.11: Pixelated hit pattern from simulated data for two values of the beam polar angle:  $109.5^\circ$ , as measured during the experiment, (a) and  $108.5^\circ$  (b).

An example of a simulated run with the polar angle of  $108.5^\circ$ , so  $1^\circ$  less than measured, is shown in Fig. 4.11b. A more detailed tuning is possible by comparing centers of gravity of the hit rates in MCP-PMT rows. Even in the presence of additional background in the data the mean values allow a meaningful comparison and tune of the parameters. The final assessment of the match is done by looking at the reconstructed Cherenkov angle. For each combination of the investigated parameters the reconstruction is performed and plotted for every row of each MCP-PMT. The outcome of this step for matched simulation is shown in Fig. 4.12. The expected  $\Theta_C^m = 821.9 \pm 0.01$  mrad is determined for the best match in simulation. After the tuning procedure the mean  $\Theta_C^m$  value in each row is close to the expected  $\Theta_C^m$  for the particle. From this distribution one can immediately recognize if there is still a problem with the beam angle ( $\Theta_C^m$  for both entire rings are shifted), the bar is not perpendicular to the expansion volume ( $\Theta_C^m$  for one entire ring is shifted), or the position of some of the MCP-PMTs is incorrect ( $\Theta_C^m$  for ring segments from these MCP-PMTs are shifted).

In the tuning process, several small shifts in the MCP-PMT positions and the polar angle of the beam were discovered. The position of the rings for the experimental data and the matched Monte Carlo data are shown in Fig. 4.13. They are in good agreement, what is crucial for the reconstruction of the Cherenkov angle using the geometric approach described in 3.4.

Look-up tables were generated for the configuration from the matched simulation. The distributions of reconstructed test beam and simulated data are shown in Fig. 4.14 and the corresponding values are listed in the first line of the Tab. 4.3.

The bin size as well as the fit range and choice of fit function have no significant influence on the results. The size of the MCP-PMT pixel is 6.5 mm, which corresponds to about 19 mrad in  $\Theta_C$  space. A few bin sizes around 4 mrad were chosen to study the effect on the final results and the error was concluded to be on the level of 0.3 mrad. The size of the chosen time window to select the hits in the event adds 0.1 mrad to systematic error. Different runs with similar configuration showed a good control of the parameters and the ability to reproduce the setup with 0.2 mrad accuracy. The statistic error is negligible in comparison to the systematic error. The individual error sources are considered to be independent and can be added in a quadrature to determine the overall error 0.3 on the photon yield and 0.4 mrad on the  $\Theta_C^m$  and the SPR.

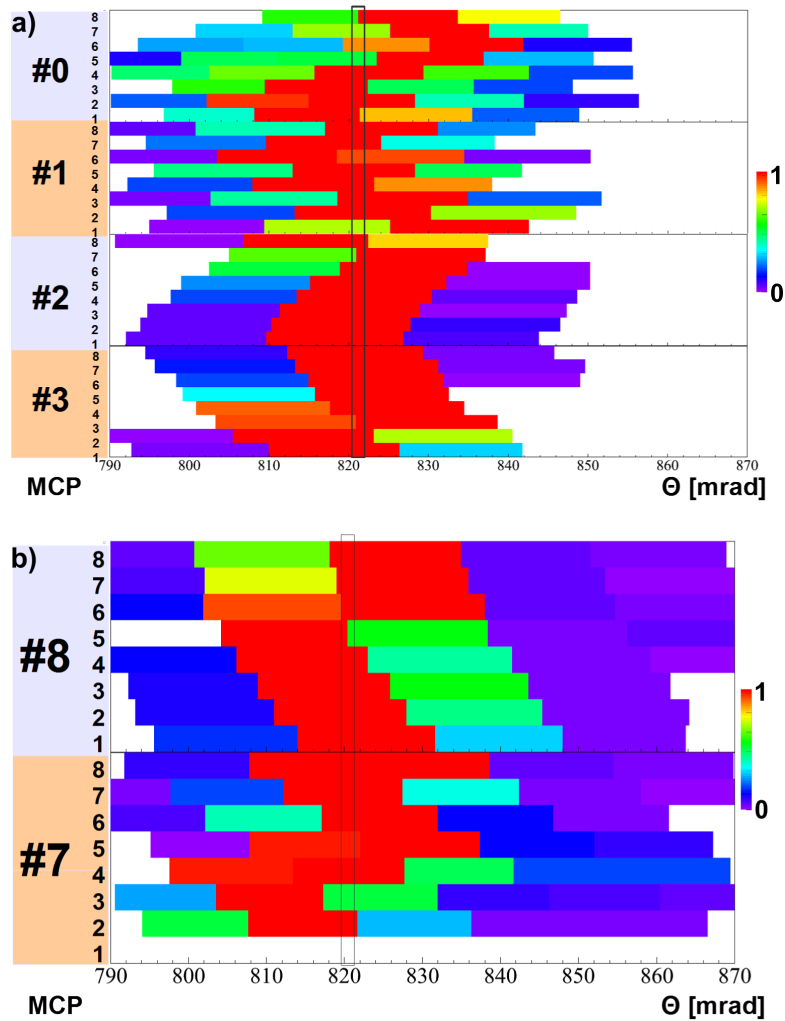


Figure 4.12: Distribution of reconstructed single photon Cherenkov angle for experimental data. The angle is plotted and normalized per each row to show the potential shift of the  $\Theta_C$  mean value indicating some mismatch in measured dimensions of the setup.

The measurements obtained for the run with  $109.5^\circ$  polar angle were compared to a run with  $120^\circ$  polar angle to verify the stability of the results. The simulation had to be tuned to this data in a similar way as to the previous run. The matched simulation has the beam polar angle of  $120.2^\circ$ . The composite view of ring locations from both runs are shown in Fig. 4.15b. (a) shows the difference in polar angle on the drawing of the setup and (b) shows the occupancy distributions. The reconstructed Cherenkov angle and the photon yield are shown in Fig. 4.16. In this configuration only 2.5 photons per trigger were measured, due to the smaller number of used MCP-PMTs. The reconstructed values for this configuration are slightly worse from obtained for the  $109.5^\circ$  case but still they are consistent with each other and the expected values from simulation.

The discussed results confirmed that the combination of a narrow bar, a standard lens, and a big oil tank expansion volume is a promising baseline design of the PANDA Barrel DIRC. The single photon Cherenkov angle resolution predicted by Monte Carlo simulation was reached and is sufficient to meet the PANDA PID requirements.

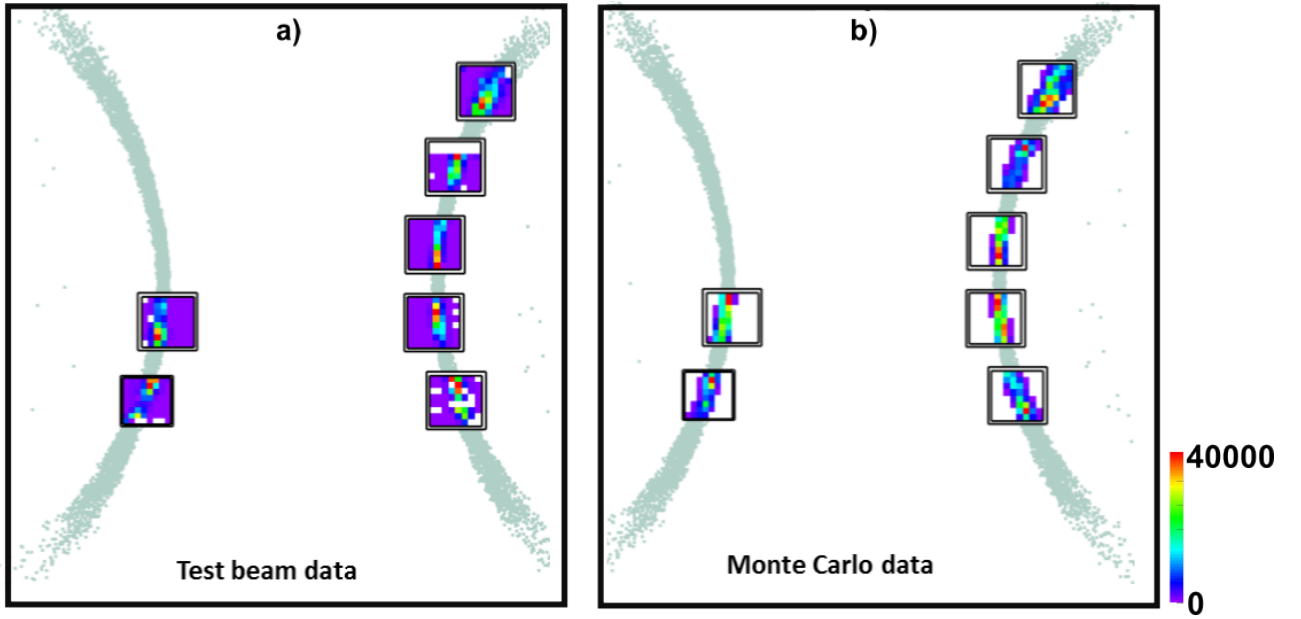


Figure 4.13: Distribution of the hits per MCP-PMT in the experimental 2011 prototype data for  $109.5^\circ$  (a) and for the matched simulated data. The true hit locations of photons between the MCP-PMTs are shown as points.

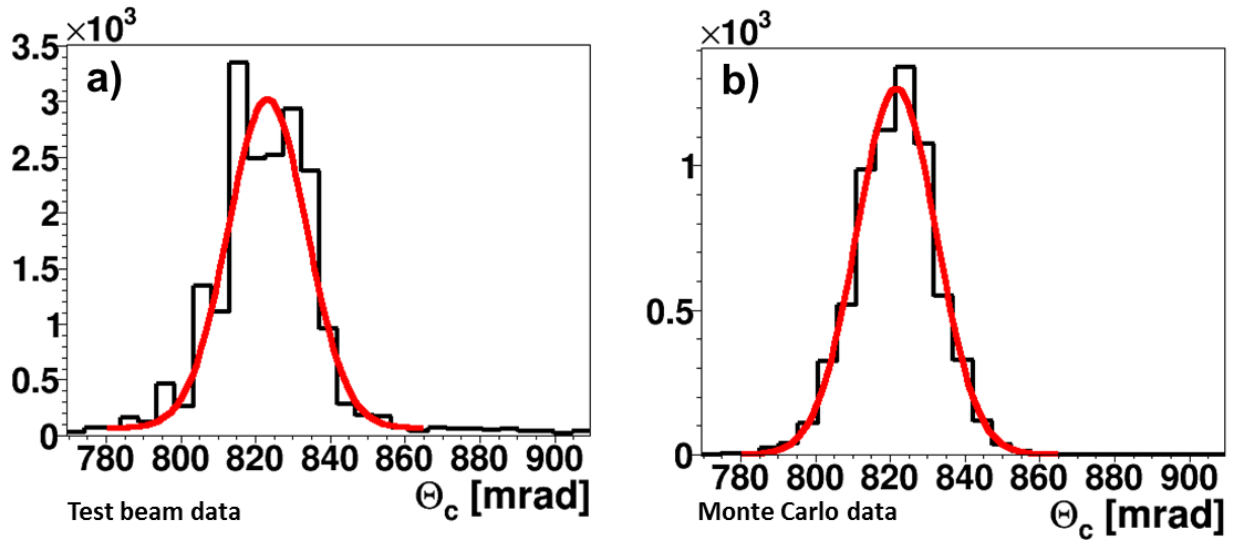


Figure 4.14: Reconstructed Cherenkov angle per photon from 2011 prototype data. a) Result from the experiment b) Prediction from Monte Carlo data.

Polar angle	Experimental Data			Simulated Data		
	$\Theta_C^m$ [mrad]	$\sigma_{\Theta_C}$ [mrad]	Hits/Track	$\Theta_C^m$ [mrad]	$\sigma_{\Theta_C}$ [mrad]	Hits/Track
$109.5^\circ$	$821.9 \pm 0.4$	$10.5 \pm 0.4$	$2.9 \pm 0.3$	$821.7 \pm 0.2$	$10.6 \pm 0.2$	$7.9 \pm 0.1$
$120.0^\circ$	$822.7 \pm 0.4$	$11.7 \pm 0.4$	$2.5 \pm 0.3$	$821.9 \pm 0.2$	$10.7 \pm 0.2$	$6.9 \pm 0.1$

Table 4.3: Results of the  $\Theta_C$  reconstruction from the 2011 prototype test beam data compared to expectation from simulation.

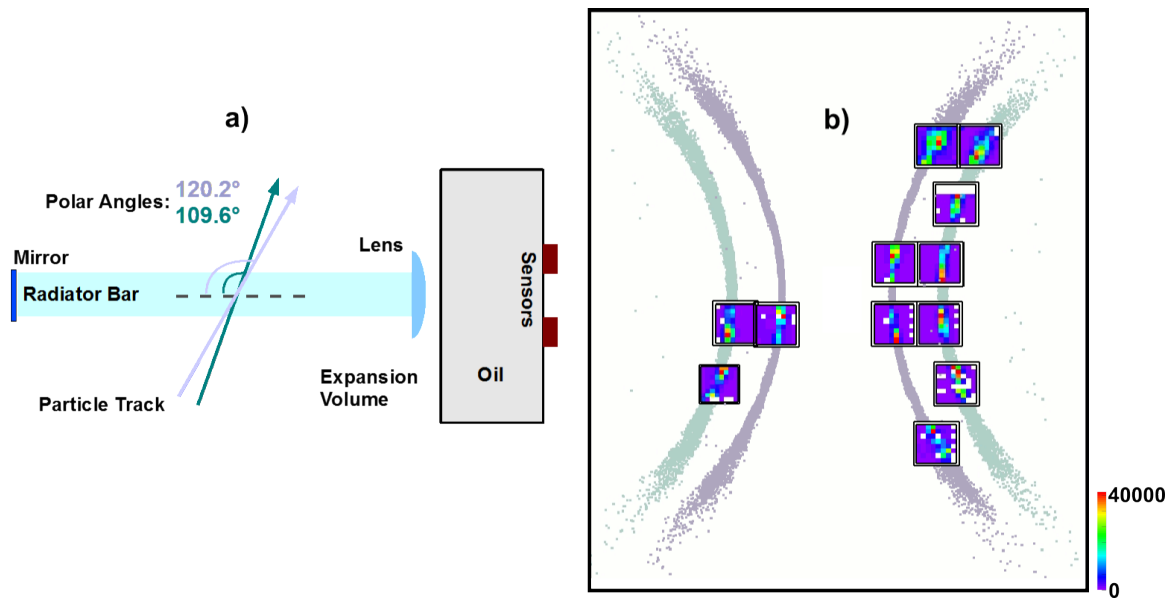


Figure 4.15: a) Drawing of the setup with two different polar angles of the track. b) Composite view of the different ring location corresponding to beam angles from drawing a).

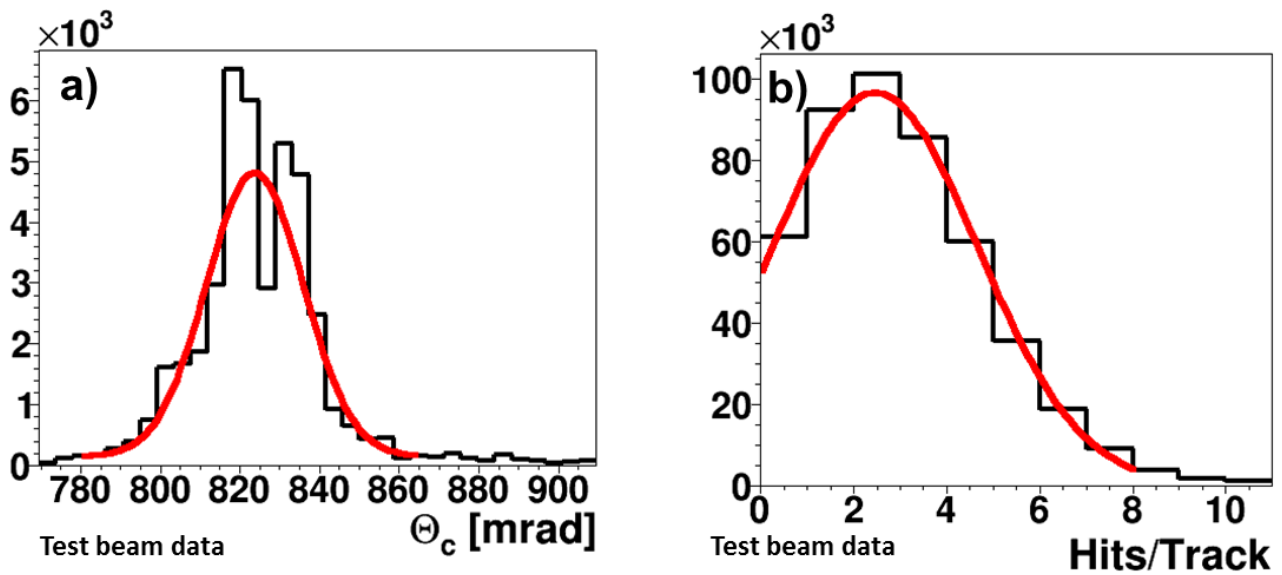


Figure 4.16: a) Reconstructed Cherenkov angle per photon from 2011 prototype data and b) number of hits measured per trigger for the run with  $122^\circ$  polar angle.

## 4.2 Prototype 2012

With the experience of the 2011 test beam and analysis of the collected data, the new prototype was built and tested in the late summer of 2012. This configuration used a compact prism made of synthetic fused silica as an expansion volume. It were the first tests with the wide plate instead of a narrow bar as a radiator with a lens without an air gap.

### 4.2.1 Preparation and Description of the Setup

The test beam campaign in 2012, like in 2011, took place in the T9 Beam Line area at the CERN PS. The beam properties were already described in 4.1.2. The arrangement of the complete prototype is shown in Fig. 4.17 and the distances of the elements are listed in Tab. 4.4. All components were aligned with the same GLL2-80 alignment laser as classified in Sec. 4.1.

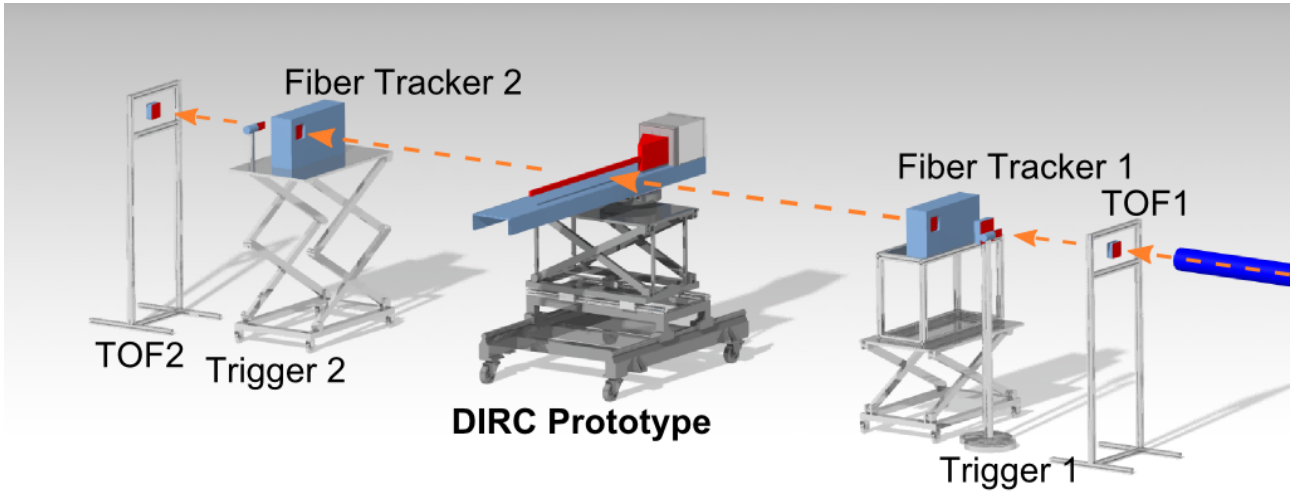


Figure 4.17: Arrangement of the prototype elements used in the 2012 test beam at CERN.

The trigger was provided by two round scintillator paddles, with a diameter of 40 mm, located before and after the prototype. In addition, the coincidence signal of the two scintillators was distributed over the TRB boards, to provide time corrections in the analysis.

TOF1	Trigger1	Fiber Tracker1	DIRC Prototype	Fiber Tracker2	Trigger2	TOF2
50	142.3	193.1	468	694.3	725.3	808

Table 4.4: The distances in cm from the end of the beam pipe to the front surface of the elements from 2012 test beam shown in Fig. 4.17.

Two time-of-flight (TOF) detectors were installed at the beginning and the end of the beamline (see Fig. 4.18) and provided pion/proton tagging. Both TOF counters consisted of Acrylic glass radiators (Polymethylmethacrylat) connected with Bicorn BC-630 optical grease to PHOTONIS Planacon XP85012-D. The size of the radiators matches the size of the MCP-PMT ( $59 \times 59 \text{ cm}^2$ ). In order to minimize the material budget before the prototype the first TOF counter used a 1 cm thick scintillator. The second one used a 2 cm thick scintillator.

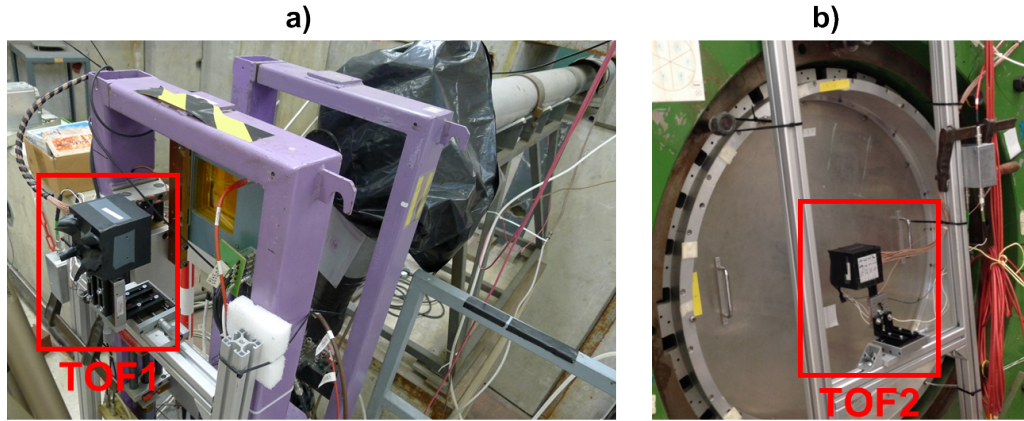


Figure 4.18: Views of the TOF system components: a) TOF1 and b) TOF2.

Signals from the MCP-PMTs were combined such that an  $4 \times 4$  array of  $12.75 \times 12.75 \text{ mm}^2$  pixels was created. More details can be found in Ref. [33].

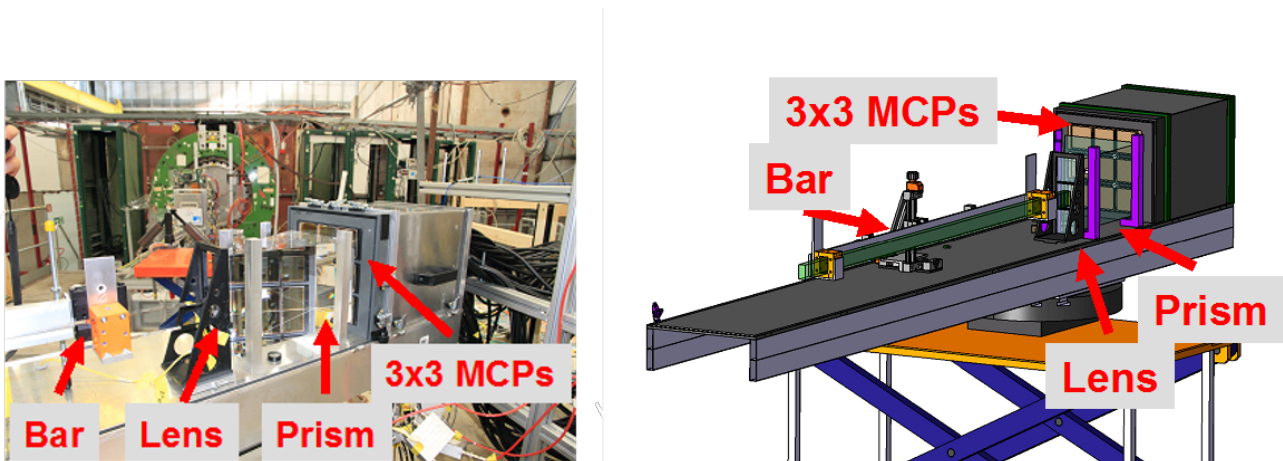


Figure 4.19: Photograph and schematic of the 2012 prototype.

In Fig. 4.19 the photograph and the schematic of the Prototype 2012 are shown. The prototype was mounted on a support structure that included rails and a rotating table to translate and rotate the bar relative to the beam. A radiator bar (later a plate) was placed on a linear stage with three micrometer screws for the precise position adjustment in all three directions. A lens was attached to one end and a mirror to the other end of the bar. A compact synthetic fused silica prism was located about 2 mm from the lens. Nine MCP-PMTs were coupled with optical grease to the back surface of the prism (see Fig. 4.20) to measure the Cherenkov photon location and time with 576 pixels. The grease used, Eljen EJ-550 [69], has better transmission properties and was applied in a much thinner layer than the Rhodorsil material that caused the large photon loss in the 2011 prototype. The aluminum sheets with feed-throughs for the high-voltage and readout cables provided a light-tight cover (see Fig. 4.20). The data acquisition for 896 detector channels was performed using the HADES trigger and readout boards with the TOF AddOns [63]. The readout system was kept on a separate table shown in Fig. 4.20e.

The prism was made by Advanced Glass Industries [70] from Corning 7980 material [52], with a size of  $300 \times 203.21 \times 170 \text{ mm}^3$ , and a top angle of  $30^\circ$ . In contrast to the big oil tank from

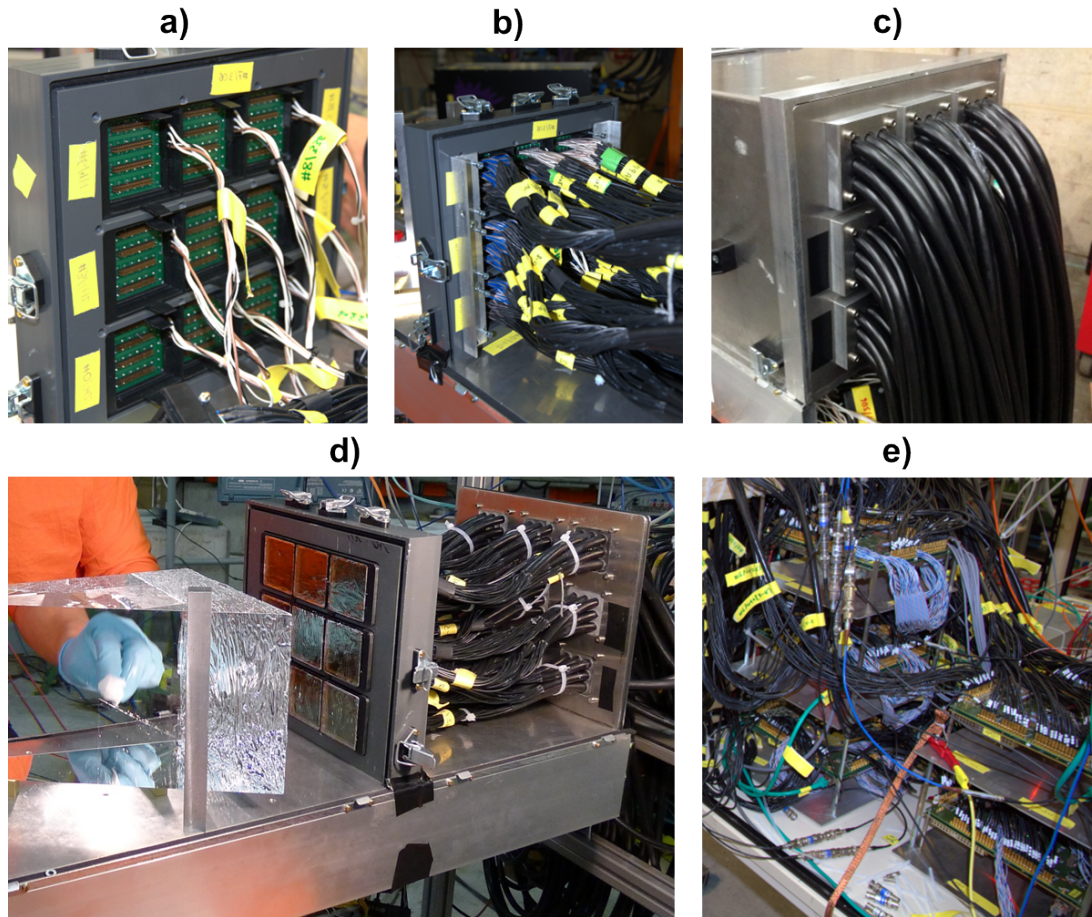


Figure 4.20: Views of the Prototype 2012: a) The back of the MCP-PMT array. b) Signal cables connected to the MCP-PMTs, c) signal cables lead out from the container through the light-tight, silicone tunnels, d) the coupling of the prism to the MCP-PMT array, and e) the readout electronics table.

the previous prototype the smaller prism made it possible to cover the entire detector plane with a much smaller number of sensors. An array of 3 x 3 PHOTONIS Planacon XP85012/A1 MCP-PMTs was supported in a matrix made of ABS plastic. The optimum placement of the photon detectors was studied with the DrcProp simulation to efficiently image the rings. The final location of the MCP-PMTs is shown in Fig. 4.21. The MCP-PMT holders created 9 mm horizontal and 2 mm vertical gaps between the sensors. Thinner gaps were used in the vertical direction because the better coverage of the detector plane in this direction is more important for the detector performance analysis. Top of the prism was left uncovered because of the limited number of available MCP-PMTs. This affects particular beam angles close to  $90^\circ$ . Without the gaps between the MCP-PMTs the coverage of the imaging plane is 80% just from ratio of the active area to the total sensor area. In the 2012 prototype the coverage of the detector plane is limited to 64.5% due to the limited number of of the MCP-PMTs and gaps required for the sensor holders.

The placement of the bar relative to the prism has a strong impact on the position of the ring patterns and the proximity of the individual ring segments. Examples of the different placements of the bar at the prism in x, y and its influence on the hit pattern are shown in Fig. 4.22 and 4.23. The study was performed to find the placement with the best separation between the two ring segments, which is important for the reconstruction process of the Cherenkov angle. The vertical distance of the bar bottom face from the bottom of the prism is called PrismStep.





Figure 4.21: Schematic (a) and photo (b) of the MCP-PMTs arrangement on the detector plane.

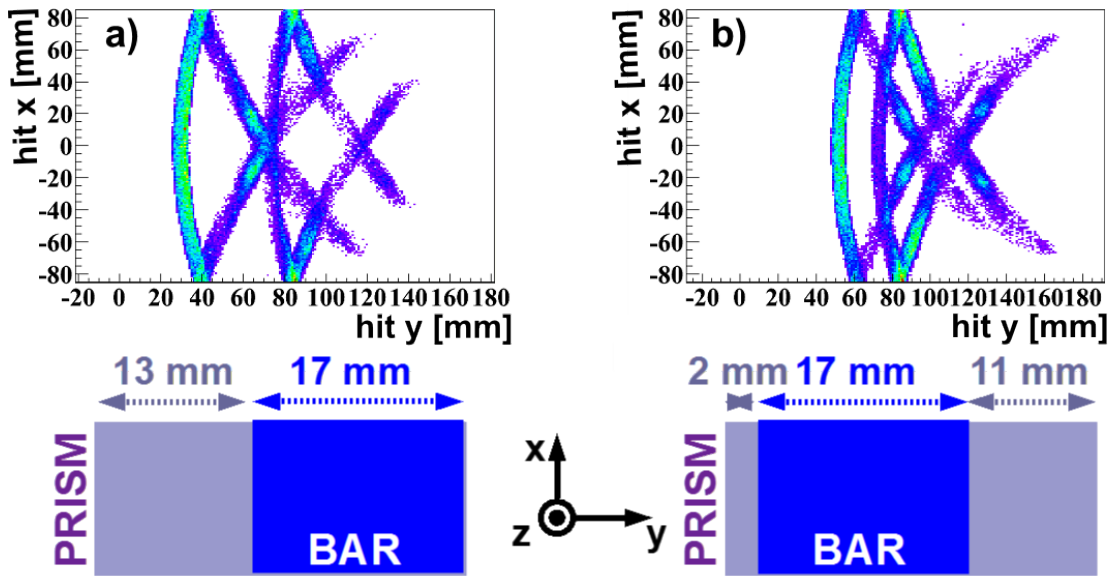


Figure 4.22: Influence of the bar position in “y” relative to the prism on the observed hit pattern, in particular on the separation of the ring images.

The size of this PrismStep defines the separation of the rings. The horizontal placement of the bar in X influences the side reflections in the prism and, therefore, the intersection point of the outer parts of the imaged half-rings in the detector plane. A few examples of the simulated ring image on the MCP-PMT array are shown in Fig. 4.24. There is not one PrismStep/ $\Delta Y$  value that works for all prototype 2012 configurations, that it had to be adjusted based on the angle and the focusing optics. In Fig. 4.24d an example of an unfocused ring image is shown. The image is less sharp and ring segments are significantly wider. In Fig. 4.25 the ring image for 3 GeV/c mix of pions and protons is shown. The studies with the low momentum beam were the most challenging in terms of finding the optimal parameters of the prototype to ensure the

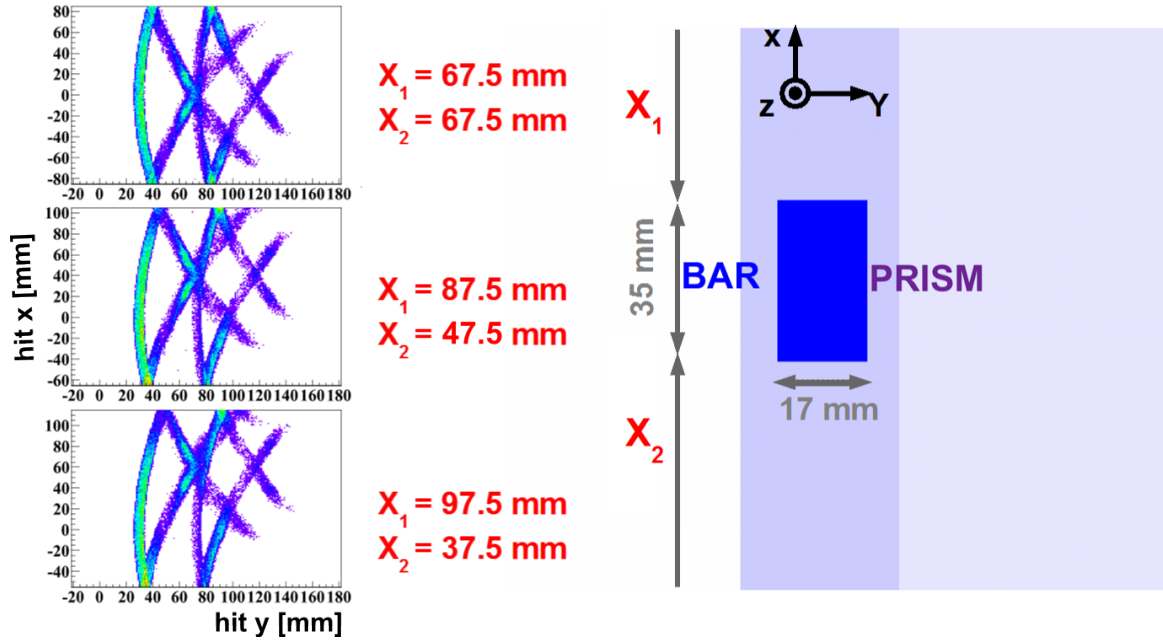


Figure 4.23: Influence of the bar position in "x" relative to the prism on the observed hit pattern.

best separation and location of the individual ring segments.

The list of the tested prototype radiators, with informations about the sizes, materials, and producers is shown in Tab. 4.5. Photos of the bars, a prism and the lenses that were used are shown in Fig. 4.26. The list of the used lenses is found in Tab. 4.6.

Bar	Manufacturer	Material Type	Finishing	Size (T,W,L) [mm]
B3	InSync	Spectrosil 2000	pitch polishing	(17.1, 35.9, 1200.0)
Z5	Zeiss	Spectrosil 2000	pitch polishing	(17.1, 32.9, 833.0)
L3	Schott/Lithotec	Lithotec Q0	abrasive polishing	(17.0, 35.0, 800.0)
BP1	InSync	Spectrosil 2000	pitch polishing	(17.1, 174.8, 1224.9)
LZ1	Lytkarino LZOS	Spectrosil 2000	abrasive polishing	(16.7, 34.8, 899.5)
P2	Roehm	Plexiglass XT	extrusion, diamond needle	(21.15, 39.7, 1200.0)

Table 4.5: List of the tested radiators in Prototype 2012.

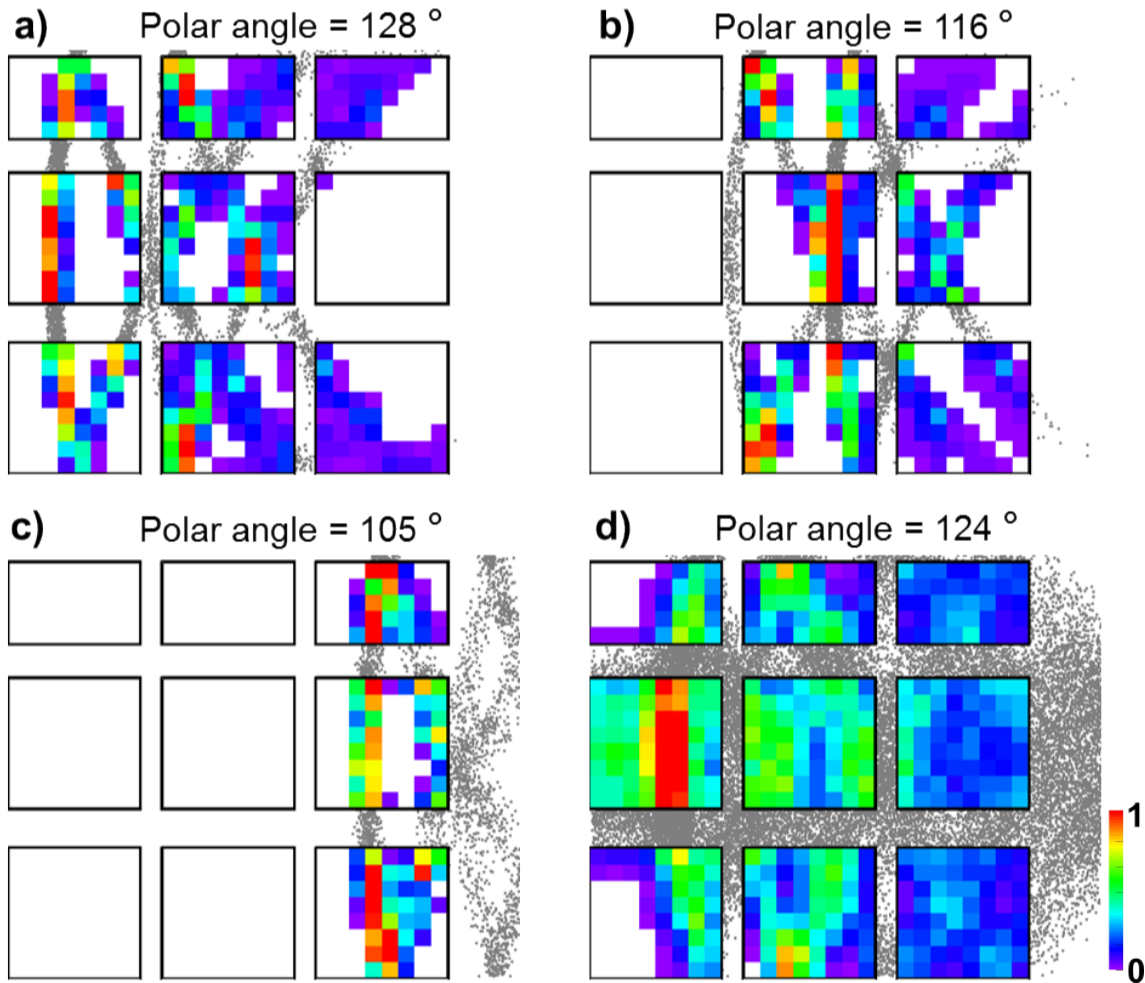


Figure 4.24: Pixelated hit patterns from simulated data for example prototype configurations with lens (a,b, and c) and without focusing (d). Gray points are the true hit locations.

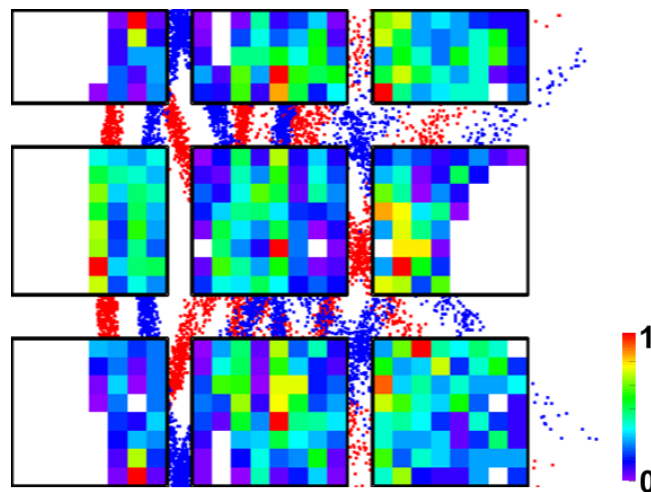


Figure 4.25: Simulated ring image for pions (red) and protons (blue) entering the bar at 124° with 3 GeV/c momentum.

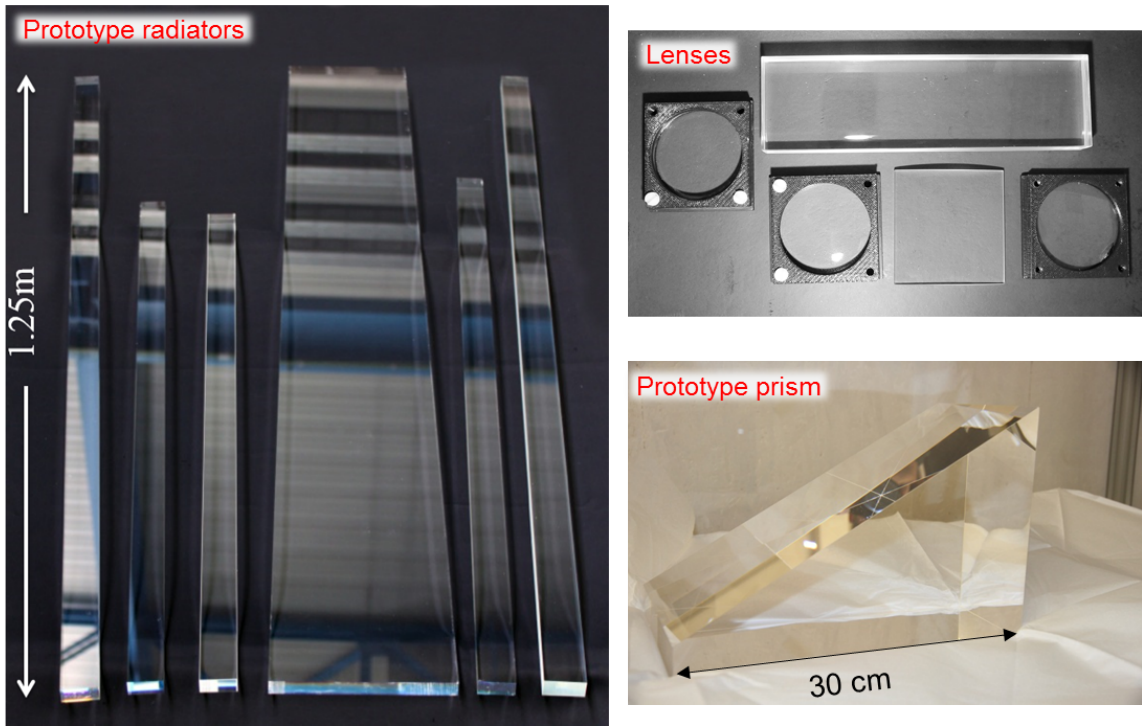


Figure 4.26: Photograph of the prototype optical elements tested in the 2012 campaign: a) radiators, b) lenses, and c) prism expansion volume.

Lens	FL	Material	Coating	Type	Size (CT,H,R)	Vendor
L1	250	Fused Silica	UV AR	spherical	(9, 50, 117.4)	Newport
L2	300	N-LaK33 fused silica	AR 330–460 nm	compound, cylindrical	(14.3, 175, 73.5)	Hellma Optik
L3	250	Fused Silica	$MgF_2$ SLMF (400–700 nm)	spherical	(9, 50, 117.4)	Melles Griot
L4	250	BK7 Glass	AR 350–400 nm	cylindrical	(7.5, 60, 129.2)	THORLABS
L5	250	Fused Silica	uncoated	spherical	(5.8, 50, 115.0)	Newport

Table 4.6: List of the lenses tested in Prototype 2012. The used shortcuts stand for: focal length (FL), central thickness (CT), height (H), and radius (R). Focal length and size of the lenses are given in mm.

### 4.2.2 Data Set

During the four weeks at CERN 230M triggers were recorded in total. Each configuration was measured typically with 1-1.5M triggers. A wide range of beam - radiator bar angles and positions was tested with different components. In particular, different prototype radiators, lenses, and coupling materials were compared. Data were also taken with the low momentum beam down to 1.5 GeV/ $c$ . At this level the TOF system is capable of separating different particles.

More than  $34 \times 10^6$  triggers were taken with the wide plate geometry but the analysis of this part of the data is the subject of another thesis [37]. The remaining time was used for the narrow bars, presented in the following analysis. Table 4.7 summarizes the details of the runs used in this analysis, including the optical components, beam parameters, and number of recorded events as well as the parameters used in the simulation. In most cases there was no need to use all recorded events. The study is always limited by systematic effects and not by statistics, which, after around 100,000 triggers, does not significantly impact the results. For reasons of computing speed, if not mentioned differently, 210,000 triggers were selected. The general performance of the prototype will be discussed using the configuration with the B3 bar made by InSync, and a regular spherical lens with UV anti-reflective coating. Although the following analysis uses only small subset of the data taken, the procedure is representative for the entire data set. For each study a set of runs with very similar configurations and recorded in similar conditions were selected to easily compare the performance in terms of photon yield and SPR.

Run	Bar	Lens	bar/beam polar angle	$p_{Beam}$ [GeV/ $c$ ]	$f_B$ [m]	Events	HitZ [mm]	Air gap [mm]	Step [mm]
<b>R1</b>	B3	L1	124° (122.4°)	10	5	680k	806	3.2	13 (11.2)
<b>R2</b>	B3	L1	124° (122.4°)	10	5	680k	412	3.2	13 (11.2)
<b>R3</b>	B3	L1	124° (121.4°)	10	5	880k	331	3.2	12 (11.2)
<b>R4</b>	B3	L1	124° (122.4°)	10	5	708k	1102	3.2	12 (11.2)
<b>R5</b>	B3	L1	122–124° (123 – 125°)	10	5	880k	332	3.2	12 (11.2)
<b>R6</b>	B3	L1	154–156° (152 – 154°)	10	5	880k	775	3.2	12 (11.2)
<b>R7</b>	Z5	L1	122–124° (121.5 – 123.5°)	10	10	880k	433	3.2	12 (11.2)
<b>R8</b>	Z5	L1	123.5° (122.5°)	10	10	880k	431	3.2	12 (11.2)
<b>R9</b>	Lz1	L1	123.5° (123.2°)	10	10	500k	421	3.2	12 (11.2)
<b>R10</b>	P2	L1	123° (123.4°)	10	10	520k	432	3.2	12 (8.8)
<b>R11</b>	L3	L1	123.5° (123.3°)	10	10	260k	420	3.2	12 (11.2)

<b>R12</b>	B3	L1	90° (91.2° )	10	10	320k	436	3.2	12 (2.0 )
<b>R13</b>	B3	L1	90° (93.1° )	10	10	340k	729	3.2	12 (2.0 )
<b>R14</b>	B3	L1	128° (128.0° )	10	5	850k	328	3.2	12 (2.0 )
<b>R15</b>	B3	L2	128° (127.5° )	10	5	1M	248	0	12 (3.5 )
<b>R16</b>	B3	L2	90° (92.0° )	10	5	870k	138	2.2	12 (11.2 )
<b>R17</b>	B3	L3	124° (121.4° )	10	5	880k	331	3.2	12 (11.2 )
<b>R18</b>	B3	No	124° (121.4° )	10	5	140k	526	0	12 (11.2 )
<b>R19</b>	B3	L1	124° (122.4° )	3	5	130k	497	3.2	12 (11.2 )
<b>R20</b>	B3	L1	66° (67.6° )	10	10	600k	116	3.2	12 (12.6 )
<b>R21</b>	B3	L1	66° (67.6° )	10	10	770k	496	3.2	12 (12.6 )
<b>R22</b>	B3	No	90° (93.1° )	10	5	600k	150	3.2	12 (11.2 )
<b>R23</b>	B3	L1	154° (153.2° )	10	5	840k	784	2.2	12 (11.2 )
<b>R24</b>	B3	L3	154° (153.2° )	10	5	780k	701	2.3	12 (11.0 )
<b>R25</b>	B3	L4	154° (153.2° )	10	5	850k	702	2.7	12 (11.2 )
<b>R26</b>	B3	L5	154° (153.2° )	10	5	790k	704	2.5	12 (11.8 )

Table 4.7: List of analyzed runs from the test beam campaign in 2012. The values used in the tuned simulation are given in parentheses. The schematic of the prototype is shown in Fig. 4.27. The description of the components can be found in Tab. 4.5 and Tab. 4.6.

### 4.2.3 Expected Performance of the Prototype

#### Single Photon Cherenkov Angle

One of the main quantities to evaluate the performance of the setup configuration are the single photon Cherenkov angle resolution (SPR). A simulation of 210,000 pions with a momentum of 10 GeV/ $c$  and the prototype configuration from run R1 is used to discuss the reconstruction of the Cherenkov angle. The method is described in detail in section 3.4. Briefly, the positions

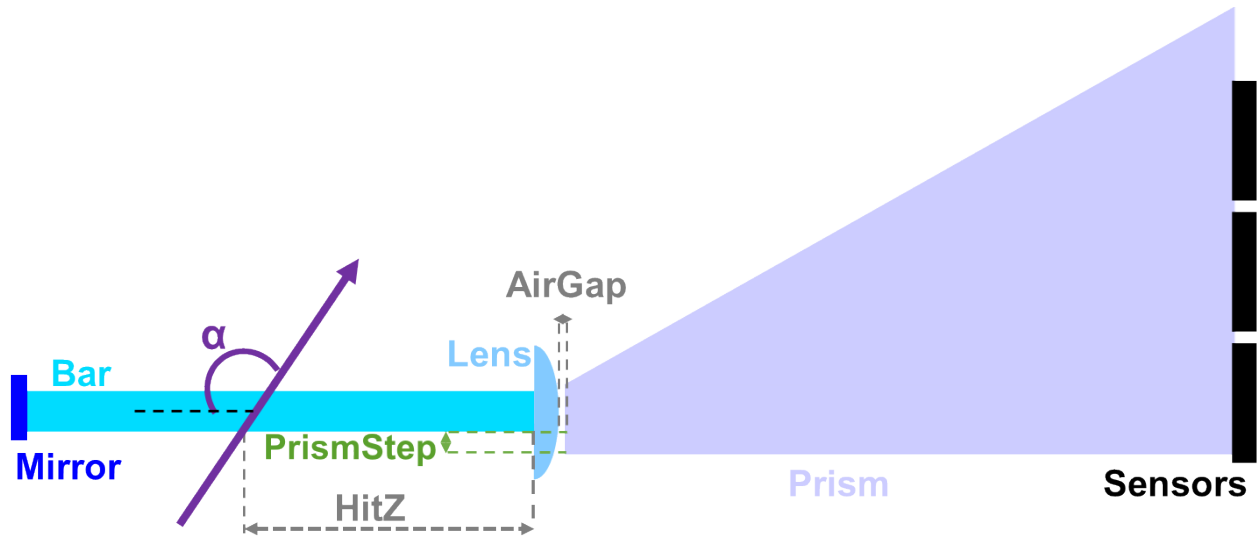


Figure 4.27: Schematic of the Prototype 2012 indicating the parameters which were changed in the experiment.

of the pixel and the center of the bar are used to define the vector as estimator for the photon direction which, combined with the beam direction is used to calculate the Cherenkov angle. However, this is not an unique assignment, and other possible paths lead to combinatorial background in  $\Theta_C$  space. Figure 4.28 shows part of the  $\Theta_C$  spectrum for a single event (a) and the 210,000 pions (b). The true  $\Theta_C$  value, in this particular case, is approximately 823 mrad.

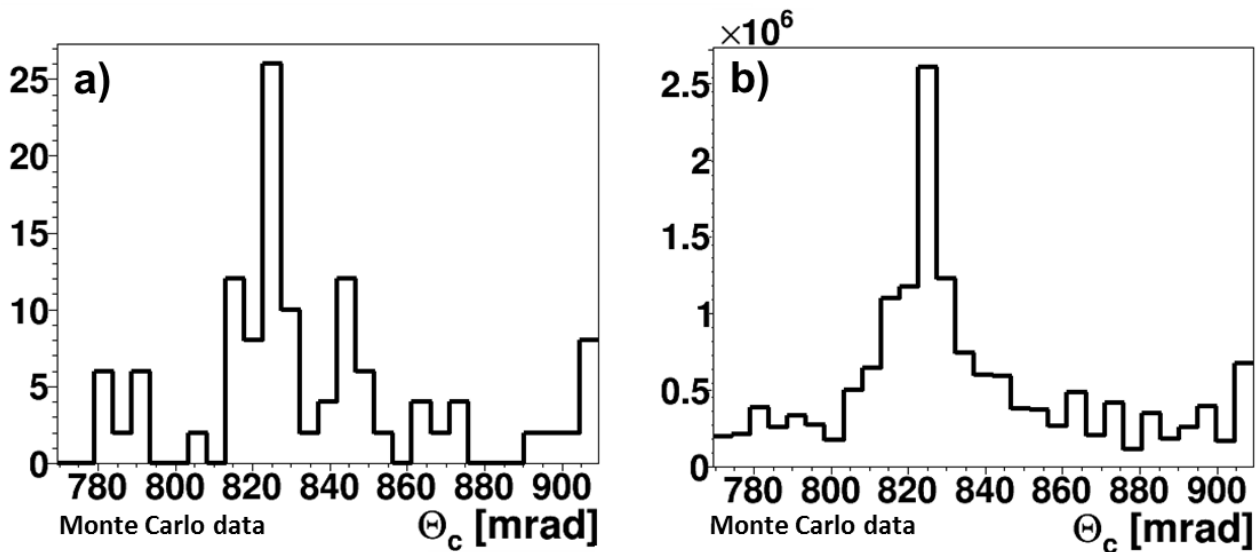


Figure 4.28: Reconstructed Cherenkov angle per photon from 2012 prototype Monte Carlo data for one pion (a) and for 210,000 pions (b) with 10 GeV/ $c$  momentum.

The discretization of the ring image by pixels and photon path ambiguities creates the background around the main peak in the distribution of the reconstructed Cherenkov angle. Even for this clean simulated case, where the photons with steep angles are lost in the air gap, the combinatorial background makes it hard to fit a function that would follow the main peak well enough to extract stable  $\Theta_C^m$  and SPR values. The MCP-PMT pixel size is 6.5 mm

what corresponds to 19 mrad in  $\Theta_C$  phase space. The expected resolution is at the level of 10 mrad, which motivates the choice of the bin size close to 5 mrad, which in Fig. 4.28 was set to 4.8 mrad. In Fig. 4.29 the influence of different bin sizes on the shape of the distribution is shown. The shape of the combinatorial background changes also with variations of some of the prototype parameters like the PrismStep or the track incidence angle, what can be observed in Fig. 4.30. The sensitivity of the  $\Theta_C$  distribution shape increases the difficulty of the fitting procedure.

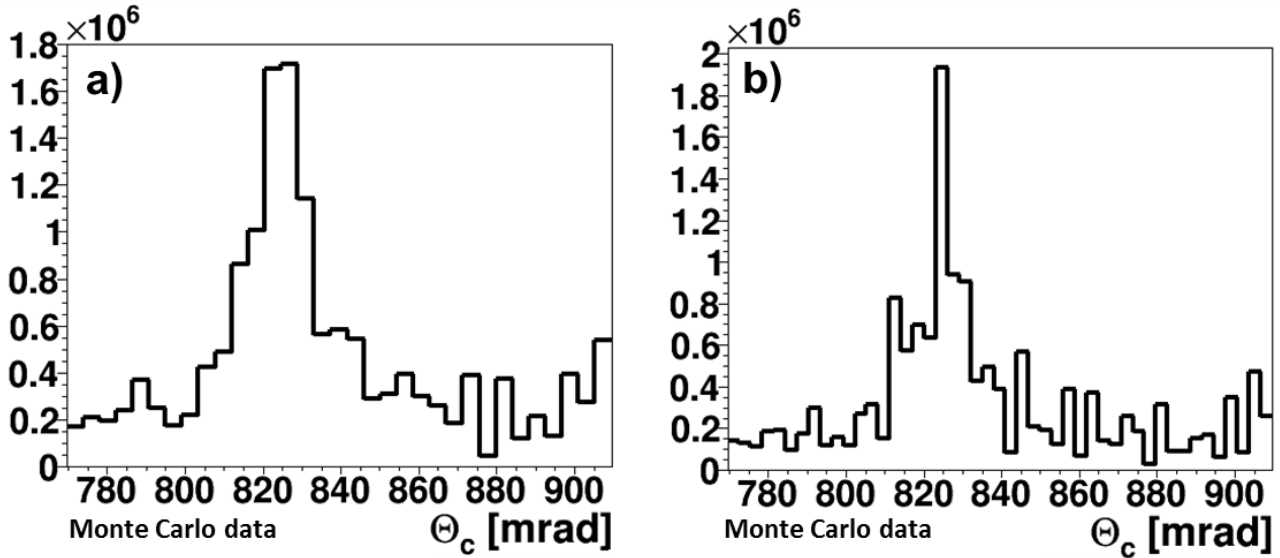


Figure 4.29: Reconstructed Cherenkov angle per photon from 2012 prototype Monte Carlo data showing the impact of different bin sizes, a) 4.2 mrad and b) 3.0 mrad, on the shape of the reconstructed  $\Theta_C$  distribution.

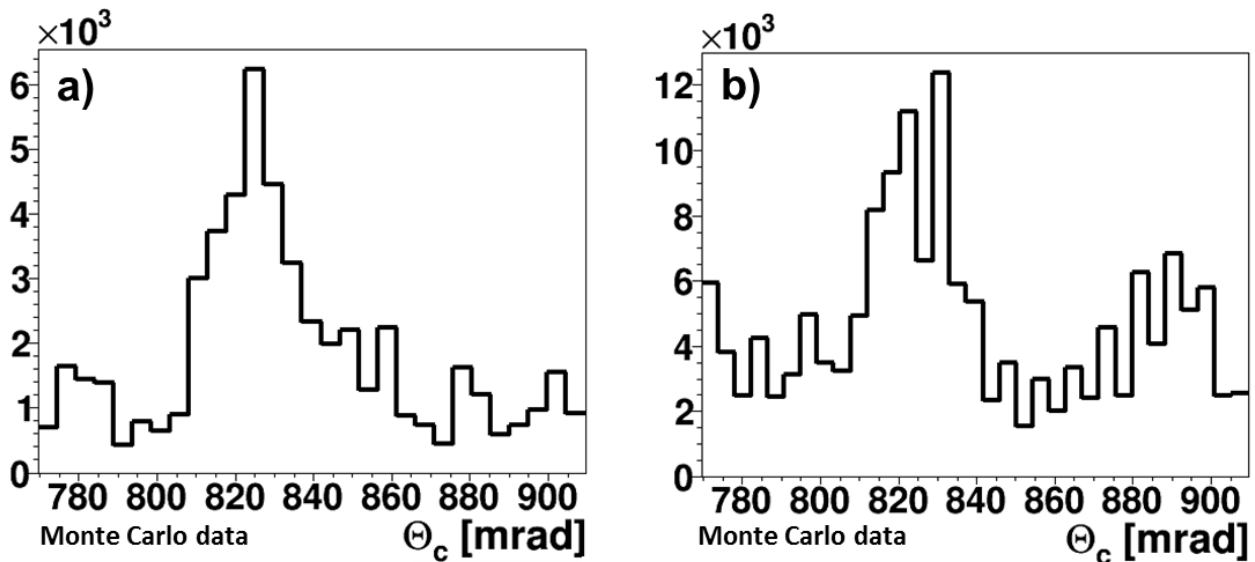


Figure 4.30: Reconstructed Cherenkov angle per photon from 2012 prototype Monte Carlo data showing the different shape of the  $\Theta_C$  distribution for other prototype configurations: a) the beam angle of  $31.2^\circ$  and the PrismStep size of 11.2 mm. b) shows  $38^\circ$  and 4 mm respectively.



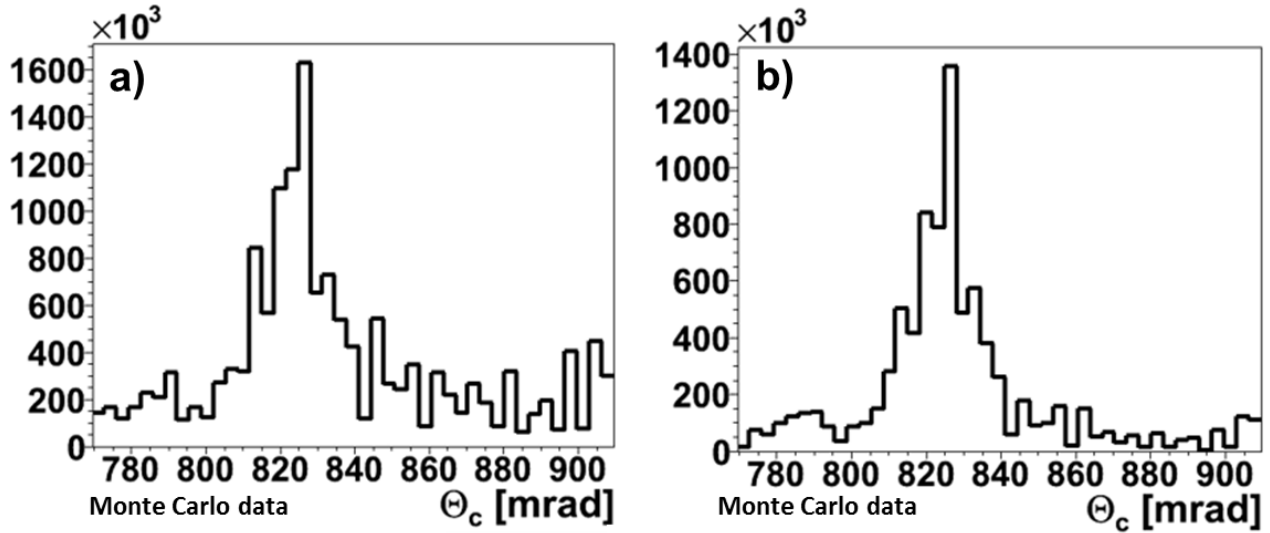


Figure 4.31: Reconstructed Cherenkov angle per photon from 2012 prototype Monte Carlo data showing the reduction of combinatorial background with the time measured minus expected cut: a) original distribution and b) distribution after a cut.

The first idea to suppress the combinatorial background to improve the reconstruction is to resolve the forward/backward ambiguity in the bar using timing information. By rejecting the ambiguity with the wrong time of arrival the background can be reduced. Fig. 4.31 shows the result of this approach on the  $\Theta_C$  spectrum. The distribution, in this case, can be fitted by the combination of a Gaussian and a polynomial much better.

In the DrcProp simulation the paths of the photons are saved and can be then used to identify which ambiguities contributed to which part of the combinatorial background. Figure 4.32a shows the  $\Theta_C$  distribution with all possible ambiguities. In Fig. 4.32b only the bar ambiguities are considered and the true path in the prism is used. Subtracting these two distributions results in the shape of the prism ambiguities background (Fig. 4.32c). It can be used as the approximation of the experimental background if the condition from the measurement are matched well enough by the tuned Monte Carlo. Result of applying this method to Monte Carlo data is shown in Fig. 4.33. The fit follows better the  $\Theta_C$  distribution and is more stable after this background subtraction is applied. However, this method adds a systematic uncertainty, the possible mismatch of parameters in the simulation and the experiment.

The best approach to extract the SPR in the most stable way without relying on the simulation is using the so-called “fine angle scan” data runs. In order to reduce the influence of the pixelization effect on the  $\Theta_C$  distribution, a set of runs can be used with small variations of the particle beam angle. The polar angle range of  $2^\circ$  in this method is scanned with  $0.25^\circ$  steps. In the data, for each step a run with around 800,000 triggers was recorded. The tuning of the simulation parameters and the reconstruction of the single photon Cherenkov angle were performed for each run and angle separately. The reconstructed  $\Theta_C$  from each sample are combined. As seen in Fig. 4.34, which compares the reconstructed single photon Cherenkov angle for a single run with a fine angle scan from 9 runs, the pixelization effect averages out and the distribution gets smoother and much easier to fit.

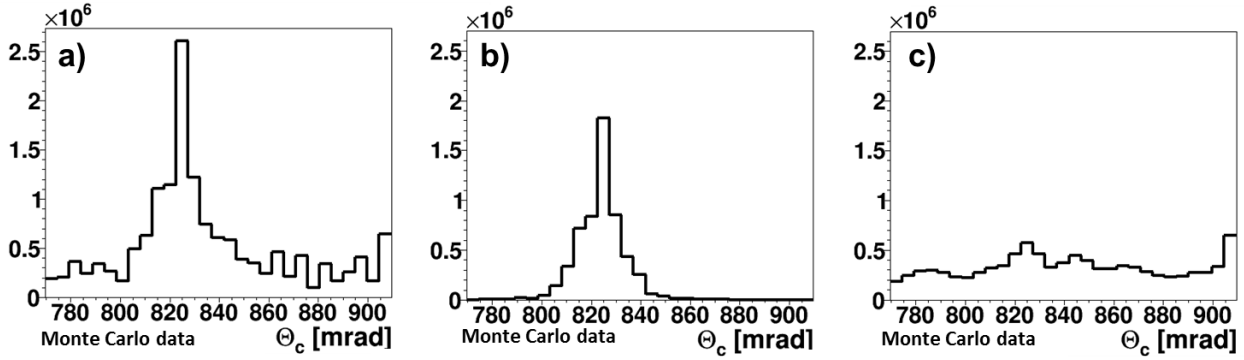


Figure 4.32: Separating the prism combinatorial background in the  $\Theta_C$  distribution. a) shows the  $\Theta_C$  distribution with both bar and prism ambiguities included, b) with bar ambiguities and information from Monte Carlo about the true path in the prism, and c) separated shape of  $\Theta_C$  distribution for only wrong solution in the prism.

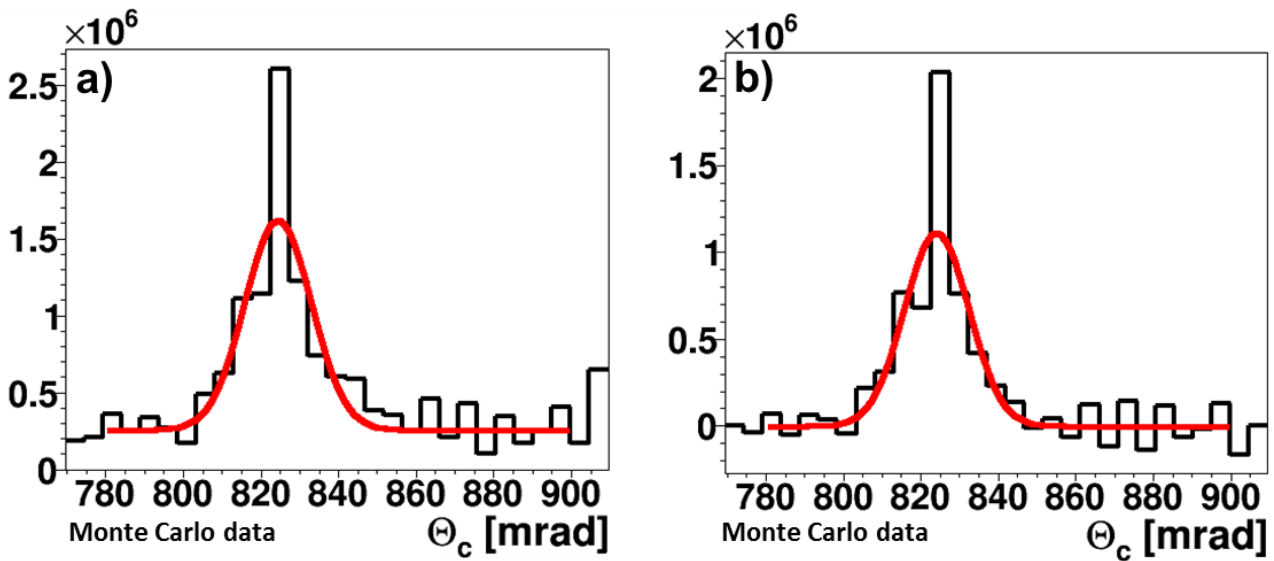


Figure 4.33: Reconstructed Cherenkov angle per photon from 2012 prototype Monte Carlo data from run MCR1: before (a) and after (b) background subtraction.

## Photon Yield

The Monte Carlo simulation of the configuration from run R1 is used for the study the expected number of photons per particle. The propagation steps from the production to detection are listed in Tab. 4.8 showing fraction of the generated photons lost at each step. The path of the particle crossing the 17 mm thick bar with  $122.4^\circ$  incidence angle is approximately 20 mm, along which on average 920 Cherenkov photons are generated for each pion used in the simulation. Similar as in 2011 prototype the Fresnel reflection and loss of the photons with large angles in the air gap reduces the photon yield at the bar-lens-air-expansion volume transition, before they enter the prism. The collection efficiency, the quantum efficiency of the MCP-PMTs and the transmission properties of the optical grease are responsible for the final loss of the photons. Ultimately only about 2% of the generated photons are detected for an expected photon yield per particle of  $N_{ph}=21.4\pm 0.04$ . The 0.04 is just the statistical error, while the full systematic error will be discussed further in that section.

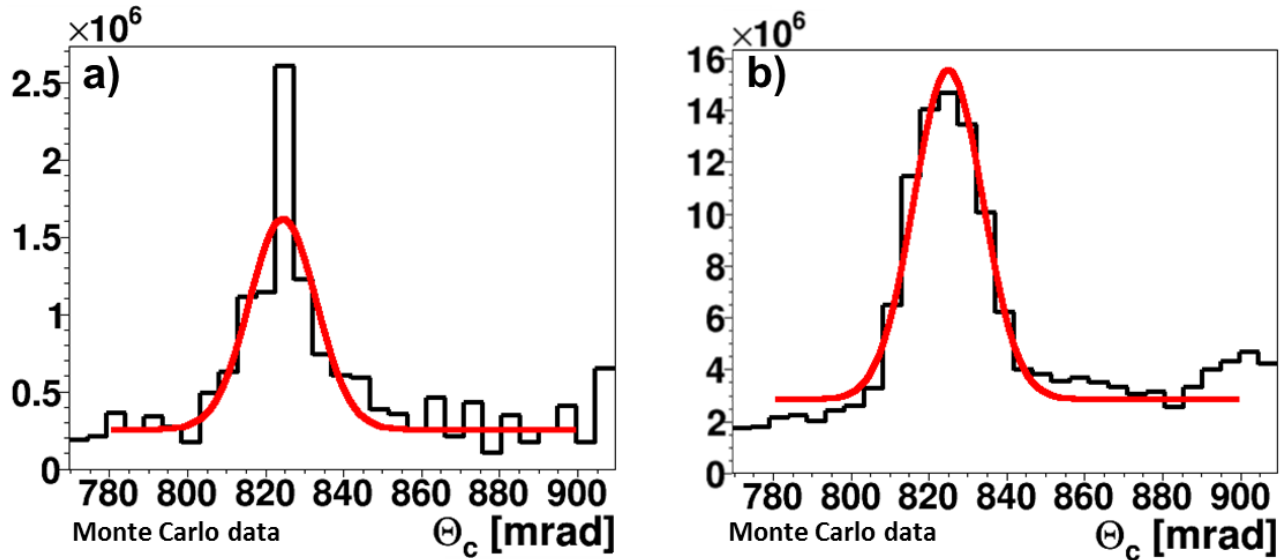


Figure 4.34: Reduction of the pixelization effect in  $\Theta_C$  distribution by using the fine angle scans measurements: a) Reconstructed  $\Theta_C$  for one particle angle and b) accumulated results for a range of  $2^\circ$  with  $0.25^\circ$  steps between runs.

	Generated	Internally reflected	Reach detector plane	Reach the MCP-PMTs cathodes	Measured
[%]	100	59	28	19	2
Number of photons	920	542	260	174	21.4

Table 4.8: The expected number of photons per pion passing the 17 mm thick bar at the beam angle of  $122.2^\circ$ . A loss of the photons in the last step comes from the detector efficiency (PDE) which is the product of quantum, collection, and packing efficiencies.

At certain angles the different parts of the image may end up in the gap between the active area of the sensors. The variation of the photon yield with the polar angle of the beam is shown in Fig. 4.35a. The black curve represents the prototype with lens L1 and a PrismStep of 11.2 mm of the bar/prism position. The red curve shows predictions for the same setup but a 3.5 mm smaller PrismStep, which decreases the separation between two ring sections. For some of the angles a small difference in the photon yield is observed but the values are very close. This dependency is shown for a larger polar angle range, and compared with other focusing options, in Fig. 4.35b. For the prototype with the standard lens L1, the biggest drop of the photon yield is expected close to  $90^\circ$  of the track polar angle. At this angle range, most of the photons are totally internally reflected at the lens curved surface. The solution to that problem is the compound L2 that is coupled directly to the bar and the prism, without air gaps. The blue line in Fig. 4.35b shows the predicted photon yield with this lens. The photon yield improves over the entire angle range, most notably for angles close to  $90^\circ$ . Finally in green, the photon yield for the prototype without focusing is presented, where the bar is coupled directly to the prism. In this case, the photon yield is highest.

The predictions from the DrcProp simulation do not include several effects present in the experiment, such as background photons from delta electrons, or optical and electronic cross talk effects. To precisely quantify the impact of these effects additional studies and Geant based

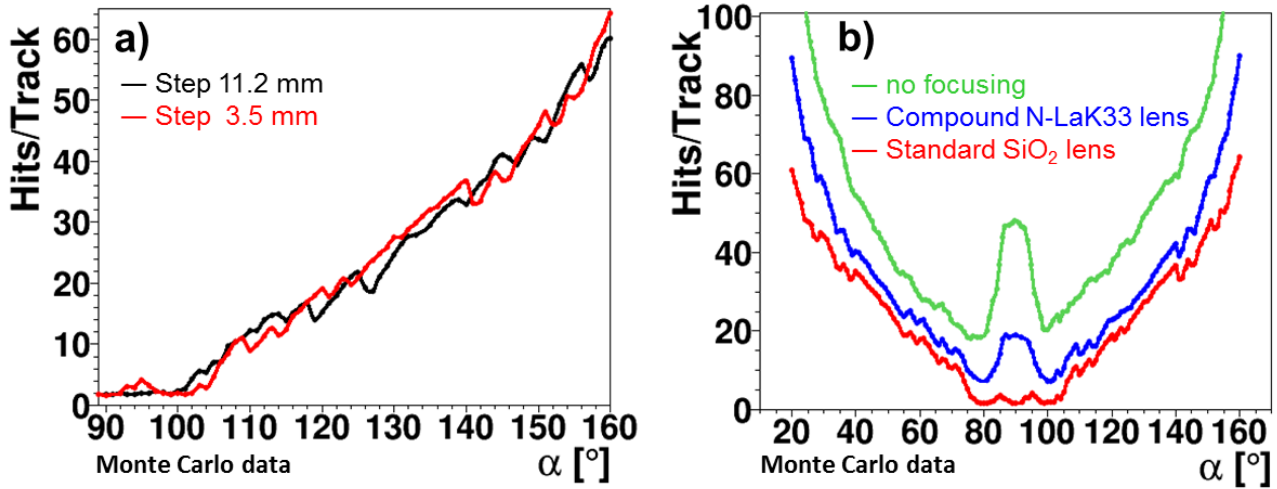


Figure 4.35: Number of photons per track as a function of the polar angle from the DrcProp simulation for different focusing configurations. a) Setup with standard lens L1 with 3.2 mm air gap and PrismStep of: 3.5 mm (red), 11.2 mm (black). b) lens L1 with a PrismStep of 3.5 mm (red), the compound lens L2 without air gap (blue) and the bar directly coupled to the prism (green).

simulations were performed and will be discussed in the following sections.

#### 4.2.4 Performance of the Baseline Configuration

The baseline configuration of the Prototype 2012 will be used as an example to present the analysis procedure of the 2012 data. This configuration used the fused silica B3 bar, with a mirror attached, and the standard lens L1. The first phase of the analysis will be presented for run R1 (see Tab. 4.7). In this run the incidence angle of the 10 GeV/ $c$  hadron-rich beam was measured to be  $124^\circ$ , the PrismStep (shift between the bottom of the bar and the bottom of the prism) was 12 mm, and the air gap between the lens and the prism was 3.2 mm.

#### Event and Hit Selection

The criteria used in the event selection is always a compromise between reaching the best efficiency to lose as few Cherenkov hits as possible and rejecting as much as possible of the background to provide more stable reconstruction of the Cherenkov angle. In this analysis higher priority was given to efficiency. The coincidence of the two start counters defines the trigger. The first event selection cut is on the total number of channels with a signal in the event. This includes the MCP-PMT out signals, as well as signals from trackers, and reference times. The distribution is shown in Fig. 4.36a. For some of the events there was almost no Cherenkov light. For the majority of events there is a clean peak corresponding to fully contained events. There are also side peaks with fewer and more hits. Low multiplicity events are probably hits from particles not going through the middle of the bar and therefore generating less photons. High multiplicity events can be a result of two particles going through the bar within the same trigger window. Figure 4.36b shows a time distribution of the two triggers coincidence logic signal. A cut is applied to eliminate accidental triggers. The distribution is very wide because the TRB readout system is designed to use relative timing and for any precise timing

information one should take the time difference between two channels. The cuts on the number of hits (Fig. 4.36a) eliminate approximately 10% of the events.

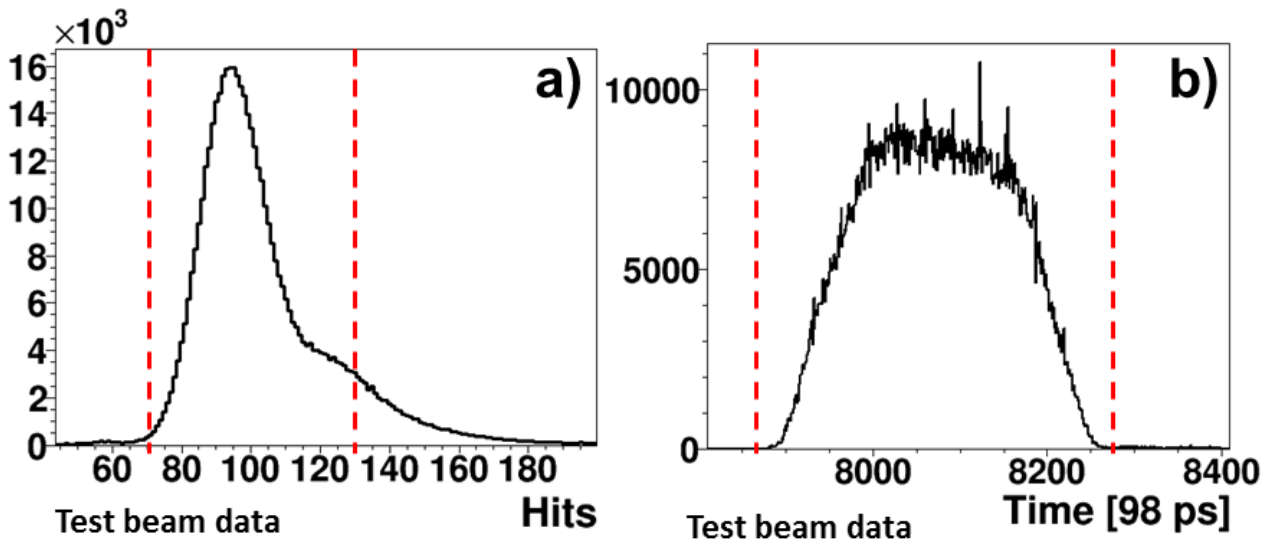


Figure 4.36: Distribution of the total number of hits per event for a) R1 and b) R10. The red lines show the selected range.

Possible beam divergence was limited with the use of the TOF system. The two MCPs (TOF1, TOF2) with the  $59 \times 59$  mm Acrylic glass windows were placed at a distance of 7.7 m from each other. The DIRC prototype was positioned approximately on halfway between them (see Fig. 4.17). They were aligned to the T9 beamline. By taking the coincidence between TOF1 and TOF2 the beam divergence is constrained to less than 4.4 mrad, what cuts additional 10% of the original triggers. Taking the center four TOF1 pixels in coincidence with any pixel from TOF2 constrains the beam direction to about 3.4 mrad and cuts the number of triggers to 57%.

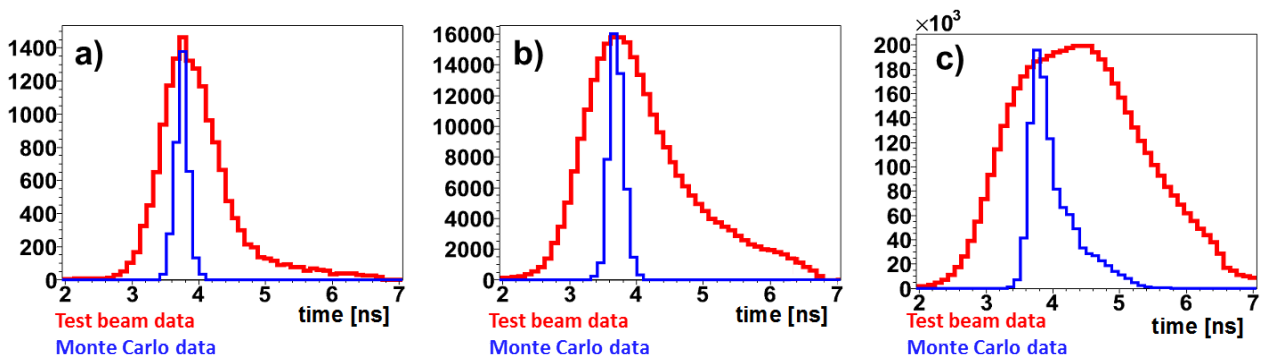


Figure 4.37: Time resolution comparison between Monte Carlo (blue) and test beam data (red) for: a) a single pixel, b) one MCP-PMT, and c) the full system.

After the event is accepted the cut on the hit time distribution is applied. The time resolution for the PANDA Barrel DIRC system includes roughly 40 ps from the sensor transit time spread and the readout electronics was designed to keep the total time resolution of the system below 100 ps. The comparison of the timing achieved, to the simulated values is shown in Fig. 4.37. The best achievable resolution in Monte Carlo data is on the level of 80 ps for the

single pixel. The different path lengths of the photon, and the chromatic smearing increase it to 360 ps for all MCP-PMTs but it can be corrected in the later analysis. However, in the 2012 test beam, the observed time resolution values are at the level of 1 ns for the entire system. For a single pixel, the time resolution of 400 ps can be reached but it decreases already, up to approximately 800 ps, when the signals for several pixels of one MCP-PMT are averaged. The irreducible term from the slow scintillators used as start counters has a significant contribution to the poor timing resolution during the test beam. Furthermore, problems with the laser calibration system made it impossible to properly correct for time shifts between pixels on an MCP-PMT and between MCP-PMTs.

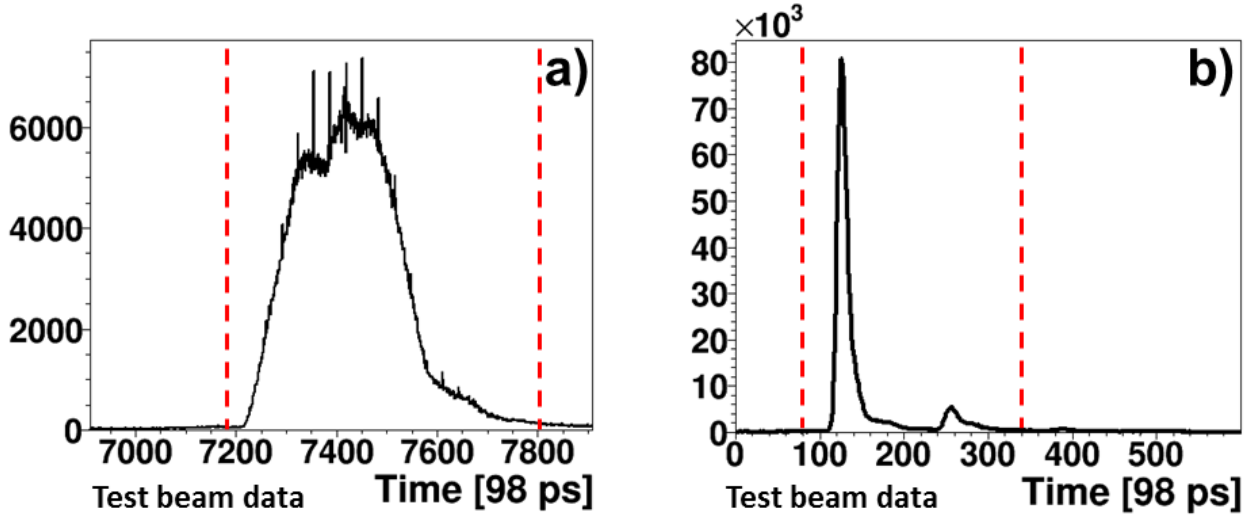


Figure 4.38: Distribution of the hit time per sensor (middle left MCP-PMT): the raw hit time distribution (a) and the trigger-corrected hit time (b). The red lines show the selected time window.

In Fig. 4.38a the MCP-PMT raw hit time distribution from run R1 is shown. Time cuts are applied in two steps to eliminate background from noisy channels, or scattered photons, showing up as a background uncorrelated with the trigger time. First, a wide time window is used to take out hot pixels and some of the scattered photons (Fig. 4.38a), which removes 8% of the hits. A second cut uses the trigger signal (Fig. 4.36b) distributed to every TRB board. The different TRBs are synchronized in time with a precision of about 10 ns. The distributed trigger signal reduces the time difference between boards down to the time resolution of the TDC. The relative timing is used by taking the difference between the MCP-PMT hit time and the trigger time from the same board (Fig. 4.38b). It gives more precise time information and allows a better cut which selects about 70% of the original hits per trigger. The distribution of accepted hits on the MCP-PMT array is shown for 9 single events in Fig. 4.39.

### Number of Hits per Event

To extract the photon yield, in each accepted event all hits within a time window of 2 ns were counted and plotted in the distribution shown in Fig. 4.40. The distribution was then fitted with a Poisson function to extract the mean value. The results are  $27.7 \pm 0.07$  for the data and  $21.4 \pm 0.03$  for the simulation where the errors at this point are only the statistical error of the fit. There is significant difference between these two numbers. However, there are two facts not yet considered at this point. This data includes contributions that are not present in the

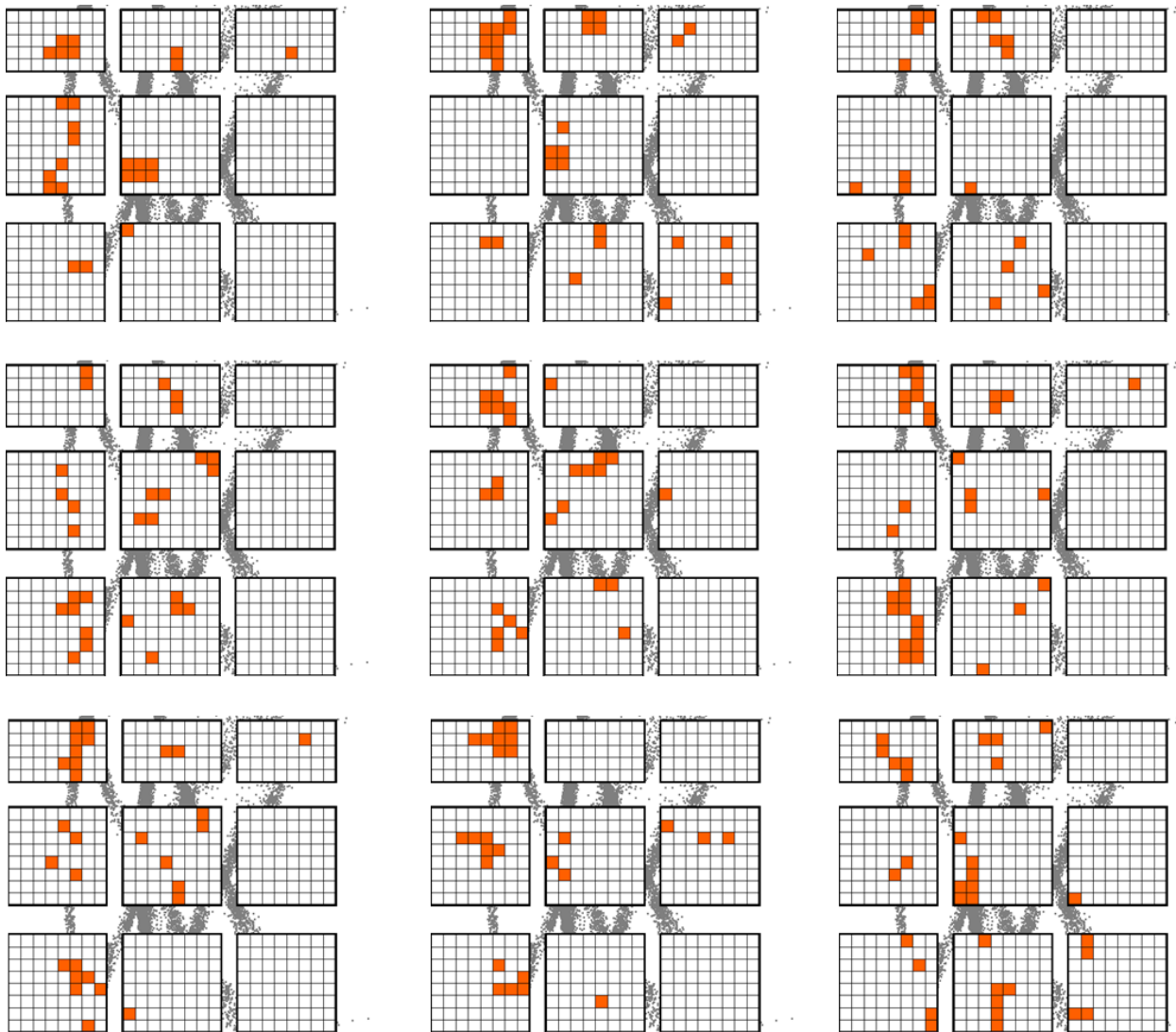


Figure 4.39: Distribution of pixels with a hit in nine example events. The gray points in the background are true hit positions from 500 simulated pions to guide the eye.

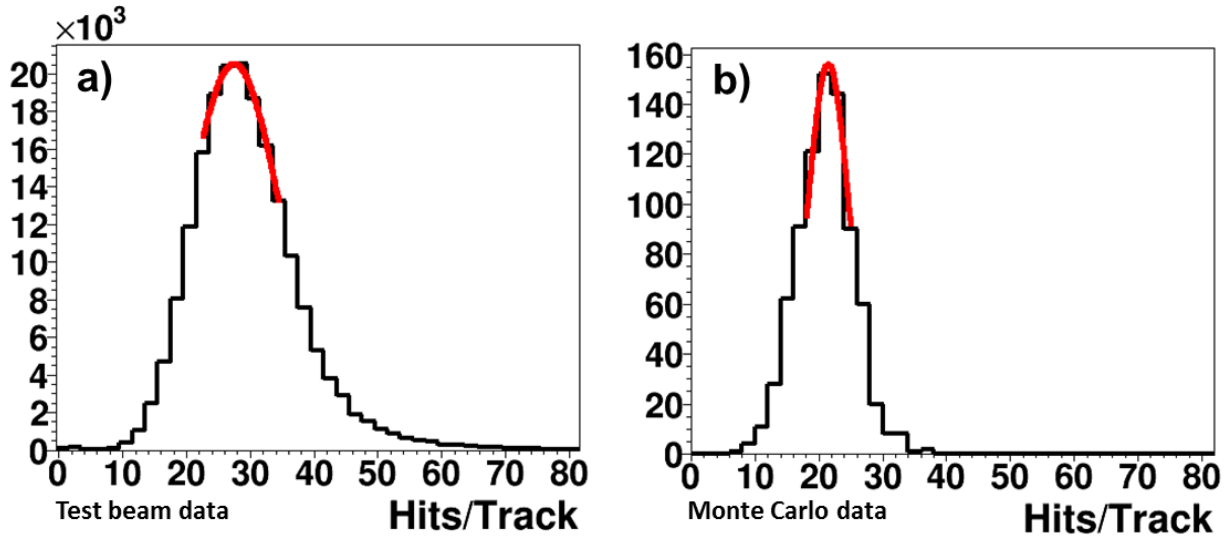


Figure 4.40: Observed number of hits per track from the 2012 prototype for run R1 (a) and for the simulated run MCR1 (b).

DrcProp simulations and in order to compare these two one needs to correct the experimental results. Secondly, it is important to evaluate the systematic error on this quantity.

### Matching the Simulation to Test Beam Data

The distribution of the hits on MCP-PMTs combined from almost  $10^6$  events recorded in run R1 is shown in Fig. 4.41a. The white pixels correspond to dead electronic channels. Non-zero counts off the rings are the result of the noise, scattered photons and charge sharing effects. The location of the observed ring segments is compared to a pixelated simulation of 210,000 pions shown in Fig. 4.41b. The particle incidence angle of  $\alpha = 124^\circ$  and a PrismStep of 13 mm were measured during the test beam. These values of the setup configuration implemented in the simulation do not match perfectly the data. The difference in the distribution of the hits between experimental and simulated data is visible specially for the left column of MCP-PMTs in Fig. 4.41.

To do the reconstruction the simulation had to be matched to the data with a tuning procedure. In contrast to 2011 the prototype was much more stable and the positions of the MCP-PMTs were defined much better and did not change during the test beam campaign. This leaves only two primary potential causes for the mismatch: the polar angle between the beam and the bar and the value of the PrismStep ( $\Delta Y$ ). The optimum angle has to match both the overall rotation angle of the prototype and the possible angle misalignment of the bar with respect to the prism on the prototype table. That explains why the difference between the experimental and optimum simulation values is not a constant offset over time and matching procedure has to be performed separately for every studied run. In order to investigate that, small ranges of these parameters are defined within the uncertainties of measured values during the beam time. A large number of simulated runs are generated with all the combinations of these parameters. The parameters that best describe the data are selected in two ways. The first evaluation is done by comparing visually the occupancies from the data and simulation. A mismatch in the beam polar angle results in a shift of the full image, while the difference in the PrismStep can be recognized in the separation of the two ring segments. However, a fine matching is difficult with this method due to the dense image with overlapping parts of the ring



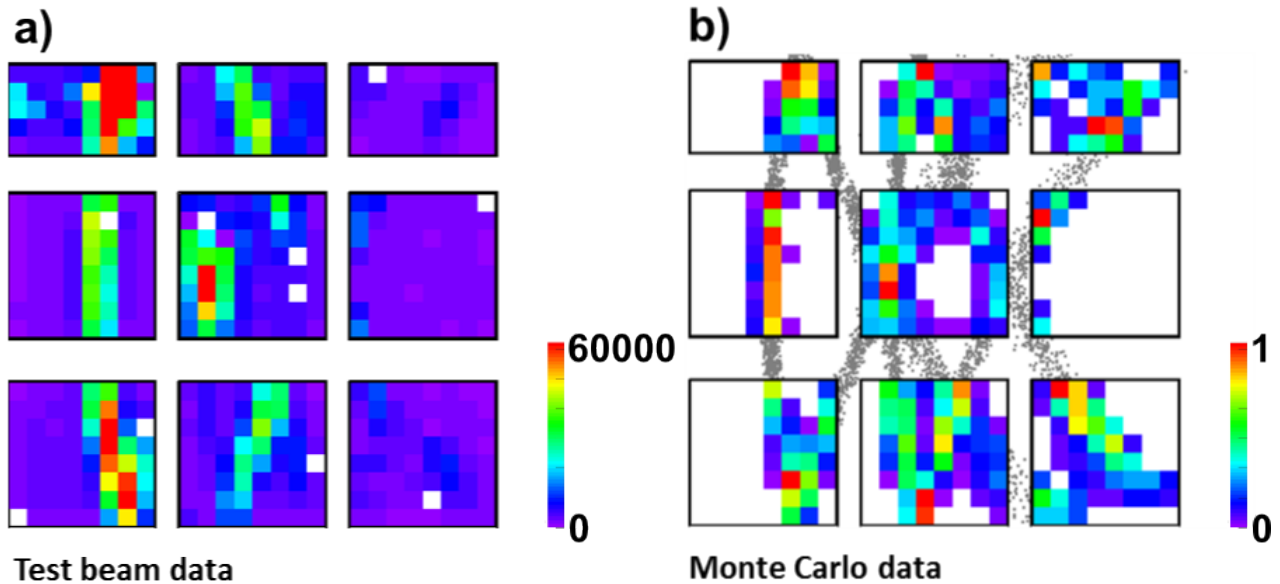


Figure 4.41: Distribution of the hits per MCP-PMT in the experimental data for run R1 (a) and for the simulated data (b) using the parameters measured during the experiment. The gray points in the background are the true hit positions from simulation to guide the eye.

segments. A more detailed assessment of the match is done by looking at the reconstructed Cherenkov angle. For each combination of the investigated parameters the reconstruction is performed. When both ring segments are shifted (polar angle mismatch) the mean  $\Theta_C$  value shifts as well. A shift in the PrismStep can be recognized by comparing the  $\Theta_C$  distribution for all nine MCP-PMTs and only for the left column. In the second case one ring segment is isolated and a potential shift is easy to observe. The comparison of the matched simulation and experimental occupancy distributions is shown in Fig. 4.42. The experimental data are very well represented by the simulation after the matching procedure. The optimized simulation parameters for this run are  $122.4^\circ$  for the polar angle and 11.2 mm for the PrismStep (compared to  $124^\circ$  and 13 mm measured during the experiment).

### Reconstruction of the Single Photon Cherenkov Angle

The Cherenkov angle  $\Theta_C$  is reconstructed using the geometric method described in Sec. 3.4. Look-up tables were generated from simulation using the values for the polar angle and step that best matched the data. The distribution of the reconstructed  $\Theta_C$  for run R1 and simulated data are shown in Fig. 4.43. The results from the experiment are:  $\Theta_C^m = 826.1 \pm 0.01$  mrad and  $\sigma_{\Theta_C} = 12.3 \pm 0.01$  mrad and the simulated values are:  $\Theta_C^m = 824.9 \pm 0.01$  mrad with a resolution of  $\sigma_{\Theta_C} = 8.5 \pm 0.01$  mrad. Where the errors at this point are statistical only. The combinatorial background, being an artifact of the reconstruction method and higher than in the simulation due to the additional background hits makes it even harder to extract stable values from the fit. Two approaches to suppress the combinatorial background and make the distribution easier to evaluate were described in 4.2.3. The result of applying these methods to the data is discussed below. The reconstructed Cherenkov angles and the resolution values for the baseline configuration are listed in the Tab. 4.9 with systematic errors. The evaluation of these errors from the individual terms is discussed further and summarized at the end of this section.

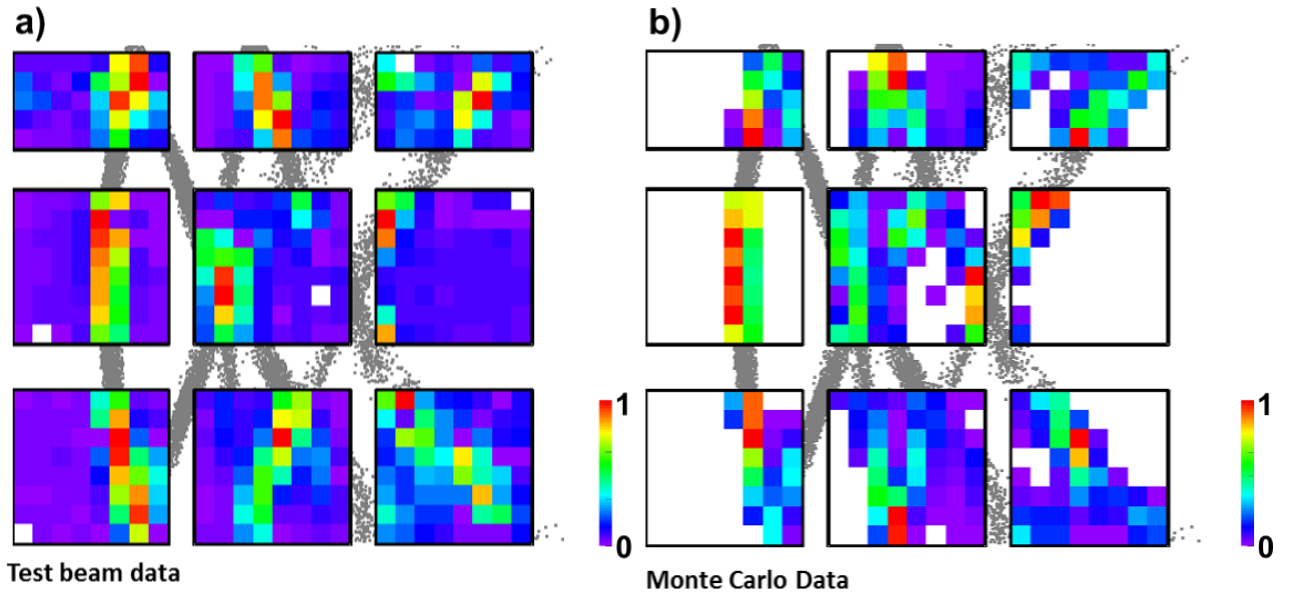


Figure 4.42: Distribution of the hits per MCP-PMT in the experimental data for run R1 (a) and for the matched simulated data MCR1 (b). The gray points in the background are the true hit positions from simulation to guide the eye.

Run	Data Type	$\Theta_C^m$ [mrad]	$\sigma_{\Theta_C}$ [mrad]	Background Treatment	Figure
R1	test beam	$826.1 \pm 0.7$	$12.3 \pm 0.7$	no	4.32a
R1	test beam	$824.3 \pm 0.9$	$11.6 \pm 0.7$	background subtracted	4.32b
R5	test beam	$823.7 \pm 0.7$	$12.0 \pm 0.7$	fine angle scan	4.45a
R6	test beam	$822.8 \pm 0.8$	$12.3 \pm 0.8$	fine angle scan	4.45b
MCR5	simulated	$824.9 \pm 0.5$	$8.5 \pm 0.6$	fine angle scan	no
MCR6	simulated	$825.4 \pm 0.5$	$11.0 \pm 0.6$	fine angle scan	no

Table 4.9: Results of the single photon Cherenkov angle reconstruction. The combinatorial background is treated with different methods. Errors are dominated by the systematic term while the statistic error is about 0.01 mrad. Details about the runs can be found in Tab. 4.7.

The first approach used to stabilize the  $\Theta_C^m$  and SPR results is using the assumption that the simulation represents the experiment well enough. In this case, the simulated prism combinatorial background can be subtracted from the test beam  $\Theta_C$  distribution. The determination of the shape of the combinatorial background was shown in Fig. 4.32. Figure 4.44 shows the  $\Theta_C$  distribution before and after the subtraction. The corrected values are listed in the second row of Tab. 4.9. To extract the values for  $\Theta_C^m$  and  $\sigma_{\Theta_C}$  the sum of a Gaussian and a first order polynomial was fitted to the  $\Theta_C$  distribution. After subtraction of the simulated prism background the mean value of the reconstructed Cherenkov angle and the SPR are closer to expectation. However, the shape is still spiky and the fit function does not describe the

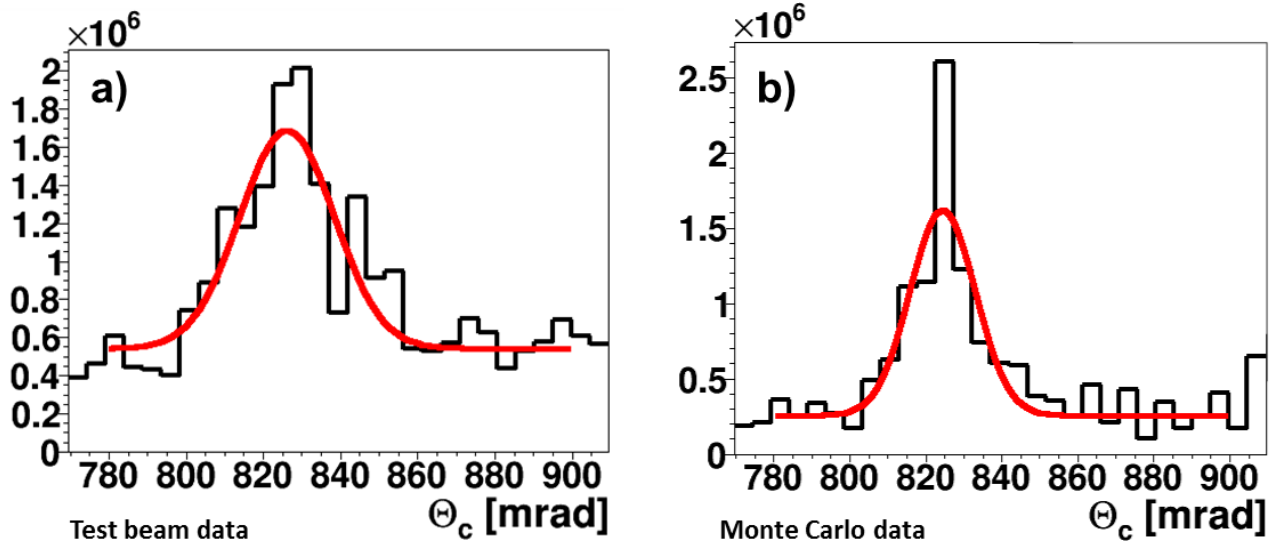


Figure 4.43: Reconstructed Cherenkov angle per photon from 2012 prototype data for run R1 (a) and simulation matched to this run MCR1 (b).

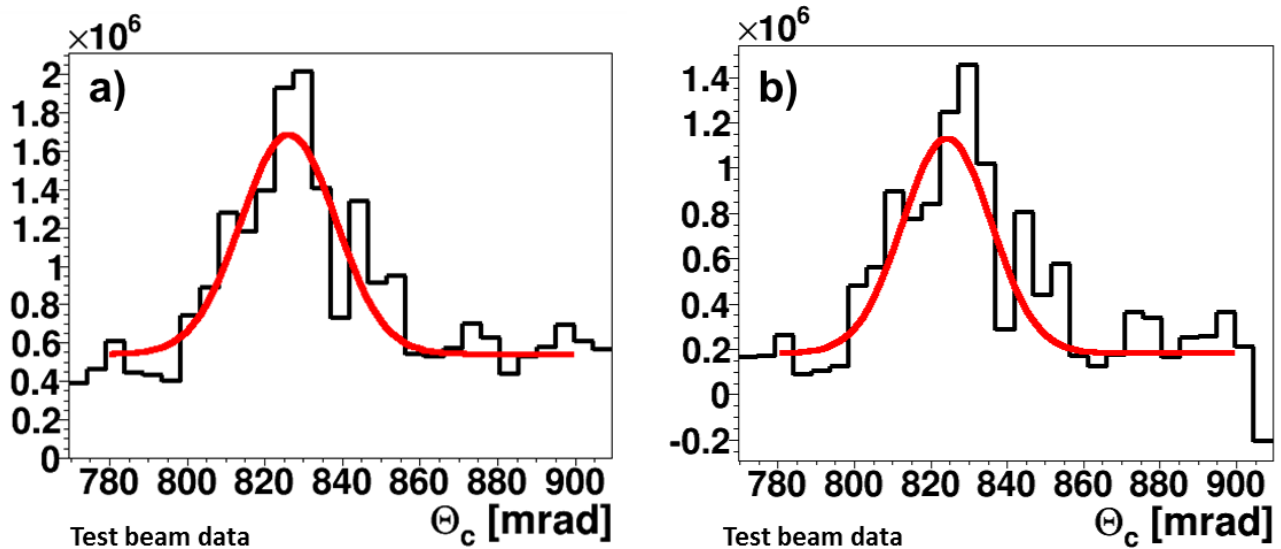


Figure 4.44: Reconstructed Cherenkov angle per photon from 2012 prototype data for run R1 (a). Same distribution after background subtraction (b).

distribution very well.

The stability of extracting  $\Theta_c^m$  and the resolution can be improved using the data from fine angle scans as explained in Sec. 4.2.3. From the 2012 test beam campaign two ranges of polar angle were scanned with the baseline configuration of the prototype. The outcome of those two fine angular scan studies is shown in Fig. 4.45 with the corresponding values listed in Tab. 4.9. The first fine angle scan, with a range of 122-124° (run R5), is close to the polar angle of the run R1 discussed above and the second was recorded by scanning a range of 154-156° (run R6). The results from simulation are listed in the last two rows. For every sub-sample from the fine angular scan the simulation is tuned and look-up tables produced, the data are reconstructed for each angle value before combining the sub-samples into one  $\Theta_c$  distribution. The fit to

extract the SPR, which is a combination of a Gaussian and a first order polynomial in the range of 780-900 mrad, follows the distribution much better and is more stable than for a single sub-sample. The obtained values from the experiment are consistent with the simulation if the contribution from the beam divergence is taken into consideration.

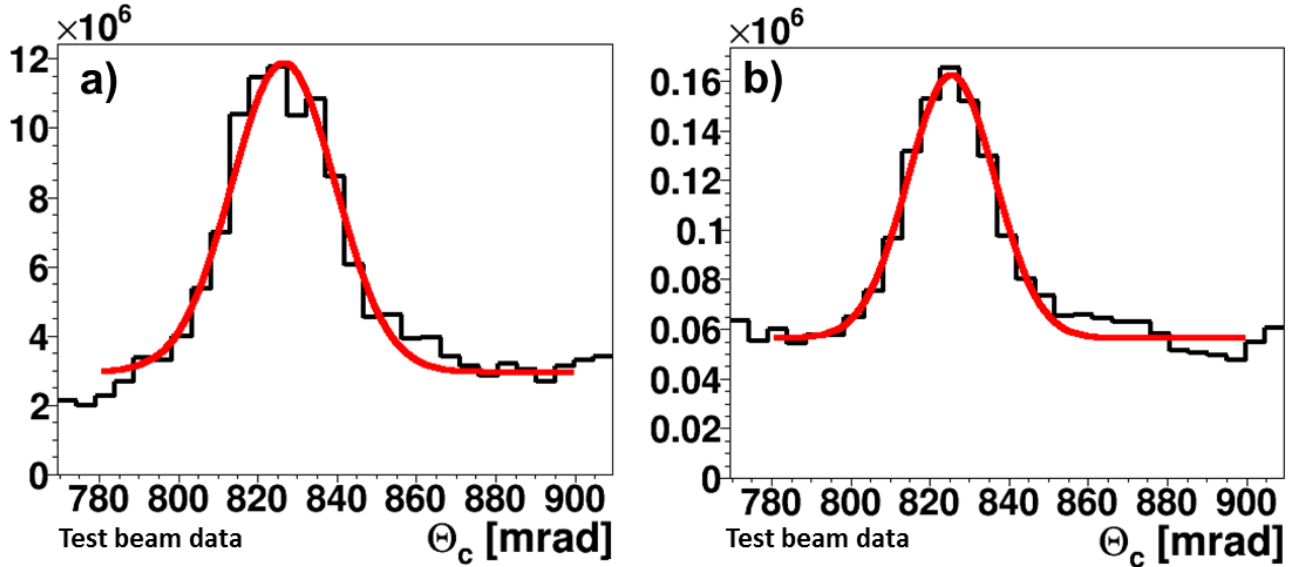


Figure 4.45: Reconstructed Cherenkov angle per photon from 2012 prototype data, using the fine angular scan method, for two different incidence angle ranges: a) 122-124° (R5) and b) 154-156° (R6).

### Effects Not Included in the Simulation

As mentioned earlier the DrcProp simulation software is based on ray tracing with parametrized implementation of photon attenuation in the material and of the photon detection efficiency. In the experimental data there is background which is not removed by the event and hit selection and is not included in the DrcProp simulation. This background has a significant impact on the determination of the photon yield.

The first of these effects is the charge sharing [71], which appears in the MCP-PMT when the electron cloud from one photon spreads to neighboring anode pads. This leads to additional pixels with hits and an overestimation of the photon yield. Of course not every pair of neighboring pixels recording a hit are the result of charge sharing but may be due to two real photons. In order to estimate the probability of having real hits in two neighboring pixels in one event, the DrcProp simulation of run R1 was studied. The value depends strongly on the prototype configuration but for run R1 the probability of two hits in pixel neighbors in the same event is about 11%.

In the experimental data a clear signature of the charge sharing effect is observed. In Fig. 4.46 an example is presented for three selected pixels (called target pixels) on the left side of the general occupancy plot of the run R1. The figures show which other pixels from the same MCP-PMT recorded a hit in an event if the target pixel has fired. A clear signature is visible, as the neighbor pixels fire more often than the pixels further away. Especially the bottom distribution, which shows a target pixel far away from the ring, is strong proof of charge sharing since in this area the probability to have even one hit is very small. The separation of

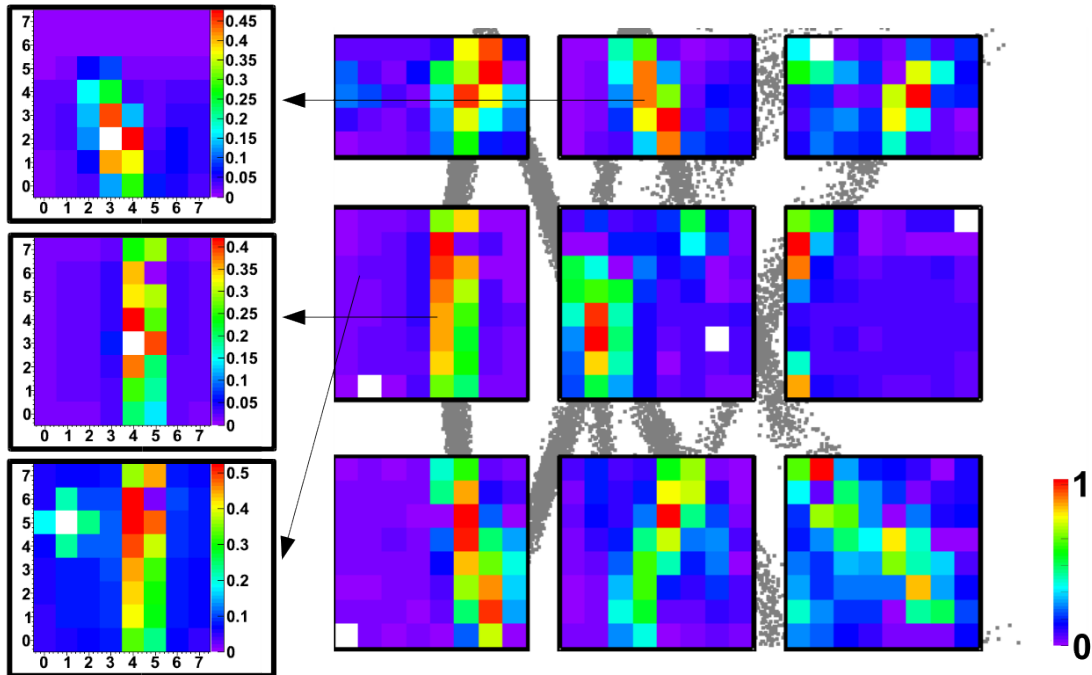


Figure 4.46: Distribution of the hits per MCP-PMT in the experimental data for run R1 (right). The signature of the charge sharing effect for three chosen pixels with the color scale shows the probability for a hit in the same event (left).

charge sharing hits from true simultaneous hits in the experimental data was not possible since the selection requires a timing resolution of 100 ps or better. Instead, previous measurements at SLAC and KEK [72] are used to estimate the impact of charge sharing on the photon yield measurement. They were performed with similar sensors and the charge sharing amounted to about 10 to 15%. For the estimation of the correct photon yield and the error evaluation the top value of 15% was taken.

The electronic cross talk effect for neighboring TRB channels was also investigated. Two channels next to each other on the TRB board, but connected to pixels on the different MCP-PMTs were studied in a similar way as describe above for the charge sharing study. No such crosstalk was observed since the electronics was designed to minimize electronic crosstalk even for the low discriminator thresholds required for the single photon identification.

The second important effect not included in DrcProp is connected to so-called delta electrons, which can produce Cherenkov photons in the radiator which add to the off-ring background and contribute to the measured photon yield. The charged particle going through the matter interacts with electrons causing excitation and ionization. In the first case the electron will de-excite by emitting electromagnetic radiation. In the second case the energy transfer exceeds the binding energy of the electron, which is then ejected from the atom. Those electrons that posses enough energy to produce further ionization, are called delta electrons.

In the tests of the prototype there are two main possible sources of delta electrons. One are the secondary particles from the Fiber tracker, the TOF system, and the scintillator. The second is the charged particle going through the bar itself, which can generate delta electrons.

The effect of background photons from delta electrons was studied with the Geant simulation. Several signatures of this effect were confirmed. A lot of the photons from delta electrons are lost by multiple scattering and part of the delta electrons are absorbed without emitting any photons. From 10,000 simulated pions crossing the bar with a momentum of 10 GeV/c at

$120^\circ$  incidence angle on average 2 detected photons per track were generated by delta electron. Delta electrons are created and propagate in both directions of the radiator bar. They do not have a preferred emission direction, or dependence on the momentum of the mother particle. One of the signatures of delta electrons in the experiment is using this isotropic emission of the Cherenkov photons. Photons from delta electrons have arrival times before the first possible hit times from the photons generated by the beam particle, especially for tracks with the polar angle below  $90^\circ$ , where all photons have long paths via the mirror. In most of the 2012 measurements the incidence angle was above  $90^\circ$  and the difference in the arrival time between the signal Cherenkov photons and the background is too small to separate them from each other. However, it is clearly observed in Fig. 4.47 for runs R20 and R21 taken with  $56^\circ$  polar angle.

Runs R20 and R21 were taken with different distances of the beam intersection point on the bar, respectively  $HitZ = 116\text{ mm}$  and  $HitZ = 496\text{ mm}$ . The difference in the path between the signal photons and the direct background photons gave a time difference big enough to observe this effect even with the limited time resolution in the experiment. The measurements were taken one shortly after another to rule out any significant differences in the setup. The results from the experiment are shown in Fig. 4.47b. The early photons are observed before the large peak that corresponds to the arrival time of the true Cherenkov photons. Early peaks are consistent with simulated arrival time of photons from delta electrons shown in Fig. 4.47c. The delta electron effect was reproduced with the ray tracing software, which does not include effects of the particle interaction with matter. That is why two cases for each run were simulated. One with the  $56^\circ$  particle angle and a symmetric one with  $180^\circ - 56^\circ = 124^\circ$ , simulating the electrons. The separation between the main peak and the early peak moves with  $\Delta HitZ$  as expected, firmly establishing delta electrons. The bigger time spread of the early photons in the experiment comes from the fact that the delta electrons have many different angles.

The late peak, visible on the right of the main peak in Fig. 4.47, are photons reflected from the lens, then from the mirror, and finally exiting the bar to be measured. An example of such a photon is shown on the event display from the DrcProp simulation in Fig. 4.48. The number of photons in the late peak in the different test beam runs is about  $2.5 \pm 0.2$  photons per event.

The study of runs R20 and R21 described above is not enough to evaluate quantitatively the impact of the delta electrons on the photon yield. Therefore, it was studied with other runs from Tab. 4.7, using the isotropic emission of the Cherenkov light from the delta electrons as the signature. For some of the polar angles the ring image is located on one side of the detector plane leaving groups of MCP-PMT pixels with very low probability to be hit by any Cherenkov photon generated from beam particle. The study was performed by looking at the group of pixels far away from the ring image in the runs with sufficient separation. The established values include background photons from delta electrons but also from the noise of the electronics and scattered photons. The study was performed for several different measurements, and the obtained numbers were extrapolated to the rest of the pixels. The impact from delta electrons, scattered photons, and the electronic noise on the photon yield was concluded to be about  $N_{Background} = 3.6 \pm 0.4$  hits per trigger. The  $\sigma_{Background} = 0.4$  is the mean uncertainty from all used runs to determine the background. In further analysis  $N_{Background}$  is used as part of the correction of measured hits in the test beam data.

## Systematic Error

In order to evaluate the systematic error on the obtained photon yield,  $\Theta_C^m$ , and SPR values several effects in the analysis procedure had to be studied. The impact of individual sources on

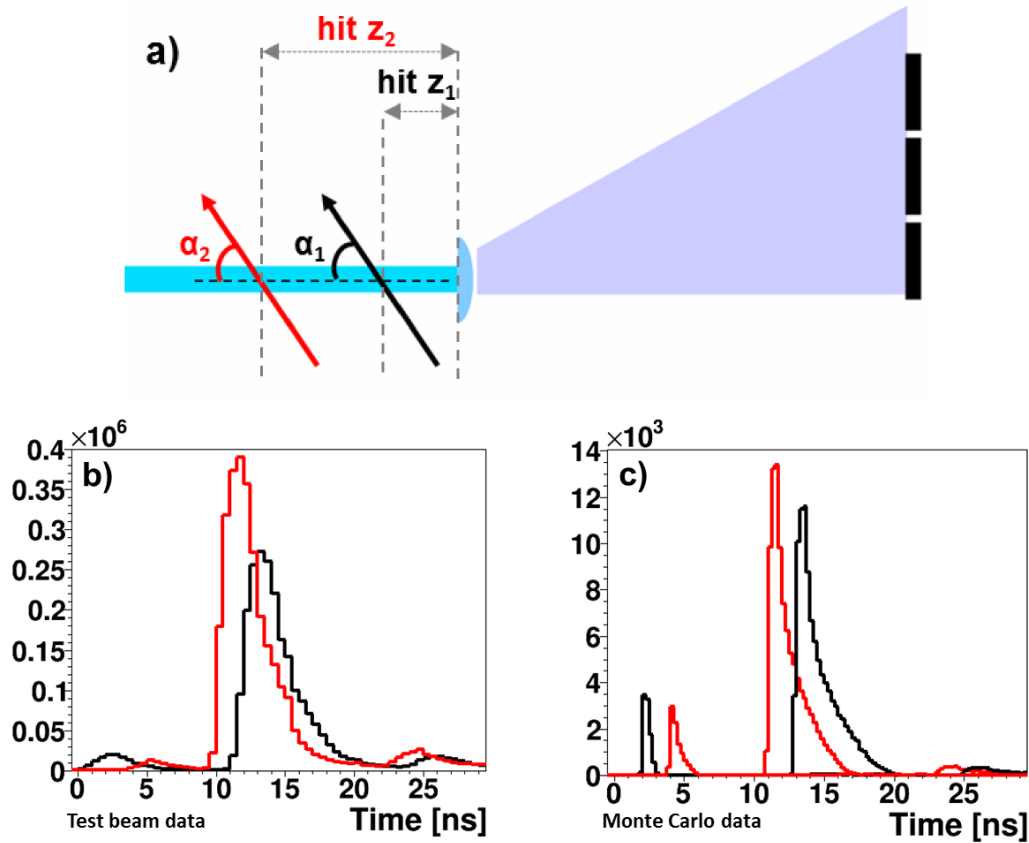


Figure 4.47: a) Schematic of the approach to study the background photons from delta electrons showing the different hit positions of the beam on the bar for R20 and R21. The photon arrival time distribution for runs R20 and R21 with different HitZ position for experimental data (b) and simulation (c). The colors correspond to the different hitZ position of the runs, shown in (a).

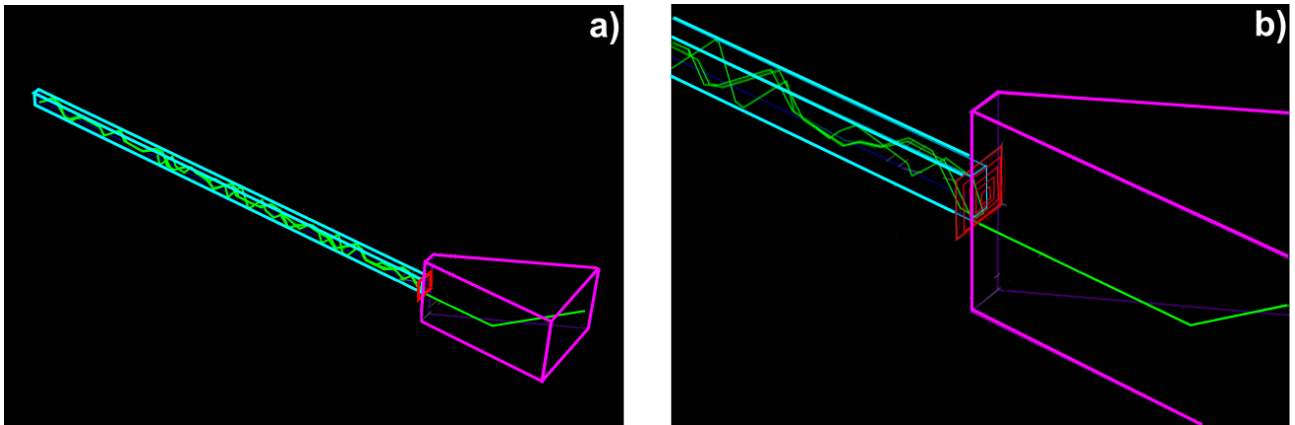


Figure 4.48: Event display from the DrcProp simulation showing the source of the late photons with a zoom (right) showing the reflection on lens.

the results was established for separate runs and compared for different configurations. Each individual source of the overall uncertainty is given as the standard deviation obtained by taking two extreme cases and, assuming a uniform distribution, dividing their difference by the square root of 12.

The event selection as the first step of processing the data, was checked for any systematic bias. This was done by comparing the photon yield using only the two scintillator counters with events selected by requiring both MCP-TOF counters to be in coincidence. The uncertainty from the event selection was established to be  $\sigma_{Event} = 0.01$  on the photon yield and 0.04 mrad on the  $\Theta_C^m$  and SPR values. As a further check the acceptance window was slightly varied. The time cut was chosen to be robust. By varying the selection window for the hit time cut the impact on the results  $\sigma_{Hit}$  was estimated to be 0.2 on the photon yield and 0.1 mrad on the  $\Theta_C^m$  and the SPR values.

The error coming from different beam particle species with different Cherenkov angles is based on the measurement with the TOF system. It was possible to separate light and heavy particles in the runs with the low momentum beam. The study in Ref. [33] showed mainly electrons, pions and much smaller amount of protons in the beam. The observed ratio of these particles and the additional information from the beamline specification gives just around 74% of electrons and pions, 23% protons, 1% of kaons, and 2% of other particles. To evaluate the possible effect in the simulation a 3 to 1 mix of pions to protons with momenta of 10 GeV/c was generated. Here, the simulated  $\Theta_C^m$  value is different for pions and protons by almost 4 mrad. The influence of taking the particle mix in comparison to the pure pion sample  $\sigma_{Beam}$  was about 0.2 mrad on  $\Theta_C^m$  and it was negligible for the SPR value.

Due to the more convoluted and folded hit pattern caused by the prism the evaluation of the errors on  $\Theta_C^m$  and the SPR was more complicated for the 2012 campaign. The single photon Cherenkov angle distribution shows large bin-to-bin fluctuations that are the result of the ring image being mostly parallel to MCP-PMT columns and large combinatorial background makes it harder to separate the peak associated with the correct photon paths. Eight different bin widths were considered resulting in the stable results. The *rms* of the differences of the fit results was used as the estimator for the error and the result is  $\sigma_{Bin} = 0.5$  mrad on  $\Theta_C^m$  and 0.6 mrad on the SPR. The impact of the fit parameterization on the systematic error was tested by fitting a combination of a Gaussian with different polynomial functions for the background, providing  $\sigma_{Fit f}$  at the level of 0.2 mrad on  $\Theta_C^m$  and 0.3 mrad on the SPR. The combination of a Gaussian and a linear background function in the 780-900 mrad range reproduces the shape well. By varying the fit range the uncertainty  $\sigma_{Fit r}$  was determined as 0.2 mrad both on  $\Theta_C^m$  and on the SPR.

In order to evaluate the stability of the setup, the photon yield and SPR were compared between runs taken at different times, with similar configuration. Runs R1, R2, R3 and one of the sub-samples from R5 were used in that study. The variation of the measured multiplicity of hits per track, the reconstructed  $\Theta_C^m$  and its resolution, was smaller than the errors in each run. This demonstrates good control of the prototype parameters and no additional error was assigned to the repeatability. The uncertainty due to the determination of the simulation parameters was studied by simulating data sets with the same configurations but small changes to beam polar angle and PrismStep. The uncertainty  $\sigma_{MC}$  is at the level of 0.1 on photon yield, 0.2 mrad on  $\Theta_C^m$ , and 0.1 mrad on the SPR.

The reconstruction of the Cherenkov angle and the determination of the photon yield were performed for different sample sizes of the same run, using 210,000, 420,000, and 840,000 events. No influence on the final results was observed and the statistical error is negligible in comparison to the systematic error.

The individual errors are listed in the table Tab. 4.10, showing how they contribute to the overall error  $\sigma_{Tot}$  in this particular run. All these sources are considered to be independent and can be added in a quadrature to determine  $\sigma_{Tot}$  as 0.7 mrad both on the mean and the width of the single photon Cherenkov angle and 0.2 on the photon yield.



Quantity	$\sigma_{Event}$	$\sigma_{Hit}$	$\sigma_{Beam}$	$\sigma_{Bin}$	$\sigma_{Fit f}$	$\sigma_{Fit r}$	$\sigma_{MC}$	$\sigma_{Stat}$	$\sigma_{Tot}$
$\Theta_C^m$ [mrad]	0.04	0.12	0.25	0.53	0.17	0.19	0.20	0.01	0.68
SPR [mrad]	0.04	0.13	0.03	0.64	0.26	0.22	0.12	0.01	0.75
Photon yield	0.01	0.19	-	-	-	0.03	0.14	0.07	0.24

Table 4.10: Individual sources of the overall error  $\sigma_{Tot}$  on  $\Theta_C^m$ , SPR and the photon yield.  $\sigma_{Tot}$  is a result of the sum of the individual terms in quadrature and is dominated by the systematic error.

The systematic error evaluation has to be modified for the results obtained using the fine angle scan method to treat the combinatorial background. This method effectively removes the effect of the pixelization and the contribution from the bin width,  $\sigma_{Bin}$ , becomes negligible. However, a new systematic error arises due to the quality of the matching of the configuration parameters in the simulation for each of the individual sub-samples. Any possible shift of the mean value in a sub-sample will lead to an increase of the width of the distribution and, thus, a larger value for  $\sigma_{\Theta_C}$ . The simulation was used to evaluate the size of this error contribution. First, a set of 8 runs was combined and reconstructed using the correct simulation parameters, this defines the best match and the most accurate measurement of the mean and width of the distribution. Next the runs were combined using in the reconstruction a set of parameters that were changed as much as allowed by the measurement precision during the beam time. The situation that reflects the worst case scenario is given by selecting four of the runs with the maximum deviation in one direction of the mean value of the distribution, and the remaining four in the opposite direction. The difference of the results from this worst case scenario and the correct parameter choice is divided by square root of 12 to define  $\sigma_{MC}$ , the uncertainty due to the tuning of the parameters in simulation. The resulting total error is approximately the same for runs analyzed using the simulated background and for runs using the fine angle scan method.

### Corrected Photon Yield

The photon yield is obtained by the following correction:

$$N_{ph} = (N_{Hits/Trigger} - N_{Background}) \times 0.85$$

$N_{Hits/Trigger}$  is the number of measured hits per trigger discussed in Sec. 4.2.4.  $N_{Background}$  is the number of background photons coming from delta electrons, scattering, and electronic noise of MCP-PMTs. The factor 0.85 corresponds to the charge sharing effect of the MCP-PMTs. Applying this correction to the values for run R1,  $N_{Hits/trigger} = 27.7 \pm 0.2$  (see Sec. 4.2.4) and  $N_{background} = 3.6 \pm 0.4$ , results in a photon yield per particle of  $N_{ph} = 20.4 \pm 0.4$  which is close to the value obtained in Monte Carlo simulation as  $21.4 \pm 0.1$  photons per particle.

### 4.2.5 Comparison of the Bars

One of the goals of the 2012 test beam campaign was to study different prototype bars. Five narrow bars were tested, four made of fused silica and one of acrylic glass. The runs used for

that study were taken with similar configurations and under very similar conditions to easily compare the bar performance in terms of photon yield and SPR. All selected runs for this study were measured with beam polar angle close to  $120^\circ$ . It was the most optimal position of the prototype in 2012 test beam to determine the photon yield and SPR. In this position, the smallest number of photons was lost in the gaps between the MCP-PMTs and the location of the ring image, with main part of one of the rings isolated on one MCP-PMT column, made it easier to study the reconstruction of the Cherenkov angle. The standard lens L1 with 3.2 mm air gap was used in the studies discussed in this section.

The analysis of the data was carried out analogously to the procedure presented in previous section. All cuts and the error evaluation were established individually for each run.

First, the analyzed runs were compared in terms of the photon yield. Roughly 20 photons per event are expected from the Monte Carlo simulations. However, the used bars differ not only in material from which they are made and fabrication methods but also in sizes. The size differences of the bars were included in the DrcProp simulation. The results from the experiment and simulation are summarized in Tab. 4.11. The photon yields for the fused silica bars are consistent with the expectations and their qualities are comparable. The only significant difference is observed for the acrylic glass bar. The comparison of the hit distributions and photon yield for the acrylic glass P2 bar to the B3 quartz bar is shown in Fig. 4.49. Not only the photon yield but also the observed ring image are significantly different. Expected “fish-like” structure with overlapping outer part of the ring segments is visible for the B3 bar. For the P2 bar the ring image is visible only for direct photons. All the photons with longer paths are presumably scattered and most of them are not detected. It is an additional argument against acrylic glass as a candidate for the DIRC radiator. The performance of the configuration with the acrylic glass bar is clearly not sufficient to meet the PANDA Barrel DIRC requirements.

Bar	Run	Measured (Raw) Hits/Event	Measured (Corrected) Photons/Event	Simulated Photons/Particle
B3	R1	$27.7 \pm 0.2$	$20.5 \pm 0.4$	$21.4 \pm 0.1$
Z5	R8	$25.4 \pm 0.2$	$18.4 \pm 0.4$	$20.8 \pm 0.1$
L3	R11	$23.7 \pm 0.2$	$17.1 \pm 0.4$	$20.8 \pm 0.1$
LZ1	R9	$23.8 \pm 0.2$	$17.2 \pm 0.4$	$20.8 \pm 0.1$
P2	R10	$7.7 \pm 0.2$	$3.5 \pm 0.4$	$25.2 \pm 0.1$

Table 4.11: Comparison of the photon yield for bars used in the 2012 test beam. The measured quantity and corrected experimental values are compared to the DrcProp predictions. The simulation used the properties of synthetic fused silica for all bars, including the acrylic bar P2. Details about the bars and the runs can be found in Tab. 4.5 and Tab. 4.7.

Two fused silica bars, B3 made by InSync and Z5 by Zeiss, were also compared in terms of the single photon resolution. The combinatorial background was reproduced in the simulation and subtracted from the  $\Theta_C$  distribution. The distributions with subtracted prism background are shown in Fig. 4.50. Since the fine angular scan measurements were performed for both bars (runs R5 and R7, see Tab. 4.7) with the beam incidence angle range of  $32\text{-}34^\circ$ , further improvement of the reconstructed values was possible. The resulting distributions are shown in Fig. 4.51, and the corresponding values for these runs as well as for the single runs analyzed with the background subtraction method are shown in Tab. 4.12. A Gaussian with a linear background was fitted to the distribution to obtain the  $\Theta_C^m$  and SPR. A mismatch of the simulation parameters can cause shifts of the  $\Theta_C$  mean value for each run which, after combining the runs in fine angular scan, would increase the measured SPR value for the combined set.

Run	Radiator	$\Theta_C^m$	$\sigma_{\Theta_C}$	Correction Method	Figure
R1	B3	$824.3 \pm 0.9$	$11.6 \pm 0.7$	background subtracted	4.50a
R8	Z5	$823.4 \pm 0.9$	$13.5 \pm 0.7$	background subtracted	4.50b
R5	B3	$823.7 \pm 0.7$	$12.0 \pm 0.7$	fine angle scan	4.51a
R7	Z5	$821.9 \pm 0.7$	$13.0 \pm 0.7$	fine angle scan	4.51b

Table 4.12: Results of the  $\Theta_C$  reconstruction for the test beam data obtained with InSync B3 and Zeiss Z5 bars. Details about the runs can be found in Tab. 4.7.

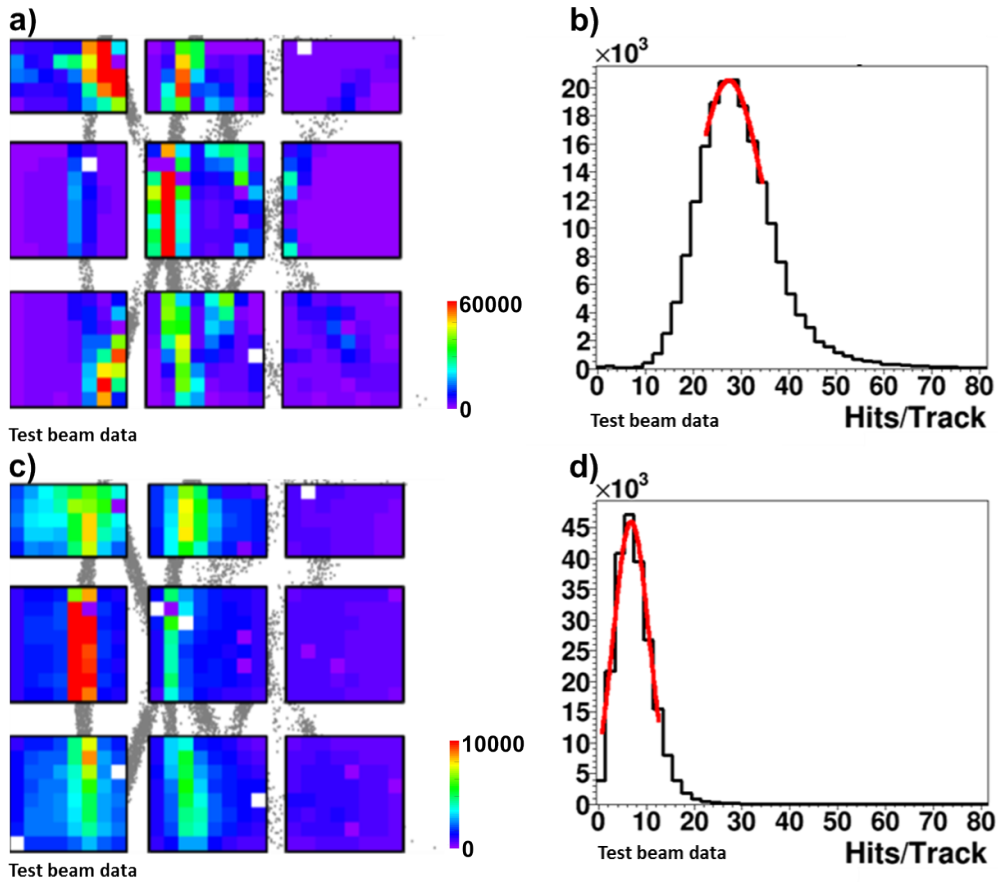


Figure 4.49: Comparison of the performance of B3 bar (fused silica) and P2 bar (acrylic glass). a) and b) show the occupancy plot and the measured number of photons per trigger for the fused silica bar. Figures c) and d) show the same quantities for the Acrylic glass bar. The corresponding results are found in Tab. 4.11.

However, the values of both  $\Theta_C^m$  and SPR are consistent with simulation, if the contribution from the beam divergence is taken into consideration, and this consistency confirms the good quality of this bars.

The differences in the SPR for the fused silica bars was expected to be small. Due to the rather short photon paths in this configuration, with photons reflected on average 30–40 times before reaching the sensor, the measurement was not sensitive enough to bar imperfections to

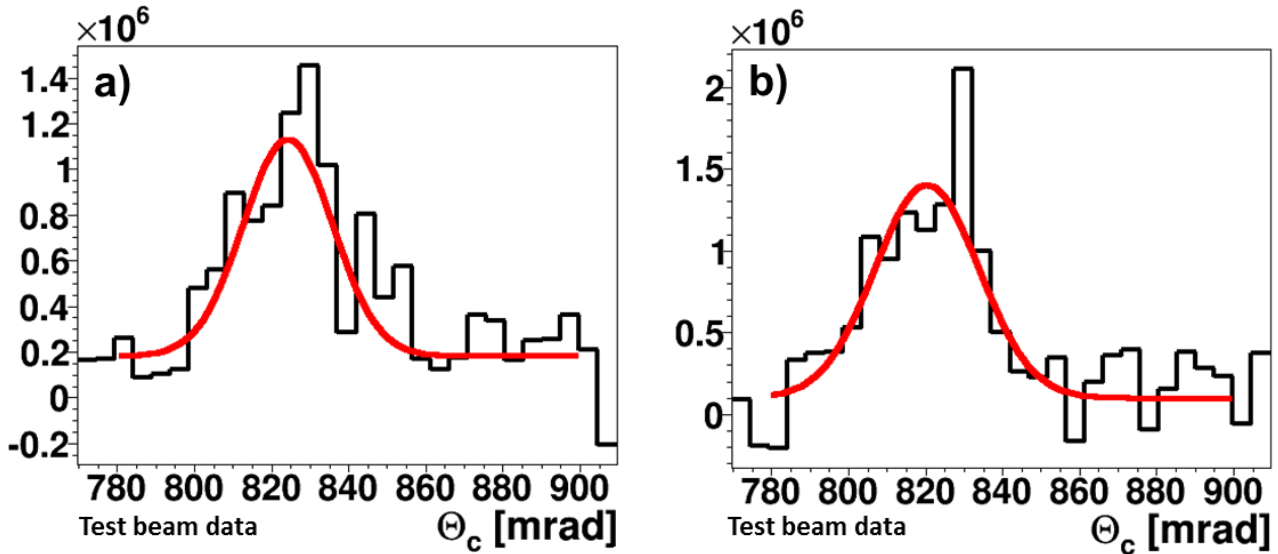


Figure 4.50: Reconstructed Cherenkov angle per photon from 2012 prototype after background subtraction for runs R1 with the InSync B3 bar (a) and R8 with the Zeiss Z5 bar (b). The results are listed in Tab. 4.12.

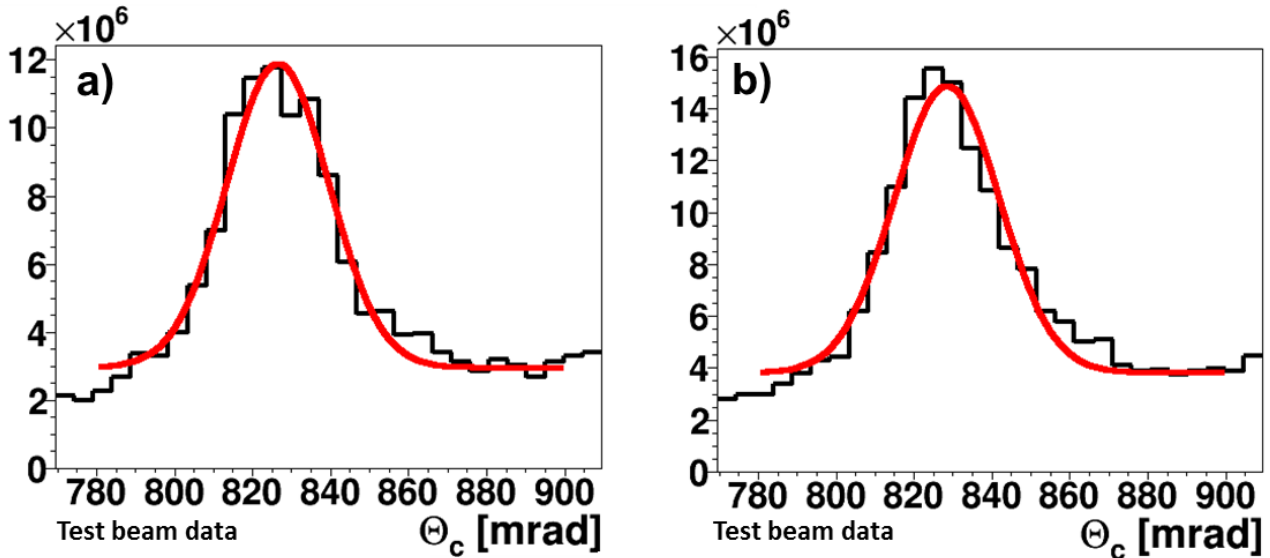


Figure 4.51: Reconstructed Cherenkov angle per photon with the fine angular scan method from 2012 prototype with the InSync B3 bar (a) and the Zeiss Z5 bar (b). Both bars were scanned over a similar range of the beam polar angle. The results are listed in Tab. 4.12.

be able to observe significant differences between fused silica bars from different manufacturers. The Barrel DIRC detector with 2.4 m radiator bars will have much longer photon paths with more reflections. Therefore, a detailed study of the optical properties of the bars is required before the final decision on the vendor for the PANDA Barrel DIRC bars can be made. This is the primary motivation for the measurements used to qualify the photon transport efficiency of the bars on test benches with a laser system, described in Sec. 3.5.1.

### 4.2.6 Focusing Optics

The 2012 test beam studies were performed with and without focusing. A number of different lenses were compared, including four standard lenses with different anti-reflective (AR) coatings, tagged L1, L3, L4, and L5 in the text. For this study runs with very similar configurations were selected to easily compare the performance in terms of photon yield and SPR. The influence of the small difference in sizes and configurations on the results is evaluated using the simulation. The results are summarized in Tab. 4.13 and Tab. 4.14. There is no significant difference in the results for different coatings. The last row in both tables show the results for lens L5 with does not have any coating and there is no difference in the performance compared to lenses with AR coating. Only the cylindrical lens L4 performed slightly worse, but the deterioration is also not significant. Lens L1 was selected for further analysis and discussion of different focusing options, due to the larger number of available runs in similar configuration to compare them.

Lens	Run	Angle	Measured (Raw) Hits/Event	Measured (Corrected) Photons/Event	Simulated Photons/Particle
L1	R23	154°	56.0 ± 0.2	44.5 ± 0.4	46.0 ± 0.1
L3	R24	154°	56.2 ± 0.2	44.7 ± 0.4	46.0 ± 0.1
L4	R25	154°	52.8 ± 0.2	41.8 ± 0.4	45.5 ± 0.1
L5	R26	154°	56.0 ± 0.2	44.5 ± 0.4	45.9 ± 0.1

Table 4.13: Comparison of the photon yield for standard lenses with different coating used in the 2012 test beam. The measured quantity and corrected experimental values are compared to the DrcProp predictions. Details about the lenses and the runs can be found in Tab. 4.6 and Tab. 4.7.

Lens	Run	Beam Angle	Experimental $\Theta_C^m$ [mrad]	Experimental $\sigma_{\Theta_C}$ [mrad]	Simulated $\Theta_C^m$ [mrad]	Simulated $\sigma_{\Theta_C}$ [mrad]
L1	R23	154°	822.5 ± 0.9	10.7 ± 0.7	825.7 ± 0.3	9.7 ± 0.5
L3	R24	154°	823.4 ± 0.9	11.2 ± 0.7	824.9 ± 0.3	10.3 ± 0.5
L4	R25	154°	825.4 ± 0.9	12.8 ± 0.7	825.1 ± 0.3	11.5 ± 0.5
L5	R26	154°	822.5 ± 0.9	11.4 ± 0.7	826.1 ± 0.3	9.5 ± 0.5

Table 4.14: Comparison of the reconstructed Cherenkov angle per photon for standard lenses with different coating used in the 2012 test beam. The measured quantity and corrected experimental values are compared to the DrcProp predictions. Details about the lenses and the runs can be found in Tab. 4.6 and Tab. 4.7.

Figure 4.52 shows photos from the test beam of two attached lenses: the standard L1 lens (a) and the compound lens L2 without an air gap (b). The comparison of the three main options: no focusing, a standard lens and a compound lens without an air gap shows a big difference already in the occupancy plots (see Fig. 4.53). Details of the prototypes are described in the Tab. 4.7. The occupancy plot for the configuration without focusing, where the bar is coupled directly to the prism shown in Fig. 4.53a is obtained from run R18. The ring image is blurred, but the main parts of the ring segments can be recognized. Even photons with steep angles are detected due to the direct coupling of the bar to the prism. Therefore, many hits are observed on the right column of the MCP-PMT array. The focused images are obtained from runs R14 (Fig. 4.53b) and R15 (Fig. 4.53c), with a slightly larger beam angle, and much smaller PrismStep. Therefore, a substantial part of both rings is visible on one column of MCP-PMTs.

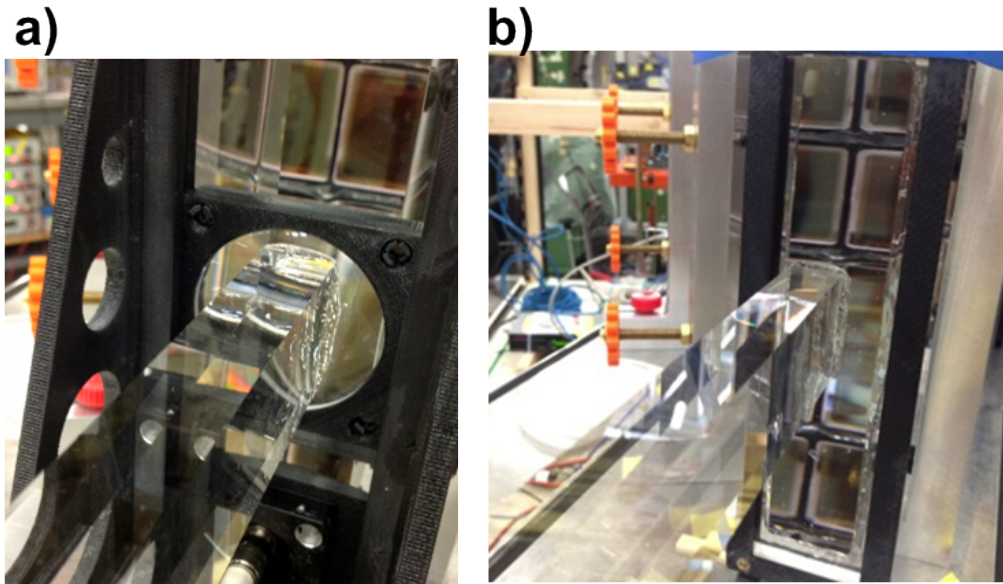


Figure 4.52: Photo of a) lens L1 and b) lens L2 in the prototype from the 2012 test beam.

The air gap in the configuration with the lens L1 is responsible for part of the photons with the steeper angles being internally reflected and part not making it to the prism. As a result, the outer parts of the ring segments are not detected. The compound lens L2 without an air gap (Fig. 4.53c) shows an improvement. The outer part of the ring images are not preserved as well as with the direct connection of the bar, but still many photons survive, and the ring image is sharp.

The photon yield was measured in the 2012 prototype at CERN for these three types of focusing configurations and two polar angles, one forward and one almost perpendicular, shown in Fig. 4.54. The measured number of hits per track includes contributions from delta electrons and from charge sharing between MCP-PMT pads, which are not included in DrcProp simulations. After correcting for background effects the measured yield is consistent with the prediction from simulation (shown earlier in Fig. 4.35b). For the angle of  $128^\circ$  the lens L2 has a 10% higher photon yield than L1, consistent with the expectation from simulation. Figure 4.54b shows results for the runs measured with same prototype configurations but for a beam angle close to  $90^\circ$ . As expected, the internal reflection at the lens/air interface causes a dramatic drop in the number of photons, while the multiplicity for lens L2 and the bar coupled directly to the prism, remains high. The measured and corrected values, together with predictions from DrcProp are listed in Tab. 4.15.

The single photon Cherenkov angle was reconstructed for runs R14 and R15 with an angle of  $128^\circ$  and different lenses, unfortunately no fine angle scan data was available for this configuration with lens L2. The reconstruction of the Cherenkov angle for configuration with lens L2 is more complicated than with standard lens L1. Photons with steep angles are not lost and have many reflections in the prism before being detected. Therefore, more ambiguities have to be considered what significantly increases the combinatorial background in the  $\Theta_C$  distribution. The Monte Carlo simulation showed that most of the measured photons have an arrival time below 12 ns, and up to 3 reflections in the prism. Therefore, only photon paths with up to three reflections in the prism are considered. The outcome of this particular approach is shown in Fig. 4.55. Predictions from the Monte Carlo simulation are shown in Fig. 4.56. The obtained  $\Theta_C^m$  values are consistent with the simulation but a full reconstruction with all ambiguities included is needed. The reconstruction of the Cherenkov angle for the configuration without

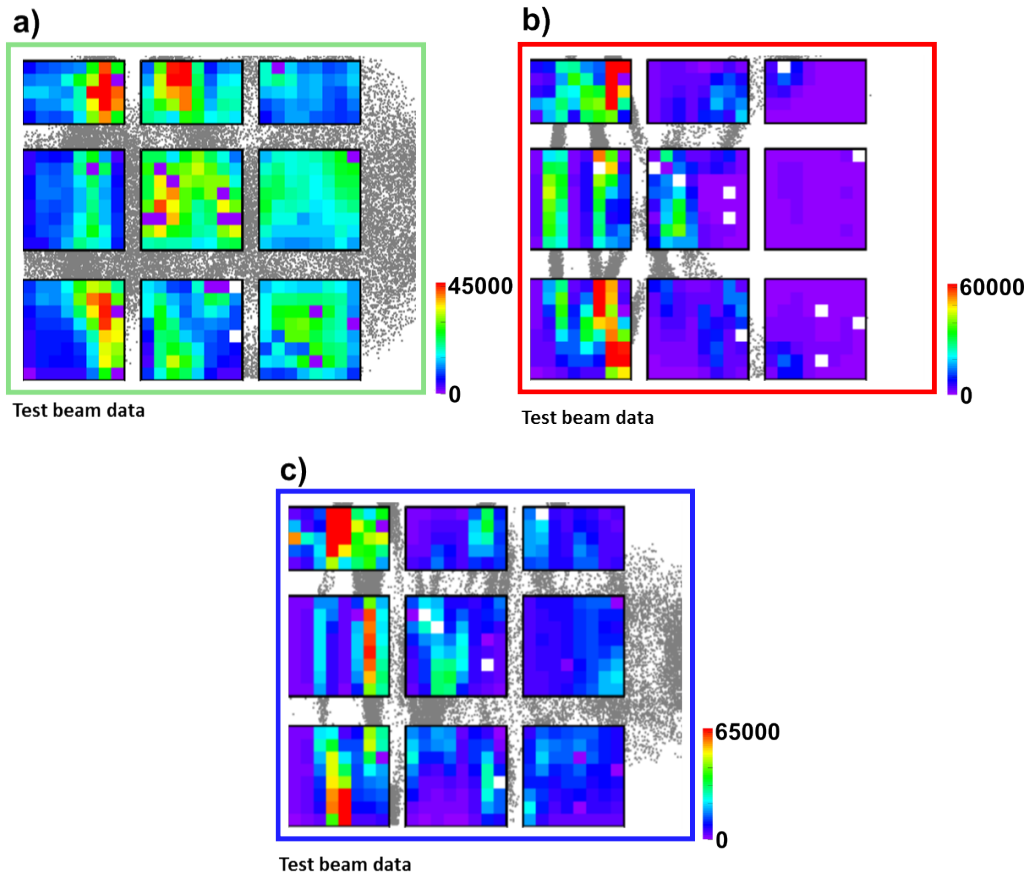


Figure 4.53: Distribution of the hits per MCP-PMT in the experimental data for runs measured with different focusing options: a) no focusing (R18), b) lens L1 (R14), and c) lens L2 (R15). The gray points in the background are the true hit positions from simulation to guide the eye.

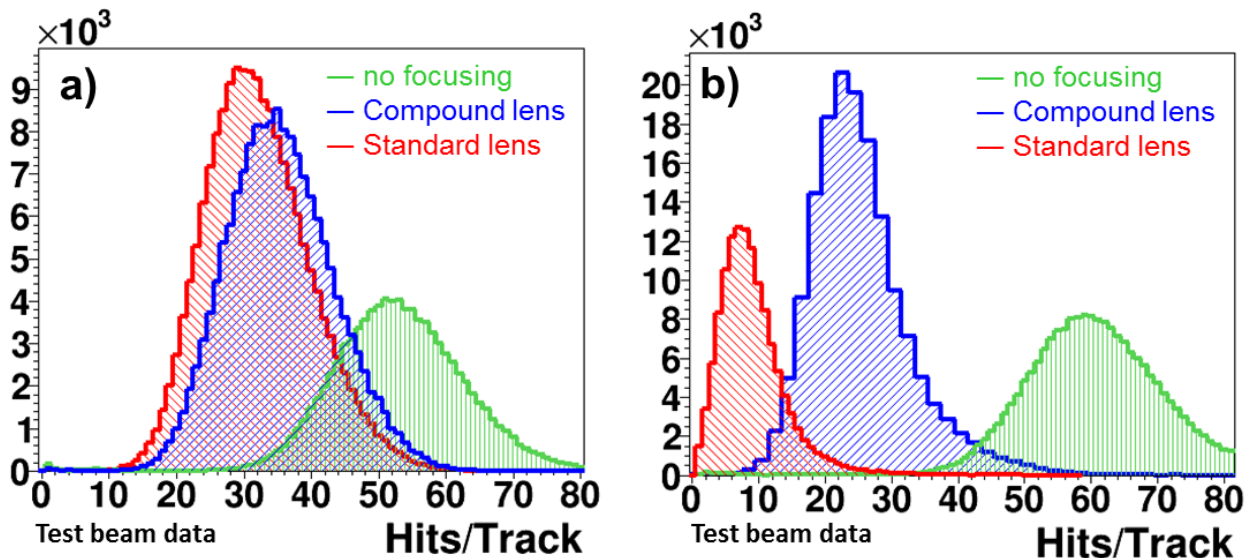


Figure 4.54: Comparison of the multiplicity of the measured hits per track in setups with different focusing options. Figure a) shows:  $124^\circ$  without focusing (R18) in green,  $128^\circ$  with lens L1 (R14) in red and  $128^\circ$  case with compound lens L2 (R15) in blue, b) shows the same for  $90^\circ$  (R22),  $92^\circ$  (R12), and  $93^\circ$  (R16).

Focusing	Run	Beam Angle	Measured (Raw) Hits/Event	Measured (Corrected) Photons/Event	Simulated Photons/Particle
No	R18	124°(124.0°)	52.0 ± 0.3	41.2 ± 0.4	41.2 ± 0.1
L1	R14	128°(128.0°)	30.4 ± 0.2	22.8 ± 0.4	26.8 ± 0.1
L2	R15	128°(127.5°)	34.3 ± 0.2	26.1 ± 0.4	28.6 ± 0.1
No	R22	90°(93.1°)	59.2 ± 0.3	47.2 ± 0.4	45.6 ± 0.1
L1	R12	90°(91.2°)	5.8 ± 0.2	1.9 ± 0.4	1.5 ± 0.1
L2	R16	90°(91.0°)	23.2 ± 0.2	16.6 ± 0.4	17.7 ± 0.1

Table 4.15: Comparison of the photon yield measured with different focusing options in the 2012 test beam. Measured quantities and corrected experimental values are compared to the DrcProp predictions in the last column. Details about the lenses and the runs can be found in Tab. 4.5 and 4.7.

focusing is challenging and the results are difficult to interpret. The fuzzy ring image and the large number of detected photons with steep angles and the resulting overlapping ring segments cause many additional ambiguities and a more complicated combinatorial background. The geometric reconstruction approach is unable to extract meaningful values from the fit to the Cherenkov angle distribution.

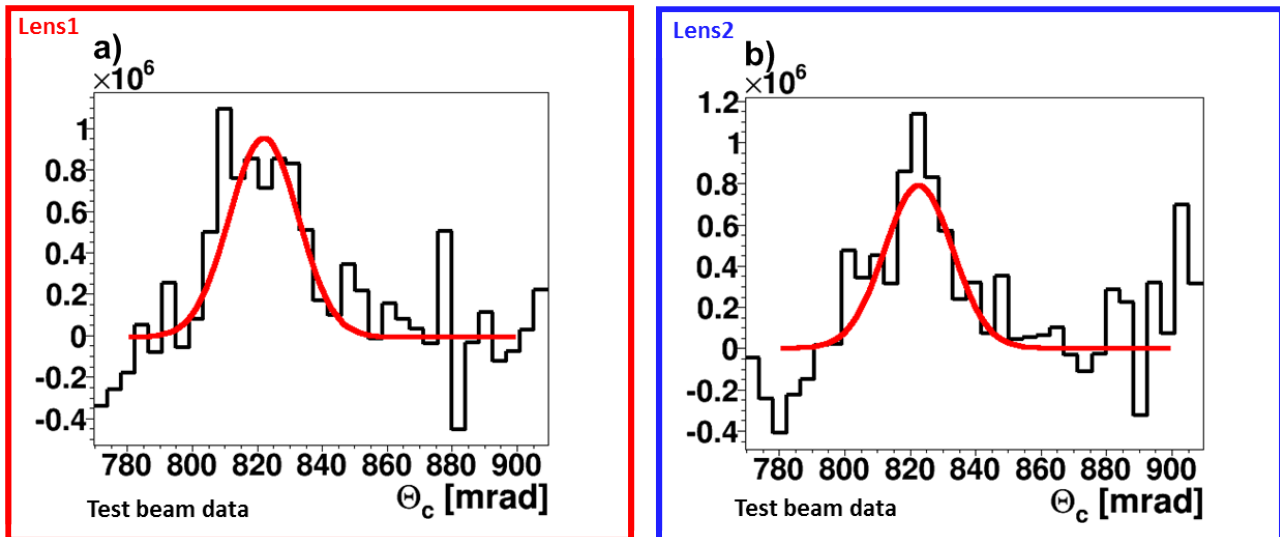


Figure 4.55: Reconstructed Cherenkov angle per photon from 2012 prototype data after subtraction of the simulated prism background for setups with a) lens L1 (R14) and b) lens L2 (R15). The corresponding results are listed in Tab. 4.16.

The configuration without focusing, where the bar is coupled directly to the prism, has two times worse SPR and only moderately better photons yield. Therefore, the track Cherenkov angle resolution is worse and does not meet the PANDA PID goals (as discussed in Ref. [15]). That is why this is no real option for PANDA barrel DIRC and the lens has to be used.

Two kinds of lenses were tested, a standard lens and a prototype compound lens without an air gap. Four standard lenses with different AR coating options were checked but no significant difference in performance was observed. The standard focusing lens provides good resolution but low photon yield specially close to 90° particle incidence angle.

The selection of the final lens is a careful optimization process. The photons at steep angles



Run	Lens	Data Type	$\Theta_C^m$	$\sigma_{\Theta_C}$ [mrad]	Figure
R14	L1	test beam	$822.0 \pm 1.1$	$10.6 \pm 0.8$	4.55a
R15	L2	test beam	$822.6 \pm 0.9$	$11.8 \pm 0.7$	4.55b
MCR14	L1	simulated	$824.2 \pm 0.4$	$8.1 \pm 0.5$	4.56a
MCR15	L2	simulated	$824.5 \pm 0.3$	$12.3 \pm 0.5$	4.56b

Table 4.16: Results of the  $\Theta_C$  reconstruction for the test beam data and simulated data for the prototype configuration with the L1 and L2 lenses. The correction of the combinatorial background in experimental data is obtained by subtraction of the simulated prism background (first two rows). Details about the runs can be found in Tab. 4.7.

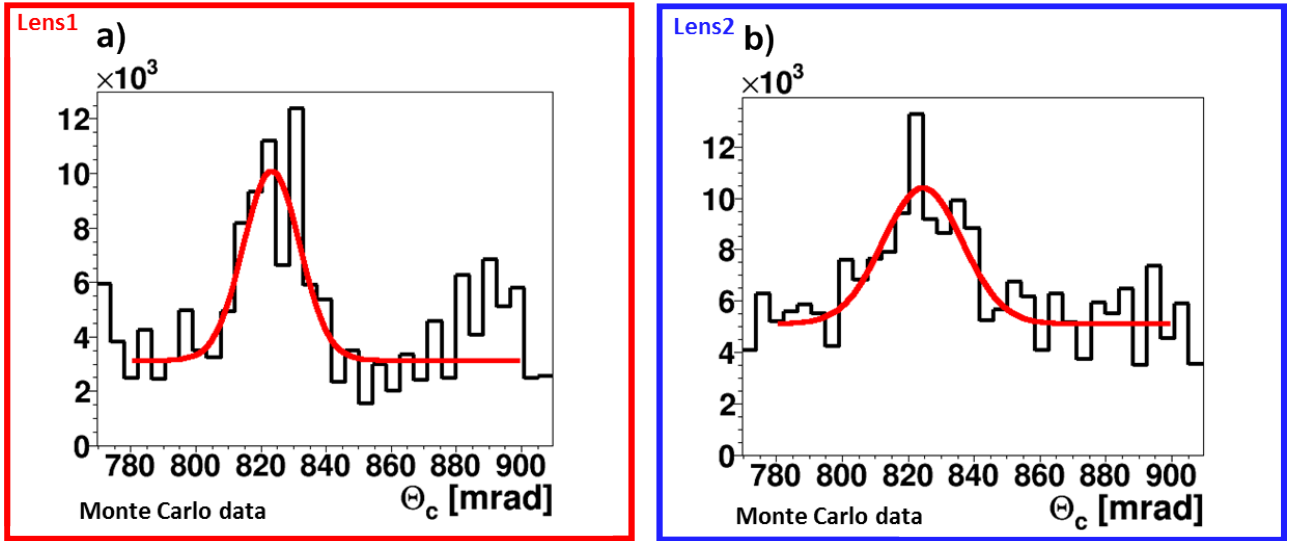


Figure 4.56: Reconstructed Cherenkov angle per photon from 2012 prototype Monte Carlo data for a) MCR14 (lens L1) b) MCR15 (lens L2). Corresponding results are listed in Tab. 4.16.

are neither for standard lens nor for high-refractive compound lens of a good quality. This is due to the shape of the focal plane discussed in 3.5.2. Those photons will have a large imaging error associated with them, not just due to the distance of the actual focal point from the imaging plane, but also due to the larger optical aberration of the system. The large loss of photons in the runs at  $90^\circ$  rules out the standard L1 lens with the air gap for the PANDA Barrel DIRC because a meaningful PID is impossible with so few detected photons. Therefore, the L2 high refractive index lens without an air gap is the best candidate for the PANDA Barrel DIRC with very good focusing and significant increase on the number of transmitted photons. The higher photon yield makes this design much more tolerant of track and event background than the standard lens with an air gap. Several technical challenges remain like how well this lenses can be produced in case of the optical finish of the sides, is it radiation hard, etc. and have to be still studied. The thickness of the lens is over 14 mm and at the moment photons hitting the sides are lost. The photon yield would be even better if it would be possible to built this lens with reflective sides.

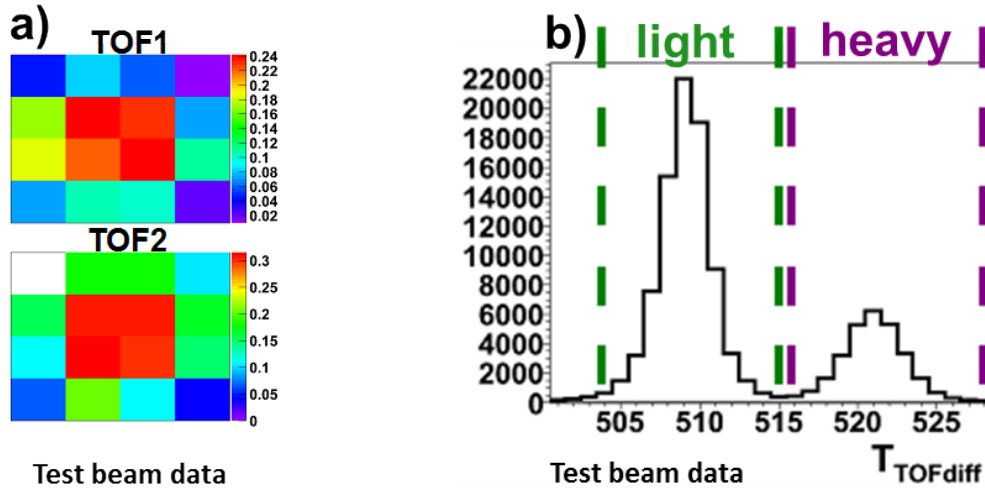


Figure 4.57: a) Distribution of hits recorded by the TOF MCPs in R19 normalized to one. b) The TOF MCP-out signal time difference.

### 4.2.7 PID Study Using the TOF System

The reconstruction procedure was validated by comparing the Cherenkov angle measurement to external PID information from the MCP-TOF system. Run R19 with a beam momentum of 3 GeV/ $c$  and a beam/bar polar angle of 124° was used for this study.

Figure 4.57 shows the occupancies for the two MCP-TOF stations and the measured time-of-flight, calculated as  $T=T_1-T_2$ . Two clearly separated time peaks can be seen, corresponding to the heavy (protons) and light (electrons, muons, and pions) particles. Events which included the coincidence of both TOF MCPs were selected from a sample of 130,000 recorded triggers. 74% of the tracks in the selected sample were tagged by the MCP-TOF time difference as light particles and 26% as heavy particles.

The location of the ring image on the MCP-PMT array for these separate samples is shown in Fig. 4.58. The occupancy on the sensors of the DIRC prototype, light versus heavy particles, shows two well-separated rings in good agreement with the positions predicted by the ray-tracing simulation.

The reconstruction of the Cherenkov angle per photon was performed on the separate samples and the outcome is shown in Fig. 4.59 and Tab. 4.17. After the subtraction of the simulated combinatorial prism background the distribution is well-described by sum of a Gaussian and a linear function. The obtained  $\Theta_C^m$  values are in very good agreement with calculations for the 3 GeV/ $c$  momentum particles. Figure 4.60 shows that, even at the single photon level, a clear separation of the reconstructed Cherenkov angle is seen for the light and heavy tagged samples at 3 GeV/ $c$ .

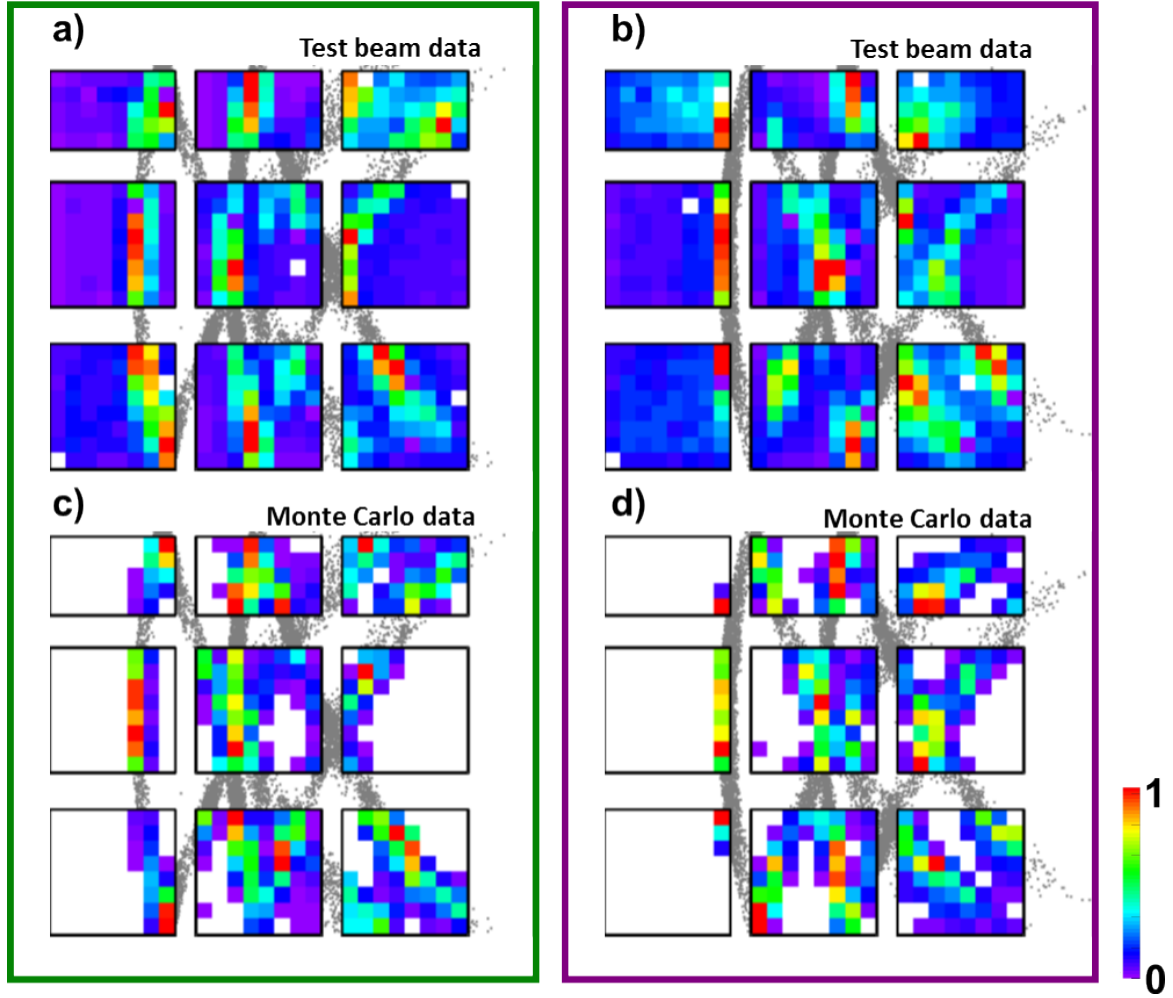


Figure 4.58: Distribution of the hits per MCP-PMT in the experimental data (a,b) and Monte Carlo data (c,d) for the samples of light (left column) and heavy (right column) particles tagged by the TOF system.

Run	Feature	Data Type	$\Theta_C^m$	$\sigma_{\Theta_C}$	Background Treatment	Figure
R19	light	test beam	$825.6 \pm 0.9$	$9.8 \pm 0.7$	background subtracted	4.59a
R19	heavy	test beam	$781.3 \pm 0.9$	$11.9 \pm 0.7$	background subtracted	4.59b
R19	pions	simulated	$823.9 \pm 0.3$	$8.9 \pm 0.5$	no	4.60b
R19	protons	simulated	$779.6 \pm 0.3$	$6.9 \pm 0.5$	no	4.60b

Table 4.17: Results of the  $\Theta_C$  reconstruction for the test beam data tagged with the TOF system as light and heavy particles. The combinatorial background is subtracted (first two rows). Details about the runs can be found in Tab. 4.7.

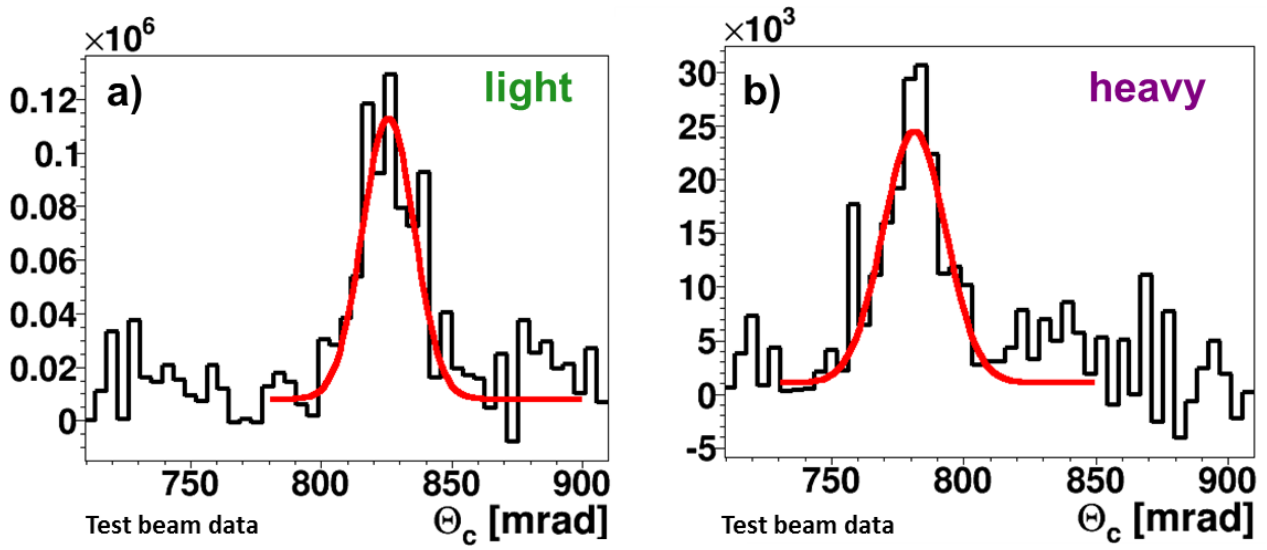


Figure 4.59: Reconstructed Cherenkov angle per photon from 2012 prototype data for the light and heavy samples from run R19 tagged by the TOF system as shown in Fig. 4.57.

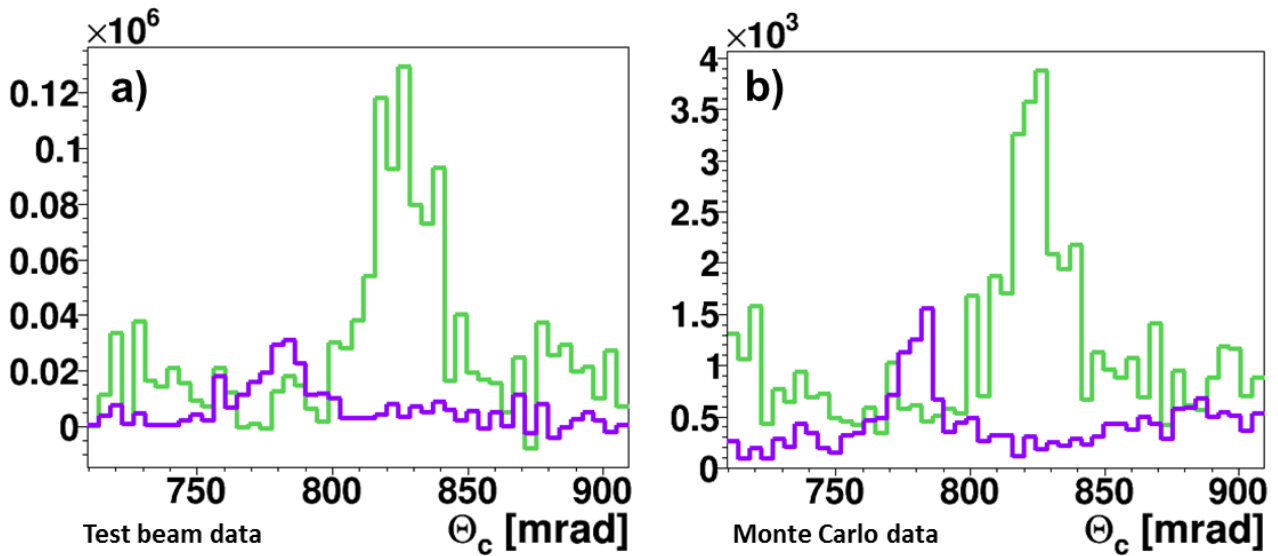


Figure 4.60: Reconstructed Cherenkov angle per photon from 2012 prototype data for 3 GeV/ $c$  particles, tagged as heavy (violet) and light particles (green) by the TOF system in a) experimental data and b) Monte Carlo data.

# Chapter 5

## Conclusion and Outlook

Hadronic particle identification (PID) in the barrel region of the PANDA detector will be provided by a DIRC detector. The baseline design is inspired by the successful *BABAR* DIRC. However, several modifications and improvements to adapt it to the PANDA environment are needed. The design has evolved through several stages, from a scaled-down version of the *BABAR* DIRC to a compact fast focusing DIRC. Detailed Monte Carlo simulation studies were performed to identify several design options capable of meeting the PANDA requirements. The performance of each design was characterized in terms of the photon yield and the single photon Cherenkov angle resolution (SPR). The goal of the prototype program is to show if the performance reached in the simulation can be experimentally confirmed. Selected options were implemented in prototypes and tested with hadronic particle beams to validate design options and critical components.

The development of two full system prototypes and the corresponding detector performance analysis from three test beam campaigns form the core of this thesis. Components were selected based on simulation studies and critical components were evaluated in the optical lab on the test benches. Measurements of the shape of the lens focal plane confirmed the strong curvature observed in simulation and motivated additional R&D on the focusing system. The DIRC radiator bars are the heart of the DIRC detector. Their optical and mechanical quality is critical for the Cherenkov angle resolution of the detector and, thus, the PID performance. The combination of tight optical and mechanical specifications makes the production of DIRC radiators challenging to optical industry. That is why a dedicated setup was built to study and validate different methods used by vendors to produce the bars. This motion-controlled setup was installed in a dark, temperature-stabilized clean room to determine the coefficient of total internal reflection and directly measure the photon transport efficiency of each bar.

The first large prototype was built in 2011 to evaluate the baseline design, consisting of a narrow bar, a standard spherical focusing lens with an air gap, and a large tank, filled with mineral oil, as expansion volume. The analysis of the data recorded in two test beam campaigns at GSI and at CERN confirmed that this design is capable of reaching the required single photon Cherenkov angle resolution.

The main focus of the second large prototype, tested in 2012, was on the compact fused silica prism used as expansion volume. However, many other aspects, design options and components of the PANDA Barrel DIRC were studied. The very versatile prototype construction made it possible to perform a lot of different studies that required fast modifications, replacing components and changing optical elements. This prototype also provided the first experience with the prism combined with a wide plate instead of a narrow bar, a geometry that offers the potential of significant cost reduction. The reconstruction of the data from the plate geometry

is the subject of Ref. [37].

The baseline configuration of the prototype tested in 2012 consisted of a narrow fused silica bar, a mirror, a standard focusing lens with anti-reflective coating and an air gap, and a synthetic fused silica prism as an expansion volume. Different components, including bars and lenses, were placed into the setup, measured, and their performance was compared in terms of the photon yield and the SPR.

Four fused silica prototype bars made by different vendors were compared. They did not show any significant difference in terms of the performance and proved to be of high quality. A bar made from acrylic glass showed large photon losses and poor image quality, confirming that this material is not suitable for long radiator bars.

Two types of focusing lenses were studied in the 2012 prototype at CERN, the standard lens with an air gap, and the compound high-refractive index fused silica/NLaK33 lens without an air gap. The photon yield and the single photon Cherenkov resolution measured with standard lenses with different anti-reflective coatings meet the requirements for the PANDA PID for most of the polar angle range. However, the air gap caused unacceptable photon losses for beam angles close to perpendicular incidence. The performance of the prototype compound lens without an air gap was proven to be a promising option for the PANDA Barrel DIRC with very good focusing and significant increase on the number of transmitted photons, especially for the beam polar angle range between 80-100°. The higher photon yield makes the PANDA Barrel DIRC design much more tolerant of track and event background.

The results of the analysis of the full system prototype tests in particle beam were shown to be consistent with simulation and allow the direct comparison of the baseline design to a number of design options. The performance obtained with the 2012 prototype confirmed that the compact focusing DIRC is promising concept for PANDA. The remaining questions are predominantly oriented towards optimization of the technical design in terms of performance versus cost. The use of the wide radiator plates and the design and test of more advanced high-refractive index spherical and cylindrical lenses will be the focus of another test beam campaign in 2014, which should form the basis for the technical design report of the PANDA Barrel DIRC, expected in 2015.

# Chapter 6

## Zusammenfassung

Das PANDA (antiProton ANnihilations at DArmstadt) Experiment ist eines der vier Hauptexperimente an der geplanten Beschleunigeranlage FAIR (Facility for Antiproton and Ion Research), welches auf dem Gebiet der bestehenden GSI Helmholtzzentrum für Schwerionenforschung GmbH in Darmstadt entstehen wird. Das PANDA-Experiment wird Untersuchungen auf dem Sektor der Hadronenphysik auf sehr hohem Niveau durchführen, wobei hierfür ein gekühlter Antiprotonenstrahl bislang unerreichter Intensität im Impulsbereich von 1,5-15 GeV/c verwendet werden wird. Es werden zwei Synchrotrone, SIS100 und SIS300, zur Teilchenbeschleunigung zum Einsatz kommen, wobei die Teilchenpakete anschließend den Experimenten zur Verfügung gestellt werden. Die Antiprotonen werden durch Protonenstöße mit dünnen Ni-Targets erzeugt, anschließend akkumuliert, gekühlt und schließlich in den HESR (High Energy Storage Ring) geleitet, an dem sich der PANDA-Detektor befinden wird. Um den vollständigen Nachweis aller Wechselwirkungsprodukte zu gewährleisten, ist der PANDA Detektor in zwei Hauptkomponenten unterteilt: das Vorwärts-Spektrometer (FS) und das Target-Spektrometer (TS). Das TS mit Axialsymmetrie umgibt den Wechselwirkungspunkt und deckt Polarwinkel im Bereich über  $22^\circ$  ab. Das FS wird die Zerfallsprodukte der Teilchenkollisionen analysieren, die in einem engen Winkelkonus von  $\pm 5^\circ$  vertikal und  $\pm 10^\circ$  horizontal emittiert werden. Zur Durchführung von Untersuchungen im open charm Sektor ist in der zentralen Region des TS ( $22^\circ$  -  $140^\circ$ ), aufgrund des hohen pionischen Untergrundes, eine Pion-Kaon Separation auf dem Niveau von mindestens drei Standardabweichungen erforderlich. Das hierfür vorgesehene Subsystem muss die Teilchenidentifikation (PID) im Impulsbereich von 0,5-3,5 GeV/c gewährleisten und in dem 2 T Magnetfeld des Solenoids betrieben werden. Es muss in der Lage sein, die extrem hohe Wechselwirkungsrate von bis zu 50 MHz zu verarbeiten. Des Weiteren muss es kompakt genug sein um die Größe des sich nach außen anschließenden Elektromagnetischen Kalorimeters in einem akzeptablen Rahmen zu halten und den Einfluss auf die Performanz dieses Subdetektors zu minimieren. Der für PANDA wichtige Impulsbereich zwischen 0,5 und 3.5 GeV/c liegt im Einsatzbereich von Cherenkov-Zählern. RICH (Ring Imaging CHerenkov counter) Detektoren kommen in vielen Experimenten zur Identifikation von geladenen Teilchen zum Einsatz. Das Funktionsprinzip basiert auf der Abhängigkeit des Emissionswinkels der erzeugten Cherenkov-Strahlung und der Zahl der emittierten Photonen von der Geschwindigkeit des einfallenden Teilchens. Es gibt verschiedene Arten von RICH Detektoren, bei PANDA wird ein Detektor zum Einsatz kommen, der auf dem DIRC (Detection of Internally Reflected Cherenkov light) Prinzip basiert.

Das grundlegende Design des PANDA Barrel DIRC wurde von dem erfolgreichen BABAR DIRC inspiriert und ist in Abb. 6.1 gezeigt. Allerdings mussten einige Modifikationen und Verbesserungen vorgenommen werden, um dieses Design an die PANDA Umgebung anzupassen.

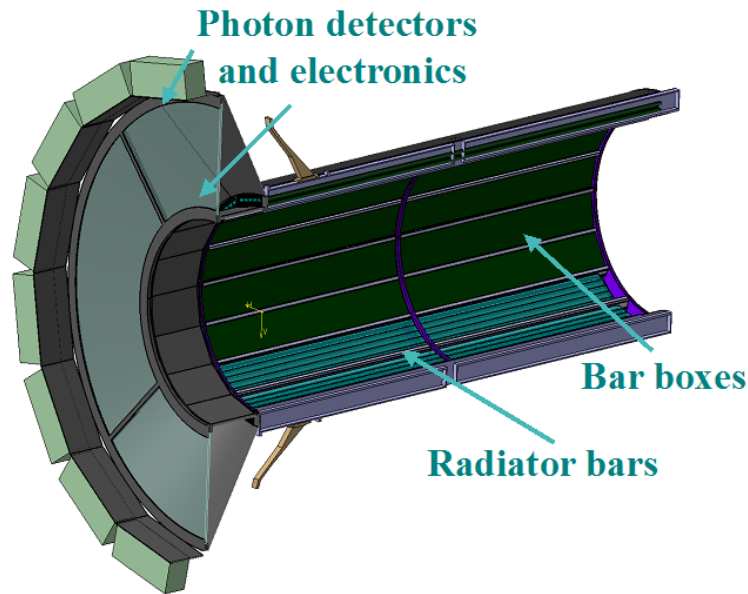


Figure 6.1: CATIA Zeichnung des PANDA Barrel DIRC Detektors.

Das Design dieses PANDA Subdetektors hat sich schrittweise von der skalierten BABAR Version zu einem kompakten, schnellen, fokussierenden DIRC Detektor entwickelt. Umfangreiche Monte-Carlo-Studien wurden durchgeführt, um verschiedene Design-Optionen zu identifizieren, die die Anforderungen des PANDA-Experimentes erfüllen können. Für jedes Design wurde die Leistungsfähigkeit hinsichtlich Photonenausbeute und Einzel-Photonen-Cherenkovwinkelauflösung (SPR) ermittelt. Das Ziel des Prototyp-Programms des PANDA Barrel DIRC ist es, zu überprüfen, ob die in den Simulationen erzielte Performanz experimentell bestätigt werden kann. Ausgewählte Optionen wurden in den Aufbau der verschiedenen Prototypen implementiert und mit hadronischen Teilchenstrahlen getestet, um kritische Komponenten und erfolgversprechende Designoptionen zu validieren. Vor dem Einsatz der Prototypen in verschiedenen Teststrahlzeiten steht die Vermessung einzelner Komponenten verschiedener Hersteller mittels hierfür entwickelter Testaufbauten. Die optischen und mechanischen Eigenschaften der DIRC Radiatorstäbe sind kritische Parameter des DIRC Detektors. Im Besonderen stellt die Kombination aus anspruchsvollen Spezifikationen der optischen und mechanischen Eigenschaften der langen Stäbe eine Herausforderung an die optische Industrie darstellt. Sieben verschiedene Hersteller fertigten über 30 Prototyp-Radiatoren für den PANDA Barrel DIRC an, wobei unterschiedliche Fabrikationstechniken zum Einsatz kamen. Im Rahmen dieser Arbeit wurde ein spezieller Testaufbau an der GSI entwickelt und zum Einsatz gebracht, um die Spezifikationen hinsichtlich der Form und Oberflächenqualität der Stäbe zu überprüfen.

Eine weitere wichtige Komponente sind fokussierende Linsen, die besondere Studien erforderlich machten. Messungen der Form der Brennebene bestätigten die erforderliche starke Krümmung, die in Simulationen bestimmt wurde und führten zur Weiterentwicklung des Fokussierungssystems. Der erste größere Prototyp wurde 2011 gebaut und ist in Abb. 6.2 zu sehen. Er bestand aus einem schmalen Radiatorstab, einem großen Tank, gefüllt mit Mineralöl, der als Ausdehnungsvolumen diente, und einer sphärischen fokussierenden Linse mit einem Luftspalt. Zwei Strahlzeiten bei GSI und am CERN wurden mit diesem Prototyp durchgeführt, die die Simulationen in Hinblick auf die für PANDA erforderliche Einzelphoton-Cherenkov-Winkelauflösung bestätigten. Eine detaillierte Darstellung der Messresultate für zwei verschiedene Konfigurationen dieses Setups ist in dieser Arbeit zu finden.

Ausgehend von den in 2011 gemachten Erfahrungen, wurde in 2012 ein weiterentwickel-



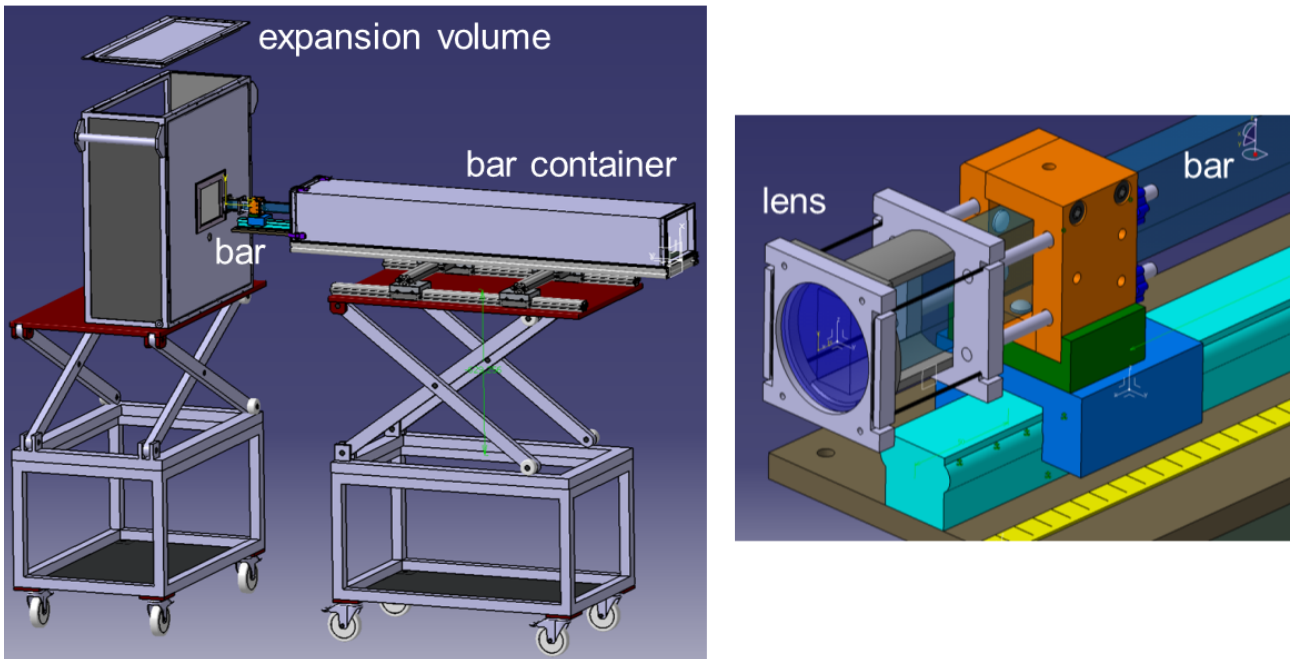


Figure 6.2: CATIA Zeichnung des 2011 Prototyps.

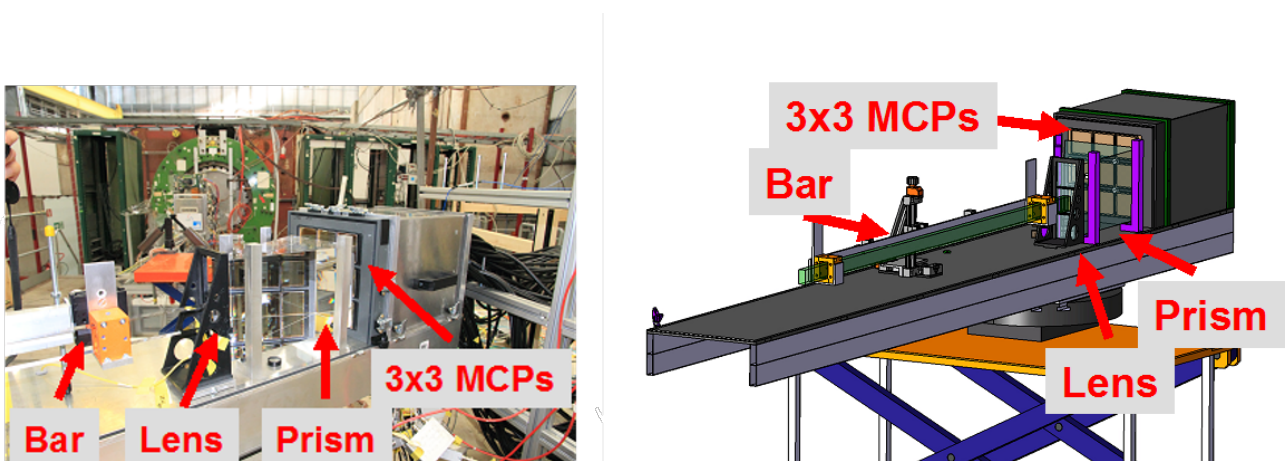


Figure 6.3: Fotografie und schematische Zeichnung des 2012 Prototyps.

ter Prototyp gebaut, der noch im Sommer des selben Jahres am CERN getestet wurde. Das Hauptaugenmerk neben vielen weiteren Komponentenuntersuchungen, lag bei dieser Strahlzeit auf der Untersuchung des neuen kompakten Quarzglas-Prismas, welches als Ausdehnungsvolumen dieses Prototyps diente. Ein Foto und eine schematische Skizze dieses Aufbaus sind in Abb. 6.3 zu finden. Die hier dargestellte äußerst modulare Konstruktion dieses Prototyps machte ein schnelles und unkompliziertes Wechseln verschiedener mechanischer und optischer Komponenten möglich. Der Prototyp wurde 2012 sich im T9 Areal am CERN PS aufgebaut. Unter Verwendung eines hadronenreichen Targets wurde ein positiver gemischter Hadronstrahl selektiert, dessen Impuls im Bereich zwischen 1,5 GeV/c und 10 GeV/c einstellbar war.

Der Polarwinkel zwischen dem einfallenden Teilchenstrahl und der lange Achse des Radiators wurde im Bereich zwischen  $20^\circ$  und  $156^\circ$  variiert. Der Schnittpunkt zwischen Strahl und Radiatorachse wurde 80 cm entlang des Stabes abgetastet, was einer Abdeckung des in

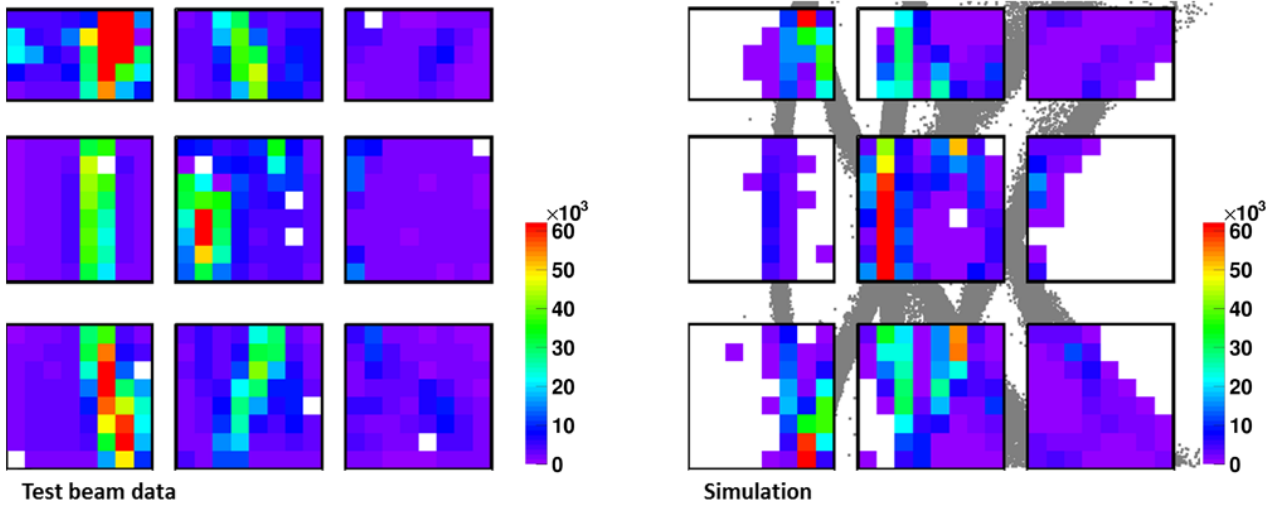


Figure 6.4: Anzahl der gemessenen Photonen pro MCP-PMT Pixel für etwa 200000 Ereignisse der 2012 Strahlzeit am CERN (a) und die entsprechende optische Simulation (b). Die Auftreffpunkte einzelner Cherenkov-Photonen zwischen den MCP-PMTs in der Simulation ist durch Punkte dargestellt.

PANDA zu erwartenden Phasenraums entspricht. Als Beispiel für eine solche Messung ist in Abb. 6.4 der beobachtete Cherenkov-Ring für den Polarwinkel von  $124^\circ$  gezeigt. Obwohl das dort gezeigte Treffermuster kompliziert erscheint und überlappende Segmente aufgrund von Reflexionen von allen Seiten des Prismas aufweist, stimmen diese Strukturen mit Vorhersagen aus einer optischen Simulation für Cherenkov-Photonen von  $10 \text{ GeV}/c$  Pionen (ebenfalls in Abb. 6.4 zu finden) überein. Die Simulation enthält deutlich weniger Untergrund als die Messdaten, da Prozesse wie delta-Elektronen, Dunkelstrom sowie Ladungsteilung der verwendeten Photosensoren (MCP-PMTs) nicht enthalten sind. Die Rekonstruktionsmethode des Cherenkov-Winkels ist der geometrischen Rekonstruktion, wie sie bei dem BABAR-DIRC zum Einsatz kam, angelehnt. Die Pixelposition und die Position des Stabes werden verwendet um dreidimensionale Richtungs-Vektoren zwischen dem Mittelpunkt des Radiatorstabes und jedem Pixel zu definieren, wobei diese in einer look-up table (LUT) abgelegt werden. Diese LUT wird mittels Simulationen generiert, wobei die gesamte Photosensorfläche gleichmäßig mit Photonen einer festen Wellenlänge aus einer Photonenkanone, platziert in Mitte des Stabes, ausgeleuchtet wird. Der Richtungsvektor wird mit dem Teilchenimpuls (gemessen mit dem Trackingsystem von PANDA) kombiniert um den Cherenkov-Winkel für jedes Photon zu berechnen. Der Weg des Cherenkov-Photons vom Teilchen zum Pixel kann jedoch nicht eindeutig rekonstruiert werden. Die Reflexionen innerhalb des Radiatorstabes erlauben für jeden Richtungsvektor bis zu 8 mögliche Photonen-Pfade oder Lösungen. Zudem tragen zusätzliche mögliche Reflexionen an den Innenseiten des Expansionsvolumens zu den Lösungen bei. Jede Lösung entspricht einem spezifischen Cherenkov-Winkel. Während die korrekten Lösungen sich in der Nähe des erwarteten Cherenkov-Winkels sammeln, formen die inkorrekten Lösungen einen kombinatorischen Untergrund.

Eines der Ziele der im Jahr 2012 durchgeführten Teststrahlzeit war die Untersuchung unterschiedlicher Prototyp-Stäbe. Fünf schmale Stäbe wurden getestet, wobei 4 davon aus künstlichem Quarzglas bestanden und einer aus Acrylglas. Es zeigte sich, dass Acrylglas als Radiatormaterial für den PANDA Barrel DIRC aufgrund der schlechten optischen Qualität nicht eingesetzt werden kann. Die Photonenausbeute der Quarzglas-Stäbe entspricht den Erwartungen und ihre Qualität ist untereinander vergleichbar. Die mit diesen Stäben gemessenen Werte für

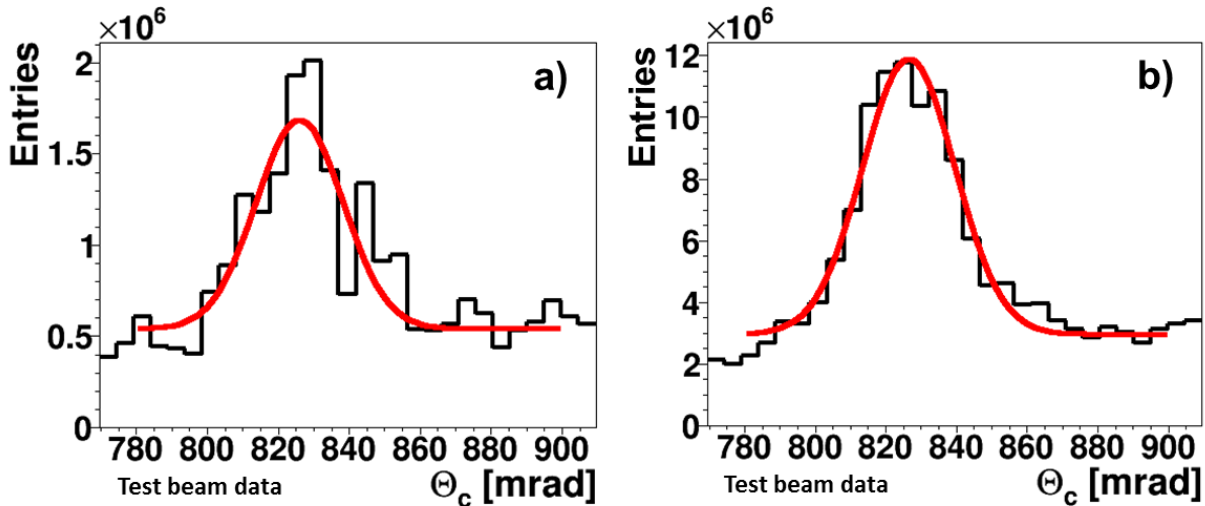


Figure 6.5: Rekonstruierter Cherenkov-Winkel pro Photon in den 2012 Daten für eine Konfiguration mit einem schmalen Quarzglas-Stabe und einer sphärischen Linse mit Luftspalt. Die Verteilung fuer den Polarwinkel von  $124^\circ$  (a) zeigt starke Fluktuationen die in der Kombination von 8 Messungen mit Polarwinkeleinstellungen zwischen  $122$  und  $124^\circ$  (b) nicht mehr entstehen. Die Werte fuer den Mittelwert und die Breite der Verteilungen sind:  $\Theta_C = 826.1$  mrad,  $\sigma_{C,\gamma} = 12.3$  mrad (a) und  $\Theta_C = 826.3$  mrad,  $\sigma_{C,\gamma} = 13.0$  mrad (b).

den Cherenkov-Winkel pro Photon und die SPR sind mit den Simulationen konsistent, wenn man den Beitrag der Strahldivergenz berücksichtigt. Der rekonstruierte Cherenkov-Winkel pro Photon unter Verwendung eines schmalen Quarzglas-Stabes und einer sphärischen Linse mit einem 2 mm breiten Luftspalt zwischen Linse und Prisma ist in Abb. 6.5a dargestellt. Die dort gezeigte Verteilung zeigt große Fluktuationen, hervorgerufen durch Ringe, die größtenteils parallel zu den MCP-PMT Spalten verlaufen. Dieser Effekt kann vermieden werden, indem man die Daten von Messungen mit verschiedenen Polarwinkeln miteinander kombiniert. In Abb. 6.5b ist das Ergebnis der Anwendung dieser Methode zu erkennen, bei dem 8 Messungen mit Polarwinkeleinstellungen zwischen  $122^\circ$  und  $124^\circ$  kombiniert wurden. Eine Gauß-Funktion mit linearem Untergrund wurde an die Verteilung angepasst. Der resultierende Mittelwert und die Breite stimmen mit der Simulation überein. Die Anzahl der pro Spur nachgewiesenen Photonen hängt sowohl von der Länge der Teilchenspur innerhalb des Stabes ab, als auch von der optischen Qualität des Radiators.

Die Vorhersage der optischen Simulation in Bezug auf die Photonenausbeute als Funktion des Spur-Polarwinkels ist in Abb. 6.6a für verschiedene Linsenkonfigurationen dargestellt. Die normale sphärische UV Linse mit Antireflex-Beschichtung und einem 2 mm breiten Luftspalt, weist für die meisten Spurwinkel eine annehmbare Ausbeute im Vergleich zu der zylindrischen Verbundlinse (Quarzglas und N-LaK33) mit hohem Brechungsindex auf. Eine Ausnahme stellt hierbei der Winkelbereich zwischen  $80$  und  $100^\circ$  dar. Die Photonenausbeute wurde in der Strahlzeit im Jahr 2012 am CERN für die in Abb. 6.6a genannten Konfigurationen unter zwei verschiedenen Polarwinkeln, gezeigt in Abb. 6.6b und Abb. 6.6c, vermessen. Die gemessene Anzahl an Treffern pro Spur beinhaltet Beiträge von delta-Elektronen (3-5 pro Spur) und von der bereits erwähnten Ladungsteilung zwischen einzelnen MCP-PMT Anoden (10-15 Die Performanz der hochbrechenden Verbundlinse stellt sich basierend auf den Messergebnissen als äußerst vielversprechend dar. Die mit dieser Linse erzielbare hohe Photonenausbeute macht das System in Hinblick auf Spur- und Ereignis-Untergrund tolerant, was im Falle der einfachen sphärischen Linse nicht der Fall ist. Basierend auf den Ergebnissen der vorliegenden Arbeit

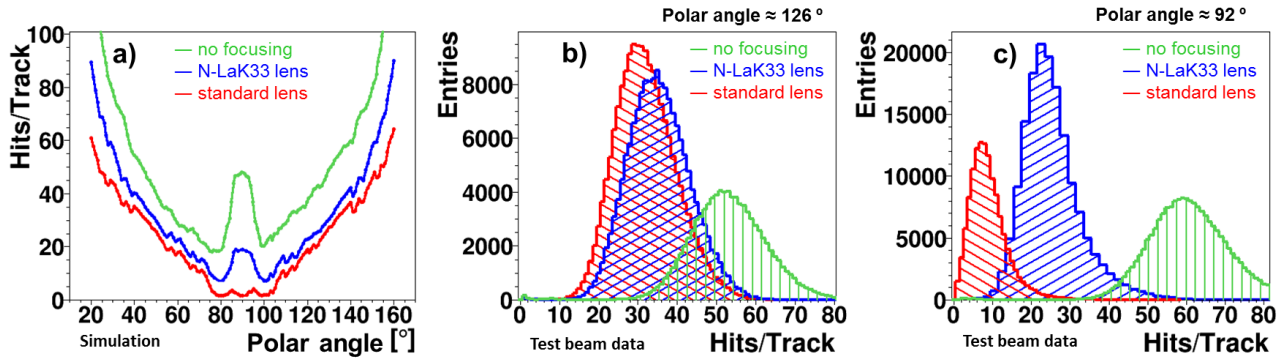


Figure 6.6: Rekonstruierter Cherenkov-Winkel pro Photon in den 2012 Daten für eine Konfiguration mit einem schmalen Quarzglas-Stabe und einer sphärischen Linse mit Luftspalt. Die Verteilung fuer den Polarwinkel von  $124^\circ$  (a) zeigt starke Fluktuationen die in der Kombination von 8 Messungen mit Polarwinkeleinstellungen zwischen  $122$  und  $124^\circ$  (b) nicht mehr entstehen. Die Werte fuer den Mittelwert und die Breite der Verteilungen sind:  $\Theta_C = 826.1$  mrad,  $\sigma_{C,\gamma} = 12.3$  mrad (a) und  $\Theta_C = 826.3$  mrad,  $\sigma_{C,\gamma} = 13.0$  mrad (b). 6 Anzahl der Photonen pro Teilchen als Funktion des Polarwinkels in der Simulation des 2012 Prototyps für drei Linsekonfigurationen (a). Gemessene Anzahl von Photonen pro Ereignis in der 2012 Strahlzeit für zwei Polarwinkel und drei Linsekonfigurationen (b, c). Die hochbrechende Verbundlinse ist in Blau markiert, die sphärische UV Linse in Rot und die direkte Kopplung des Stabs ohne Linse in Grün.

wird eine weiterentwickelte Version dieses fokussierenden Linsensystems in einer Teststrahlzeit im Jahr 2014 zum Einsatz kommen, um die Studien hinsichtlich des Fokussierungssystems für den PANDA Barrel DIRC zu einem erfolgreichen und einsatzfähigen Abschluss zu bringen.

# Bibliography

- [1] The PANDA Micro Vertex Detector. Technical report, 2012. <http://arxiv.org/abs/1207.6581>.
- [2] The PANDA Straw Tube Tracker. Technical report, 2013. <http://arxiv.org/abs/1205.5441>.
- [3] K. Föhl. Nucl. Instr. and Meth., A732:346, 2013.
- [4] The PANDA Electromagnetic Calorimeter. Technical report, 2008. <http://arxiv.org/abs/0810.1216v1>.
- [5] The PANDA Muon System. Technical report, 2011.
- [6] The PANDA Solenoid and Dipole Spectrometer Magnets. Technical report, 2009. <http://arxiv.org/abs/0907.0169>.
- [7] Technical progress report for PANDA. Technical report, 2005.
- [8] D. Bettoni. Journal of Physics: Conference Series, 9:309, 2005.
- [9] FAIR Conceptual Design Report. Technical report, 2001.
- [10] Physics Performance Report for PANDA: Strong Interaction Studies with Antiprotons <http://arxiv.org/abs/0903.3905v1>. Technical report.
- [11] B. Aubert, et al. Phys. Rev., D74:032007, 2006.
- [12] S. Godfrey and N. Isgur. Phys. Rev., D32:189, 1985.
- [13] M. C. Mertens. Determination of the  $Ds_0^*(2317)$  width with the PANDA detector. PhD thesis, EXA Wien, 2011.
- [14] J. Beringer, et al. Phys. Rev., D86:010001, 2012.
- [15] M. Patsyuk. Simulation, reconstruction and design optimization for the PANDA Barrel DIRC. PhD thesis, Johann Wolfgang Goethe-Universität in Frankfurt am Main, 2015. In preparation.
- [16] J. Seguinot and T. Ypsilantis. Nucl. Instr. and Meth., A 433:1, 1999.
- [17] I. Adam, et al. Nucl. Instr. and Meth., A 538(281), 2005.
- [18] P. Beckmann and A. Spizzichino. The Scattering of Electromagnetic Waves from Rough Surfaces. Pergamon, 1963.
- [19] P. Cherenkov. Phys. Rev., 52:378, 1937.

- [20] I. Tamm I. Frank. Doklady Akademii Nauk, 14:109, 1937.
- [21] B. Ratcliff and J. Schwiening. Cherenkov Counters in: Handbook of Particle Detection and Imaging. Springer, 1st edition, December 2011.
- [22] H. Motz and L. Schiff. Am. J. Phys., 21:258, 1952.
- [23] B. N. Ratcliff. Imaging rings in ring imaging cherenkov counters. RICH2002 in Pylos Greece, 2002.
- [24] P. Coyle, et al. Nucl. Instr. and Meth., A 346:292, 1994.
- [25] Eugene Hecht. Optics. Addison-Wesley Longman, 4 edition, 2002.
- [26] SLAC National Accelerator Laboratory, 2575 Sand Hill Road, Menlo Park, CA 94025, USA. <https://www6.slac.stanford.edu/>.
- [27] J. Va'vra, et al. Nucl. Instr. and Meth., A 595:104, 2008.
- [28] SuperB Technical Design Report. Technical Report INFN-13-01/PI, LAL 13-01, SLAC-R-1003, 2013.
- [29] Particle identification at PANDA, report of the PID TAG. Technical report, 2009.
- [30] PHOTONIS. 660 Main Street, Sturbridge, MA 01518, USA. <http://www.photonis.com/en/ism/63-planacon.html>.
- [31] J. Vavra, et al. Nucl. Instr. and Meth., A 572:459, 2007.
- [32] J. Vavra, et al. Nucl. Instr. and Meth., A 606:404, 2005.
- [33] A. Britting. Analyse und signifikante Verbesserung der Lebensdauer von Microchannel-Plate Photomultipliern hinsichtlich ihrer Applikation für das PANDA-Experiment. PhD thesis, Friedrich-Alexander-Universität Erlangen-Nürnberg, 2014.
- [34] A Lehmann, et al. JINST, 9:C02009, 2014.
- [35] Private communication - Gianluigi Boca.
- [36] R. Dzhygadlo. Nucl. Instr. and Meth., A, 2014. DOI: 10.1016/j.nima.2014.04.073.
- [37] M. Zühlendorf. Alternative Geometrical Designs for Quartz-based Cherenkov Detectors for the PANDA Barrel DIRC Detector. PhD thesis, Johann Wolfgang Goethe-Universität in Frankfurt am Main, 2014. In preparation.
- [38] Radiant Zemax, 22908 NE Alder Crest Drive, WA 98053 USA. <https://www.radiantzemax.com>.
- [39] ExxonMobil Lubricants & Specialties Europe, Hermeslaan 2, 1831 Machelen, Belgium.
- [40] R. Hohler. Prototyp-Radiatoren eines Barrel-DIRC fuer das PANDA-Experiment. PhD thesis, Johann Wolfgang Goethe-Universität in Frankfurt am Main, 2011.
- [41] S. Agostinelly, et al. Nucl. Instr. and Meth., A 506:250, 2003.
- [42] J. Allison, et al. Nuclear Science, 53:270, 2006. <http://arxiv.org/abs/1205.5441>.

- [43] S. Spataro. J. Phys. Conf. Ser., 119:032035, 2008.
- [44] M. Al-Turany and F. Uhlig. Proceedings of Science, ACAT08:48, 2008.
- [45] [svn+shn://charme@lxi001.gsi.de/v/charme/svn/drcprop](http://svn+shn://charme@lxi001.gsi.de/v/charme/svn/drcprop).
- [46] InSync, Inc. 2511C Broadbent Parkway NE, Albuquerque, New Mexico 87107, USA. <http://www.insyncoptics.com>.
- [47] J. Cohen-Tanugi, et al. Nucl. Instr. and Meth., A 515:680, 2003.
- [48] Vitreosil natural fused silica material and Spectrosil are trademarks of TSL Group PLC, Wallsend, Tyne on Wear, NE28 6DG, UK.
- [49] Heraeus Amersil Inc., 3473 Satellite Blvd. 300, Duluth, GA 30136, USA.
- [50] EPO-TEK 301-2, Epoxy Technology Inc., 14 Fortune Drive, Billerica, MA 01821, USA.
- [51] M. Hoek et al. Nucl. Instr. and Meth., A 595:190, 2008.
- [52] Corning Incorporated, One Riverfront Plaza, NY 14831 USA. <http://www.corning.com/index.aspx>.
- [53] J. Schwiening, et al. JINST, 4:P10004, 2009.
- [54] Market Tech, Inc., 340 El Pueblo Rd Suite C Scotts Valley, CA 95066, USA. [http://www.markettechinc.net/pdf/MicroChip\\_SNVU.pdf](http://www.markettechinc.net/pdf/MicroChip_SNVU.pdf).
- [55] Newport Corporation 1791 Deere Avenue, Irvine CA 92606, USA.
- [56] Hamamatsu Photonics Deutschland GmbH, Arzbergerstr. 10, D-82211 Herrsching am Ammersee, Germany. <http://www.hamamatsu.com>.
- [57] CTLab, 15 Termo Lane Techno Park Stellenbosch, South Africa. <http://www.ctlab.com/>.
- [58] J. Va'vra, et al. SLAC-PUB-13464, 2008. DOI: 10.1109/NSSMIC.2008.4774841.
- [59] J. Benitez. Measurement of the  $D_s^-$  Leptonic Decay Constant  $f_{D_s}$  and Observation of New Resonances Decaying to  $D^*\pi$ . PhD thesis, Stanford University, 2011.
- [60] Hellma Optik GmbH, Mühlenstrasse 30, 07704 Jena, Germany. <http://www.hellma-optics.com>.
- [61] A.G. Schott, Hattenbergstrasse 10, 55122 Mainz, Germany.
- [62] Advanced Laser Diode Systems A.L.S. GmbH, Schwarzschildstr. 6, D-12489 Berlin, Germany. [http://www.bbnint.co.uk/publications/manuals/MANUAL\\_1MHzPiLas\\_engl\\_SN0297.pdf](http://www.bbnint.co.uk/publications/manuals/MANUAL_1MHzPiLas_engl_SN0297.pdf).
- [63] I. Frohlich, et al. IEEE Trans. Nucl. Sci., NS-55:59, 2008.
- [64] F. Anghinolfi, et al. Nucl. Instr. and Meth., A 533:183, 2004.
- [65] Developed in CERN low power front-end amplifier discriminator NINO ASIC chip. <http://knowledgetransfer.web.cern.ch/technology-transfer/external-partners/nino>.

- [66] NXP Semiconductors, PO Box 80073, 5600 KA Eindhoven, The Netherlands.
- [67] The Bosch Group. <http://www.boschtools.com>.
- [68] Silitech SA, Worbstrasse 173, 3073 Gmligen. USA <http://www.silitech.ch>.
- [69] Eljen Technology, 1300 W. Broadway Sweetwater, TX79556, USA. <http://www.eljentechnology.com/index.php/products/accessories/93-ej-500>.
- [70] Advanced Glass Industries. 1335 Emerson Street, Rochester, NY 14606. <http://www.advancedglass.net>.
- [71] A. Lehmann A. Britting and F.Uhlig. JINST, 6:C10001, 2011.
- [72] Private communication - J. Schwiening.



## Acknowledgment

First of all, I want to thank my mentor Dr. Joachim Schwiening. Apart from his contributions of time and ideas to make my Ph.D. experience productive and stimulating, he was and remains my best role model for a scientist, mentor, and teacher.

I would like to express my special appreciation to my supervisor Prof. Dr. Klaus Peters. His support and advice on both research as well as on my career have been invaluable.

I will forever be grateful to Dr. Carsten Schwartz. His way of approaching technical challenges driven by his natural curiosity and joy ensured me of physics being the right path for me.

I also thank the physicists Dr. Bogdan Zwieglinski, Dr. Tomasz Pawlak, Dr. Marek Kowalski, and Grazyna Fox. They had a great influence on deepening my love for physics during the past years, after I decided to become a physicist at the age of eleven.

I would like to thank all the colleagues from the Had1 group, other groups of PANDA, and people out of the collaboration for the great support, and making my Ph.D time enjoyable.

The funding sources by the Helmholtz Graduate School for Hadron and Ion Research “HGS-HIRe for FAIR” are gratefully acknowledged.

Last but not least, I would like to thank my family for all their love and encouragement.

# Akademische Lehrer

Prof. dr hab. J. Zebrowski

Prof. dr hab. J. Holyst

Prof. dr hab. A. Zagorski

Prof. dr hab. J. Pluta

Prof. dr hab. M. Maczynsk

Prof. dr hab. A. Kolodziejczyk

Prof. dr hab. J. Garbarczyk

Prof. dr hab. R. Bacewicz

Prof. dr hab. J. Kosinski

Prof. dr hab. R. Swirkowicz

Prof. dr hab. B. Slowinski

Prof. dr hab. A. Sukiennicki

Prof. dr hab. Z. Gontarz

Prof. dr hab. I. Strzakowski

Prof. dr hab. J. Jasiski

Prof. dr hab. L. Adamowicz

---

# Curriculum Vitae

**Grzegorz Kalicy**

Born 24.04.1984 in Warsaw



## Experience/Education:

*2010-2014:*

- Research for PhD thesis at GSI Helmholtzzentrum für Schwerionenforschung in Darmstadt, Germany
- PhD student at Johann Wolfgang Goethe-Universität in Frankfurt am Main
- Fellow of the Helmholtz Graduate School for Hadron and Ion Research

*2006-2009:*

- Research for Master thesis at the Andrzej Soltan Institute for Nuclear Studies (SINS) in Świerk, Poland ending in a master's degree.  
**Thesis:** "Amplitude and time response of cooled PWO scintillators, readout with Avalanche photodiodes, to low-energy gamma-rays in 4-20 MeV range"

*2003-2006:*

- Student at the Faculty of Physics at Warsaw University of Technology in Warsaw, Poland. Master of Science in Engineering in the field of Applied Physics.

*2000-2003:*

- Student at the E. Jankowski High School Nr. 39 in Warsaw, Poland.

*1999-2000:*

- Student at the High School Nr. 1 in Milanówek, Poland.

*1993-1999:*

- Student at the F. Chopin Elementary School Nr. 3 in Milanówek, Poland.

*1991-1993:*

- Student at the Elementary School Nr. 37 in Warsaw, Poland.